

IEEE Press Series on Sensors

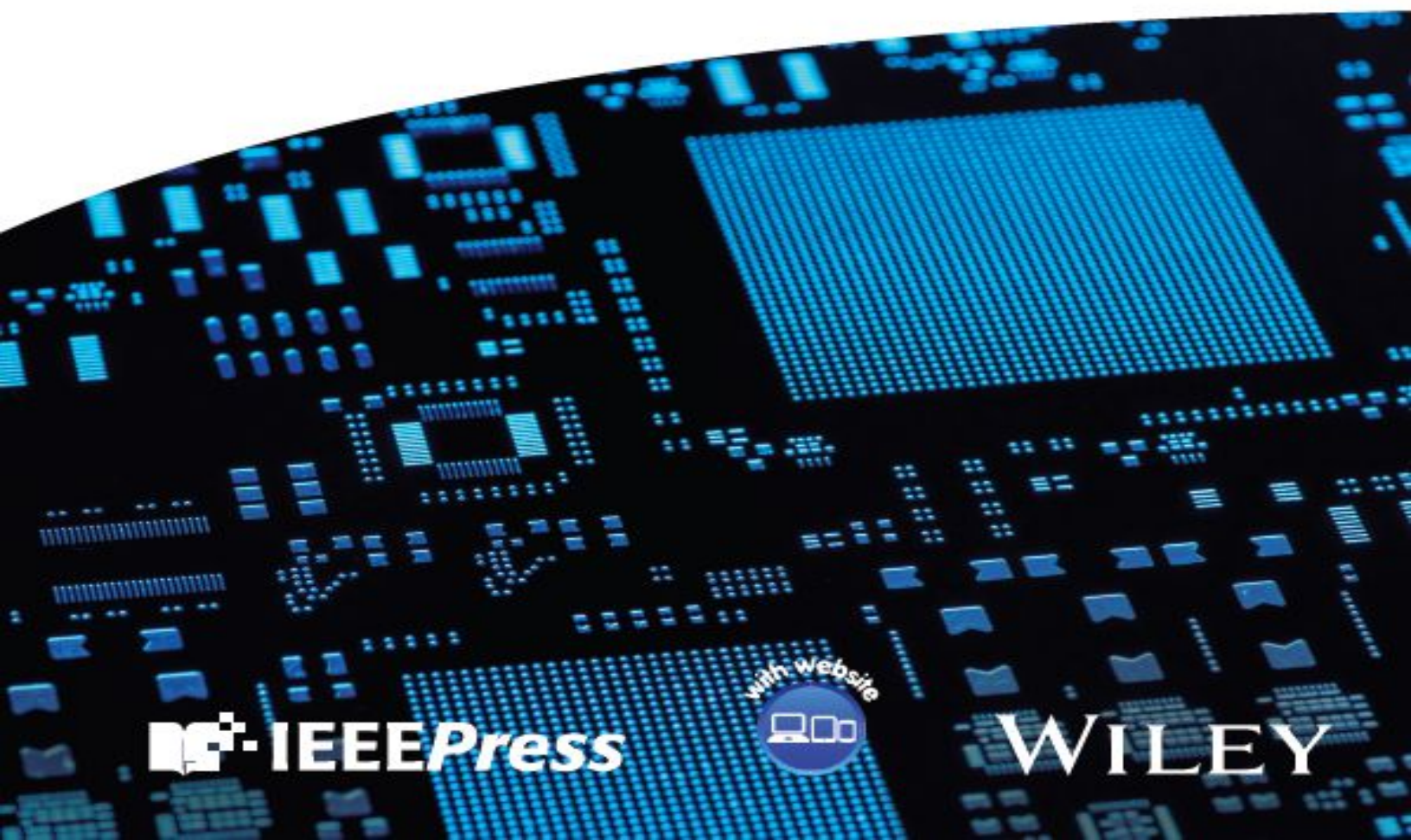
Vladimir Lumelsky, Series Editor



Micro Electromechanical Systems (MEMS)

Practical Lab Manual

Edited by Sanket Goel



 **IEEE Press**



WILEY

Table of Contents

[Cover](#)

[Table of Contents](#)

[Series Page](#)

[Title Page](#)

[Copyright Page](#)

[About the Editor](#)

[List of Contributors](#)

[Preface](#)

[About the Companion Website](#)

[1 Multiphysics Simulations on the Effect of Fluidic
Concentration Profiles Over Y-Channel and T-Channel Designs](#)

[1.1 Introduction](#)

[1.2 Real-Time Applications of This Study](#)

[1.3 Simulation Section](#)

[1.4 Results and Discussions](#)

[1.5 Conclusion](#)

[References](#)

[2 Droplet Generation in T-Junction Microchannel Using
Multiphysics Software](#)

[2.1 Introduction](#)

[2.2 Simulation Section](#)

[2.3 Result and Discussion](#)

[2.4 Conclusion](#)

[References](#)

[3 Cleanroom-Assisted and Cleanroom-Free Photolithography](#)

[3.1 Introduction](#)

[3.2 Photolithography Basics, Classification and Applications](#)

3.3 Experimental Section on Designing and Development of Features Using Photolithography

3.4 Conclusion

References

4 Additive Manufacturing (3D Printing)

4.1 Stereolithography (SLA) Printing of Y-Channeled Microfluidic Chip

4.2 Fused Deposition Modeling (FDM): Fabrication of Single Electrode Electrochemiluminescence Device

References

5 Laser Processing

5.1 CO₂ Laser for Electrochemical Sensor Fabrication

5.2 One-Step Production of Reduced Graphene Oxide from Paper via 450 nm Laser Ablations

5.3 Conclusion

References

6 Soft Lithography: DLW-Based Microfluidic Device Fabrication

6.1 Introduction

6.2 Designing Section

6.3 Conclusion

References

7 Electrode Fabrication Techniques

7.1 Inkjet Printing Technique: Electrode Fabrication for Advanced Applications

7.2 Screen Printing Technique for Electrochemical Sensor Fabrication

7.3 Physical Vapor Deposition (PVD) Technique for Electrode Fabrication

7.4 Conclusion

References

8 Morphological Characterization

8.1 Morphological Studies with Different Techniques

[8.2 Scanning Electron Microscopy](#)

[8.3 Steps Involved in the Scanning Electron Microscope Characterization](#)

[8.4 X-Ray Diffraction \(XRD\)](#)

[8.5 Optical LED Microscope](#)

[8.6 Contact Angle](#)

[References](#)

[9 Spectroscopic Characterization](#)

[9.1 Introduction](#)

[9.2 Ultraviolet-Visible \(UV-Vis\) Spectrophotometers](#)

[9.3 X-Ray Photoelectron Spectroscopy \(XPS\)](#)

[9.4 Raman Spectroscopy](#)

[9.5 Fourier Transform Infrared \(FTIR\) Spectroscopy](#)

[References](#)

[10 Microfluidic Devices](#)

[10.1 Electrochemical Detection of Bacteria, Biomarkers, Biochemical, and Environmental Pollutants](#)

[10.2 Microfluidics Integrated Electrochemiluminescence System for Hydrogen Peroxide Detection](#)

[10.3 Development of Microfluidic Chip for Colorimetric Analysis](#)

[10.4 Development of Disposable and Eco-Friendly \$\mu\$ PADs as Chemiluminescence Substrates](#)

[10.5 Microfluidic Devices for Polymerase Chain Reaction \(PCR\)](#)

[References](#)

[11 Wearable Devices](#)

[11.1 Application of Laser-Induced Graphene in Breath Analysis](#)

[11.2 Wearable Microfluidic Device for Nucleic Acid Amplification](#)

[11.3 Wearable Patch Biofuel Cell](#)

[References](#)

[12 Energy Devices](#)

[12.1 Introduction](#)

[12.2 Enzymatic Biofuel Cells and Microbial Fuel Cells](#)

[12.3 Microbial Fuel Cells \(MFCs\)](#)

[12.4 Electrochemical Characterization of Supercapacitor Energy Devices](#)

[References](#)

[13 Conclusion and Future Outlook](#)

[Index](#)

[IEEE Press Series on Sensors](#)

[End User License Agreement](#)

List of Tables

Chapter 1

[Table 1.1 Y- and T-channel simulations with a varying flow rate of Inlet 2 ...](#)

Chapter 2

[Table 2.1 Variable process definitions.](#)

Chapter 3

[Table 3.1 Classification of different classes of clean room.](#)

[Table 3.2 Comparative analysis between both approaches of photolithography....](#)

Chapter 9

[Table 9.1 IR regions and respective spectra.](#)

[Table 9.2 Functional groups and respective frequency ranges.](#)

List of Illustrations

Chapter 1

[Figure 1.1 CAD images of Y and T-shaped channels \(All dimensions are in mm\)....](#)

Chapter 2

[Figure 2.1 T-junction microfluidic channel.](#)

[Figure 2.2 Model and geometry definition \(a\) T-junction microfluidic channel...](#)

[Figure 2.3 Output result for the T-junction droplet breakout \(a\) Volume frac...](#)

Chapter 3

[Figure 3.1 A schematic showing the difference between the positive and negat...](#)

[Figure 3.2 An illustration of step-by-step procedures followed to develop a ...](#)

Chapter 4

[Figure 4.1 CAD process to develop a Y-channeled microfluidic chip: \(a\) line ...](#)

[Figure 4.2 Slicing operations over the Y-channeled microfluidic chip using t...](#)

[Figure 4.3 The final SLA printed Y-channeled microfluidic chip leveraged for...](#)

[Figure 4.4 \(a\) Real picture of 3D Printed MSEC held by universal support,...](#)

[Figure 4.5 Step-by-step process to fabricate electrodes using 3D printer.](#)

Chapter 5

[Figure 5.1 \(a\) Fabrication procedure of glucose monitoring LIG sensor, \(b...](#)

[Figure 5.2 Step-by-step process to fabricate electrodes using laser-induced ...](#)

[Figure 5.3 Design of a three-electrode system \(all dimensions are in mm\).](#)

[Figure 5.4 Gcode conversion via GUI of Voxelizer software, \(a\) File import a...](#)

[Figure 5.5 Gcode conversion via GUI of Voxelizer software, \(a\).gcode convers...](#)

[Figure 5.6 Production of conductive rGO patterns via blue diode 450 nm laser...](#)

Chapter 6

[Figure 6.1 Step-by-step process involved in creating micro patterns with a D...](#)

[Figure 6.2 Procedure to prepare a PDMS mold by mixing PDMS base and curing a...](#)

[Figure 6.3 Fabrication of Y-channel microfluidic device.](#)

Chapter 7

[Figure 7.1 CAD model to develop a microelectrode system, creating \(a\) a 25 m...](#)

[Figure 7.2 \(a\) Import the DXF file to convert it into Gerber format using DI...](#)

[Figure 7.3 \(a\) Glass slide as substrate, \(b\) clamp the glass slides on the p...](#)

[Figure 7.4 \(a\) schematic for detecting plant biomarkers using screen printed...](#)

[Figure 7.5 Step-by-step process to fabricate electrodes using screen printin...](#)

[Figure 7.6 The schematic of the basic setup used in the PVD.](#)

[Figure 7.7 The SS masks, the substrate arrangement, and the fabricated gold ...](#)

Chapter 8

[Figure 8.1 Steps involved in SEM characterization.](#)

[Figure 8.2 SEM image of the sample with a resolution of 10 and 500 \$\mu\text{m}\$.](#)

[Figure 8.3 The schematic diagram of bragg's law.](#)

[Figure 8.4 The schematic operational diagram of XRD.](#)

[Figure 8.5 Setup for the X-ray diffraction.](#)

[Figure 8.6 The sample preparation on the sample holder.](#)

[Figure 8.7 \(a\) Design of microchannel; \(b\) Developed master on glass slides ...](#)

[Figure 8.8 Optical Leica DM 2000 LED microscope.](#)

[Figure 8.9 Contact angle measurement with its surface wetting.](#)

[Figure 8.10 Setup of contact angle measurement.](#)

[Figure 8.11 Computer software for dispensing/filling the droplet-based syrin...](#)

[Figure 8.12 Obtained data of the contact angle measured for the substrate of...](#)

Chapter 9

[Figure 9.1 Device operation flowchart.](#)

[Figure 9.2 UV-Vis spectroscopy of the laser-induced reduced graphene oxide \(...\)](#)

[Figure 9.3 The schematic view of the photoelectron spectrometer.](#)

[Figure 9.4 XPS analysis graphs for the Co-Co₃O₄-rGO, including survey spectr...](#)

[Figure 9.5 Schematic to show the arrangement of the sample on a glass slide ...](#)

[Figure 9.6 Raman spectra for the formation of rGO \[2\]/with permission of IOP...](#)

[Figure 9.7 Brief overview of FTIR spectroscopy.](#)

[Figure 9.8 FTIR spectra of polyimide films.](#)

Chapter 10

[Figure 10.1 Working principle of an electrochemical sensor.](#)

[Figure 10.2 Stepwise fabrication process to develop an electro-microfluidic ...](#)

[Figure 10.3 Electrochemical response from cyclic voltammetry study for bacterial gro...](#)

[Figure 10.4 \(a\) A microfluidic-based device developed for lactate detection ...](#)

[Figure 10.5 Schematic of fabricated three-electrode system \(a\) LIrGO three-e...](#)

[Figure 10.6 Fabrication of LIG-based electrochemical sensor for detecting \(a...](#)

[Figure 10.7 Types of electrode configurations in the ECL process.](#)

[Figure 10.8 Visual image of the emitted ECL signal over a bipolar ECL electr...](#)

[Figure 10.9 Illustrative diagram of reduction in the intensity \(dark blue to...](#)

[Figure 10.10 A zig-zag design to develop a photoresist using a direct laser ...](#)

[Figure 10.11 \(a\) UV exposed photoresist coated over a glass slide \(b\) post-d...](#)

[Figure 10.12 Measuring the dimensions of the developed photoresist at \(a\) st...](#)

[Figure 10.13 Step-by-step bonding of glass and PDMS microchip to develop a m...](#)

[Figure 10.14 Design of hydrophobic barrier for fluidic flow \(all dimensions ...](#)

[Figure 10.15 Overview of process steps to be followed in the slicing tool.](#)

[Figure 10.16 3D printed hydrophobic barriers on paper. The traces are of PCL...](#)

[Figure 10.17 Real-time validation of fluid transport through the 3D printed ...](#)

[Figure 10.18 Schematic for the Microfluidic Channel. Dimensions may be selec...](#)

Chapter 11

[Figure 11.1 Laser ablation for sensor fabrication \(a\) attaching the polyamid...](#)

[Figure 11.2 Functionality of the sensor is explained \(a\) when exhaled air or...](#)

[Figure 11.3 Represents the fabrication of wearable microchamber. The soft li...](#)

[Figure 11.4 Represents the amplified product using Isothermal amplification,...](#)

[Figure 11.5 Wearable biofuel cell setup: \(a\) substrate grade 1 filter paper;...](#)

Chapter 12

[Figure 12.1 Fabrication methodology of the hydrogen fuel cell: \(a\).3D printe...](#)

[Figure 12.2 \(a\) PET sheet: \(b\) adhesive tape over PET sheet; \(c\) carbon clot...](#)

[Figure 12.3 Fabrication steps of microbial fuel cell: \(a\).glass slide; \(b\) f...](#)

[Figure 12.4 Electrode fabrication process steps to form doped laser induced ...](#)

[Figure 12.5 Electrochemical analysis: \(a\)–\(c\) CV, \(d\)–\(f\) GCD analysis \(g\) E...](#)

IEEE Press
445 Hoes Lane
Piscataway, NJ 08854

IEEE Press Editorial Board
Sarah Spurgeon, *Editor-in-Chief*

Moeness Amin	Ekram Hossain	Desineni Subbaram Naidu
Jón Atli Benediktsson	Brian Johnson	Tony Q. S. Quek
Adam Drobot	Hai Li	Behzad Razavi
James Duncan	James Lyke	Thomas Robertazzi
	Joydeep Mitra	Diomidis Spinellis

Micro Electromechanical Systems (MEMS)

Practical Lab Manual

Edited by

Sanket Goel

BITS Pilani, Hyderabad Campus, Hyderabad, India

IEEE Press Series on Sensors

 **IEEE*Press***

WILEY

Copyright © 2025 by The Institute of Electrical and Electronics Engineers, Inc.
All rights reserved.

Published by John Wiley & Sons, Inc., Hoboken, New Jersey.
Published simultaneously in Canada.

No part of this publication may be reproduced, stored in a retrieval system, or transmitted in any form or by any means, electronic, mechanical, photocopying, recording, scanning, or otherwise, except as permitted under Section 107 or 108 of the 1976 United States Copyright Act, without either the prior written permission of the Publisher, or authorization through payment of the appropriate per-copy fee to the Copyright Clearance Center, Inc., 222 Rosewood Drive, Danvers, MA 01923, (978) 750-8400, fax (978) 750-4470, or on the web at www.copyright.com. Requests to the Publisher for permission should be addressed to the Permissions Department, John Wiley & Sons, Inc., 111 River Street, Hoboken, NJ 07030, (201) 748-6011, fax (201) 748-6008, or online at <http://www.wiley.com/go/permission>.

Trademarks: Wiley and the Wiley logo are trademarks or registered trademarks of John Wiley & Sons, Inc. and/or its affiliates in the United States and other countries and may not be used without written permission. All other trademarks are the property of their respective owners. John Wiley & Sons, Inc. is not associated with any product or vendor mentioned in this book.

Limit of Liability/Disclaimer of Warranty: While the publisher and author have used their best efforts in preparing this book, they make no representations or warranties with respect to the accuracy or completeness of the contents of this book and specifically disclaim any implied warranties of merchantability or fitness for a particular purpose. No warranty may be created or extended by sales representatives or written sales materials. The advice and strategies contained herein may not be suitable for your situation. You should consult with a professional where appropriate. Further, readers should be aware that websites listed in this work may have changed or disappeared between when this work was written and when it is read. Neither the publisher nor authors shall be liable for any loss of profit or any other commercial damages, including but not limited to special, incidental, consequential, or other damages.

For general information on our other products and services or for technical support, please contact our Customer Care Department within the United States at (800) 762-2974, outside the United States at (317) 572-3993 or fax (317) 572-4002.

Wiley also publishes its books in a variety of electronic formats. Some content that appears in print may not be available in electronic formats. For more information about Wiley products, visit our web site at www.wiley.com.

Library of Congress Cataloging-in-Publication Data Applied for:

Hardback: 9781394229833

Cover Design: Wiley

Cover Image: © Jordan Lye/Getty Images

About the Editor



Sanket Goel is a professor with the Department of Electrical and Electronics Engineering at BITS Pilani, Hyderabad Campus. He previously headed the same department and R&D department at UPES, Dehradun. He is the principal investigator of MEMS, Microfluidics and Nanoelectronics (MMNE) Lab, which works toward realizing futuristic smart sensors and intelligent energy harvesters encompassing various multidisciplinary domains. Prof. Goel has published more than 350 scientific articles in various domains, including microfluidics, biosensors, nanoelectronics, fuel cells, smart sensors, MEMS, solar energy, wearable devices and

cyber-physical systems. He has 60+ patents (including 12 granted) to his credits, has delivered more than 110 invited talks and has supervised 50+ PhD students. Prof. Goel is also on the editorial board of numerous journals and has a multitude of accolades including Fulbright and JSPS fellowships. Currently, he is also the dean (Research and Innovation) at BITS Pilani and Distinguished Lecturer of IEEE Sensors Council. Prof. Goel is a co-founder of three spin-offs: Cleome Innovations, Pyrome Innovations, and Sensome Innovations.

List of Contributors

Himanshi Awasthi

MEMS, Microfluidics and
Nanoelectronics (MMNE) Lab
Department of Electrical and
Electronics Engineering
Birla Institute of Technology and
Science (BITS) Pilani
Hyderabad Campus
Hyderabad, Telangana, India

Aniket Balapure

MEMS, Microfluidics and
Nanoelectronics (MMNE) Lab
Department of Electrical and
Electronics Engineering
Birla Institute of Technology and
Science (BITS) Pilani
Hyderabad Campus
Hyderabad, Telangana, India

Manish Bhaiyya

MEMS, Microfluidics and
Nanoelectronics (MMNE) Lab
Department of Electrical and
Electronics Engineering
Birla Institute of Technology and
Science (BITS) Pilani
Hyderabad Campus
Hyderabad, Telangana, India

K.S. Deepak

MEMS, Microfluidics and
Nanoelectronics (MMNE) Lab
Department of Electrical and
Electronics Engineering
Birla Institute of Technology and

Science (BITS) Pilani, Hyderabad
Campus, Hyderabad, Telangana, India

Department of Mechanical
Engineering, Birla Institute of
Technology and
Science (BITS) Pilani
Hyderabad Campus, Jawahar Nagar
Telangana, India

Satish Kumar Dubey

MEMS, Microfluidics and
Nanoelectronics (MMNE) Lab
Department of Electrical and
Electronics Engineering, Birla
Institute of Technology and Science
(BITS) Pilani, Hyderabad Campus
Hyderabad, Telangana, India

Department of Mechanical
Engineering, Birla Institute of
Technology and Science (BITS) Pilani
Hyderabad Campus, Hyderabad
Telangana, India

Sohan Dudala

MEMS, Microfluidics and
Nanoelectronics (MMNE) Lab,
Department of Electrical and
Electronics Engineering, Birla
Institute of Technology and Science
(BITS), Pilani, Hyderabad Campus
Hyderabad, Telangana, India

Sonal Fande

MEMS, Microfluidics and
Nanoelectronics (MMNE) Lab
Department of Electrical and
Electronics Engineering
Birla Institute of Technology and

Science (BITS) Pilani, Hyderabad
Campus, Hyderabad, Telangana, India

Department of Pharmacy, Birla
Institute of Technology and Science
(BITS) Pilani, Hyderabad Campus
Hyderabad, Telangana, India

Sanket Goel

MEMS, Microfluidics and
Nanoelectronics (MMNE) Lab,
Department of Electrical and
Electronics Engineering, Birla
Institute of Technology and Science
(BITS), Pilani, Hyderabad Campus
Hyderabad, Telangana, India

Amreen Khairunnisa

MEMS, Microfluidics and
Nanoelectronics (MMNE) Lab
Department of Electrical and
Electronics Engineering, Birla
Institute of Technology and Science
(BITS) Pilani, Hyderabad Campus
Hyderabad, Telangana, India

Imran Khan

MEMS, Microfluidics and
Nanoelectronics (MMNE) Lab
Department of Electrical and
Electronics Engineering, Birla
Institute of Technology and Science
(BITS) Pilani, Hyderabad Campus
Hyderabad, Telangana, India

Abhishek Kumar

MEMS, Microfluidics and
Nanoelectronics (MMNE) Lab,
Department of Electrical and
Electronics Engineering, Birla
Institute of Technology and Science

(BITS) Pilani, Hyderabad Campus
Hyderabad, Telangana, India

Pavar Sai Kumar

MEMS, Microfluidics and
Nanoelectronics (MMNE) Lab,
Department of Electrical and
Electronics Engineering, Birla
Institute of Technology and Science
(BITS) Pilani, Hyderabad Campus
Hyderabad, Telangana, India

Sanjeet Kumar

MEMS, Microfluidics and
Nanoelectronics (MMNE) Lab
Department of Electrical and
Electronics Engineering
Birla Institute of Technology
and Science (BITS) Pilani
Hyderabad Campus
Hyderabad, Telangana, India

Department of Mechanical
Engineering, Birla Institute of
Technology and Science (BITS) Pilani
Hyderabad Campus, Jawahar Nagar
Telangana, India

Sreerama Amrutha Lahari

MEMS, Microfluidics and
Nanoelectronics (MMNE) Lab,
Department of Electrical and
Electronics Engineering, Birla
Institute of Technology and Science
(BITS) Pilani, Hyderabad Campus
Hyderabad, Telangana, India

Yuvraj Maphrio Mao

MEMS, Microfluidics and
Nanoelectronics (MMNE) Lab
Department of Electrical and

Electronics Engineering, Birla
Institute of Technology and Science
(BITS) Pilani, Hyderabad Campus
Hyderabad, Telangana, India

Dhoni Nagaraj

MEMS, Microfluidics and
Nanoelectronics (MMNE) Lab
Department of Electrical and
Electronics Engineering, Birla
Institute of Technology and Science
(BITS) Pilani, Hyderabad Campus
Hyderabad, Telangana, India

Department of Mechanical
Engineering, Birla Institute of
Technology and Science (BITS) Pilani
Hyderabad Campus, Jawahar Nagar
Telangana, India

Parvathy Nair

MEMS, Microfluidics and
Nanoelectronics (MMNE) Lab
Department of Electrical and
Electronics Engineering, Birla
Institute of Technology and Science
(BITS) Pilani, Hyderabad Campus
Hyderabad, Telangana, India

N. K. Nishchitha

MEMS, Microfluidics and
Nanoelectronics (MMNE) Lab
Department of Electrical and
Electronics Engineering, Birla
Institute of Technology and Science
(BITS) Pilani, Hyderabad Campus
Hyderabad, Telangana, India

Abhishesh Pal

MEMS, Microfluidics and
Nanoelectronics (MMNE) Lab,

Department of Electrical and
Electronics Engineering, Birla
Institute of Technology and Science
(BITS), Pilani, Hyderabad Campus
Hyderabad, Telangana, India

Department of Mechanical
Engineering, Birla Institute of
Technology and Science (BITS) Pilani
Hyderabad Campus, Hyderabad
Telangana, India

R.N. Ponnalagu

MEMS, Microfluidics and
Nanoelectronics (MMNE) Lab,
Department of Electrical and
Electronics Engineering, Birla
Institute of Technology and Science
(BITS) Pilani, Hyderabad Campus
Hyderabad, Telangana, India

Ramya Priya Pujari

Department of Mechanical
Engineering, Birla Institute of
Technology and Science (BITS) Pilani
Hyderabad Campus, Hyderabad
Telangana, India

MEMS, Microfluidics and
Nanoelectronics (MMNE) Lab,
Department of Electrical and
Electronics Engineering, Birla
Institute of Technology and Science
(BITS) Pilani, Hyderabad Campus
Hyderabad, Telangana, India

K. Ramya

MEMS, Microfluidics and
Nanoelectronics (MMNE) Lab
Department of Electrical and

Electronics Engineering
Birla Institute of Technology
and Science (BITS) Pilani
Hyderabad Campus
Hyderabad, Telangana, India

S. Vanmathi

MEMS, Microfluidics and
Nanoelectronics (MMNE) Lab,
Department of Electrical and
Electronics Engineering, Birla
Institute of Technology and Science
(BITS) Pilani, Hyderabad Campus
Hyderabad, Telangana, India

Preface

Emerging technologies assist in effortlessly identifying and addressing crucial scientific challenges in multiple fields. Of these, prominent contemporary areas include molecular diagnostics, cell biology, neuroscience, drug delivery, micro-biotechnology, micro-engineering (fabrication), sensors (wearable), and nano/micro-material engineering, micro electro mechanical systems (MEMS) and microfluidics. MEMS technology excels in integrating microsensors within the system, using its submicron precision fabrication process. At the same time, microfluidics advances its potential in manipulating nano/micro-volume fluids for automated testing through MEMS-supported microchannel fabrications. Interestingly, MEMS technology encompasses a broad range of advanced microfabrication techniques, including photolithography, submicron additive manufacturing, printed electronics, nano/micron thin film depositions, hot embossing, e-beam deposition, laser micromachining, laser-assisted fabrications, micro-electro discharge machining, and phase etching.

The potential of MEMS technologies is often limited due to their inaccessibility and high-level technical language, which poses challenges for undergrads, postgrads, and entry-level industrial researchers. To unlock the great potential and ensure that these researchers can make real-time advances in MEMS products, the language must be made more understandable to a broader audience.

The book addresses this critical gap by compiling technical information into a lab manual designed for hands-on practice and clear understanding. It provides expertise from research scholars to create a comprehensive library to facilitate knowledge transfer. The written content is supported by detailed instructional videos, offering the readers additional step-by-step guidance.

This book is classified into four major parts:

1. Microfluidic simulations ([Chapters 1–2](#))

2. Advanced MEMS fabrication techniques ([Chapter 3–7](#))
3. Material characterizations ([Chapters 8–9](#))
4. Interesting applications ([Chapters 10–12](#)), followed by the outlook of the book and future scope ([Chapter 13](#))

The complexity in experimental studies can be overcome by using computational tools, which help uncover and optimize unknown parameters for deeper insights. [Chapter 1](#) offers a step-by-step guide on using the COMSOL simulation tool to understand concentration profiles in microfluidic channels (Y-shaped and T-shaped designs). The chapter begins with the fundamentals of CAD design for required microfluidic channel shapes, file conversions, and setting of computational parameters. The reader will explore how variations in flow rates of two fluids with unique concentrations affect mixing or concentration profiles. Moreover, this simulation allows the reader to create individual concentration profiles by changing the concentrations of fluids, flow parameters, and channel shapes at the end of this experiment.

[Chapter 2](#) highlights the importance of microfluidic droplet generations, exploring the mechanism of generation and their applications in real-time scenarios. The most used microfluidic shapes for droplet generations include T-Junction, flow focusing, and co-flow devices. This chapter focuses on the T-Junction design (CAD modeling is discussed in [Chapter 1](#) as well) and sets up the process parameters in computational tools to obtain numerical data for generating varying microdroplets. This will help the reader to simulate and generate microdroplets before conducting real-time studies for multiple applications, including lab-on-chip experimentations, chemical synthesis, and cell analysis.

Further, this book provides practical insights into advanced microfabrication concepts using MEMS technologies. [Chapter 3](#) emphasizes the critical role of the photolithography process and photoresist material for MEMS device development. It highlights the information on the classification of clean rooms and the comparison between both processes (i.e., clean room assisted and unassisted). It discusses dimensional accuracy, cost, training, automation, and suitability. Additionally, step-by-step information on these two

processes is disclosed, i.e., via cleanroom assistance (i.e., conventional masked lithography) and without cleanroom assistance (i.e., using a laser unit) to develop microdevices. Moreover, the pictorial flowchart representations of both photolithography processes simplify complex concepts, enabling readers to come up with innovative ideas for develop microdevices.

Advances in additive manufacturing are documented in state-of-the-art literature; however, translating this research into practical applications remains a challenge. [Chapter 4](#) provides insights into two important 3D printing technologies (i.e., stereolithography (SLA) or dynamic light processing (DLP) and fused deposition modeling (FDM). This chapter introduces the concepts of 3D printing, types, their functioning, and related applications, all of which add hands-on value to the reader. It begins with designing and developing a practical functioning Y-shaped microfluidic device fabricated using SLA technology. All the steps are clearly explained, from the initial design of the chip to the slicing operations performed in 3D printing software until the final printed part is achieved. Further, the printed microfluidic device is validated through generating microdroplets, offering proof of concept.

In FDM-based printing, the use of the thermoplastic filaments and the slice parameters are discussed in detail. As with other 3D printing methods, FDM-based printing requires the initial CAD modeling, followed by the slicing tool used to load to the respective 3D printer. Each step is discussed in detail to help the reader easily reproduce the results. This chapter demonstrates the fabrication of an electrochemiluminescence (ECL) sensor to capture the luminescence signals. Interestingly, this process combines conductive PLA filament (for the sensor region) and standard PLA filament (for the supporting structure) to create the complete sensor. This process creates never-before-seen insights for the reader in making customized sensors using 3D printing technology.

Graphene is a revolutionary 2D material with exceptional electrophysical properties, making it a key component in developing sensitive sensors for multiple applications. Nevertheless, the tedious conventional production process limits its potential for real-time applications. [Chapter 5](#) introduces an alternative, ultrafast process

for the one-step production of graphene-based sensors. The chapter also details the production of a one-step graphene derivative (reduced graphene oxide (rGO)). The assistance of an advanced photothermal reduction approach via two different laser systems, CO₂ (10.6 μm) and blue diode (450 nm) lasers, respectively, in producing graphene and rGO, is also elaborated. The process leverages commercially available substrates like polyimide (PI) and grade 1 filter paper to produce user-defined conductive graphene and rGO patterns. Critical laser optimization and working parameters are demonstrated to help readers reproduce the process to obtain conductive graphenized material. In addition, detailed steps for designing and fabricating a three-electrode sensor for electrochemical validations are provided. The chapter's detailed guidance of this process encourages the reader to utilize this advanced laser-assisted technology to develop one-step user-defined graphene traces for additional applications.

Microfluidics, a fascinating micro-world field that delivers faster reaction responses with low consumption of reagent volumes, is first introduced in [Chapter 1](#) (via simulations) and revisited in [Chapter 3](#) to familiarize the reader with key concepts. [Chapter 6](#) then provides the fundamentals for producing microfluidic devices using a soft lithography technique (i.e., using cleanroom free fabrication). This chapter also discusses the properties of flexible polymer polydimethylsiloxane (PDMS). Interestingly, a nonconventional direct laser writing (DLW) system is introduced to perform maskless lithography. It benefits the reader to develop microfluidic devices in the quickest possible technology at high resolutions. The chapter discusses photosensitive material coatings on glass slides (positive and negative resists), on which the mold formations are made via laser writings. The chapter details the development and etching mechanism, including suitable reagents needed to produce the desired pattern. Later, the concentration ratios of PDMS elastomers to their curing agents are discussed. Step-by-step guidance ensures proper spreading and curing of the mixture on the glass mold so that readers can avoid potential handling errors. Further, the stamped patterns onto the cured polymer are bonded to the glass slides through plasma treatment to make a functioning microfluidic device. This information encourages the reader to design their own

microchannels and devices in multiple fields, from biomedical diagnostics to engineering.

One-step production of graphene electrodes was introduced in [Chapter 5](#), while [Chapter 7](#) explores the next generation methods for electrode fabrication. The three prominent ways (automated inkjet printing, screen printing, and physical vapor deposition (PVD)) to fabricate the electrodes are discussed in this chapter. Automated inkjet printing highlights simplicity and avoids using photomask, stencil, and physical assistance in making electrodes. The design of three electrode systems in CAD and the introduction of the graphical user interface (GUI) of the inkjet printer is described in detail. The chapter also covers file formatting and optimizing the ink properties during printing to ensure ease of reproduction. Moreover, screen printing technology is introduced as an additional section for mass-producing electrodes. The chapter discusses the importance of ink, its viscosity, and the simplified adoption process. In addition, to enhance the reader's hands-on experience, step-by-step instructions are provided to design, fabricate, and print three-electrode systems on the flexible polymer (PI). In the search to provide high-resolution sensor fabrication technology, the PVD approach is introduced to obtain nanometer thick conductive coatings. Gold is the precursor or source in this demonstration to develop the biosensor. A high-voltage supply creates an electron beam to infuse on the gold source, while the fumes of the vaporized gold are directed to the region of interest to obtain nm coatings. All the deposition and precaution steps are noted in clear, straightforward language to enable the readers to replicate the process successfully.

Understanding the structural, morphological, and optical properties of the materials used to fabricate sensors is crucial for achieving the desired reaction outcomes. To address this concern, [Chapters 8](#) and [9](#) introduce several hands-on material characterization techniques. [Chapter 8](#) provides comprehensive information on morphological characterization techniques, including high-resolution scanning electron microscopy (SEM), optical microscopy (LED-based), optical goniometer, and additionally structural characterization method, X-ray diffraction (XRD). Detailed fundamental theoretical information on each technique and the experimentation steps are provided.

In SEM, secondary electrons emitted from the sample surface are directed to the detector to capture high-resolution surface topography. The section begins by explaining the basic steps of sample preparation, including the deposition of a conductive layer (i.e., via sputtering) on the surface, followed by detailed instructions on the instrument parameters, and the final image analysis. Interestingly, the produced rGO material on filter paper in [Chapter 5](#) is used as the test sample for better understanding and connectivity to the reader. Similarly, in optical microscopy, the procedure for capturing images and the limitations of resolutions of 100x are discussed. This technique is suitable for applications that do not require electron microscopy resolutions. The photoresist-based microfluidic channels using the DLW technique produced in [Chapter 6](#) are used in this experiment, and images captured at various resolutions are compared.

The section also covers use of an optical goniometer or tensiometer to identify the materials surface nature (hydrophobicity and hydrophilicity). The surface tension between the solid, liquid, and gaseous phases is responsible for the droplet shape, which is discussed practically to measure its magnitude. The steps include sample preparation, parameter settings, imaging, and contact angle measurements. Additionally, the powerful technique XRD, which measures the crystal structure of the materials, is presented. The fundamentals of Bragg's law and constructive interference patterns to record the peak signals are explained. The complete process (source, detector, and working parameters) on this high-end instrument in depth is provided to the reader. Furthermore, step-by-step instructions on sample preparation, precautions, data collection, analysis, and interpretations are provided so that readers can replicate this process.

[Chapter 9](#) provides detailed information on spectroscopy-based characterization techniques, including UV-Visible Spectroscopy (UV-Vis), Fourier Transform Infrared Spectroscopy (FTIR), Raman spectroscopy, and X-ray photoelectron spectroscopy (XPS). The electronic transitions within the material are analyzed through unique peak positions (wavelength-based) in UV-Vis, with each step described in detail. The steps are broken down into device calibration, blank or reference measurement, and sample analysis. A

working flowchart of the procedure is provided to enhance understanding. In addition, the rGO material discussed in [Chapter 5](#) is again tested using UV-Vis to verify its existence, and the analysis discussed in the chapter provides further insights. Furthermore, the concept of the XPS based on the photoelectric effect is briefly discussed. Where materials are exposed to electromagnetic radiation, electrons are emitted. By capturing these electrons with varying binding energies, XPS helps characterize any given material. All the components and the parameters in operating the XPS instrument of a specified instrument are explained. Similarly, sample preparation, cleaning, required sample size, and types are provided to give the reader more clarity. Merely obtaining data does not help interpret the data to the reader. The most widely used deconvolution tool is explained in detail to help readers analyze and understand the data. Moreover, the chapters clearly discuss an interesting composite material ($\text{Co}_3\text{O}_4/\text{rGO}$), comparing the peak positions concerning their respective binding energy values.

In Raman spectroscopy, the sample materials chemical and structural information can be derived using the principle of inelastic scattering. This chapter provides all the information on sample preparation, experimental procedures, instrument handling, and data interpretation. For a better description of the procedure, rGO material is chosen for experimentation. The obtained data is clearly explained with all the quantitative information on characteristic peak intensities, with I_D and I_G ratios determining its quality. At the same time, FTIR is demonstrated to identify the organic and inorganic materials molecular information and their functional groups. The crucial sampling techniques attenuated total reflectance, specular reflectance, and transmission are discussed. In a sub-section, the interpretation of FTIR data (bond types and mode of vibrations) is mentioned with hands-on experimentations using a carbon-derived material. Through [Chapter 8](#) and [Chapter 9](#), the book aims to cover all the primary material characterization techniques, providing a single reference source for readers.

The chapters in the book begin with foundational concepts, covering computational tools and simulation techniques, followed by fabrication techniques and material characterization. The following

chapters ([Chapters 10–12](#)) describe the real-time applications showing practical use of the knowledge learned from previous chapters. [Chapter 10](#) discusses the vital applications of combining multiple detection approaches, including electrochemical sensing, electrochemiluminescence (ECL), colorimetric analysis, micro paper analytical devices (μ PAD), and DNA amplification through PCR technique within microfluidic systems. In electrochemical sensing, the previously presented processes for electrode fabrication are leveraged in sensing bacteria, biomarkers (lactate), biochemical analytes, and environmental pollutants, individually in each subsection. In ECL sensing methodology, the capture of luminescence signals from the fabricated conductive 3D-printed sensors is demonstrated.

In addition, the well-elucidated fabricated microfluidic devices are leveraged to produce a micromixer to quantitatively perform the colorimetric studies. The analysis reveals the prompt detection of nitrite within the microreactor. Another case study using 3D printers revealed that hydrophobic barriers are produced on paper substrates and sourced to demonstrate the constrained passive fluid flow within microchannels. Similarly, once again, microfluidics is leveraged to perform the onsite polymerase chain reaction (PCR) to amplify the DNA samples, allowing readers to visualize all the amplification steps within the microchip and observe the results.

[Chapter 11](#) presents the applications based on wearable devices, including breath pattern monitoring from the LIG sensor, a microfluidic patch for nucleic acid amplification (NAA), and, excitingly, a biofuel cell energy harvester. The fabrication of this breath sensor builds on the graphene sensor development process first presented in [Chapter 5](#). Readers are presented with the results of the obtained respiration patterns using the LIG material. This application can assist in health monitoring in non-touch-based conditions. In the NAA application introduces a novel isothermal (i.e., constant temperature) method for amplifying the nucleic acid, a crucial biomarker for biological research and health diagnosis. This application recaps the importance of soft lithography technology, as discussed in [Chapter 6](#). At the same time, a patch-based biofuel cell (i.e., via integrating with the commercially available Band-Aid) is demonstrated, wherein the human body sweat (contains lactate) is

used as fuel to produce energy. This interesting mechanism can be adapted to power devices and wearable electronics on a larger-scale applications.

The provided methodologies to develop sensors can also be leveraged to create standalone energy devices. [Chapter 12](#) is dedicated to exploring energy devices, their fabrication, and data interpretation. This chapter provides an overview of current research trends in energy devices, including hydrogen fuel cells (HFC), enzymatic biofuel cells (EBFC), microbial fuel cells (MFC), and supercapacitors. A carbon cloth-based device production is presented in HFC development, and the noted process parameters help the reader reproduce the information. The power generation of $25.6 \mu\text{W}/\text{cm}^2$ via hydrogen gas in HFC with a small working (100 mm^2) area is a testimonial in scaling up the protocol for higher power generations. In EBFC, enzymes act as catalysts to harvest the energy, e.g., glucose oxidase reaction with glucose to generate peroxides, which in turn are used to generate energy ($85 \mu\text{W}/\text{cm}^2$). In MFCs, microorganisms (i.e., bacteria or any microorganisms) are leveraged to generate electricity from organic matter ($4 \mu\text{W}/\text{cm}^2$).

In addition to fuel cells, the chapter delves into the development of flexible supercapacitors, their characterization parameters, and their performance are discussed in depth to benefit the reader.

Supercapacitors are an excellent energy device source that combines high power density and energy densities compared to the existing batteries. A composite material is developed using the laser-induced methodology presented in [Chapter 5](#). Later, all the characterization techniques (cyclic voltammetry (CV), galvanostatic charge/discharge (GCD), and electrochemical impedance spectroscopy (EIS)) are discussed in detail to interpret the energy harvested from the developed supercapacitor. The book concludes with a summary of its contents and a perspective of its future vision.

About the Companion Website

This book is accompanied by a companion website:

www.wiley.com/go/goel



This website includes videos.

1

Multiphysics Simulations on the Effect of Fluidic Concentration Profiles Over Y-Channel and T-Channel Designs

Pavar Sai Kumar and Sanket Goel

*MEMS, Microfluidics and Nanoelectronics (MMNE) Lab,
Department of Electrical and Electronics Engineering, Birla
Institute of Technology and Science (BITS) Pilani, Hyderabad
Campus, Hyderabad, Telangana, India*

1.1 Introduction

Miniaturization of systems and processes has recently gained tremendous interest due to its viable control over countless parameters in chemical reactions, including pressure, temperature, mass transport, and volumes. Further, the microfluidic lab-on-chip devices, manipulating the fluid behaviors at dimensions of less than 1 mm, benefit various applications, including clinical diagnostics, biological and chemical reactions, DNA amplification studies, and biomarker detections [1–3]. The exceptional performance of microfluidics is due to its mixing efficiency for most chemical and biological applications [4–8]. Molecular diffusions are generally used to facilitate desired reactions between more than two fluids at the microfluidic scale. Further, the flow in microscale devices is laminar ($Re < 100$) and needs a micromixer for efficient mixing. However, fluid mixing is not a problem in macro devices owing to the turbulent flow [9].

Microfluidic mixing is classified as either active or passive [10]. Active mixing utilizes external sources, including magnetic beads, acoustic waves, and electric fields. Moreover, active mixers can provide higher mixing efficiencies but are more complex and costly, limiting their incorporation into point-of-care (PoC) devices. By contrast, passive mixing occurs through the advection, and diffusion entirely relies on the microfluidic channel dimension and device

designs [11]. The commonly adopted channel designs include serpentine, dynamic focusing, chaotic advection, multiphase flow, creation of obstacles (i.e., grooves, baffles, curves, and ridges), herringbone, T-shape, Y-shape, pico injections, and flow focusing [12]. However, in order to avoid larger channel lengths and reaction times, passive mixing must be optimized for effective mixings [13, 14]. This chapter reviews a simulation conducted with an active mixer to determine the optimal mix using the Y- and T-shaped channels through the COMSOL.

1.2 Real-Time Applications of This Study

Reza Mahdavi et al. leveraged the COMSOL simulations for organ-on-a-chip microfluidic platforms toward in vitro liver zonation studies (simulate flow rates, cell densities, and cell consumptions) [15]. Similarly, Ashok Kumar Loganathan et al. represented the microfluidic design optimizations for revolutionized blood plasma separation using simulations [16]. Nevertheless, microfluidic simulation plays a vital role in several advanced applications, including gas sensor optimizations [17], engineering of nanoparticles [18], acoustophoresis [19], and single-cell fluid shear stress studies [20].

1.3 Simulation Section

1.3.1 Prerequisites

Windows 10/11 operating system, a minimum of 4 GB RAM, storage of 250 GB, and a licensed version of above or equal to 5.0 COMSOL software.

1.3.2 Computer-Aided Designing (CAD)

CAD modeling and designing are performed in the student-licensed Solidworks 2021 version. The channel dimensions are 1 mm wide for both T and Y-shaped designs. [Figure 1.1](#) shows the representation of the designed CAD models. Further, the designs are saved in .dxf format, allowing for direct import into COMSOL.

1.3.3 Simulation Parameters

Concentration of $c_1 = 1 \text{ mM}$ at inlet 1.

Concentration of $c_2 = 5 \text{ mM}$ at inlet 2.

Velocity of inlet 1 = $2000 \text{ } \mu\text{l/min} = 0.03334 \text{ m/s}$.

Velocity of inlet 2 = varied as $2000 \text{ } \mu\text{l/min} = 0.03334 \text{ m/s}$, $1000 \text{ } \mu\text{l/min} = 0.016667 \text{ m/s}$, $500 \text{ } \mu\text{l/min} = 0.008333 \text{ m/s}$, $100 \text{ } \mu\text{l/min} = 0.0016667 \text{ m/s}$.

Time of observation = 0–10 seconds at a step of 0.1 second.

The above parameters are limited to this study; however, users can change and simulate each parametric variation.

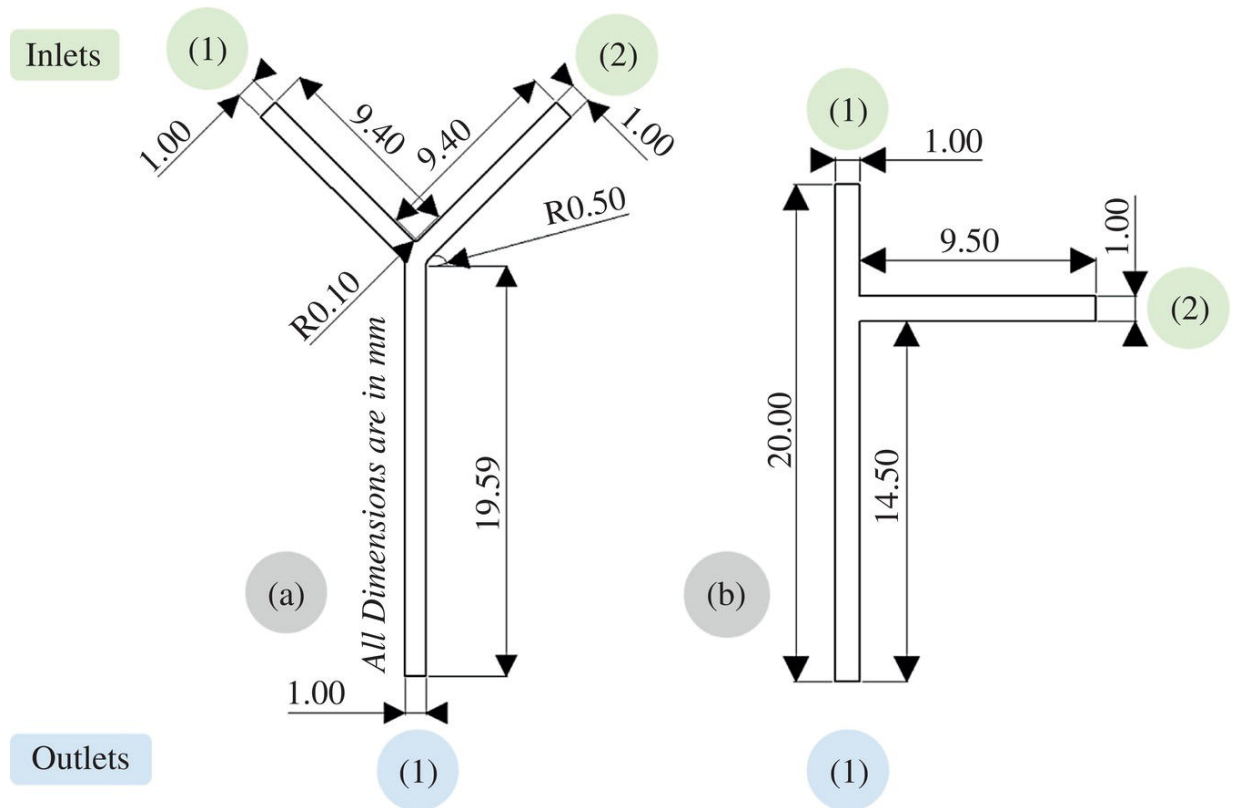


Figure 1.1 CAD images of Y and T-shaped channels (All dimensions are in mm).

1.4 Results and Discussions

1.4.1 Model Designing

Step 1: Use any computer-aided designing (CAD) tool (this case uses SOLIDWORKS 2021).

Step 2: Draw the respective T-shaped and Y-shaped 2D channels, as shown in [Figure 1.1](#).

Step 3: Create an offset or channel width in both designs as 1 mm.

Step 4: Save the respective files individually through the relevant CAD tool extension.

Step 5: Convert the respective saved files to .dxf format individually for easy import into COMSOL.

1.4.2 COMSOL Simulations

In COMSOL, open the new window and select Model Wizard.

Step 1: Click on the default 2D space dimension.

Step 2: Select physics in the search bar and add (i) Transport of diluted species and (ii) Laminar flow.

Step 3: Select the study as Time-dependent (i.e., to study the dependency of results with time) and click done.

Step 4: Change the default dimensions in the popup window of Geometry to “mm.”

Step 5: Right-click on the Geometry: import the saved Y-channel.dxf and T-channel.dxf files individually for two studies, respectively.

Step 6: Right-click on the Materials: add the materials from the library (search PDMS and apply as boundary excluding the inlets and outlet, as shown in [Figure 1.1](#); search WATER and apply as domain)

Step 7: Right-click on the Laminar flow: Select inlet and choose the edge as inlet 1, shown in [Figure 1.1](#), and, keeping the boundary condition as velocity, enter the normal inflow velocity

values of user-defined, respectively (in this case $2000 \mu\text{l}/\text{min} = 0.03334 \text{ m/s}$, $1000 \mu\text{l}/\text{min} = 0.016667 \text{ m/s}$, $500 \mu\text{l}/\text{min} = 0.008333 \text{ m/s}$, $100 \mu\text{l}/\text{min} = 0.0016667 \text{ m/s}$). Repeat the same for inlet 2, respectively. Similarly, right-click on the Laminar flow section, select outlet, and choose the outlet edge, shown in [Figure 1.1](#), respectively, and leave the default settings as it is, $P = 0$.

Step 8: Click on the transport of diluted species section, and here, the number of dependent variables (i.e., concentrations) can be set. In this case, we set the number of species as 2 and concentrations named c1 and c2.

Step 9: Click on the transport properties to ensure the convection was set to the velocity field.

Step 10: Right-click on the transport of diluted species. Select the concentration, and in the boundary selection, select inlet 1, concentration species c1, and provide the user-defined concentration. In this case, concentration c1 was set to $1 \text{ mol}/\text{m}^3$, i.e., 1 mM.

Step 11: Similarly, right-click on the transport of diluted species, select the concentration, provide inlet 2 as the boundary, and select c2, enter a user-defined value. In this case, the c2 was set to $5 \text{ mol}/\text{m}^3$, i.e., 5 mM.

Step 12: Meshing: click on the mesh and select the element size depending on the user. In this case, the mesh size was set to fine with physics-controlled default mesh selection and selected build all to process the meshing.

Step 13: Click on the study/step 1-Time dependent: In the study settings, adjust the time unit output times (start, step, end) as (0, 0.1, 10) s. It is, again, user-defined.

Step 14: Compute the study in the time-dependent section and wait until the process is complete to visualize the results.

Step 15: The concentration profiles can be seen in the results section, concentration c1 and concentration c2. Right-click on any one of the concentrations c1 or c2 and click duplicate.

Step 16: In the duplicated concentration, select the surface and change the expression to $\max(c_1, c_2)$ such that the simultaneous fluid interactions can be visualized during the animation of the file. Also, the mixing pattern can be seen effectively.

Step 17: Right-click on the duplicated concentration: select the arrow surface, adjust the coloring arrow positioning (in this case, set to 20 for each of x and y), and click plot.

Step 18: Click the results section in the main toolbar, click Animation Player to visualize the fluid interactions from the set time of 0–10 seconds, or select the animation file to export the animations.

Step 19: Click on the selected animation, and the player (on, off, and pause) can be seen in the top left corner of the graphics window. Click on the play, then the COMSOL simulates the data and plays the graphics.

Step 20: In the animation settings, change the target to file to export as user-defined formats (i.e., gif, avi).

Step 21: Each time the inlet velocities or concentrations change, the study must be computed to reflect the same in the results section.

Step 22: Right-click on the export: Images, plots, or data, if any, can be exported from here.

Step 23: Right-click on the reports: select the type of report (brief, intermediate, or complete) that can be exported at desired locations.

Step 24: Save the COMSOL simulated file for future modifications and close the simulations.

[Table 1.1](#) shows the simulations performed by varying the velocity of inlet 2 as 2000 $\mu\text{l}/\text{min}$, 1000 $\mu\text{l}/\text{min}$, 500 $\mu\text{l}/\text{min}$, and 100 $\mu\text{l}/\text{min}$ at a fixed velocity of inlet 1 as 2000 $\mu\text{l}/\text{min}$. However, it is user-defined and can be adjusted depending on the requirements.

In this study, the concentrations of the c_1 and c_2 were fixed during the change velocity studies. However, this also can be varied depending on the requirement and simulated.

As shown in [Table 1.1](#), both the Y-channel and T-channel exhibit similar behaviors, including at the same flow rates of inlet 1 and 2 (2000 $\mu\text{l}/\text{min}$ each). It can be observed that the mixing profile of both fluids was aligned in the middle of the outlet channel, and the labeling provided on the right side of the image shows the concentrations at each level at 10th seconds.

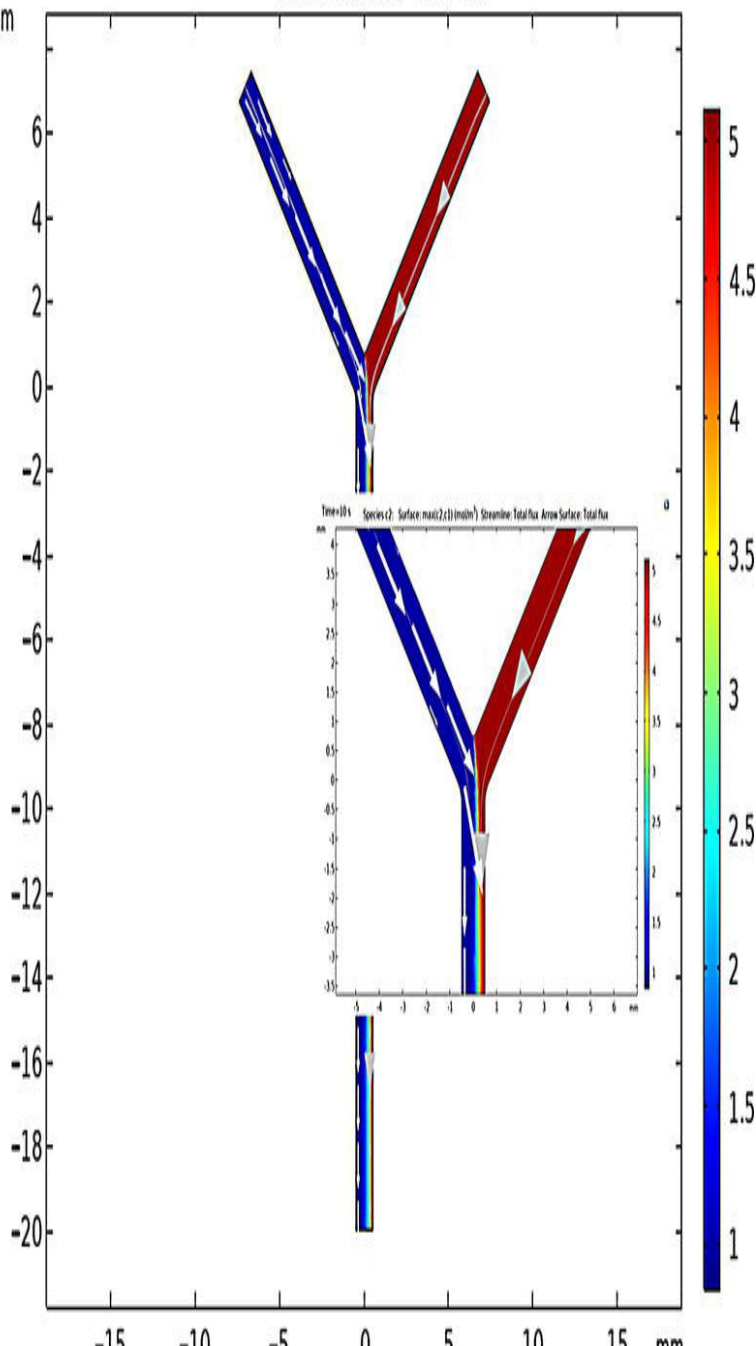
Moreover, decreasing the velocity of inlet 2 shows the right side shift of fluid alignment and the concentration changes, which could be seen from the label provided.

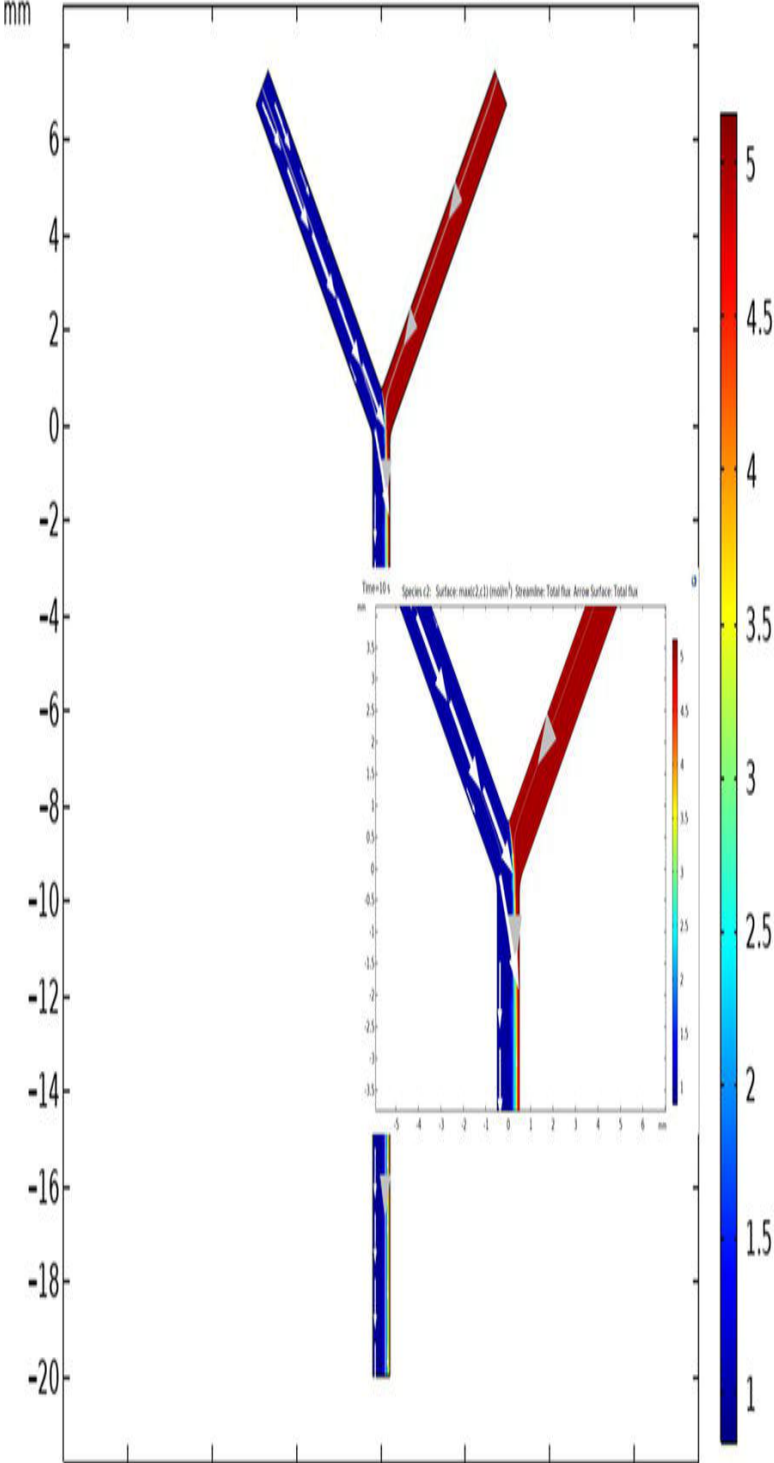
It was observed that the lower flow rates of inlet 2 with concentration c_2 at 5 mM could mix effectively with the higher flow rate of inlet 1 with concentration c_1 at 1 mM. Also, the mixing profile indicates that the 5 mM was consumed to ~ 2.5 mM after mixing at 10th seconds. However, if the path length of the channel increases, then the complete consumption can be seen.

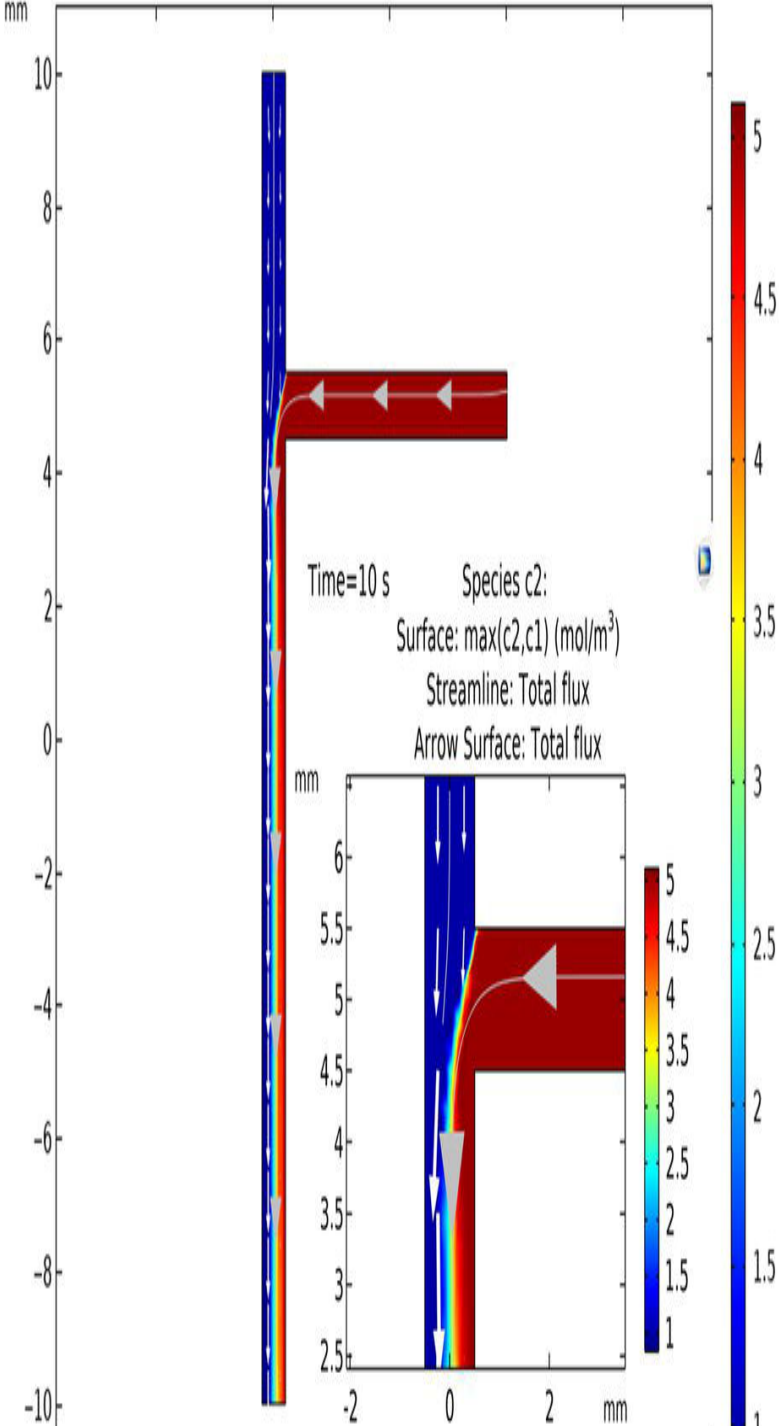
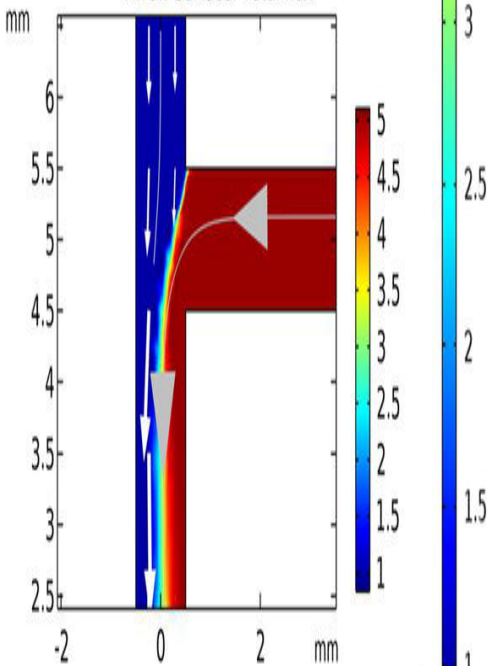
Table 1.1 Y- and T-channel simulations with a varying flow rate of Inlet 2 (fixed concentrations of $c_1 = 1\text{ mM}$, $c_2 = 5\text{ mM}$, and time at 10th seconds).

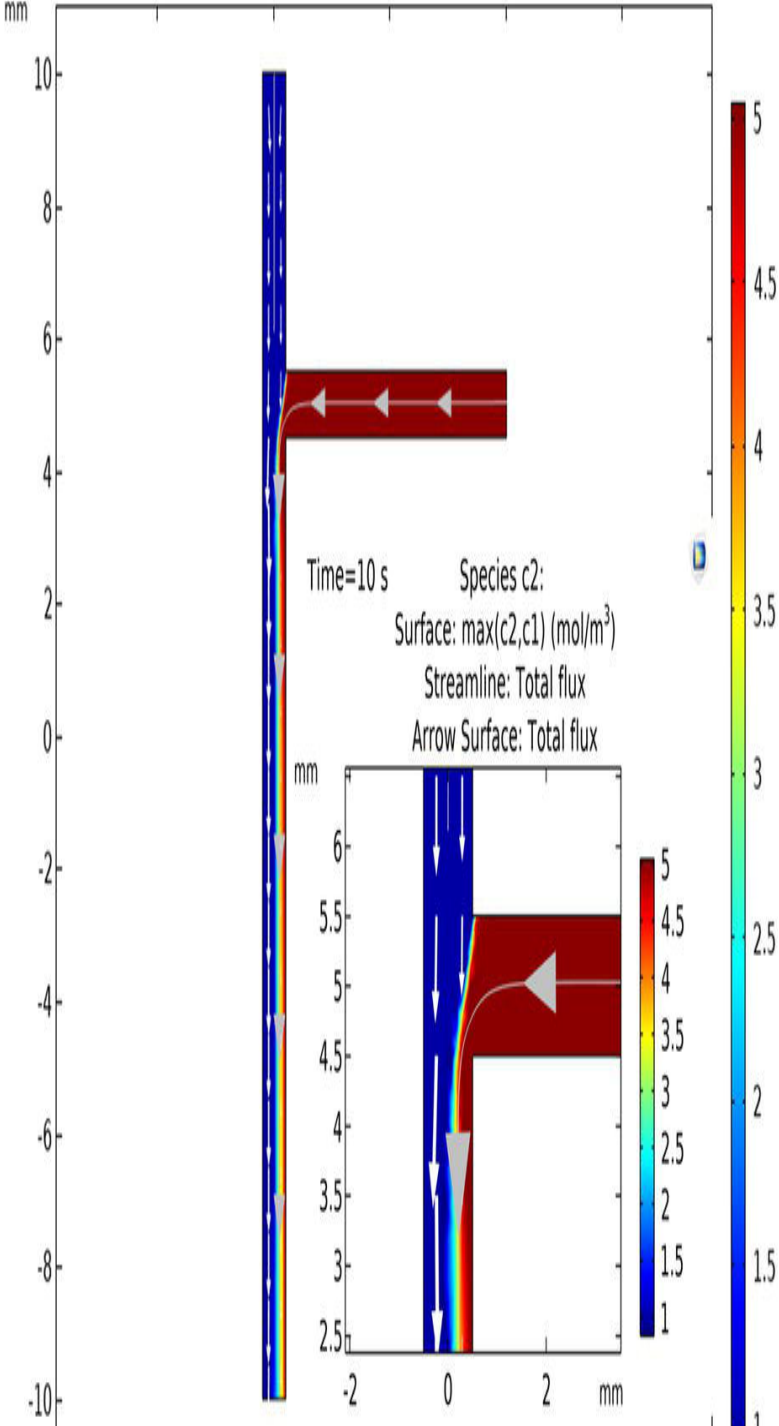
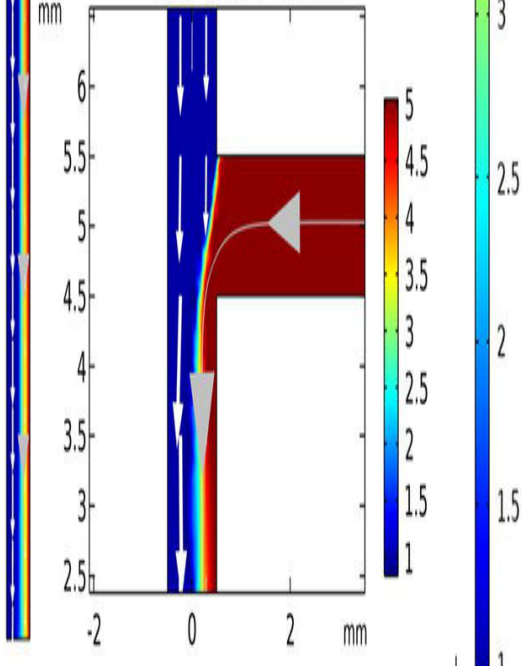
Channel type	Inlets		Images
	1	2	
	Flowrate (µl/min)		
Y-channel	2000	2000	

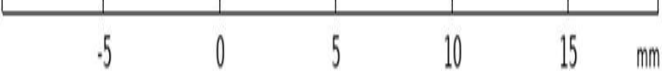
Channel type	Inlets	Images
		<div><div>Time=10 s Species c2: Surface: max(c2,c1) (mol/m³) Streamline: Total flux Arrow Surface: Total flux</div><div><p>The figure displays a 2D simulation of a Y-junction channel. The main plot shows the channel geometry with streamlines and surface concentration. The x-axis ranges from -15 to 15 mm, and the y-axis ranges from -20 to 6 mm. The left inlet is blue, the right inlet is red, and the bottom outlet is a mix of colors. A color bar on the right indicates concentration from 1 to 5 mol/m³. An inset plot shows a zoomed-in view of the junction with axes from -4 to 4 mm on the x-axis and -25 to 35 mm on the y-axis, with its own color bar from 1 to 5.</p></div></div>

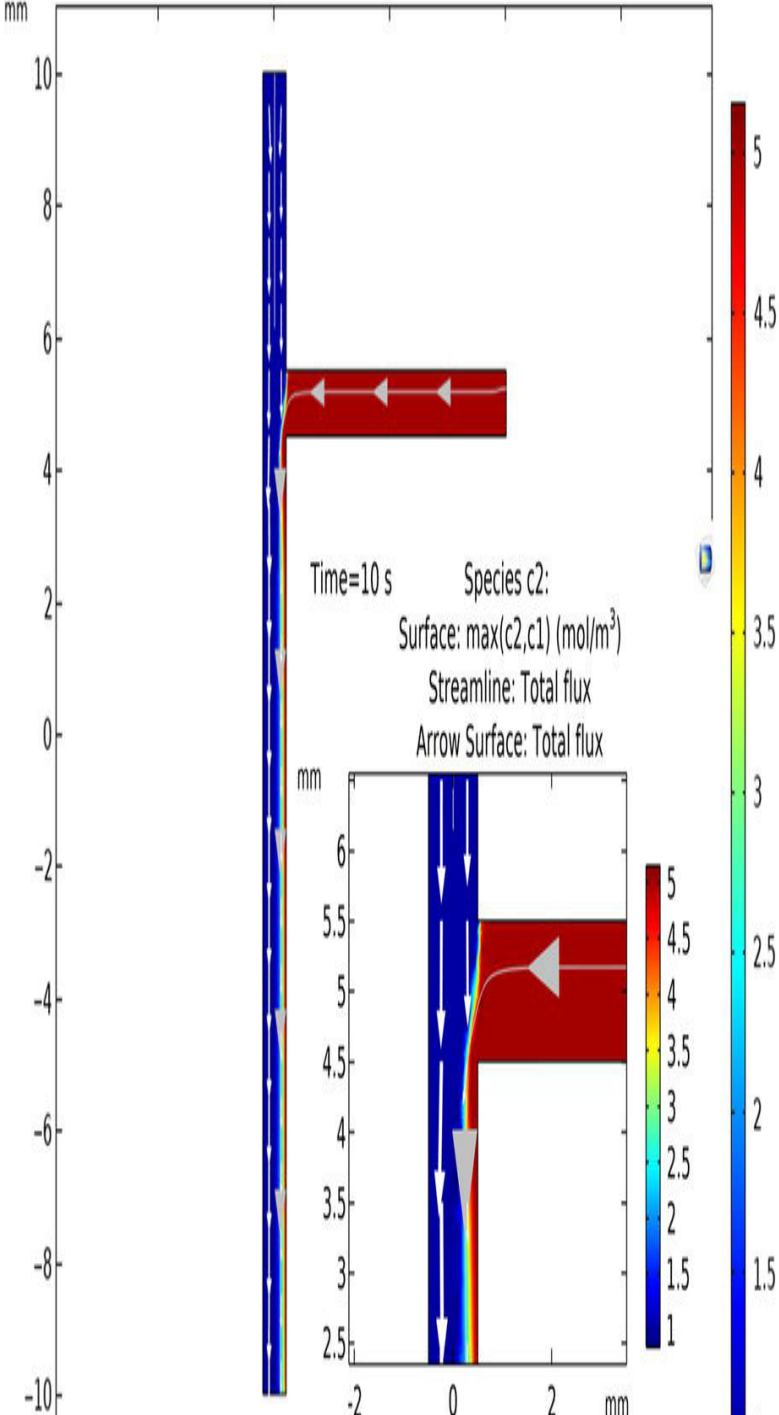
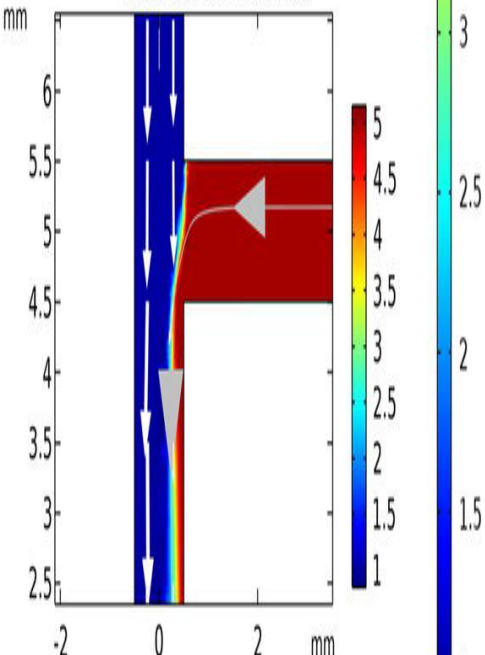
Channel type	Inlets	Images
	2000 1000	<div data-bbox="630 323 1382 428"> <p>Time=10 s Species c2: Surface: max(c2,c1) (mol/m³) Streamline: Total flux Arrow Surface: Total flux</p> </div> 
	2000 500	

Channel type	Inlets	Images
		<div>Time=10 s Species c2: Surface: max(c2,c1) (mol/m³) Streamline: Total flux Arrow Surface: Total flux</div> 

Channel type	Inlets	Images
		<div><div><p>Time=10 s Species c2: Surface: $\max(c_2, c_1)$ (mol/m³) Streamline: Total flux Arrow Surface: Total flux</p></div><div><p>Time=10 s Species c2: Surface: $\max(c_2, c_1)$ (mol/m³) Streamline: Total flux Arrow Surface: Total flux</p></div></div>

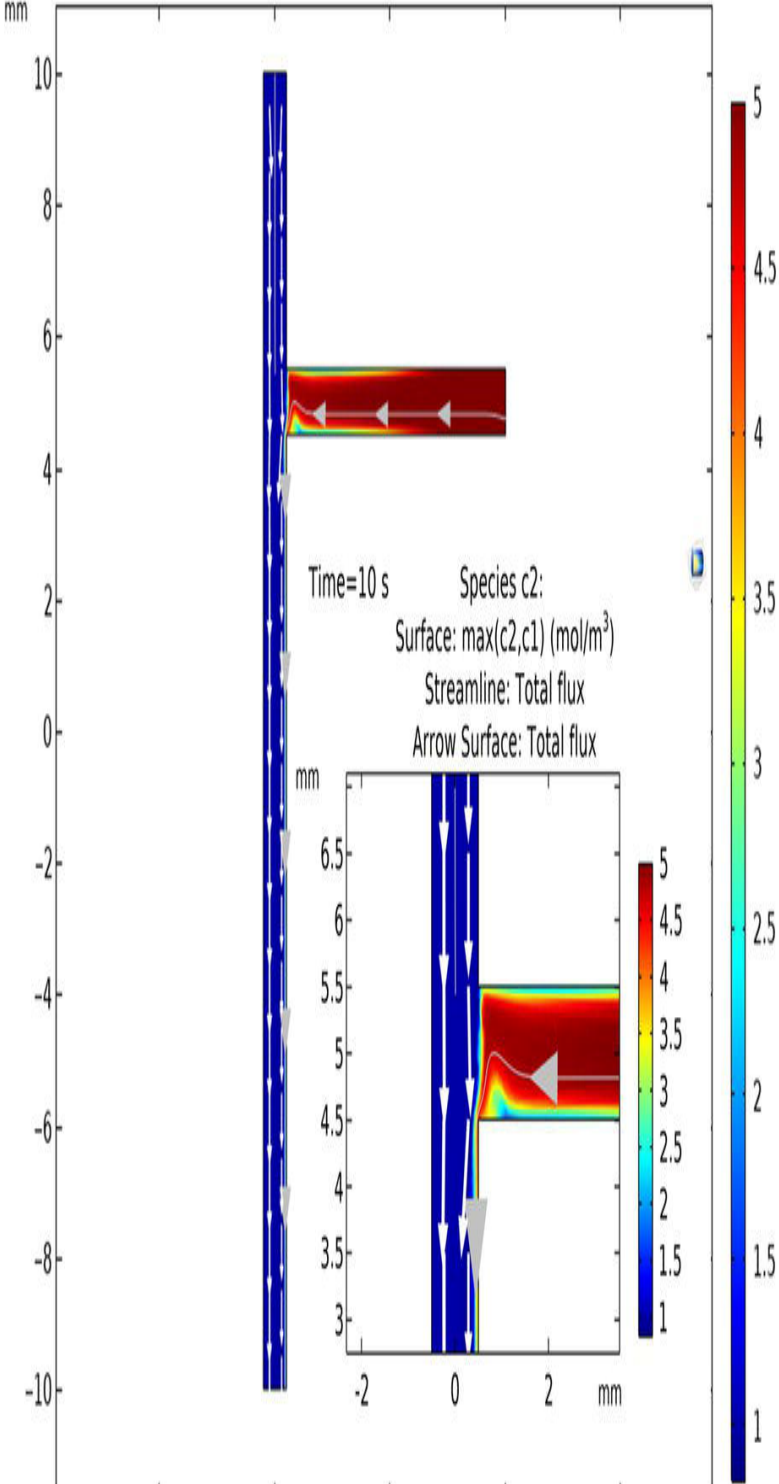
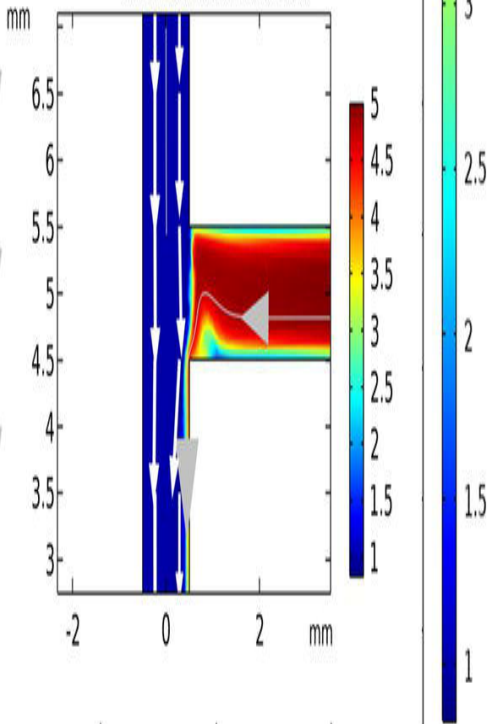
Channel type	Inlets	Images
		<div><div>Time=10 s Species c2: Surface: max(c2,c1) (mol/m³) Streamline: Total flux Arrow Surface: Total flux</div><div>Time=10 s Species c2: Surface: max(c2,c1) (mol/m³) Streamline: Total flux Arrow Surface: Total flux</div></div>

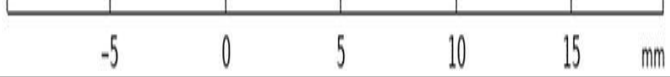
Channel type	Inlets		
	2000	500	

Channel type	Inlets	Images
		<div><div>Time=10 s Species c2: Surface: max(c2,c1) (mol/m³) Streamline: Total flux Arrow Surface: Total flux</div><div>Time=10 s Species c2: Surface: max(c2,c1) (mol/m³) Streamline: Total flux Arrow Surface: Total flux</div></div>

Channel type	Inlets	
	2000	100



Channel type	Inlets	Images
		<div><div>Time=10 s Species c2: Surface: max(c2,c1) (mol/m³) Streamline: Total flux Arrow Surface: Total flux</div><div><div>Time=10 s Species c2: Surface: max(c2,c1) (mol/m³) Streamline: Total flux Arrow Surface: Total flux</div></div></div>

Channel type	Inlets	
---------------------	---------------	--

1.5 Conclusion

Y- and T-channel designs were simulated to observe the change in the concentration profiles with varying flow rates. The flow rates or velocities of inlets significantly impact the mixing profiles of concentrations. This study observed that the lower flow rates of inlet 2 facilitated the increased mixing at 10th seconds than the higher flow rates. It was also shown that users can change the concentration parameters, velocity parameters, and the time of observation to obtain significant and specific simulations.

References

- 1 Hama, B., Mahajan, G., Fodor, P.S. et al. (2018). Evolution of mixing in a microfluidic reverse-staggered herringbone micromixer. *Microfluid. Nanofluidics* 22 (5): 54.
<https://doi.org/10.1007/s10404-018-2074-0>.
- 2 Singh, R.K., Kumar, P.S., Amreen, K. et al. (2022). Disposable miniaturized electrochemical sensing platform with laser-induced reduced graphene oxide electrodes for multiplexed biochemical analysis. *IEEE Trans. Nanobiosci.* 1.
<https://doi.org/10.1109/TNB.2022.3216312>.
- 3 Wagh, M.D., Renuka, H., Kumar, P.S. et al. (2022). Integrated microfluidic device with MXene enhanced laser-induced graphene bioelectrode for sensitive and selective electroanalytical detection of dopamine. *IEEE Sens. J.* 22 (14): 14620–14627.
<https://doi.org/10.1109/JSEN.2022.3182293>.
- 4 Jung, Y., Hyun, J., Choi, J. et al. (2017). Manipulation of cells' position across a microfluidic channel using a series of continuously varying herringbone structures. *Micro Nano Syst. Lett.* 5 (1): 6. <https://doi.org/10.1186/s40486-016-0040-8>.

- 5** Singh, R.K., Kumar, P.S., Amreen, K. et al. (2023). Miniaturized paper based sensor with reduced graphene oxide as interdigitated electrodes for multiple applications. *IEEE Sens. J.* 23 (13): 14950–14956. <https://doi.org/10.1109/JSEN.2023.3277800>.
- 6** Kumar, P.S., Madapusi, S., and Goel, S. (2023). 3D printed microfluidic chemiluminescence PoC device with self-powering and integrated incubating system: validation via ALP detection on disposable μ PADs. *Microchem. J.* 189: 108518. <https://doi.org/10.1016/j.microc.2023.108518>.
- 7** Kumar, P.S., Advincula, P., and Goel, S.G. (2022). First report on onsite temperature based recovery of quenched chemiluminescence signal from graphenized μ PADs: validation by catechins radical scavenging. *Nano Futur.* <https://doi.org/10.1088/2399-1984/ac9d78>.
- 8** Kumar, P.S., Bhand, S., Das, A.K., and Goel, S. (2022). Microfluidic paper device with on-site heating to produce reactive peroxide species for enhanced smartphone enabled chemiluminescence signal. *Talanta* 236: 122858. <https://doi.org/10.1016/j.talanta.2021.122858>.
- 9** Julius, L.A.N., Jagannadh, V.K., Michael, I.J. et al. (2016). Design and validation of on-chip planar mixer based on advection and viscoelastic effects. *Biochip J.* 10 (1): 16–24. <https://doi.org/10.1007/s13206-016-0103-1>.
- 10** Le The, H., Ta, B.Q., Le Thanh, H. et al. (2015). Geometric effects on mixing performance in a novel passive micromixer with trapezoidal-zigzag channels. *J. Micromech. Microeng.* 25 (9): 94004. <https://doi.org/10.1088/0960-1317/25/9/094004>.
- 11** Shah, I., Kim, S.W., Kim, K. et al. (2019). Experimental and numerical analysis of Y-shaped split and recombination micro-mixer with different mixing units. *Chem. Eng. J.* 358: 691–706. <https://doi.org/10.1016/j.cej.2018.09.045>.
- 12** Mansour, M. et al. (2017). Numerical study of liquid-liquid mixing in helical pipes. *Chem. Eng. Sci.* 172: 250–261. <https://doi.org/10.1016/j.ces.2017.06.015>.

- 13** Kumar, P.S., Madapusi, S., and Goel, S. (2023). Sub-second synthesis of silver nanoparticles in 3D printed monolithic multilayered microfluidic chip: enhanced chemiluminescence sensing predictions via machine learning algorithms. *Int. J. Biol. Macromol.* 245: 125502.
<https://doi.org/10.1016/j.ijbiomac.2023.125502>.
- 14** Ansari, M.A., Kim, K.-Y., and Kim, S.M. (2018). Numerical and experimental study on mixing performances of simple and vortex micro T-mixers. *Micromachines* 9 (5):
<https://doi.org/10.3390/mi9050204>.
- 15** Mahdavi, R., Hashemi-Najafabadi, S., Ghiass, M.A., and Adiels, C.B. (2024). Microfluidic design for in-vitro liver zonation – a numerical analysis using COMSOL multiphysics. *Med. Biol. Eng. Comput.* 62 (1): 121–133. <https://doi.org/10.1007/s11517-023-02936-6>.
- 16** Loganathan, A.K., Devaraj, R., and Krishnamoorthy, L. (2023). Revolutionizing plasma separation: cutting-edge design, simulation, and optimization techniques in microfluidics using COMSOL. *Microfluid. Nanofluidics* 27 (11): 73.
<https://doi.org/10.1007/s10404-023-02684-x>.
- 17** Rananavare, M., Shah, R., Makwana, M., and Rathod, S.S. (2021). Design and simulation of microfluidic based carbon monoxide gas sensor using COMSOL Multiphysics®. In: *2021 International Conference on Advances in Computing, Communication, and Control (ICAC3)*, 1, 1–4, 4. Mumbai, India: IEEE
<https://doi.org/10.1109/ICAC353642.2021.9697247>.
- 18** Soheili, S., Mandegar, E., Moradikhah, F. et al. (2021). Experimental and numerical studies on microfluidic preparation and engineering of chitosan nanoparticles. *J. Drug Deliv. Sci. Technol.* 61: 102268.
<https://doi.org/10.1016/j.jddst.2020.102268>.
- 19** Zareei, S.M., Sepehrirahnama, S., Jamshidian, M., and Ziaei-Rad, S. (2023). Three-dimensional numerical simulation of particle acoustophoresis: COMSOL implementation and case studies. *Eng.*

Comput. 39 (1): 735–750. <https://doi.org/10.1007/s00366-022-01663-0>.

- 20** Lin, X., Su, J., and Zhou, S. (2022). Microfluidic chip of concentration gradient and fluid shear stress on a single cell level. *Chin. Chem. Lett.* 33 (6): 3133–3138. <https://doi.org/10.1016/j.cclet.2021.10.026>.

2

Droplet Generation in T-Junction Microchannel Using Multiphysics Software

Abhishek Kumar and Sanket Goel

*MEMS, Microfluidics and Nanoelectronics (MMNE) Lab,
Department of Electrical and Electronics Engineering, Birla
Institute of Technology and Science (BITS) Pilani, Hyderabad
Campus, Hyderabad, Telangana, India*

2.1 Introduction

A subfield of microfluidics known as droplet microfluidics deals with the generation of discrete volumes of droplets utilizing two or more immiscible fluid phases. Oil and water are the most used immiscible phases for generating droplets [1]. The fundamental idea behind droplet creation is to split the stream of immiscible phases into distinct microdroplets by applying shear forces. These microdroplets function as microreactors, offering excellent autonomous control over the flow and volume of fluid. It makes high throughput experimental analysis feasible and offers efficient mixing efficiencies [2, 3]. Droplet microfluidics is widely used in pharmaceuticals, food quality, and biochemical reactions [4]. The microdroplet size distribution influences the droplet microfluidics properties. A strong simulation program called COMSOL Multiphysics makes it possible to create a virtual environment for gaining a rough knowledge of the microsystems. Furthermore, in order to provide rapid and precise results across a range of experimental parameters, computational modeling must be carried out prior to experimental validation. It covers the product design cycle, the cost of prototyping, the removal of material waste, and optimizations for product development [5]. The advantages of stationary and transient flows in 2D and 3D spaces are also offered by the Multiphysics program. Also, the microfluidic physics interface is predetermined with suitable formulation for different types of flows, such as laminar, creeping, two-phase, and slip media [6].

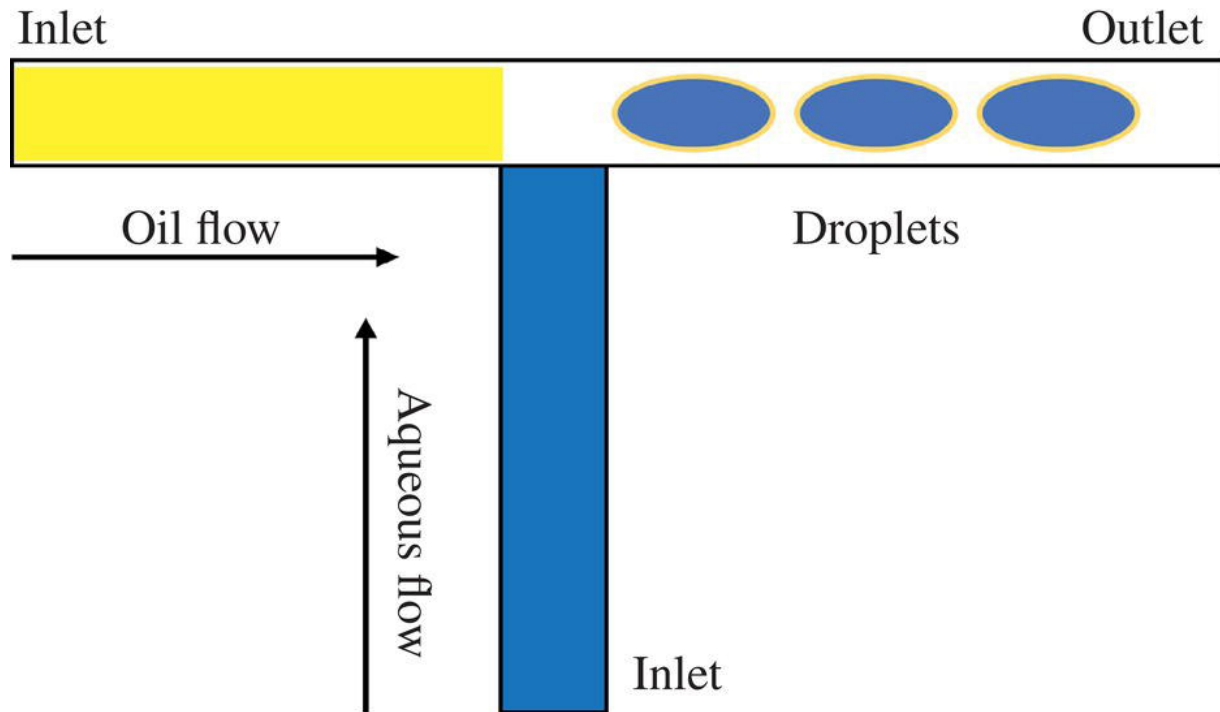


Figure 2.1 T-junction microfluidic channel.

Droplet generation in microfluidic devices can be achieved using three geometry types: T-junction, flow focusing, and co-flow devices. The most widely used method for producing droplets on microfluidic chips is T-junction. T-junction geometry comprises two symmetric microchannel arms to shear the fluid stream, causing elongation of the fluid stream and then its rupture [7, 8, 9]. Shear faces are formed at or close to the microchannel junction interface in droplet generations, which have an impact on how flowing fluids – such as aqueous and oil phase fluids – split into distinct micro droplets [8, 9, 10].

This experiment uses a Multiphysics software environment to create and analyze a T-junction microfluidic channel for producing water in oil droplets. The designed microfluidic T channel junction geometry involves two inlets (i.e., perpendicular to each other) and one outlet, as shown in [Figure 2.1](#). The simulation model also implements the coupling of solid wall and wetted well boundary condition with a 135° contact angle.

2.1.1 Brief Overview

Droplet microfluidic is a sub-branch of microfluidics with several applications in biology, pharmaceuticals, cell and protein encapsulation, etc. Using simulation packages to model the real-time scenario, a deeper understanding of real-time experimentation, validation, and product development can be obtained for design considerations. The following experimental procedure highlights the general mechanism for generating droplets in T-junction microfluidics geometry using a simulation software suite.

2.2 Simulation Section

2.2.1 Prerequisites

Microsoft Windows 10 and above operating system. A minimum of 4 GB RAM, storage of 250 GB, and an installed COMSOL Multiphysics software suite.

2.2.2 Model and Geometry Definition

Step 1: Start the Multiphysics software and set up the new model from the main wizard.

Step 2: Select the 3D geometry module and navigate to the physics module tree.

Step 3: Select the fluid flow from the interface (present in the left window) and add multiphase flow.

Step 4: Select the Laminar flow and the time-dependent study with phase initialization.

Step 5: Click on the geometry option in the model builder and change the units by default to μm .

Step 6: Select the Work Plane toolbar and right-click to create a rectangle (R1) positioned at 0.05 yw axis with a width of 0.05 and a height of 0.2.

Step 7: Similarly, draft another rectangle (R2) positioned at -0.35 xw , with a height (channel width) of 0.05 (as shown in [Figure 2.2a](#)).

Step 8: Right-click on the plane geometry and create an open curve polygon (P1) (i.e., it is present in the more primitives option) by locating the coordinates in table field for xw and yw as 0, 0.05 and 0.1, 0.1, respectively.

Step 9: Similarly, right-click on the plane geometry and create an open curve polygon (P2) by locating the coordinates in table field for xw and yw as 0.05, 0.05, and 0, 0.05, respectively, as shown in [Figure 2.2b](#).

Step 10: To create the 3D model select the extrude command by right-clicking on the work plane and provide the height up to $0.025\text{ }\mu\text{m}$, shown in [Figure 2.2c](#).

Step 11: Now, create an assembly of all the geometry parts by selecting the union command from the transform option under plane geometry. Build all command to visualize the final constructed 3D model of microfluidic channel shown in [Figure 2.2d](#).

2.2.3 Simulation Parameters

Step 1: Right-click on the add variable definitions from the function option under home toolbar, assign step size of $1\text{e-}3$ with the smoothing transition size of $2\text{e-}3$.

Step 2: Right-click on definitions under “component” and select a local variable. Define a local variable for the volume flow of inlet 1 (V1), volume flow of inlet 2 (V2), and the effective diameter of the droplet by inputting value as shown in [Table 2.1](#).

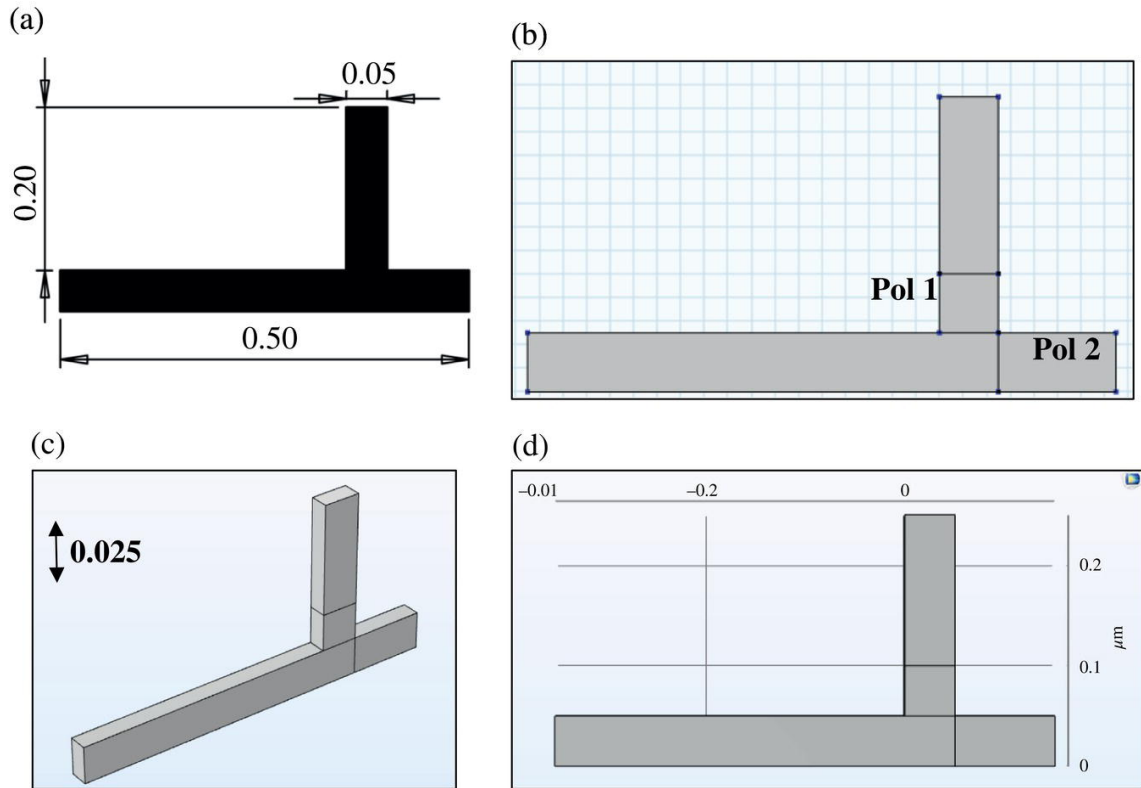


Figure 2.2 Model and geometry definition (a) T-junction microfluidic channel (b) 2D sketch of geometry designed in COMSOL (c) T-junction extruded up to 0.025 μm, and (d) 3D sketch of constructed T-junction microfluidic channel.

Table 2.1 Variable process definitions.

Variable	Expression	Unit	Equation
Inlet 1 (V1)	$0.0000002/3600 \times \text{step1}(t[1/s])$ [m ³ /s]	m ³ /s	1
Inlet 2 (V2)	$0.0000001/3600 \times \text{step1}(t[1/s])$ [m ³ /s]	m ³ /s	2
Droplet dia	$1 \times (\text{intop1}((\text{phils} > 0.5) \times (x < -0.2[\text{mm}]))) \times 3/(4 \times \text{pi}))^{(1/3)}$	m	3

Step 3: Right-click on component under model tree section and select Multiphysics option. Select the two-phase flow level set under Multiphysics flow from the prompt.

Step 4: Assign material properties for fluids 1 and 2 by right-clicking on the material command. Selecting blank material. Input material properties for fluids 1 and 2 with a 1000 kg/m^3 density and dynamic viscosity of 0.00195 and $0.00671 \text{ Pa}\cdot\text{s}$, respectively.

Step 5: Click on Multiphysics under the model tree, select the two-phase flow level set, and input $2.5\text{e-}3[\text{N/m}]$ as the surface tension coefficient.

Step 6: Similarly, click on Multiphysics under the model tree again, select the wetted wall option, and input $3 \times \pi/4[\text{rad}]$ for the contact angle.

Step 7: Right-click on the laminar flow under the model tree, select inlet 1, and assign domain 24 and flow rate as V_1 for the flow of fluid 1.

Step 8: Similarly, right-click on the laminar flow again under the model tree select inlet 2 and assign domain 12 and flow rate as V_2 for the flow of fluid 2.

Step 9: Similarly, as in steps 7 and 8, right-click on the laminar flow under the model tree, select outlet, and assign domain 1 as an outlet with a pressure value of 0.

Step 10: Similarly, right-click on the level set option in the model tree and follow steps 7, 8, and 9 to assign domains 24, 12, and 1 as inlet 1, inlet 2, and outlet, respectively.

Step 11: Right-click on the mesh option in the model tree, select the user-controlled mesh option available, and assign an extra fine mesh size.

Step 12: Click on the time-dependent study and input the output time range (start, step, and end) as 0.1, 0.005, and 0.08, respectively, and click on the compute option to obtain the results.

2.3 Result and Discussion

Step 1: Right-click on the velocity option available under result section of model tree. Select isosurface and input expression for fluid 1.

Step 2: Similarly, right-click on the volume fraction option in the result section and select the slice option and input expression for fluid 1.

Step 3: Click on the result from the menu bar and select the animation option. Select the file or player option to save or visualize the simulated result in the main interface respectively and finally click on export to observe the droplet breakout (as shown in [Figure 2.3a–c](#)).

2.4 Conclusion

In this experiment, COMSOL Multiphysics software was used to mimic a T-junction geometry for the purpose of producing microdroplets. The physical principles with the corresponding initial and boundary conditions are expressed in fluid flow interfaces, with the objective of understanding the mechanism of droplet generation in a T-junction microfluidic channel. The output result from the simulation highlights the generation of microdroplets in the active surface of the microchannel. Multiphysics simulation can improve the traditional product cycle of microfluidics chips to design, optimize, and accelerate the production of highly efficient microfluidics system for applications like lab-on-chip, chemical synthesis, cell analysis.

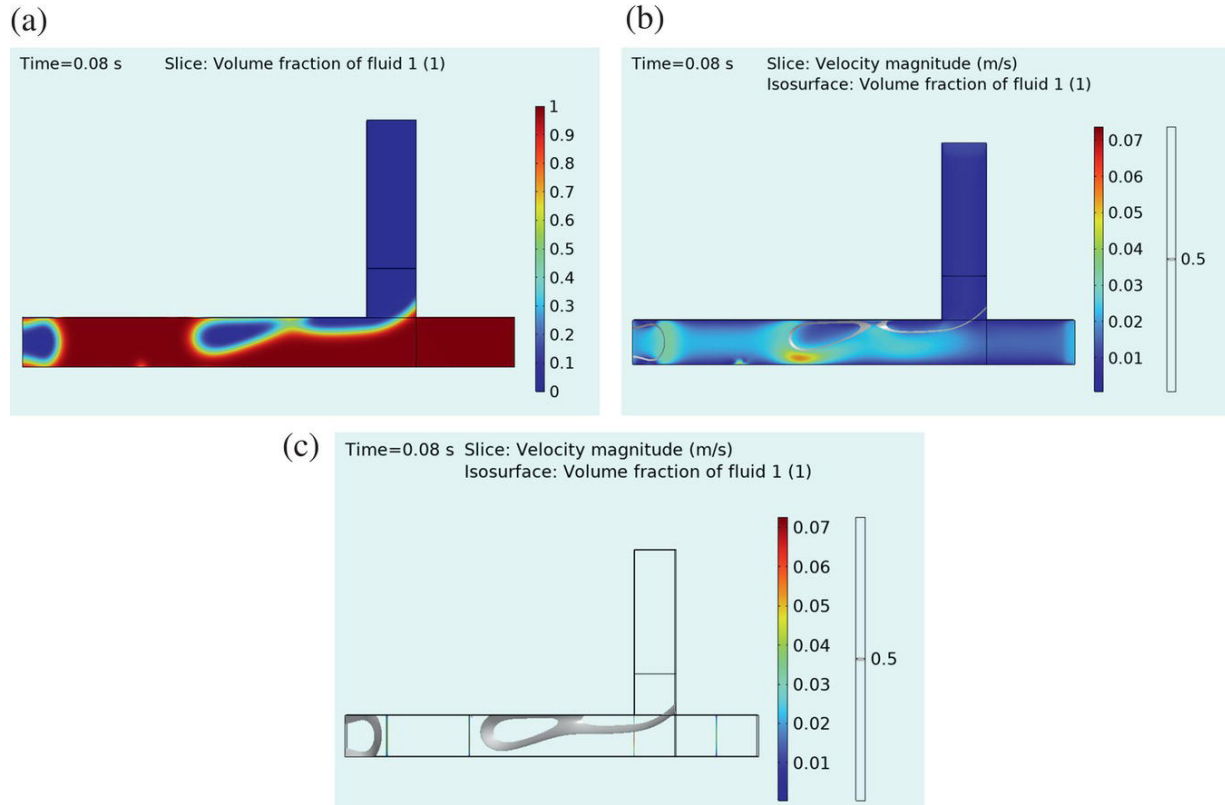


Figure 2.3 Output result for the T-junction droplet breakout (a) Volume fraction of fluid 1 (b) Velocity magnitude of fluid 1, and (c) Streamline velocity field for fluid 1 T-junction droplet breakout.

References

- 1 Yin, J. and Kuhn, S. (2022). Numerical simulation of droplet formation in a microfluidic T-junction using a dynamic contact angle model. *Chem. Eng. Sci.* 261: <https://doi.org/10.1016/j.ces.2022.117874>.
- 2 Luo, S., Schiffbauer, J., and Luo, T. (2016). Effect of electric field non-uniformity on droplets coalescence. *Phys. Chem. Chem. Phys.* 18 (43): 29786–29796. <https://doi.org/10.1039/c6cp06085d>.
- 3 Ringkai, H., Tamrin, K.F., Sheikh, N.A., and Mohamaddan, S. (2021). Evolution of water-in-oil droplets in t-junction microchannel by micro-piv. *Appl. Sci.* 11 (11): <https://doi.org/10.3390/app11115289>.

- 4 Srikanth, S., Jayapiriya, U.S., Dubey, S.K. et al. (2022). A lab-on-chip platform for simultaneous culture and electrochemical detection of bacteria. *iScience* 25 (11):
<https://doi.org/10.1016/j.isci.2022.105388>.
- 5 Kocbach, J. (2011). A simulation approach to optimizing performance of equipment for thermostimulation of muscle tissue using COMSOL Multiphysics. *Biophys. Bioeng. Lett.* 4: Available:
<https://www.researchgate.net/publication/264840070>.
- 6 COMSOL Multiphysics (2019). *Introduction to COMSOL Multiphysics®*. Burlington, MA: COMSOL First published 1998.
<https://cdn.comsol.com/doc/5.5/IntroductionToCOMSOLMultiphysics.pdf>.
- 7 Cimrák, I., Gusenbauer, M., and Schrefl, T. (2012). Modelling and simulation of processes in microfluidic devices for biomedical applications. *Comput. Math. Appl.* 64 (3): 278–288.
<https://doi.org/10.1016/j.camwa.2012.01.062>.
- 8 Nekouei, M. and Vanapalli, S.A. (2017). Volume-of-fluid simulations in microfluidic T-junction devices: influence of viscosity ratio on droplet size. *Phys. Fluids* 29 (3).
- 9 Jena, S.K., Srivastava, T., Bahga, S.S., and Kondaraju, S. (2023). Effect of channel width on droplet generation inside T-junction microchannel. *Phys. Fluids* 35 (2):
<https://doi.org/10.1063/5.0134087>.
- 10 Huang, D., Wang, K., Wang, Y. et al. (2020). Precise control for the size of droplet in T-junction microfluidic based on iterative learning method. *J. Franklin Inst.* 357 (9): 5302–5316.
<https://doi.org/10.1016/j.jfranklin.2020.02.046>.

3

Cleanroom-Assisted and Cleanroom-Free Photolithography

Abhishesh Pal^{1,2}, Satish Kumar Dubey^{1,2}, and Sanket Goel¹

*¹ MEMS, Microfluidics and Nanoelectronics (MMNE) Lab,
Department of Electrical and Electronics Engineering, Birla
Institute of Technology and Science (BITS) Pilani, Hyderabad
Campus, Hyderabad, Telangana, India*

*² Department of Mechanical Engineering, Birla Institute of
Technology and Science (BITS) Pilani, Hyderabad Campus,
Hyderabad, Telangana, India*

3.1 Introduction

Photolithography is a method of selective exposure of a photosensitive material to create a controlled pattern. The resultant regions of interest are then processed as per the fabrication requirements, such as etching, deposition, and surface treatment. As a result, the polymer has a concealed image that may be selectively dissolved to produce predetermined patterns on the substrate underneath [1].

Photoresist can be mainly categorized into two types: positive and negative. Positive photoresists are developed by removing the exposed regions, leaving behind the patterned photoresist on the substrate. In contrast, negative photoresists are developed by eliminating the unexposed regions, leaving behind the substrate material in the patterned areas. The difference between a positive and negative photoresist is shown in [Figure 3.1](#). Normally, positive photoresists are employed for thick film applications to fabricate high-aspect-ratio structures. In contrast, negative photoresists are used to fabricate thin film devices, such as integrated circuits [2].

Chemically amplified photoresists are generally used to develop submicron devices for advanced microprocessors and memory devices [3]. The choice of photoresist depends on the specific

requirements of the photolithography process, including the desired pattern resolution, the thickness of the substrate, and the desired pattern aspect ratio [4].

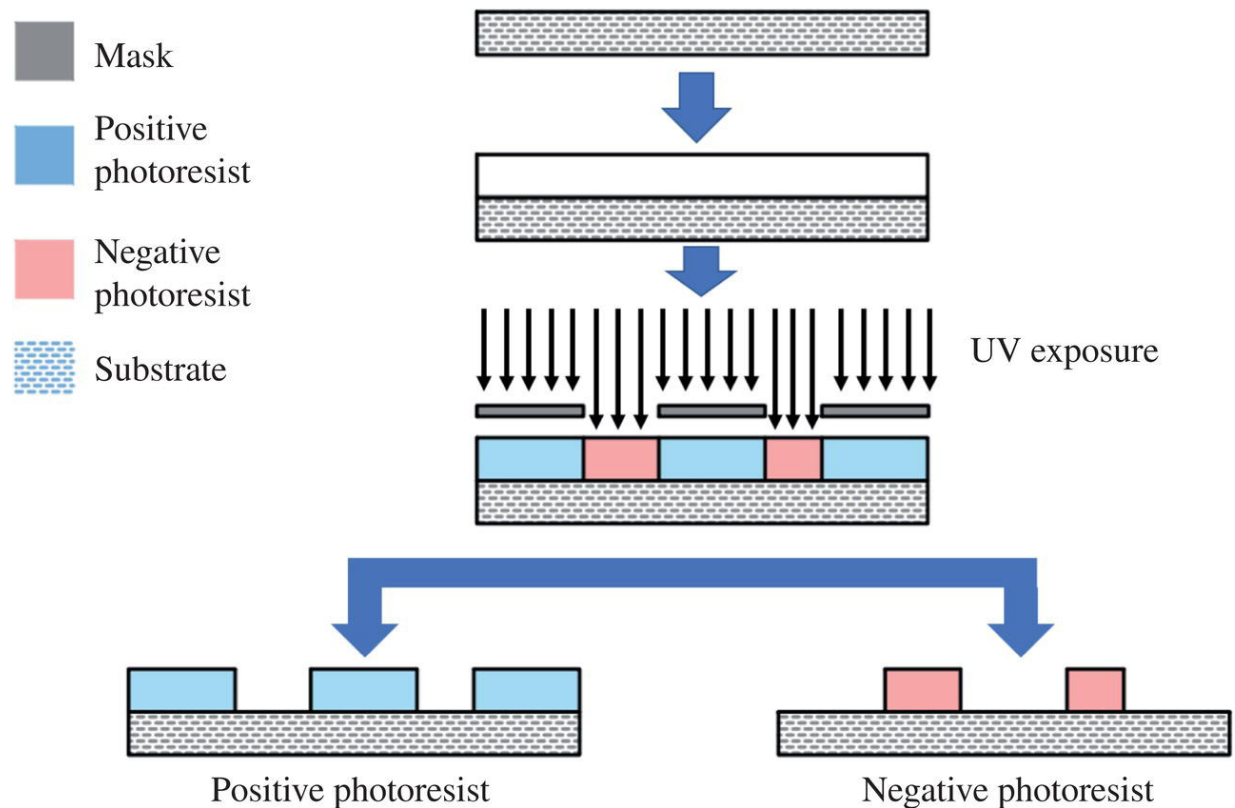


Figure 3.1 A schematic showing the difference between the positive and negative photoresists when exposed to ultra-violet radiation (UV-rays).

3.2 Photolithography Basics, Classification and Applications

Photolithography is highly precise and crucial to produce high-quality microelectronic and nanoscale devices. Using cleanroom conditions in photolithography is essential for minimizing the introduction of contaminants and ensuring the accuracy of the pattern transfer process. However, the photolithography method can also be performed in a cleanroom-unassisted environment, but with lesser accuracy, compromising the design [1].

The application of photolithography is vast, such as for producing microfluidic devices and photovoltaic cells [5]. Additionally, nanoscale devices such as nanoscale transistors, nanoscale sensors, and nanoscale electronic circuits are also achieved through photolithography [6]. Besides, it also finds its application in the development of biomedical devices and display technologies. Advanced computing through manipulating quantum bits is also achieved through photolithography [7, 8].

3.2.1 Cleanroom-Assisted Photolithography

A cleanroom environment is vital for photolithography because it helps keep the process accurate and free of contaminants that could affect the final product. It also helps to make the process repeatable and scalable so that the same process can be used repeatedly to make multiple products. Depending on the scale and requirement of the fabrication, cleanrooms can be designed. They are classified according to the maximum allowed particle count per cubic meter (Table 3.1).

The photolithography process consists of several steps, including substrate preparation, photoresist deposition, light exposure, pattern transfer, etching, photoresist removal, and post-processing. The steps are shown in detail with the help of the Figure 3.2.

Cleanroom-assisted photolithography is a unique way of making micro/nanostructures and devices. It uses light to project a pattern onto a material, which is then developed to create a final product.

3.2.2 Cleanroom-Unassisted Photolithography

Instead of using a cleanroom, photolithography also provides an alternative flexibility of using it to attain lower resolutions in cleanroom-free environments. It is a trade-off between the controlled environment and the scale of objects that can be fabricated. Herein, the process occurs in a regular laboratory or industrial setups with dust, particles, or other contaminants that can settle on the material being used. Because these contaminants can affect the accuracy of the transferred pattern, this type of photolithography is not as

precise as the cleanroom-assisted version. This can lead to lower-quality products and reduced yields [9].

Table 3.1 Classification of different classes of clean room.

Clean room class	ISO standard	Maximum allowable particle count (particles/m³)
Class 1	ISO 3	≤10 particles ≥ 0.1 μm, 0 particles ≥ 0.5 μm
Class 2	ISO 4	≤100 particles ≥ 0.1 μm, 5 particles ≥ 0.5 μm
Class 3	ISO 5	≤1000 particles ≥ 0.1 μm, 100 particles ≥ 0.5 μm
Class 4	ISO 6	≤10 000 particles ≥ 0.1 μm, 1000 particles ≥ 0.5 μm
Class 5	ISO 7	N/A (Reference: ISO 4 or ISO 5 level cleanliness)
Class 6	ISO 8	N/A (Reference: ISO 7 or ISO 6 level cleanliness)
Class 7	ISO 9	N/A (Reference: ISO 8 or ISO 7 level cleanliness)
Class 8	N/A	N/A (Reference: ISO 9 level cleanliness or lower)

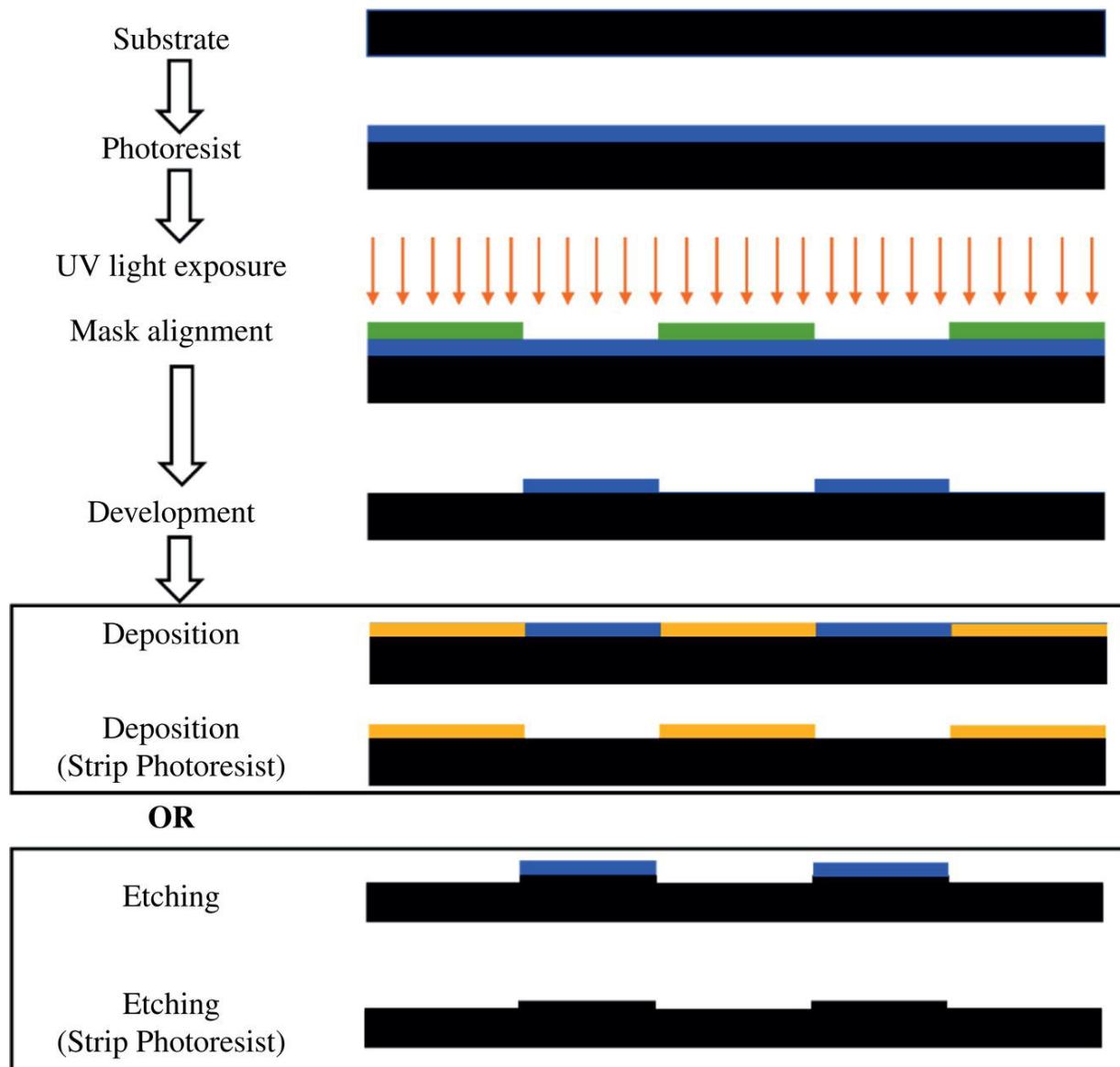


Figure 3.2 An illustration of step-by-step procedures followed to develop a pattern using photolithography for its application in deposition and etching.

Because these contaminants can affect the accuracy of the transferred pattern, this type of photolithography is not as precise as the cleanroom-assisted version. This can lead to lower-quality products and reduced yields.

For high-quality and precise microelectronic and nanoscale devices, cleanroom-assisted photolithography is typically recommended to ensure pattern transfer accuracy. However, cleanroom-unassisted

photolithography may still be used in some cases for research and development or for small-scale projects where precision is not as important. In such cases, the cost can be reduced drastically [10].

3.2.3 Cleanroom-Assisted vs. Cleanroom-Unassisted Photolithography

The difference between cleanroom-assisted photolithography and photolithography without a cleanroom is the level of control and reduction of contaminants in the processing environment.

Table 3.2 Comparative analysis between both approaches of photolithography.

S. No.	Features	Cleanroom-assisted photolithography	Cleanroom-unassisted photolithography
1	Scale	Nanometers	Micrometers
2	Dimensional accuracy	Excellent	Moderate
3	Cost	Very high	Low-cost
4	Training	Intensive	Moderate
5	Repeatability	Excellent	Moderate
6	Automation	Excellent	Moderate to none
7	Suitability	For high precision	For moderate precision

In photolithography without a cleanroom, the process occurs in a laboratory or factory floor environment that may not be specifically designed to control the level of contaminants present. As a result, dust, particles, and other contaminants can settle on the substrate and affect the pattern transfer accuracy. In contrast, cleanroom-assisted photolithography takes place in a specially designed cleanroom environment controlled to minimize the introduction of contaminants.

Utilizing a controlled cleanroom setting in the photolithography process plays a vital role in ensuring the fabrication of microelectronic and nanoscale devices that exhibit exceptional

precision and superior quality. Cleanroom photolithography plays a crucial role in enhancing the reproducibility and scalability of the pattern transfer process while improving the accuracy of final products by minimizing impurities. Cleanroom-assisted photolithography is a technique that facilitates photolithography within a controlled environment, thereby minimizing the occurrence of impurities and guaranteeing the precision and consistency of the pattern transfer procedure. On the other hand, photolithography without a cleanroom takes place in an uncontrolled environment that may introduce contaminants and affect the quality of the final product. [Table 3.2](#) gives a comparative analysis of both approaches to photolithography.

3.3 Experimental Section on Designing and Development of Features Using Photolithography

3.3.1 Brief Overview

Cleanroom-based lithography is vital for fabricating micro- and nanoscale devices with high precision and cleanliness, essential for semiconductor manufacturing, MEMS, and nanotechnology. Its applications include producing integrated circuits, sensors, and microfluidic devices. The controlled environment minimizes contamination, ensuring the reliability and performance of intricate patterns and structures necessary for advanced electronics and biomedical devices.

3.3.2 Prerequisites

Foundational use of computer-aided design (CAD) software for creating 2-D drawings or 3-D models for designing patterns as the user requires.

3.3.3 Instrumentation and Software

Micro-designs were plotted on a glass substrate using a Direct UV Laser (DLW) system (Holmarc, Cochin, India) in conjunction with a thin film of DuPont PM240 photoresist (Dupont Electronic Technologies, NC, USA). Using a static head motion, the device transfers the pattern onto the photoresist through the emission of light at 405 nm. Licensed AutoCAD and Mach 3 CNC control software.

3.3.4 Stepwise Photolithography Procedure to Develop a Pattern

Step 1: As shown in [Figure 3.2](#), lithography starts with substrate cleaning, on which operation has to be performed.

Step 2: Photoresist is spin-coated or laminated on the surface of the substrate.

Step 3: The substrate with photoresist undergoes UV radiation exposure. The exposed regions get cured (in case of negative photoresist and vice versa).

Step 4: After exposure, the samples are developed with appropriate developer solutions. The developer solution accurately removes the unexposed regions of the photoresist. Only the exposed regions remain.

Step 5: The substrate can now undergo various processes, such as the deposition of metal oxides or etching, to remove the substrate.

Step 6: The remaining photoresist is removed to obtain the desired sample.

3.4 Conclusion

This chapter gives a brief introduction and procedures for operating under photolithography in clean room-assisted and unassisted setups. Photolithography is essential to obtain outstanding features and is used in various domains such as microfluidics, microelectromechanical systems, aviation, and the automotive industry.

References

- 1 Liu, W., Wang, J., Xu, X. et al. (2021). Single-step dual-layer photolithography for tunable and scalable nanopatterning. *ACS Nano* 15 (7): 12180–12188.
- 2 Erratum (2020). *Proceedings of the Institution of Mechanical Engineers, Part C: Journal of Mechanical Engineering Science*, vol. 235. Sage (1).
- 3 Luo, C., Xu, C., Lv, L. et al. (2020). Review of recent advances in inorganic photoresists. *RSC Adv.* 10 (14): 8385–8395.
- 4 Martinez-Duarte, R. (2012). Microfabrication technologies in dielectrophoresis applications – a review. *Electrophoresis* 33 (21):

3110–3132.

- 5 Pal, A., Dubey, S.K., and Goel, S. (2022). IoT enabled microfluidic colorimetric detection platform for continuous monitoring of nitrite and phosphate in soil. *Comput. Electron. Agric.* 195: 106856.
- 6 Kartopu, G., Oklobia, O., Tansel, T. et al. (2023). A facile photolithography process enabling pinhole-free thin film photovoltaic modules on soda-lime glass. *Sol. Energy Mater. Sol. Cells* 251: 112112.
- 7 Ayub, A., Shoukat, A., Tahir, M.B. et al. (2021). Nanostructures: a solution to quantum computation and energy problems. In: *Nanotechnology* (ed. M.B. Tahir, M. Rafique, and M. Sagir), 83–107. Singapore: Springer Singapore.
- 8 Kelly, J., Barends, R., Fowler, A.G. et al. (2015). State preservation by repetitive error detection in a superconducting quantum circuit. *Nature* 519 (7541): 66–69.
- 9 Mohd Asri, M.A., Nordin, A.N., and Ramli, N. (2021). Low-cost and cleanroom-free prototyping of microfluidic and electrochemical biosensors: techniques in fabrication and bioconjugation. *Biomicrofluidics* 15 (6): 061502.
- 10 Ha, D., Hong, J., Shin, H., and Kim, T. (2016). Unconventional micro-/nanofabrication technologies for hybrid-scale lab-on-a-chip. *Lab Chip* 16 (22): 4296–4312.

4

Additive Manufacturing (3D Printing)

Pavar Sai Kumar^{}, Abhishek Kumar^{*}, and Sanket Goel
MEMS, Microfluidics and Nanoelectronics (MMNE) Lab,
Department of Electrical and Electronics Engineering, Birla
Institute of Technology and Science (BITS) Pilani, Hyderabad
Campus, Hyderabad, Telangana, India*

4.1 Stereolithography (SLA) Printing of Y-Channeled Microfluidic Chip

4.1.1 Introduction

The complex three-dimensional (3D) objects of specific significant interests and applications can be custom-developed through the advanced fabrication technique of additive Manufacturing (AM) [1]. The concept was proposed in the 1980s, commonly known as 3D Printing (3DP) or rapid prototyping. 3DP refers to building objects in x , y , and a layer-by-layer addition process in the z -direction to complete the model [2, 3]. Modern 3D printers are capable of printing micron-range objects (jewelry, toys, mimicking bio teeth, and scaffolds) to large-scale objects (automobile spare parts, houses, gadgets, and engines) [4, 5]. 3DP applications cover conventional manufacturing methods and expand their capabilities in various industries, including medical, electrical, food processing, pharmaceutical, textile, automotive, and aerospace [6, 7].

The widely adopted 3DP techniques include fused deposition modeling (FDM), direct ink writing (DIW), selective laser sintering (SLS), inkjet printing, photocuring printings including SLA, and digital light processing (DLP) [8, 9]. However, photocuring printing provides fine resolutions ranging from 100 nm to 100 μ m, compared to other existing methods [8]. Photocuring techniques use a photocurable or photosensitive resin that solidifies via a photochemical process. Moreover, topic-focused SLA printing uses

UV light to solidify the photocurable resin into solid objects [[10](#), [11](#)]. This chapter provides insights into leveraging the SLA technique to obtain a 3D-printed object. Moreover, COMSOL fluid flow mixing simulations are provided in [Chapter 2](#) for the designed and developed Y-channeled microfluidic chip.

4.1.2 Real-Time Applications of This Study

Xiaoyan Xu et al. highlight the importance of SLA printing or VAT photopolymerization towards drug delivery, medical device fabrication, aerospace, jewelry making, water filtration, and automotive, industrial applications [[12](#)]. Similarly, Callum Guttridge et al. described the biocompatibility of SLA printer resins in medical applications (orthopedics, oncology, neurosurgery, endoprosthesis, dental crowns, endoluminal stents, guides, and templates) [[13](#)].

4.1.3 Designing Section

4.1.3.1 Prerequisites

Windows 10/11 operating system, a minimum of 4 GB RAM, storage of 250 GB, and a licensed version of computer-aided designing (CAD) tool.

4.1.3.2 Software and Instrumentation

SLA 3D Printer, cleaning (isopropanol [IPA] solvent), and curing stations (Form 3, Formlabs, Germany), and installed Preform slicing software of Formlabs.

4.1.3.3 Designing a Y-Channeled Microfluidic Chip

Step 1: Open the CAD tool (Solidworks, in this case).

Step 2: Create a new part file.

Step 3: Select a plane (front, top, or right plane) and create a rectangle of length 20 mm and breadth 30 mm, shown in [Figure 4.1a](#).

Step 4: Exit sketch, click extrude in the features section, and provide the extrusion length as 2 mm.

Step 5: Select the formed rectangle face and create a new sketch on its face.

Step 6: Create a Y channel with a channel width of 1 mm, and the overall dimensions are shown in [Figure 4.1b](#).

Step 7: Exit the sketch and select extrude cut from the features section, 1 mm in the negative direction, shown in [Figure 4.1c](#).

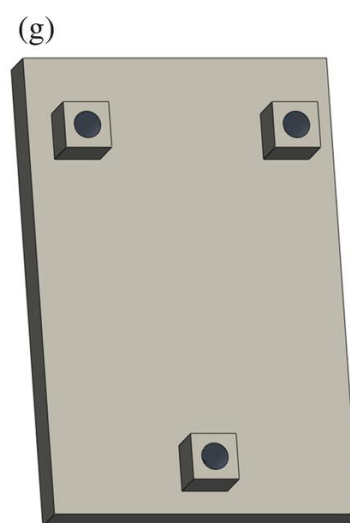
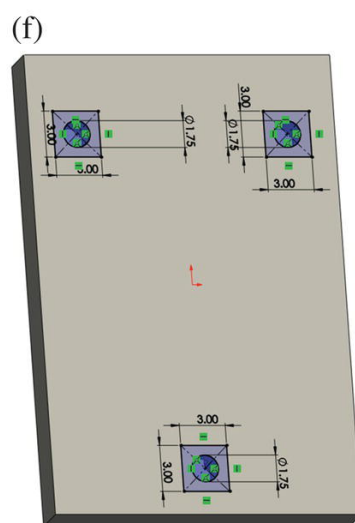
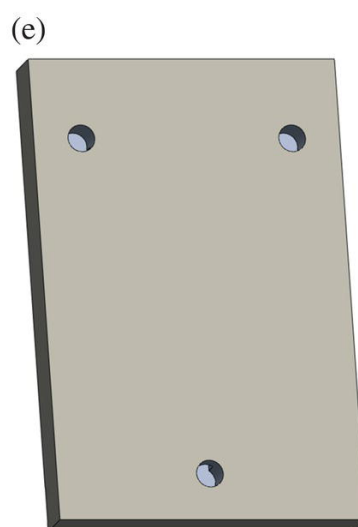
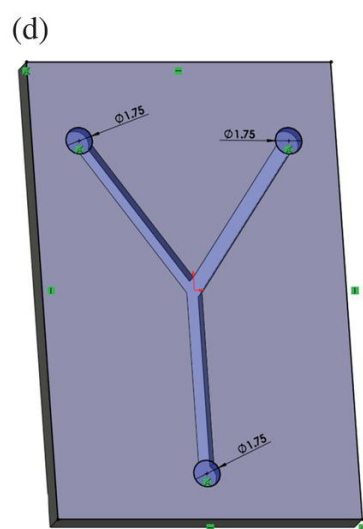
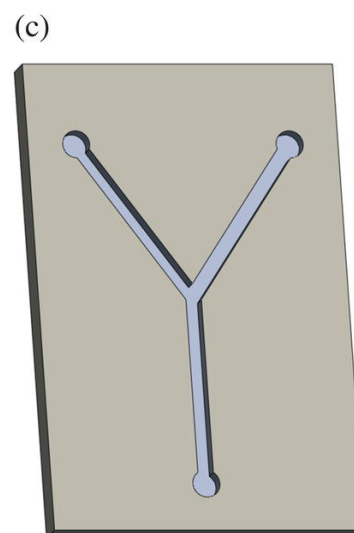
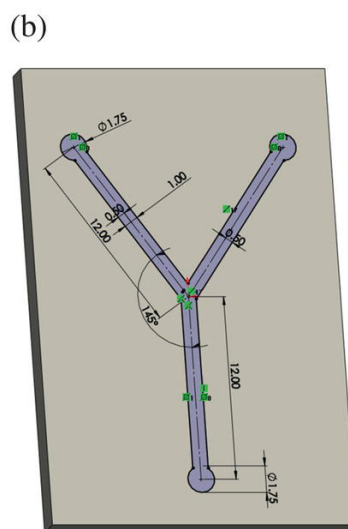
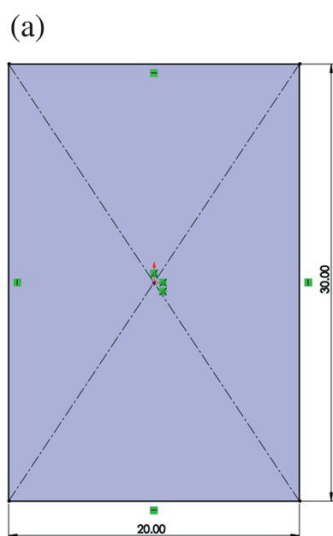


Figure 4.1 CAD process to develop a Y-channeled microfluidic chip: (a) line drawings of rectangle, (b) Y-shaped channel design, (c) extrude cut to create channel grooves, (d) addition of one more layer, (e) extrude in z direction to close the open Y-channel, (f) creation of inlets and outlet, and (g) final model (Y-shaped microfluidic device).

Step 8: Create a new sketch on the face of the Y-channeled extrude cut.

Step 9: Create another rectangular covering of 20 mm in length and 30 mm in breadth. Also, add outlet circles, as shown in [Figure 4.1d](#).

Step 10: Extrude the sketch to 1 mm in height, shown in [Figure 4.1e](#).

Step 11: Create a new sketch on the previous rectangular face and draw a circle (1.75 mm \varnothing) covered by square (3 mm²), shown in [Figure 4.1f](#).

Step 12: Exit the sketch, select the sketch, and extrude to a height of 3 mm, shown in [Figure 4.1g](#).

Step 13: Save the CAD file for any future iterations.

Step 14: Save as the 3DP readable STL format for the successive operations.

Step 15: Close the Solidworks files.

4.1.4 3D Printing Section

4.1.4.1 Slicing Operations

Step 1: Open the slicing software Preform.

Step 2: Import the previously saved Y-channeled STL file.

Step 3: Select the model and position at the required spot on the print bed, shown in [Figure 4.2a](#).

Step 4: Select the printer type and choose form 3 (i.e., by entering the internet protocol [IP] address of the printer), in this

case; select the print material as clear; select the print layer thickness as adaptive (i.e., layer thickness adjusts according to the part geometry); select the print settings as default; and click on apply, shown in [Figure 4.2b](#).

Step 5: Select the supports option from the left side toolbar and untick the raft label and internal supports. Change the touch point size to 0.5 mm, while others remain default.

Step 6: Click on the auto-generate selected option in the supports section to visualize the supports for the object, shown in [Figure 4.2c](#).

Step 7: Click on Print, and the established connection with the printer will send the file to the printer.

Step 8: Once uploaded to the printer, select the print option in the printer interface, and the printer will begin printing.

4.1.4.2 Cleaning and Curing Operations

Step 1: The printed part contains the sticky resin around the object. Drop the printed part into the cleaning tank containing IPA for 15 minutes.

Step 2: The dried part could be kept in the curing station at 60 °C for 15 minutes to obtain the final product, as shown in [Figure 4.3](#).

Step 3: The obtained Y-channeled 3D printed microfluidic chip can be leveraged for user-defined applications. [Figure 4.3](#) shows the real-time deployment of the developed Y-channeled microfluidic chip for the droplet generations.

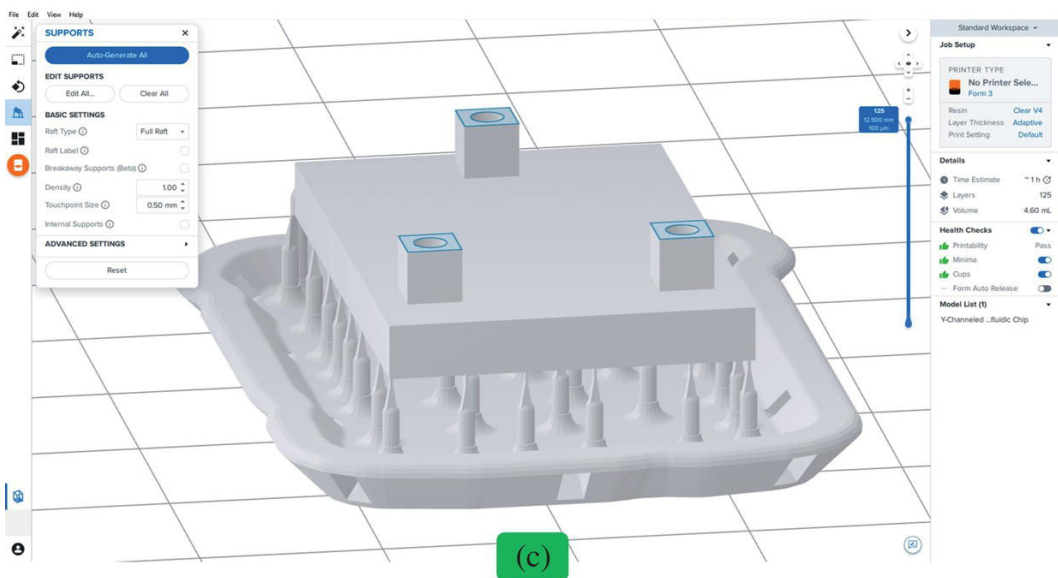
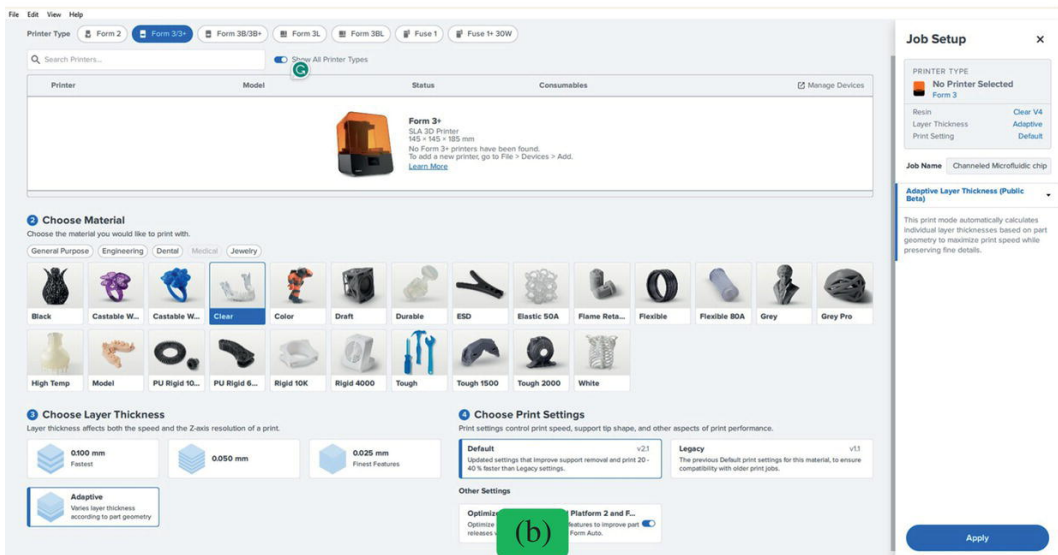
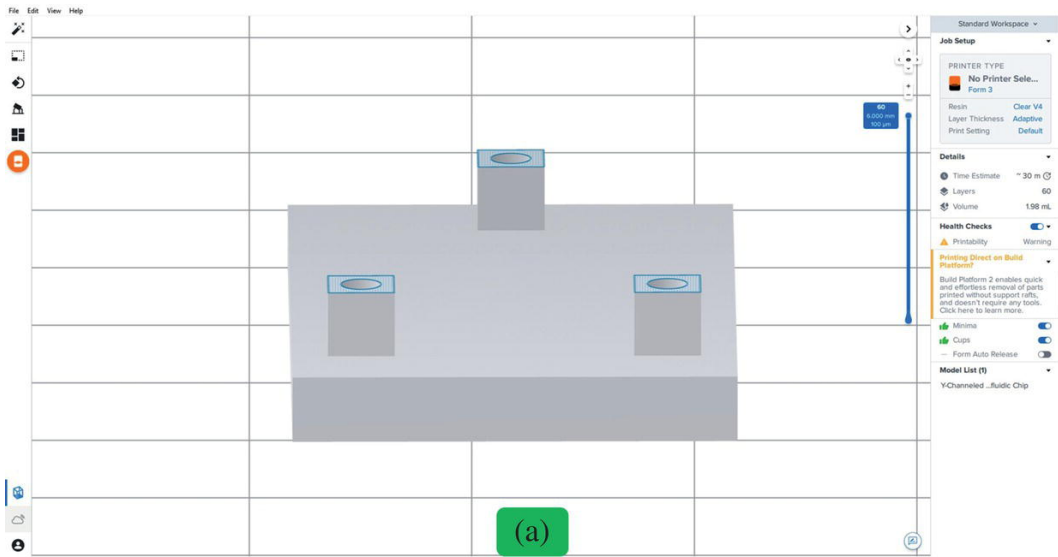


Figure 4.2 Slicing operations over the Y-channeled microfluidic chip using the preform slicing tool, (a) importing and positioning the object, (b) print settings window, and (c) supports generation window.

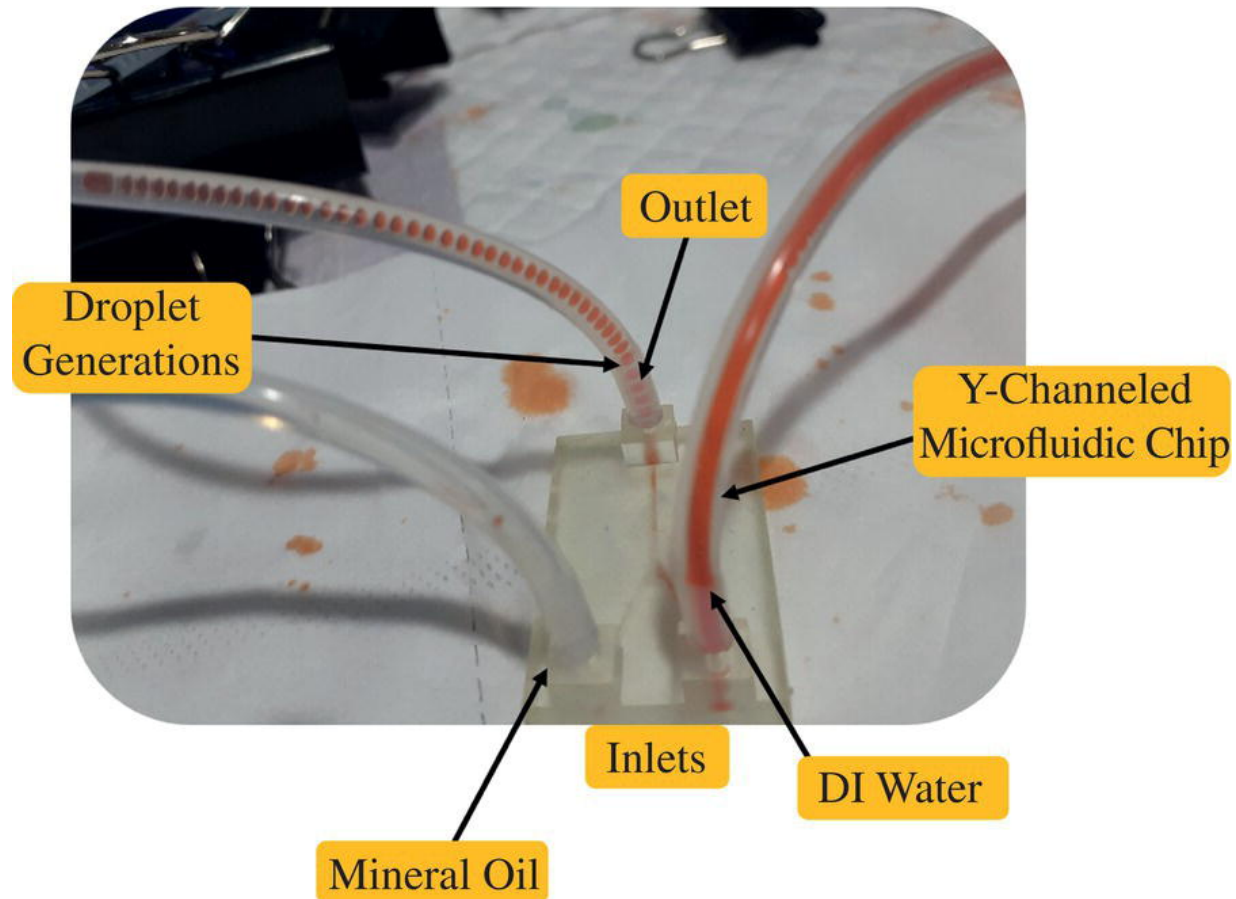


Figure 4.3 The final SLA printed Y-channeled microfluidic chip leveraged for droplet generations.

4.1.5 Conclusion

This chapter concentrated on using SLA printing to design and create a Y-channeled microfluidic chip. This chapter provides detailed steps for designing and developing. The information given is useful for creating microfluidic channels with 3DP for a range of uses.

4.2 Fused Deposition Modeling (FDM): Fabrication of Single Electrode Electrochemiluminescence Device

4.2.1 Introduction

The FDM process is categorized as an AM technique within the material extrusion category. The FDM technique involves extruding polymeric material (thermoplastic, thermosetting, and their composites) in feedstock filament form through a liquefier head and depositing the material in a preset path that has been computer-programmed [14]. The build plate, extruder head, cooling unit, stepper motor, filament holder, display unit, and power supply unit are the key parts of FDM printers. Since the rapid prototyping process and CAD engineering have advanced and improved the capability of FDM machines, which were formerly used to produce product prototypes, they are now used for the realization of finished products. Geometries with precise details and elaborate architecture can be constructed with its help. Many nonstructural and structural applications make use of the FDM technique [15]. There are three main steps in the process flow of an FDM 3D printer: part production, post-processing, and pre-processing. Pre-processing entails part slicing and design conceptualization to manipulate the extruder action and transform the design layer by layer. The process of melting and extruding semimolten feedstock filament from the nozzle in a controlled manner, as well as creating support for the overhanging structure, are included in the production step. During the post-processing stage, support material is manually removed and dissolved in solvents [14]. Several industries, including aerospace, automotive, manufacturing, biomedical, and food engineering, use the FDM method.

1.75 and 2.85 mm are the two common feedstock filament sizes used by FDM 3D printers. Many characteristics are offered by the FDM process, including the capacity to print intricate structures, a user-friendly interface, some degree of design flexibility, affordable material availability with a favorable price-to-performance ratio, the removal of fixtures and jigs, mass customization, etc. Acrylonitrile

butadiene styrene (ABS) and poly-lactic acid (PLA) are the most often utilized materials in FDM printers [14, 16, 17].

A few recent studies developed a variety of sensors for real-world applications using 3DP techniques. Bishop et al. has proposed SLA 3D printed fluidic devices to perform electrochemiluminescence (ECL) measurements. They have fabricated a clear resin-based fluidic device incorporated with graphite pencils rod electrodes to detect $[\text{Ru}(\text{bpy})_3]^{2+}$ from 9 to 900 μM concentration. They observed a detection limit of 7 μM and demonstrated a simpler, cheaper, and easily adaptable solution for measuring ECL signals [18].

Likewise, Ferreira et al. [19] proposed a unique 3D-printed electrochemical cell, shown in Figure 4.4a used for screening drugs using the voltammetry approach. They have used FDM desktop 3D printer for fabricating the cell's body using ABS material, which includes three parts viz; solution vessel, stick and closing cover embedded with 3D pen printed dual conductive electrodes (counter and reference) using carbon black PLA material. The fabricated electrochemical cell enables a simpler approach for assembling interchangeable planar working electrodes.

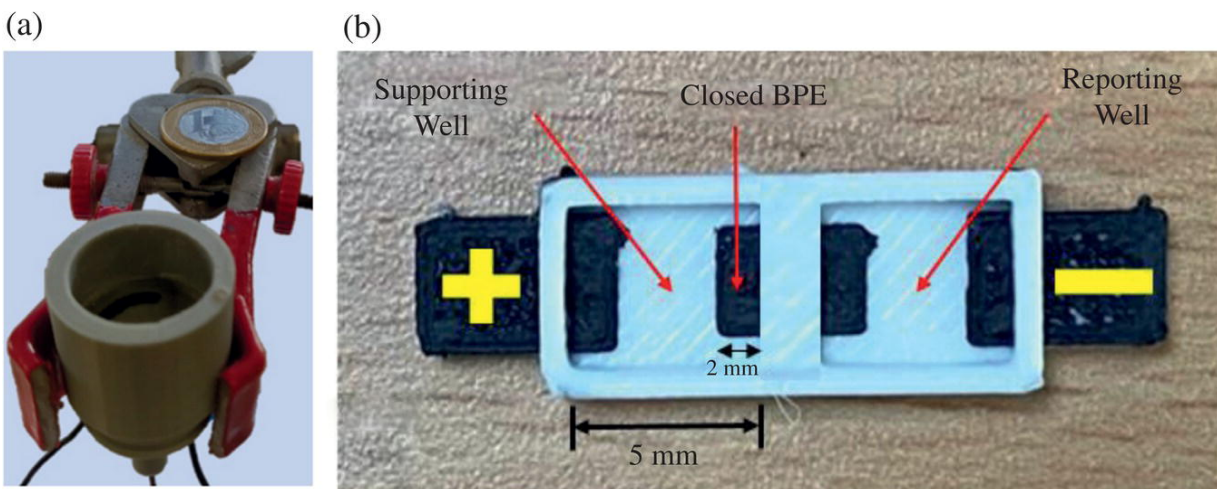


Figure 4.4 (a) Real picture of 3D Printed MSEC held by universal support,

Source: Taken from [19], with the permission of Elsevier.

(b) 3D-printed closed bipolar ECL device for cholesterol sensing,

Source: Taken from [20], with the permission of IEEE.

Chen et al. reported a novel smartphone-assisted colourimetric reader integrated with 3D printed attachment for onsite colourimetric detection. They demonstrated the utility of the developed device in conjunction with ELISA to detect zearalenone. The developed liquid colorimetric assay system has shown promising capabilities such as less cost, and high accuracy for performing clinical diagnosis, environment monitoring, and food quality testing [21].

Bhaiyya et al. presented a standalone 3D-printed ECL platform for performing the enzymatic detection of cholesterol, as shown in [Figure 4.4b](#). A dual extruder FDM-based 3D printer system is utilized to fabricate a nonconductive substrate of PLA material and graphene filament-based conductive material to fabricate a closed bipolar electrode ECL platform. The linear range is observed from 0.5 to 10 mM, and the detection limit is 0.12 mM. The developed ECL platform has the potential to perform enzymatic detection of other analytes like glucose, lactate, choline, etc. [20].

4.2.1.1 Brief Overview

Prototypes that are both functional and nonfunctional are the primary applications for FDM 3DP of polymeric materials. The fast development of materials, technology, and dual material printing has made FDM more applicable to real-time applications. An easy way to create ECL-based biosensors that can be quickly used for different biomarkers detection procedures is demonstrated in the experimental technique that follows.

4.2.2 Designing Section

4.2.2.1 Prerequisites

Windows 10/11 operating system, a minimum of 4 GB RAM, storage of 250 GB, and a licensed version of CAD tool.

4.2.2.2 Software and Instrumentation

FDM 3D Printer (BCN 3D, Sigma D25, USA), PLA filament, Conductive PLA filament, and installed slicing software

4.2.2.3 Fabrication Step

Step 1. 2D sketch of electrode design using Solid Works.

Step 2. Machine setup priming, build plate calibration and dual filament loading (Conductive and Nonconductive material), and designing electrodes in CAD model.

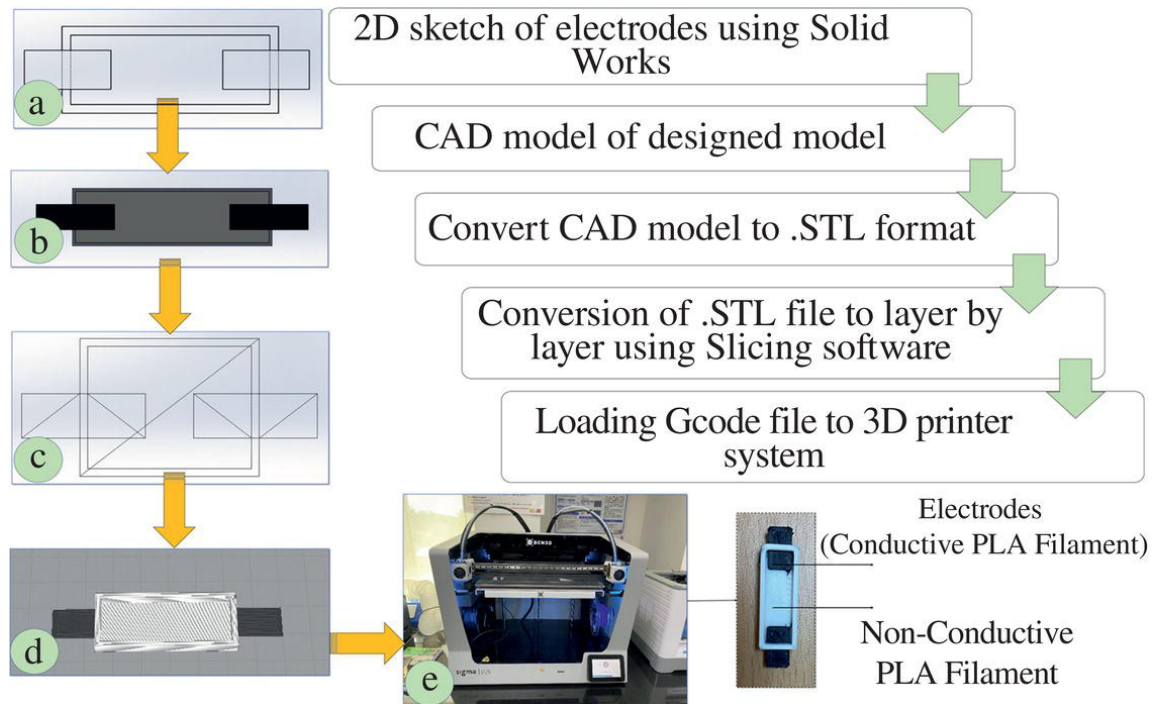


Figure 4.5 Step-by-step process to fabricate electrodes using 3D printer.

Step 3. Convert CAD model to STL format.

Step 4. Load Gcode file to 3D printer system.

Step 5. The process parameters, such as build plate temperature, printing temperature, and slicing parameters, are encoded in programmed code and executed for part fabrication (as shown in [Figure 4.5](#)).

4.2.3 Conclusion

This methodology illustrates a one-step fabrication method for ECL biosensors using fuse deposition modeling. To achieve 3DP ECL biosensor manufacture, inexpensive biodegradable polymers like as

PLA and conductive carbon-based PLA filament are used. The electrode's geometry and shape can be changed to suit the needs of the user. Therefore, the FDM process offers a simple design and manufacture method for the creation of biosensors.

References

- 1 Quan, H., Zhang, T., Xu, H. et al. (2020). Photo-curing 3D printing technique and its challenges. *Bioact. Mater.* 5: 110–115.
<https://doi.org/10.1016/j.bioactmat.2019.12.003>.
- 2 Kumar, P.S., Bhand, S., Das, A.K., and Goel, S. (2022). Microfluidic paper device with on-site heating to produce reactive peroxide species for enhanced smartphone enabled chemiluminescence signal. *Talanta* 236: 122858.
<https://doi.org/10.1016/j.talanta.2021.122858>.
- 3 Kumar, P.S., Madapusi, S., and Goel, S. (2023). 3D printed microfluidic chemiluminescence PoC device with self-powering and integrated incubating system: validation via ALP detection on disposable μ PADs. *Microchem. J.* 189: 108518.
<https://doi.org/10.1016/j.microc.2023.108518>.
- 4 Umair, M. and Kim, W.S. (2015). An online 3D printing portal for general and medical fields. In: *2015 International Conference on Computational Intelligence and Communication Networks (CICN)*, 278–282. IEEE.
- 5 Kumar, P.S., Advincula, P., and Goel, S.G. (2022). First report on onsite temperature based recovery of quenched chemiluminescence signal from graphenized μ PADs: validation by catechins radical scavenging. *Nano Futur.*
<https://doi.org/10.1088/2399-1984/ac9d78>.
- 6 Maines, E.M., Porwal, M.K., Ellison, C.J., and Reineke, T.M. (2021). Sustainable advances in SLA/DLP 3D printing materials and processes. *Green Chem.* 23: 6863–6897.
<https://doi.org/10.1039/D1GC01489G>.

- 7** Bhaiyya, M., Kumar, P.S., Pattnaik, P.K. et al. (2023). Stereolithography 3-D printed electrochemiluminescence platform with random grade graphite electrodes: detection of HO and cholesterol using a smartphone. *IEEE Sens. J.* 23: 750–757. <https://doi.org/10.1109/JSEN.2022.3221728>.
- 8** Karakurt, I. and Lin, L. (2020). 3D printing technologies: techniques, materials, and post-processing. *Curr. Opin. Chem. Eng.* 28: 134–143. <https://doi.org/10.1016/j.coche.2020.04.001>.
- 9** Kumar, P.S., Madapusi, S., and Goel, S. (2023). Sub-second synthesis of silver nanoparticles in 3D printed monolithic multilayered microfluidic chip: enhanced chemiluminescence sensing predictions via machine learning algorithms. *Int. J. Biol. Macromol.* 245: 125502. <https://doi.org/10.1016/j.ijbiomac.2023.125502>.
- 10** Wagh, M.D., Renuka, H., Kumar, P.S. et al. (2022). Integrated microfluidic device with MXene enhanced laser-induced graphene bioelectrode for sensitive and selective electroanalytical detection of dopamine. *IEEE Sens. J.* 22: 14620–14627. <https://doi.org/10.1109/JSEN.2022.3182293>.
- 11** Bhaiyya, M., Kumar, P.S., Pattnaik, P.K. et al. (2022). Stereolithography 3-D printed electrochemiluminescence platform with random grade graphite electrodes: detection of HO and cholesterol using a smartphone. *IEEE Sens. J.* 23: 750–757.
- 12** Xu, X., Awad, A., Robles-Martinez, P. et al. (2021). Vat photopolymerization 3D printing for advanced drug delivery and medical device applications. *J. Control. Release* 329: 743–757. <https://doi.org/10.1016/j.jconrel.2020.10.008>.
- 13** Guttridge, C., Shannon, A., O'Sullivan, A. et al. (2022). Biocompatible 3D printing resins for medical applications: a review of marketed intended use, biocompatibility certification, and post-processing guidance. *Ann. 3D Print. Med.* 5: 100044. <https://doi.org/10.1016/j.stlm.2021.100044>.
- 14** Gibson, I., Rosen, D., Stucker, B., and Khorasani, M. (2020). *Additive Manufacturing Technologies*. Springer International

Publishing <https://doi.org/10.1007/978-3-030-56127-7>.

- 15** Abdulhameed, O., Al-Ahmari, A., Ameen, W., and Mian, S.H. (2019). Additive manufacturing: challenges, trends, and applications. *Adv. Mech. Eng.* 11: <https://doi.org/10.1177/1687814018822880>.
- 16** J. Scott, N. Gupta, C. Weber, T. Caffrey, Additive Manufacturing: Status and Opportunities, 2012.
- 17** Wong, K.V. and Hernandez, A. (2012). A review of additive manufacturing. *ISRN Mech. Eng.* 2012: 1–10. <https://doi.org/10.5402/2012/208760>.
- 18** Bishop, G.W., Satterwhite-Warden, J.E., Bist, I. et al. (2016). Electrochemiluminescence at bare and DNA-coated graphite electrodes in 3D-printed fluidic devices. *ACS Sens.* 1: 197–202. <https://doi.org/10.1021/acssensors.5b00156>.
- 19** Ferreira, P.A., de Oliveira, F.M., de Melo, E.I. et al. (2021). Multi sensor compatible 3D-printed electrochemical cell for voltammetric drug screening. *Anal. Chim. Acta* 1169: <https://doi.org/10.1016/j.aca.2021.338568>.
- 20** Bhaiyya, M., Kumar, P.S., Pattnaik, P.K. et al. (2022). Stereolithography 3D printed electrochemiluminescence platform with random grade graphite electrode: detection of H₂O₂ and cholesterol using a smartphone. *IEEE Sens. J.* <https://doi.org/10.1109/JSEN.2022.3221728>.
- 21** Chen, Y., Fu, Q., Li, D. et al. (2017). A smartphone colorimetric reader integrated with an ambient light sensor and a 3D printed attachment for on-site detection of zearalenone. *Anal. Bioanal. Chem.* 409: 6567–6574. <https://doi.org/10.1007/s00216-017-0605-2>.

Note

* Equally Contributing Authors.

5

Laser Processing

Pavar Sai Kumar^{}, Abhishek Kumar^{*}, Manish Bhaiyya, and Sanket Goel*

*MEMS, Microfluidics and Nanoelectronics (MMNE) Lab,
Department of Electrical and Electronics Engineering, Birla
Institute of Technology and Science (BITS) Pilani, Hyderabad
Campus, Hyderabad, Telangana, India*

5.1 CO₂ Laser for Electrochemical Sensor Fabrication

5.1.1 Introduction

Graphene (two-dimensional [2D], honeycomb lattice structure), an allotrope of carbon, has gained attention from researchers owing to its diverse applications in various fields [1]. Excellent mechanical strength, exceptional electrical and thermal conductivity, and rapid electron mobility are only a few of the many advantages of graphene [2]. With appropriate speed and power, a CO₂ laser can be used to easily generate graphene on suitable (carbonized) material; this fabricated material is referred as laser-induced graphene (LIG) [3–5]. Globally, low-cost, commercially viable polyimide sheets have become a clear choice for researchers to form LIG owing to ease of fabrication via a single-step fabrication approach [6]. Polyimide sheets are widely employed in several applications, including biomedical, supercapacitors, and fuel cells. This chapter describes how to use a CO₂ laser to produce LIG over a polyimide sheet.

5.1.2 Real-Time Applications of This Study

Here are a few recent publications showing how LIG is leveraged to develop various types of sensors for practical usage. Betty Edem Nugba et al. described the nonenzymatic detection of glucose levels from saliva using a LIG electrode system, as shown in [Figure 5.1a](#).

Here, 3D morphological structures of graphene on PI are developed by means of a laser irradiation technique based on galvanic pulses. The developed electrodes are highly sensitive, with a response time of less than 5 seconds. The sensor showed a wide calibration range of 0.03–4.5 mM with a 0.023 μ M of the detection limit. The developed sensor can diagnose real-time applications with a 97% accuracy level [7].

Nitrite detection in water is demonstrated by the Jingxia Wang et al. group using the facile LIG technology, as shown in [Figure 5.1b](#). Herein, the developed LIG is functionalized with gold (Au) and nano carbons for effective capture of nitrate ions from water samples. The modified material is thoroughly characterized to ensure the enhanced adsorption capacity of nitrate on the electrode surface. The developed methodology is able to capture nitrate ions in a range of 7–700 and 700–1050 μ g/l with good recovery values [8].

Lin Cheng et al. demonstrated the potential of LIG modification (shown in [Figure 5.1c](#)) using silver nano wires (AgNWs) for improved surface enhanced Raman spectroscopy (SERS) phenomenon. The modified surface is further encapsulated using polydimethyl siloxane (PDMS) owing to the flexible substrate. The developed methodology is efficient in extracting the target molecule information from complex constituents. The method is leveraged for nondestructive extraction and surface peel detections. It also promoted the collection of information from fingerprint residues in real time, enabling molecular-level trace identification applicable in food safety and forensic examination [9].

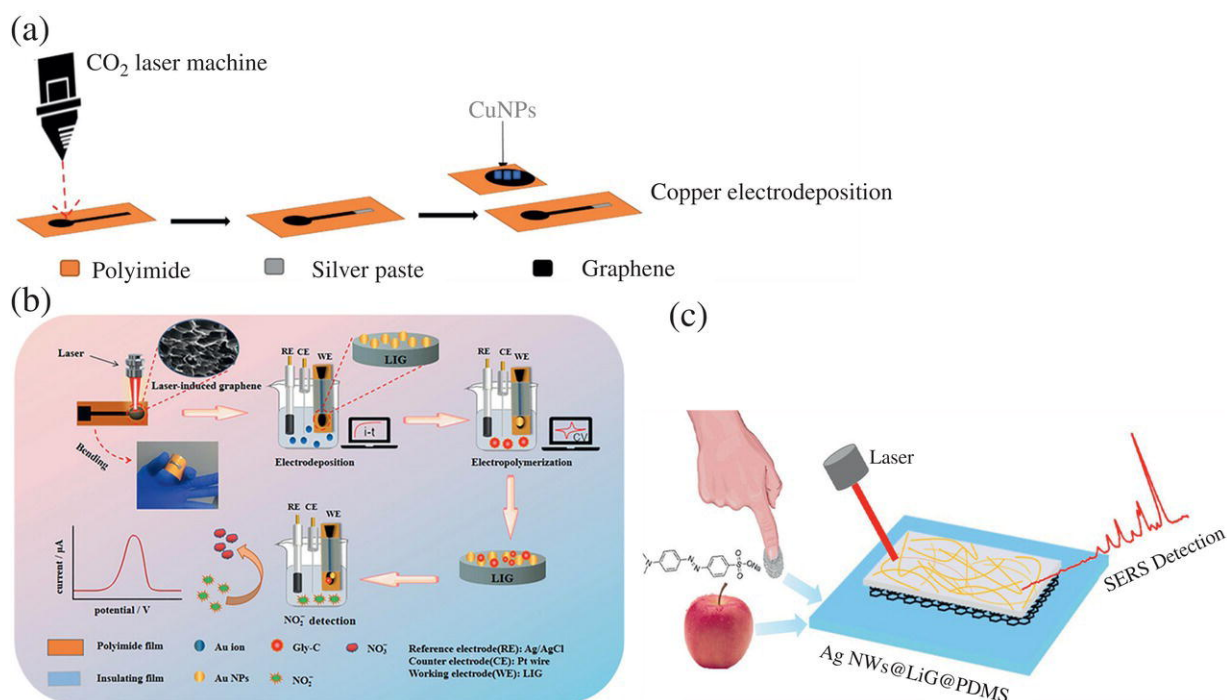


Figure 5.1 (a) Fabrication procedure of glucose monitoring LiG sensor,

Source: [7] / Springer Nature / CC BY 4.0.

(b) Schematic for the nitrate capture using modified LiG electrodes,

Source: [8] / with permission of ELSEVIER. @ Elsevier.

(c) Improved SERS phenomenon using modified LiG surface,

Source: [9] / with permission of American Chemical Society.

In another interesting report, Ju Zhang et al. used LiG to disinfect saltwater. Here, the developed LiG electrodes are supplied with electrical impulse of 2 V to inactivate the bacterial activities of two primary bacteria, *E. coli* and *Bacillus subtilis*. The same research group also worked on varying the different water parameters to monitor the bacterial activities via electrochemical studies. The proposed methodology is highly effective in disinfection using LiG electrodes [10].

5.1.3 Brief Overview

LiG is formed by direct CO₂ laser writing on the polyimide substrate. It emerges as a clean process for fabricating LiG. It allows a simple

approach for forming graphene-based electrodes for electrochemical biosensing to detect various analytes, bacteria, cells, proteins, and pesticides. It has gained attention due to its promising electrical, cost-effective, flexible, and simple-step fabrication approach. The following experimentation highlights the procedure to obtain LIG on the polyimide substrate.

5.1.4 Experimental Section

5.1.4.1 Prerequisites

Microsoft Windows 10/11 operating system, a minimum of 4 GB RAM, storage of 250 GB, and a licensed version of computer-aided designing (CAD) tool.

5.1.4.2 Materials, Instrumentation, and Software

Polyimide sheet, Corel Draw, CO₂ laser system VLS 3.60 (Universal Laser Systems), and installed VLS 3.60 OEM software.

5.1.4.3 Fabrication Steps

Step 1. Draw an electrode design in CAD software and convert it into .dxf format (see [Figure 5.2a](#)).

Step 2. Transfer the model to the CO₂ laser machine (see [Figure 5.2b](#)).

Step 3. Select the appropriate mode of operation, i.e., rast or event; see [Figure 5.2c](#). Go to the Settings menu bar and select the appropriate speed and power.

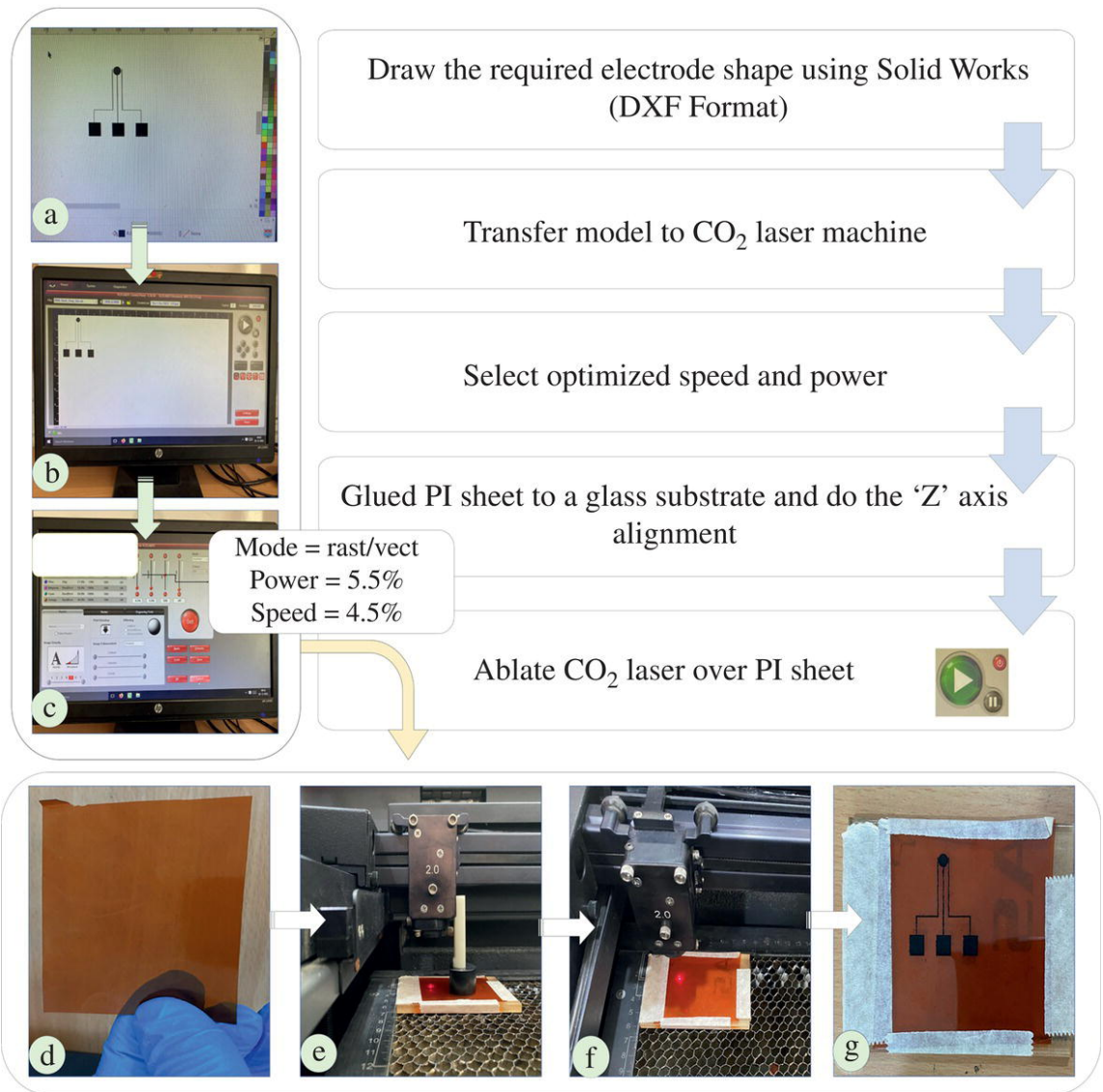


Figure 5.2 Step-by-step process to fabricate electrodes using laser-induced graphene: (a) Design of three electrode system in Corel draw application suite. (b) Exporting the designed three electrode system design file to UWS commercial application suite. (c) The optimized speed and power is set up in the model. (d) Polyimide sheet glued to a rigid base for proper. alignment. (e) Calibration of Z axis with respect to polyimide sheet. (f) Initialization of laser ablation process. (g) Final obtained laser induce graphene electrode pads.

Step 4. Take a piece of polyimide sheet, glue it with a glass slide with double-side tape, and do the “Z” axis alignment (see [Figure 5.2d, e](#)).

Step 5. Ablate CO₂ laser over polyimide sheet to form LIG (see [Figure 5.2f, g](#)).

5.1.5 Conclusion

Herein, a simple methodology for fabricating three-electrode system pads is demonstrated for electrochemical detection using CO₂ laser. The present work highlights an innovative approach to utilize a polyimide sheets to prepare a three-electrode system by laser ablation method. The developed three electrode comprised biosensor can detect human metabolites such as glucose, cholesterol, lactate, dopamine, choline, etc.

5.2 One-Step Production of Reduced Graphene Oxide from Paper via 450 nm Laser Ablations

5.2.1 Introduction

A single carbon atom thickness sheet distributed by a hexagonal crystal lattice structure with sp² hybridization characterizes graphene, a 2D material. Given that it is thought to be the thinnest material and has exceptional electrical, mechanical, and chemical qualities [\[11\]](#), it is widely adopted in a variety of applications, including pollutant detection (environmental gasses and heavy metals), biomedical substance analysis (biomarker and biological samples), ecological remediations (seawater-desalination), and energy harvesting (solar cells, supercapacitors, and batteries) [\[12–17\]](#). However, the existing surplus ways to produce graphene lack scalability, stability, tedious production time, and costs, limiting its potential [\[18\]](#). Thereby, the graphene derivatives, including carbon nanotubes (CNTs), fullerenes, graphene oxide (GO), and reduced graphene oxide (rGO) mainly, are explored [\[18\]](#).

GO is chemically prepared by strong oxidants and extensive exfoliations of graphitic basal planes, typically containing the carbon/oxygen (C/O) ratio of 3 : 1–2 : 1. Moreover, the electrical and thermal characteristics of the highly oxygen functionalized GO are

constrained [19]. Nonetheless, its main use is as a base element for the production of graphene [20]. rGO is produced using the traditional method of lowering the oxygen content of GO via chemical, thermal, microwave, photochemical, photothermal, and green synthesis. [21]. The restoration of graphene-like properties attracts the exploration of rGO for various applications [22, 23].

This chapter aims to provide unconventional advanced insights on the one-step production of rGO from paper via 450 nm blue diode laser irradiations.

5.2.2 Experimentation

5.2.2.1 Prerequisites

Fire-retardant solution (7.3 g of Borax powder and 3.3 g of Boric acid in deionized [DI] water):, dip coat and dry the Whatman filter paper grade 1 paper samples in the FR solution for 20 minutes at 75 °C in an oven, ensuring complete drying. It is optional to stick a parafilm tape underneath the paper (80 °C) by using a laminator press to increase its mechanical stiffness, as reported in our previous work [23].

5.2.2.2 Instrumentation and Software

Blue diode laser system of 450 nm wavelength (ZMorph VX, Multitool model, Poland), laser-specific user interface software (Voxelizer 3.0), and any CAD software (Solidworks, in this case).

Step 3: Save the file in the respective extension for future iterations. Further, save the file in DXF format for successive processes.

Step 4: Open the Voxelizer 3.0 software to convert the DXF file to a gcode file.

Step 5: Import the saved DXF file and position the file over the bed to print in the Voxelizer 3.0 software, as shown in [Figure 5.2a](#).

Step 6: Adjust the X and Y positions of the file from the left side toolbar, shown in [Figure 5.4a](#).

Step 7: Click Next after positioning.

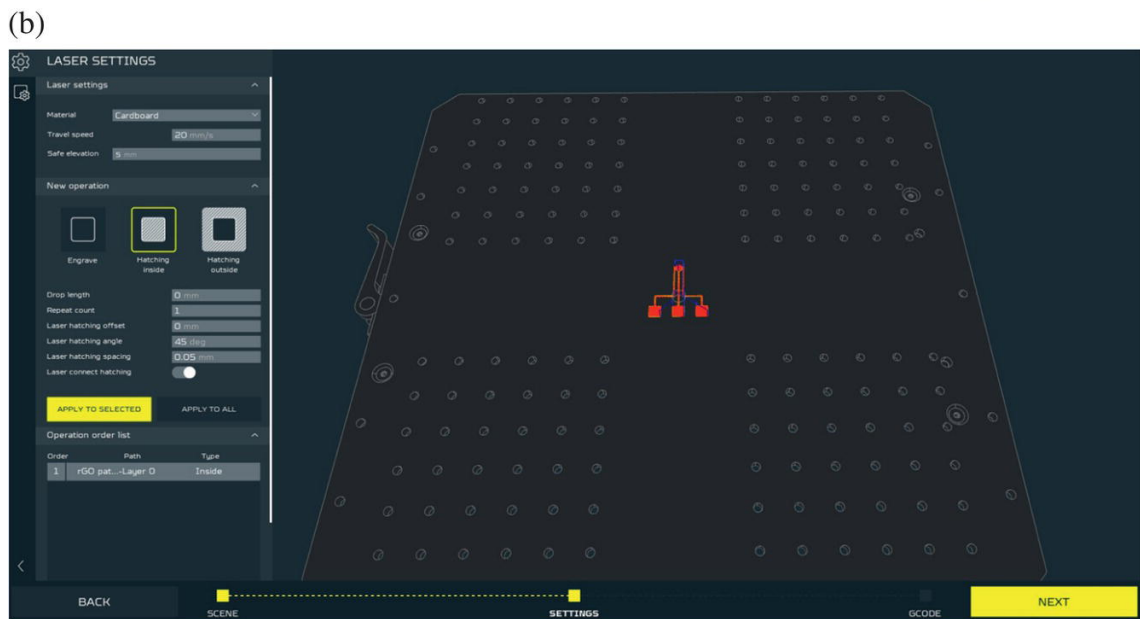
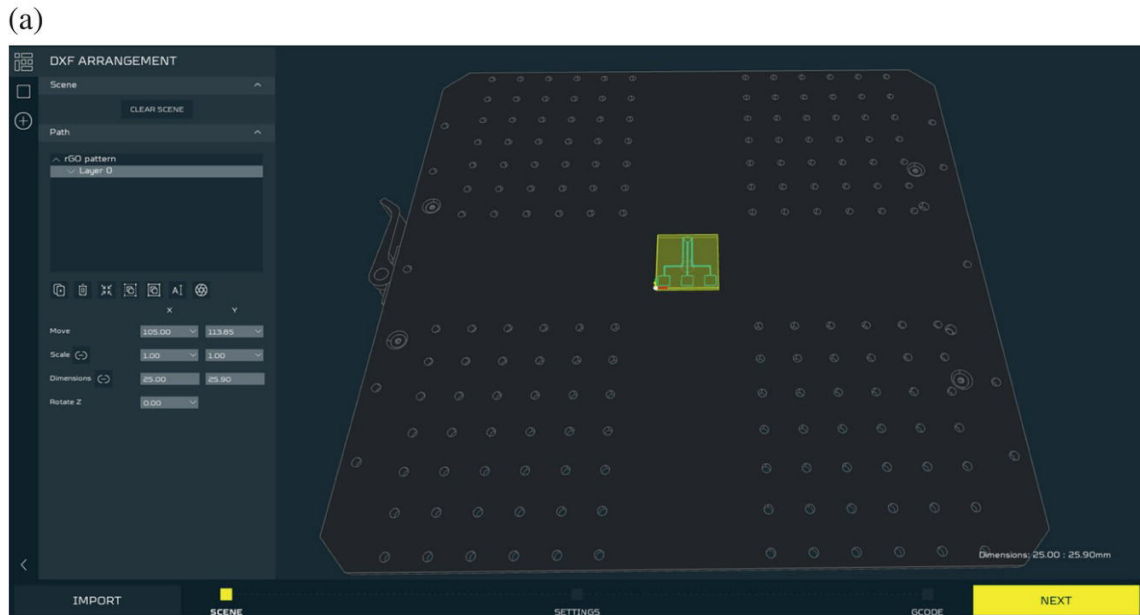


Figure 5.4 Gcode conversion via GUI of Voxelizer software, (a) File import and positioning, and (b) Setting of laser parameters.

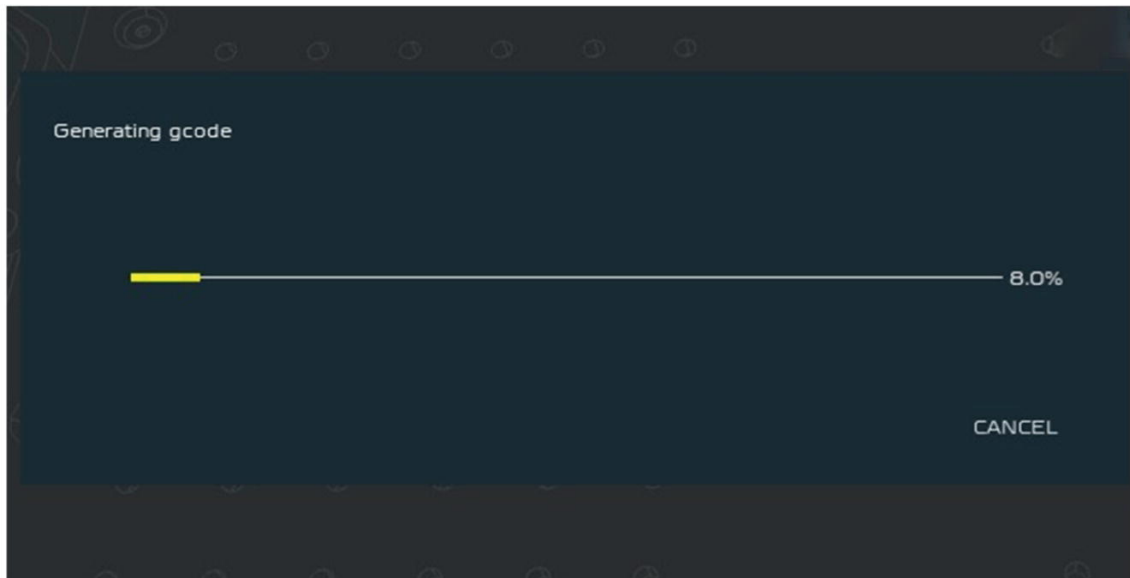
Step 8: Select the file, and in the laser settings window, select the hatch inside option, shown in [Figure 5.2b](#) left.

Step 9: Enter the below-provided parameters in the same window.

Default drop length = 0 mm (model height from the base);
default repeat count = 1 (number of repetitions); laser hatching

offset = 0 (hatching offset creates the print offset of the patterns); laser hatching angle = 45° (preferred); and laser hatching spacing = 0.05 mm (hatch spacing between two consecutive lines). Click on Apply to select. Further, the application of parameters is represented by changing the file to red, as shown in [Figure 5.4b](#).

(a)



(b)

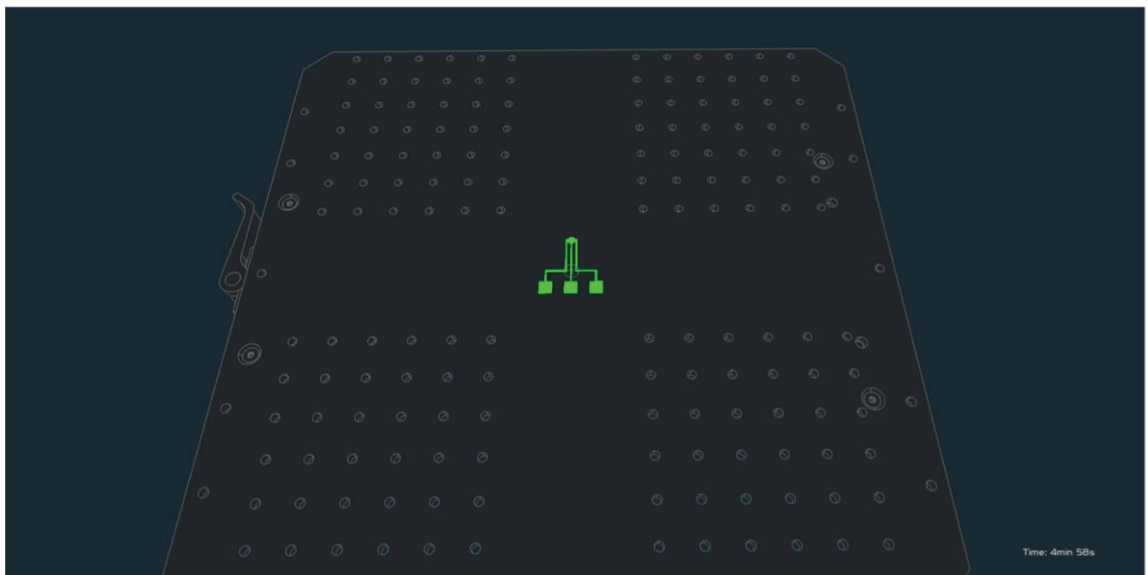


Figure 5.5 Gcode conversion via GUI of Voxelizer software, (a) gcode conversion progress window, and (b) final converted file in green representation.

Step 10: Click Next to create the gcode. The progress is shown in [Figure 5.5a](#). Depending on the design dimensions and complexity, the conversion might take a few minutes.

Step 11: As shown in [Figure 5.5b](#), the ready-to-save gcode file is highlighted in green color. Click on. Save to save as gcode.

5.2.3 Production of rGO Patterns

Step 1: The saved gcode file is to be loaded into the SD card of the printer.

Step 2: Return the SD card to the printer, and in the printer GUI, select the new file, and open the saved gcode.

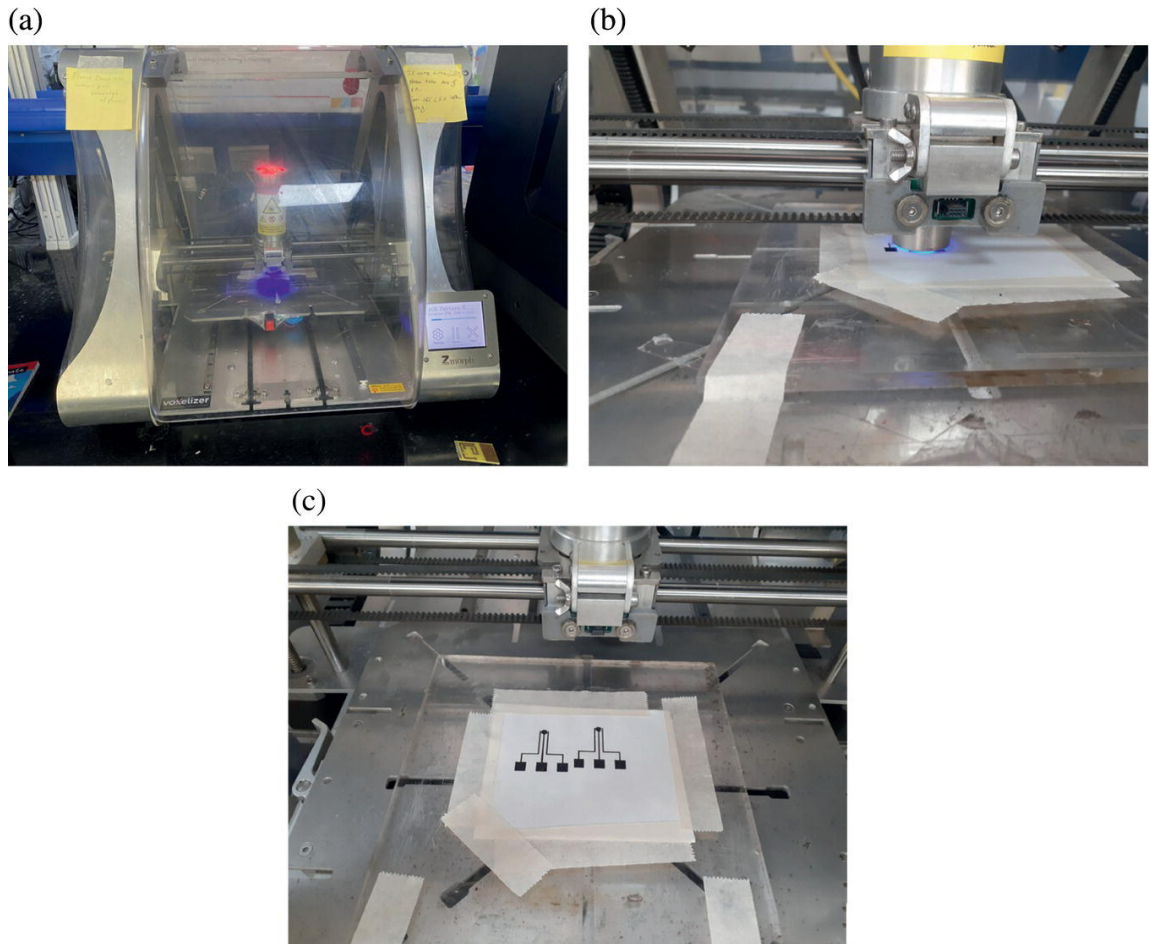


Figure 5.6 Production of conductive rGO patterns via blue diode 450 nm laser irradiations, (a) Printing process, (b) The optimized focus clearance of 1.3 mm between the laser head and the paper, and (c) Final printer rGO 3-electrode systems.

Step 3: Take any substrate or printer bed itself that can be leveraged. Tape the FR treated paper onto the substrates or bed. Position the paper at the same position provided during the generation of the gcode file, shown in [Figure 5.6a](#).

Step 4: Calibrate the Z-axis height to 0 mm, i.e., precisely the printer head to hold the FR paper on the bed tight and click set Z = 0 (where the printer starts printing). However, do not start printing in this position since the printer head is holding tight to the bed, which could damage the printer.

Step 5: Return to the calibration, from current Z = 0 position, lift by 1.3 mm, and set Z = 0. The optimized clearance focus

distance of 1.3 mm should be between the printer head and the substrate, as shown in [Figure 5.6b](#).

Step 6: Select the laser power settings and change the laser power to 15% (i.e., 15% of max power = 2.8 W) and default speed of 100% (max speed of laser, 300% = 120 mm/s).

Step 7: After ensuring all three steps (file selection, calibration, and laser parameter settings); click on start printing.

Step 8: Printing continues and takes time according to the design dimensions, as shown in [Figure 5.6b](#).

Step 9: Click OK after print finishes.

Step 10: Take out the ready-to-use printed conductive rGO patterns on paper, as shown in [Figure 5.6c](#), and switch off the laser after usage.

5.3 Conclusion

The one-step production of conductive rGO patterns on paper is provided step-by-step. In the demonstrated process, the user can develop customized conductive traces of rGO for various applications. Moreover, the simple methodology enables its potential to be adopted in industrial applications.

References

- 1 Vivaldi, F.M., Dallinger, A., Bonini, A. et al. (2021). Three-dimensional (3D) laser-induced graphene: structure, properties, and application to chemical sensing. *ACS Appl. Mater. Interfaces* 13 (26): 30245–30260.
- 2 Nag, A., Mitra, A., and Mukhopadhyay, S.C. (2018). Graphene and its sensor-based applications: a review. *Sens. Actuators A Phys.* 270: 177–194.
- 3 Bhaiyya, M., Rewatkar, P., Salve, M. et al. (2021). Miniaturized electrochemiluminescence platform with laser-induced graphene

electrodes for multiple biosensing. *IEEE Trans. Nanobioscience* 20 (1): 79–85.

- 4 Bhaiyya, M.L., Pattnaik, P.K., and Goel, S. (2021). Miniaturized electrochemiluminescence platform with laser-induced graphene-based single electrode for interference-free sensing of dopamine, xanthine, and glucose. *IEEE Trans. Instrum. Meas.* 70: 1–8.
- 5 Kothuru, A., Rao, C.H., Puneeth, S.B. et al. (2020). Laser-induced flexible electronics (LIFE) for resistive, capacitive and electrochemical sensing applications. *IEEE Sens. J.* 20 (13): 7392–7399.
- 6 Lin, J., Peng, Z., Liu, Y. et al. (2014). Laser-induced porous graphene films from commercial polymers. *Nat. Commun.* 5 (1): 5714.
- 7 Nugba, B.E., El-Moneim, A.A., Mousa, N.O., and Osman, A. (2023). A nonenzymatic laser-induced flexible amperometric graphene electrode for glucose detection in saliva. *Carbon Lett.* 33 (6): 1767–1780.
- 8 Wang, J., Shan, X., Xue, Q. et al. (2023). Detection of nitrite in water using glycine-modified nanocarbon and Au nanoparticles co-modified flexible laser-induced graphene electrode. *Inorg. Chem. Commun.* 152: 110652.
- 9 Cheng, L., Qian, J., Ruan, D. et al. (2023). Flexible and highly sensitive sandwich-structured PDMS with silver nanowires and laser-induced graphene for rapid residue detection. *ACS Appl. Polym. Mater.* 5 (4): 2336–2344.
- 10 Zhang, J., Huang, L., Ng, P.H. et al. (2023). Rapid and safe electrochemical disinfection of salt water using laser-induced graphene electrodes. *Aquaculture* 571.
- 11 Kiranakumar, H.V., Thejas, R., Naveen, C.S. et al. (2022). A review on electrical and gas-sensing properties of reduced graphene oxide-metal oxide nanocomposites. *Biomass Convers. Biorefin.* 14: 12625–12635.

- 12** Bahri, M., Gebre, S.H., Elaguech, M.A. et al. (2023). Recent advances in chemical vapour deposition techniques for graphene-based nanoarchitectures: from synthesis to contemporary applications. *Coord. Chem. Rev.* 475: 214910.
- 13** Divya, V., Pavar, S.K., Shilpa Chakra, C. et al. (2021). Applications of carbon-based nanomaterials in health and environment: biosensors, medicine and water treatment. In: *Carbon Nanomaterial Electronics: Devices and Applications* (ed. A. Hazra and R. Goswami), 261–284. Springer.
- 14** Singh, R.K., Kumar, P.S., Amreen, K. et al. (2022). Disposable miniaturized electrochemical sensing platform with laser-induced reduced graphene oxide electrodes for multiplexed biochemical analysis. *IEEE Trans. Nanobioscience* 22 (3): 548–553.
- 15** Nishchitha, N.K., Kumar, P.S., and Goel, S. (2023). Laser-induced in situ synthesis of nano-composite Co–Co₃O₄–rGO on paper: miniaturized biosensor for alkaline phosphatase detection. *Nanotechnology* 34 (29): 295502.
- 16** Rewatkar, P., Nath, D., Kumar, P.S. et al. (2022). Internet of things enabled environmental condition monitoring driven by laser ablated reduced graphene oxide based Al-air fuel cell. *J. Power Sources* 521: 230938.
- 17** Kumar, P.S., Advincula, P., and Goel, S.G. (2022). First report on onsite temperature based recovery of quenched chemiluminescence signal from graphenized μ PADs: validation by catechins radical scavenging. *Nano Futur.* 6: 045002.
- 18** Rowley-Neale, S.J., Randviir, E.P., Abo Dena, A.S., and Banks, C.E. (2018). An overview of recent applications of reduced graphene oxide as a basis of electroanalytical sensing platforms. *Appl. Mater. Today* 10: 218–226.
- 19** Dave, S.H., Gong, C., Robertson, A.W. et al. (2016). Chemistry and structure of graphene oxide via direct imaging. *ACS Nano* 10 (8): 7515–7522.

- 20** Razaq, A., Bibi, F., Zheng, X. et al. (2022). Review on graphene-, graphene oxide-, reduced graphene oxide-based flexible composites: from fabrication to applications. *Materials* 15 (3): 1012.
- 21** Al-Gaashani, R., Najjar, A., Zakaria, Y. et al. (2019). XPS and structural studies of high quality graphene oxide and reduced graphene oxide prepared by different chemical oxidation methods. *Ceram. Int.* 45 (11): 14439–14448.
- 22** Kumar, P.S., Gohel, K., and Goel, S. (2021). Graphenized papertronic devices using blue laser ablated polyimide resin paper. In: *IEEE 16th Nanotechnology Materials and Devices Conference (NMDC)*, 1–4. IEEE.
- 23** Kumar, P.S. and Goel, S. (2021). First report on graphene oxide free, ultrafast fabrication of reduced graphene oxide on paper via visible light laser irradiation. *Diamond Relat. Mater.* 120: 108680.

Note

 Equally Contributing Authors.

6

Soft Lithography: DLW-Based Microfluidic Device Fabrication

K. Ramya and Sanket Goel

*MEMS, Microfluidics and Nanoelectronics (MMNE) Lab,
Department of Electrical and Electronics Engineering, Birla
Institute of Technology and Science (BITS) Pilani, Hyderabad
Campus, Hyderabad, Telangana, India*

6.1 Introduction

Soft lithography is a collection of methodologies employed to create or duplicate structures using flexible stamps, molds, and adaptable photomasks. The term “soft” is attributed to this particular technology due to its utilization of elastomeric materials, with a notable emphasis on polydimethylsiloxane (PDMS). Soft lithography is a fabrication technique commonly employed to construct micro- and nano-scale features [1].

Photosensitive substrates are patterned using standard photolithography (UV lithography) techniques. Materials that respond positively or negatively to UV light are the two categories of photosensitive materials. To remove certain targeted areas over the substrate, a positive photoresist exposes them to UV light. In contrast, the chemical structure of a negative photoresist is cemented when exposed to UV radiation, making it easy to remove the unexposed portion [2]. To achieve the desired pattern, the substrate can be covered with a mask during the exposure. Incremental exposure can also be achieved by employing a stepper to project the UV light through a mask in phases. A mask-aligner, a UV source, a microscope, a mask, and an operator are among the many specialized instruments needed for the time-consuming and costly conventional photolithography process. One potential solution to these challenges involves employing direct UV laser writing (DLW) onto the substrate to achieve the pattern. One notable characteristic

of DLW is its utilization of a software mask instead of a physical mask to facilitate the scanning of the UV laser. This technique is referred to as maskless photolithography (MPL) [3, 4]. Various methods exist for fabricating micropatterns, including 3D printing and CO₂ laser machines [5].

Microfluidic devices fabricated using DLW techniques are used in biomedical research for purposes such as cell culture and diagnostics. It allows for accurate control of fluids at a very small scale, making it easier to study how cells behave and understand the processes of diseases. These devices have use in industry for chemical synthesis, microscale manufacturing, and environmental monitoring. They provide benefits such as increased data processing speed, capacity to handle larger workloads, and the ability to combine several functionalities onto a single microchip. DLW-based microfluidic devices thus emerge as versatile instruments, transcending disciplinary boundaries to impact research endeavors in biological sciences, environmental studies, and industrial processes alike.

This chapter presents a detailed procedure for creating a microfluidic device utilizing the DLW technique-based soft lithography methodology.

6.2 Designing Section

6.2.1 Prerequisites

Foundational use of computer-aided design (CAD) software for creating 2-D drawings or 3-D models designing patterns as the user requires.

6.2.2 Instrumentation and Software

A custom-made maskless DLW system (Holmarc, Cochin, India), DuPont PM240 negative photoresist (Dupont Electronic Technologies, NC, USA). Plasma chamber (Femto Science, Gyeonggido, South Korea) for oxygen plasma treatment. Licensed AutoCAD and Mach 3 CNC control software.

6.2.3 Step-by-Step Procedure for DLW-Soft Lithography Microfluidic Device Design

Step 1: A microfluidic device with a Y-channel design was created using AutoCAD design software and saved as a “.dxf” file. The file was converted into a “g code” format using Mach3 CNC software and imported into the DLW equipment.

Step 2: To produce the design using a DLW, a glass substrate was washed with isopropanol, ensuring complete drying. Further coated with a negative dry film photoresist ($N = 3$ layers, thickness of $\sim 105 \mu\text{m}$) using a Laminator (Mega A3, Dhaka, Bangladesh). Subsequently, the design was imprinted onto the glass surface using photo polymerization via direct laser writing, as shown in [Figure 6.1](#). The pattern was developed using a solution containing 0.85% sodium carbonate.

Step 3: *Preparation of PDMS mold*

Mix the Sylgard 184 components (Sigma Aldrich Co., [St. Louis, USA]) or QSil 216 A (CHT, Bangalore, India) and curing agent like Qsil 216 B (CHT, Bangalore, India) in a 1 : 10 ratio in a plastic cup and use a spatula to mix it to a homogenous mixture. After thoroughly mixing the curing agent and base in the plastic cup, removing any air bubbles from the mixture is essential. To do this, use a vacuum desiccator, which creates a vacuum environment that helps air bubbles rise to the surface and escape from the mixture. Place the mixed silicone cup inside a vacuum desiccator. A vacuum pump is connected to the desiccator to create the vacuum environment, as shown in [Figure 6.2](#). As the vacuum is applied, the air bubbles within the silicone mixture will rise to the surface and expand, causing the mixture to foam up. Therefore, it is crucial to have enough space in the cup to accommodate this expansion. The silicone mixture will change in appearance as trapped air bubbles are removed. Initially, the mixture might expand and look foamy, but the silicone will settle and become transparent over time. The developed microfluidic pattern was placed into a petri dish, and PDMS was subsequently poured into petri dish containing pattern.

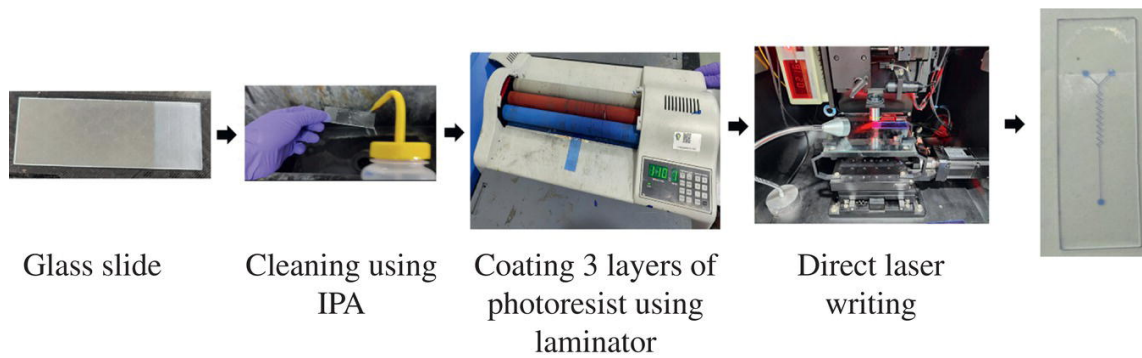


Figure 6.1 Step-by-step process involved in creating micro patterns with a DLW printer.

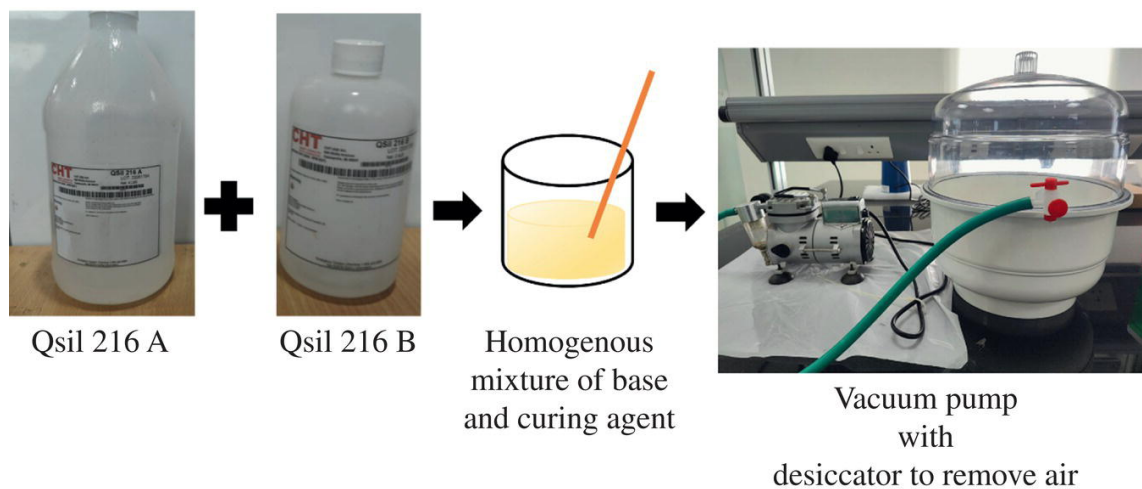


Figure 6.2 Procedure to prepare a PDMS mold by mixing PDMS base and curing agent followed by curing the mixture on a master template.

Step 4: *Curing and PDMS hydrophilic/Bonding PDMS*

The petri dish is then kept for curing in an oven, with a curing time of 1.5 hours at 25 °C, and otherwise can be left at room temperatures for about 48 hours for curing. The heat cure time at 100 °C is 35 minutes, 125 °C is 20 minutes, and 150 °C is 10 minutes. With a sharp scalpel or tweezers, carefully cut along the outline of the design preserving the integrity of the pattern from getting damaged or deformed. Then, place the PDMS design in a glass slide.

Position the PDMS sample and glass slide in a plasma chamber with the intended surface oriented upward. Allocate 60 seconds for the PDMS material to undergo plasma treatment. Introducing oxygen

atoms through plasma processing will induce hydrophilicity on the surface of PDMS and the glass slide. This treatment enhances the adhesive properties of the material. Appropriate treatments must be applied to the PDMS surface and the glass slide to achieve robust adhesion.

Assemble the plasma-treated PDMS and the untreated substrate, ensuring that the treated surface of the PDMS is in direct contact with the untreated surface of the other material. Facilitate the contact between the two materials for several hours. During this temporal interval, the bond will experience significant strengthening.

Therefore, this fabricated microfluidic device comprised two inlets and one outlet. The device is equipped with inlets to introduce the analyte (disperse phase) and the liquid (continuous phase), while the outlet served to facilitate the removal of trash from the device. [Figure 6.3](#) shows the fabricated microfluidic Y-channeled device after curing and plasma bonding.

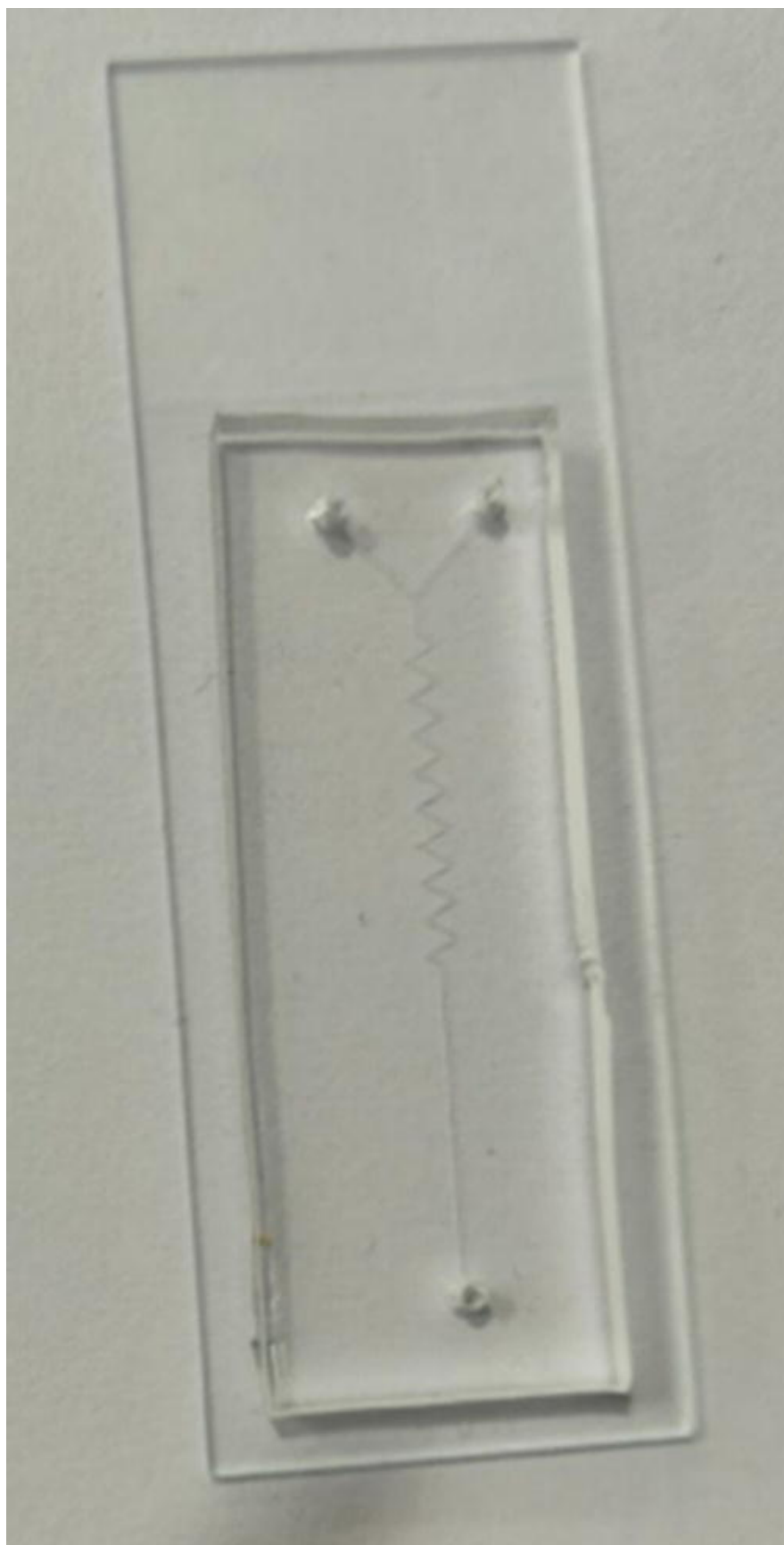


Figure 6.3 Fabrication of Y-channel microfluidic device.

6.3 Conclusion

This chapter primarily focuses on designing and fabricating a microfluidic device using a DLW-based soft lithography approach with comprehensive guidelines for the design and development processes.

References

- 1 Xia, Y. and Whitesides, G.M. (1998). Soft lithography. *Annu. Rev. Mater. Sci.* 28: 153–184.
- 2 Lee, J.B., Choi, K.H., and Yoo, K. (2014). Innovative SU-8 lithography techniques and their applications. *Micromachines* 6 (1): 1–18.
- 3 Srikanth, S., Dudala, S., Raut, S. et al. (2020). Optimization and characterization of direct UV laser writing system for microscale applications. *J. Micromech. Microeng.* 30 (9): 095003.
- 4 Pal, A., Dubey, S.K., and Goel, S. (2022). IoT enabled microfluidic colorimetric detection platform for continuous monitoring of nitrite and phosphate in soil. *Comput. Electron. Agric.* 195: 106856.
- 5 Ahmadian Yazdi, A., Popma, A., Wong, W. et al. (2016). 3D printing: an emerging tool for novel microfluidics and lab-on-a-chip applications. *Microfluidics and Nanofluidics* 20: 50.

7

Electrode Fabrication Techniques

Sanjeet Kumar^{1,2}, Abhishek Kumar^{1*}, K.S. Deepak^{1,2*}, Manish Bhaiyya^{1*}, Aniket Balapure^{1*}, Satish Kumar Dubey^{1,2}, and Sanket Goel¹*

¹ MEMS, Microfluidics and Nanoelectronics (MMNE) Lab, Department of Electrical and Electronics Engineering, Birla Institute of Technology and Science (BITS) Pilani, Hyderabad Campus, Hyderabad, Telangana, India

² Department of Mechanical Engineering, Birla Institute of Technology and Science (BITS) Pilani, Hyderabad Campus, Jawahar Nagar, Telangana, India

7.1 Inkjet Printing Technique: Electrode Fabrication for Advanced Applications

7.1.1 Introduction

Inkjet printing is a simple, rapid, customizable, low-cost fabrication technology for microelectrodes. It is a reprographic method that takes digital data from a computer system representing an image or text and reproduces it onto a substrate using the ink droplet. It is a maskless printing technology used in various applications [1]. Often projected as an alternative for printing microelectrodes and nanomaterials in applying point-of-care biosensors and printed electronics technology [2]. The inkjet approach has several advantages over other fabrication methods, including screen printing, lithography, and 3D printing. For example, it doesn't require a photo mask, stencils, or physical assistance, which makes patterning easier [3]. Traditional printing technique has been applied to a wide range of industries. Its benefits include precision control over the droplets over the designated area and the capacity to print solutions of different materials with minimal waste [4].

Biosensors, chemo-resistive sensors, tactile sensors, field effect transistor (FET) transistors, microelectrodes, complex integrated circuits like polymer thin-film transistors, medicine, and biomedical engineering applications like genomics, biosensors, and medicine screening are just a few of the uses for inkjet printing [5]. Low-cost ink deposition techniques have been developed using a variety of strategies, including electrohydrodynamic jet printing and microfluidic impact printing (MIP). Microelectrodes are printed using a Voltera V-one inkjet printer. Numerous benefits come with this method, such as sturdy hardware, flexible printing, quick ink calibration, quick reflow, and its iterations [6, 7].

7.1.2 Designing Section

7.1.2.1 Prerequisites

Windows 10/11 operating system, a minimum of 4 GB RAM, storage of 250 GB, and a licensed version of computer-aided designing (CAD) tool (AutoCAD).

7.1.2.2 Instrument and Equipment Required

Substrate (paper, glass, PET sheet, etc.), Voltera V-one (Voltera), carbon ink, carbon conductive ink, IPA, tissue paper, buds, dispenser, dispenser nozzle, ink cartridge.

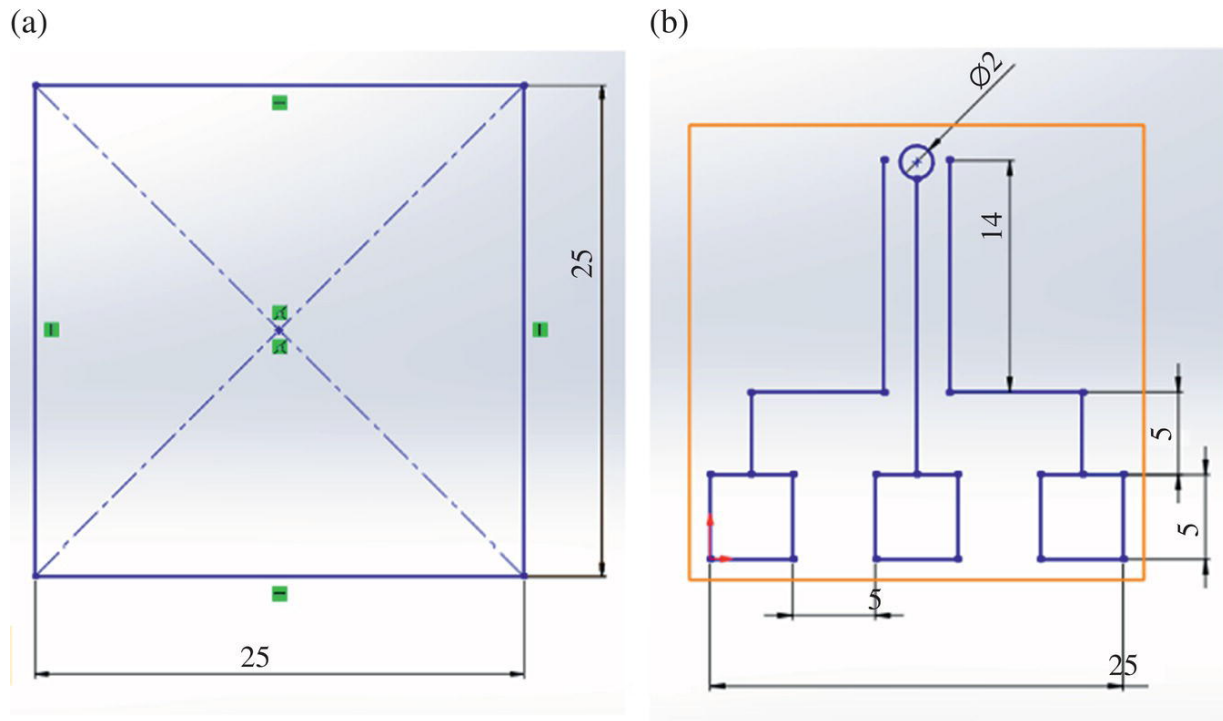


Figure 7.1 CAD model to develop a microelectrode system, creating (a) a 25 mm \times 25 mm rectangle, and (b) with 5 mm \times 5 mm rectangles.

7.1.2.3 Designing a Microelectrode Device

Step 1: Open the CAD tool.

Step 2: Create a new part file.

Step 3: Select a plane (front, top, or right plane) and create a rectangle with a length of 25 mm and breadth of 25 mm, as shown in [Figure 7.1a](#).

Step 4: Exit the sketch, click the “line” tool in the sketch section, and provide the rectangular as 5 mm \times 5 mm ([Figure 7.1b](#)).

Step 5: Create a line to extend to 5 mm and then circle a diameter of 2 mm in the middle of the line (thoroughly 200 μ M thickness).

Step 6: Save the CAD file for any future iterations.

Step 7: Save as the “.dxf” file for the successive operations.

Step 8: Close the CAD file.

7.1.3 Dip Trace and Voltera V-One Microfabrication Section

7.1.3.1 Gerber Format File Generation

Step 1: Open Dip Trace open-source software.

Step 2: Import the previously saved DXF file into the Dip Trace Launcher and convert the file into Gerber format.

Step 3: Convert the DXF file to Gerber format.

7.1.3.2 Voltera V-One Software

Step 1: Open Voltera V-one software.

Step 2: Import the previously saved Gerber file shown in [Figure 7.2a](#).

Step 3: Transfer the Gerber file to an inkjet printer (Voltera V-one) and follow the steps according to the user interface, as shown in [Figure 7.2b](#).

The following is the step-by-step process to fabricate electrodes using an inkjet printer.

Step 4: Place the glass substrate shown in [Figure 7.3a](#) on the dedicated slot on the printer shown in [Figure 7.3b](#).

Step 5: Finally, after printing electrodes, keep electrodes in a hot air oven ([Figure 7.3c](#)) for 30 minutes at 70°C to dry the interface shown in [Figure 7.3d](#).

7.1.4 Conclusion

The chapter focused on designing and fabricating a microelectrode through Voltera V-one inkjet printing. Step-by-step designing and development steps are provided in this chapter.

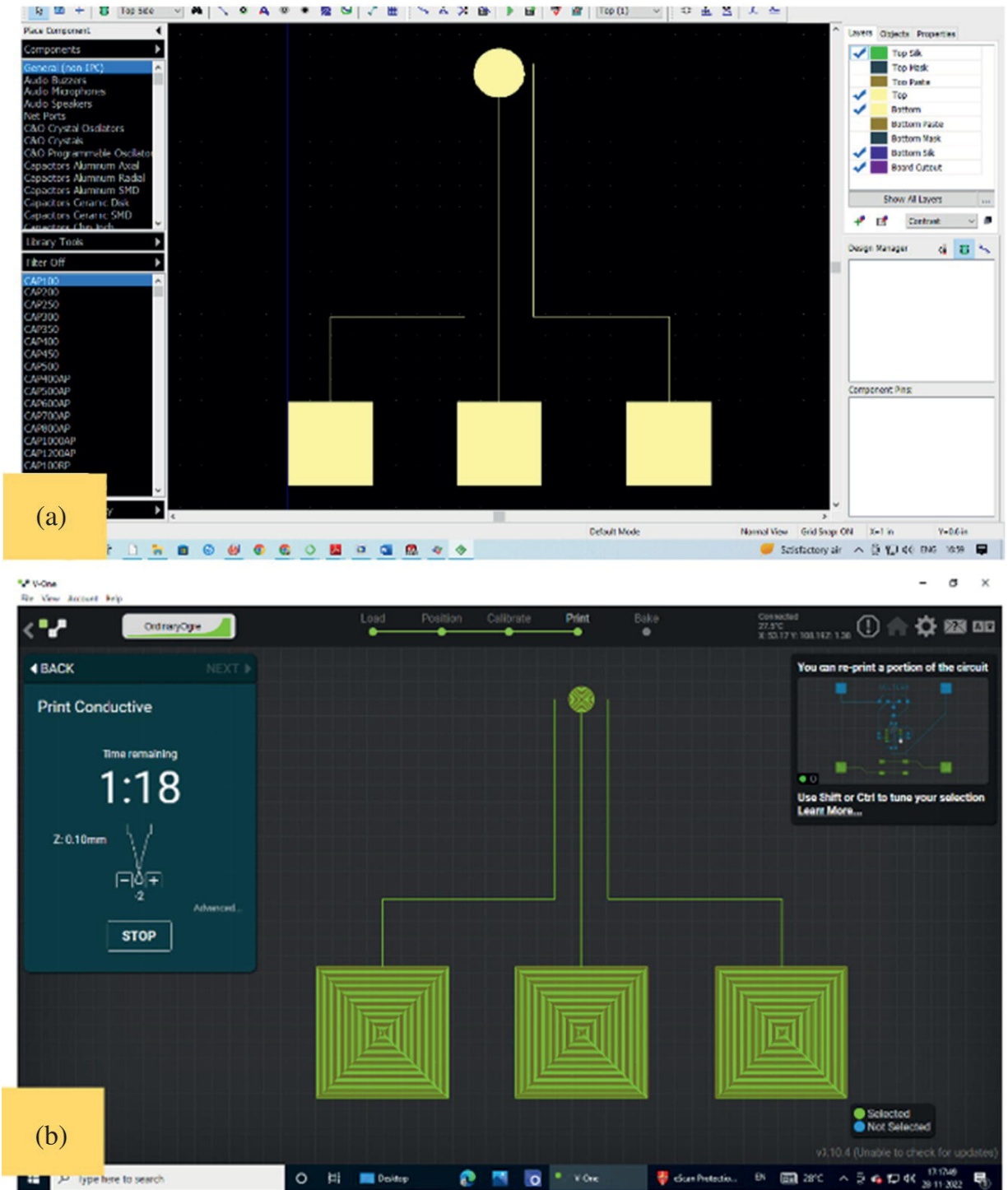


Figure 7.2 (a) Import the DXF file to convert it into Gerber format using DIP Trace Launcher software. (b) The microelectrode design is imported into Voltera V-One software for fabrication on the substrate.

7.2 Screen Printing Technique for Electrochemical Sensor Fabrication

7.2.1 Introduction

Chemical and biosensors are frequently made using the screen-printing technique. Compared to other methods currently in use, this procedure for creating electrodes is simpler. In order to print conductive paste on a dielectric foundation, a screen printer must first prepare the mask. The conductive paste is then baked in thermal ovens to dry. The screen-printing technology is now used in more fields, including printed-circuit fabrication, biosensors, and flexible electronics, thanks to the quick advancement of sensors [8].

Electrode fabrication is a simple, user-friendly, and easily adjustable procedure. Here, the choice of conductive ink has a significant impact on the electrode material's conductivity. Screen-printed electrodes are used in a variety of sensing methods, including biological analysis, electrochemistry, and electrochemiluminescence [9]. It is a versatile, straightforward, low-cost, and easily scalable electrode fabrication process. During MEMS and microfluidics experiments/fabrication, different substrates, such as paper, polyimide sheets, cloth, and glass, are explicitly used to print electrodes using screen printing.

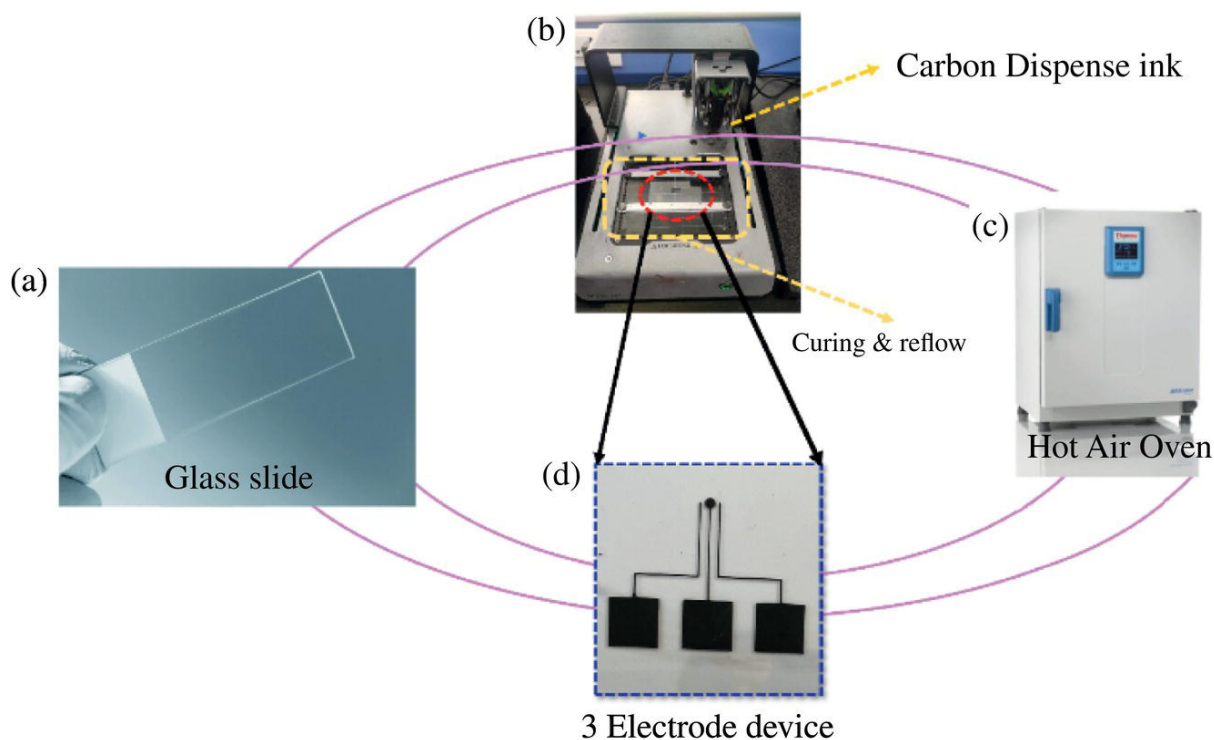


Figure 7.3 (a) Glass slide as substrate, (b) clamp the glass slides on the printing slots, where the carbon ink gets dispensed, (c) electrodes are placed in a hot air oven, and (d) finished microelectrode device.

The previously reported work on screen printing highlights its employability in developing various types of sensors for practical usage. Sangam Srikanth et al. [10] described the lab on a chip platform integrated with screen-printed carbon electrodes and a microfluidic chamber to detect bacteria. Herein, the electrochemical approach is utilized to study bacterial growth using CV. This device shows bacterial quantification in the linear range of 2×10^4 – 1.1×10^9 CFU/ml without any modification of electrodes. The microbial fuel cell is used to verify the metabolic activity of the bacteria and compare the viability of the farmed bacteria with fluorescence imaging. For on-field application and real-time detection, the entire platform is utilized. The Antonio Ruiz-Gonzalez et al. team found several plant indicators in vivo. This group studies a low-cost detection device for detecting sap K^+ and pH in living plants with reverse iontophoresis. The screen-printed electrodes were modified (shown in Figure 7.4a) with K^+ selective membrane, and sensitivity is achieved of $70 \text{ mV Log}[K^+]^{-1}$, and a detection limit in the

micromolar range is achieved. The low-cost microcontroller-based portable device is validated with the concentration of K^+ and pH in tomato plants before and after watering with DI water. The group developed noninvasive and affordable device monitoring plant biomarkers [11]. Gabriela Martins de Araújo et al. [12] described the detection of progesterone with a screen-printed electrode (shown in [Figure 7.4b](#)) with conductive ink such as polyaniline and graphene. The CV is used to characterize the redox behavior of the PANI with the modified electrode. The electrode characterization is carried out with SEM, CV, and EIS. Progesterone hormone is detected using screen-printed electrodes; the detection limit and quantification were 211 and 703 nmol/l, respectively.

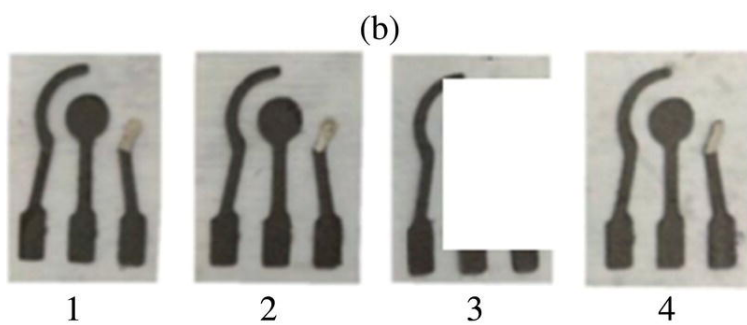
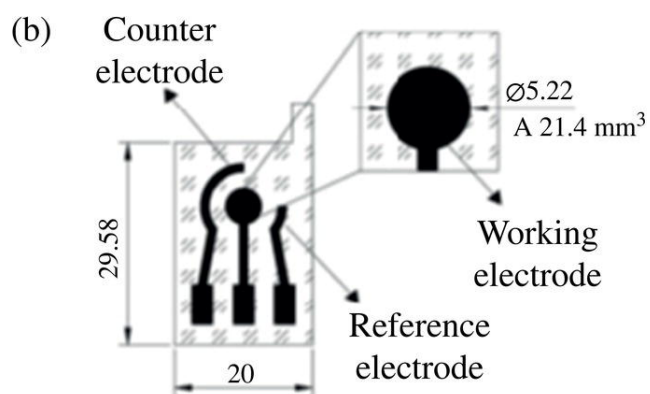
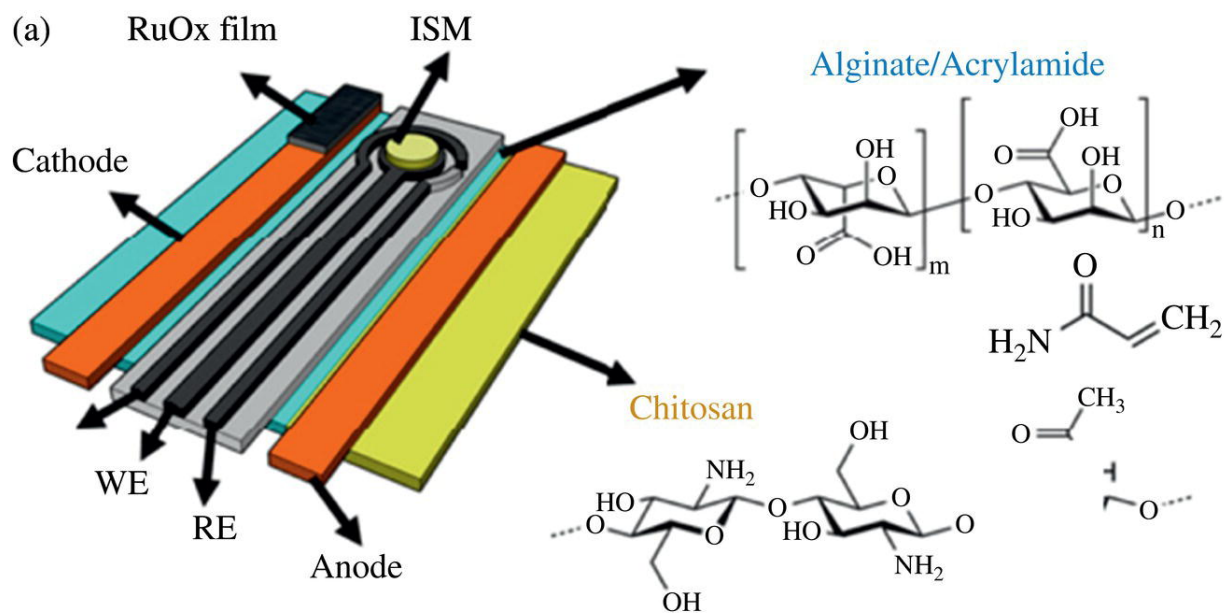


Figure 7.4 (a) schematic for detecting plant biomarkers using screen printed-based devices,

Source: Adapted from [4]

. (b) The schematic diagram for using screen printed-based devices to detect Progesterone hormone,

Source: Adapted from [5].

7.2.2 Brief Overview

Screen printing is an extensively used method for electrode fabrication for biosensing applications. The screen-printing method involves using a mask or a stencil to create electrode patterns on the substrate. Screen-printed carbon paste-based electrodes are widely used for electrochemical energy storage, biosensing, and water-quality monitoring. In the following experimental procedure, the simple strategy to fabricate the screen-printed electrodes is highlighted.

7.2.3 Experimental Section

7.2.3.1 Prerequisites

Microsoft Windows 10/11 operating system, a minimum of 4 GB RAM, storage of 250 GB, and a licensed version of CAD tool.

7.2.3.2 Materials, Instrumentation, and Software

Polyimide sheet, carbon conductive paste, Corel Draw, CO₂ laser system VLS 3.60 (Universal Laser Systems), and VLS 3.60 OEM software installed.

7.2.3.3 Fabrication Steps

Step 1: Take substrate material; a polyimide sheet is taken as a substrate, and then the PVC sheet is glued to the polyimide sheet (see [Figure 7.5a, b](#)).

Step 2: Draw a mask design using computer-aided design software and convert it into .dxf format.

Step 3: Cut the required area to form a mask. Here, a CO₂ laser (30 W) with optimized speed (30%) and power (7%) is used. Then, remove the unwanted area from the PVC sheet (see [Figure 7.5c, d, e](#)).

Step 4: Transfer the conductive ink to form electrodes. Then, dry the electrodes in a hot air oven for 2–3 hours at 70 °C. Finally, peel out the mask to get the electrodes ([Figure 7.5f–i](#)).

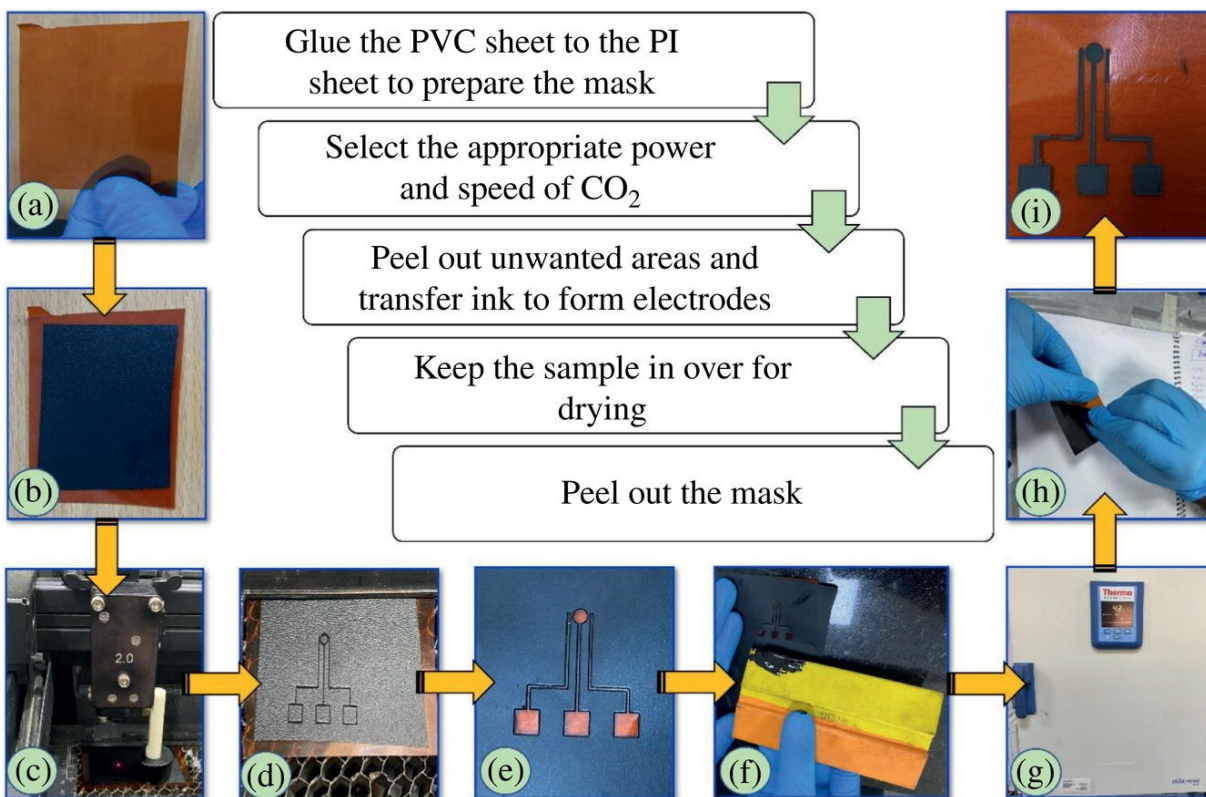


Figure 7.5 Step-by-step process to fabricate electrodes using screen printing, shown in (a) through (i).

7.2.4 Conclusion

Herein, a simple methodology for fabricating three-electrode system pads is demonstrated for electrochemical detection. The screen-printing method provides a feature to prototype electrochemical biosensors rapidly. The presented work highlights using polyimide sheets and carbon conductive ink to prepare a three-electrode system. The developed biosensor can detect human metabolites such as glucose, cholesterol, lactate, dopamine, and choline.

7.3 Physical Vapor Deposition (PVD) Technique for Electrode Fabrication

7.3.1 Introduction

7.3.1.1 Physical Vapor Deposition (PVD)

Physical vapor deposition (PVD) is a method widely used in industry to deposit exceptional-quality thin films. PVD deposits a thin material layer onto a substrate under a vacuum [13]. Numerous methods of PVD exist, including sputtering, ion-plating, magnetron sputtering, and electron beam sputtering. In the sputtering process, the thickness of the material layer can be modified to span the range of angstroms to millimeters [14]. This chapter focuses on vacuum thermal evaporation and e-beam evaporation methods for depositing metal films, specifically for fabricating gold electrodes.

7.3.1.2 Gold Electrodes as Biosensors

Biosensors are sensors capable of detecting or sensing a biomarker. In electrochemical detection, biosensors are used similarly to other sensors wherein the reaction produces or consumes electrons, thus causing a change in electrical parameters like voltage or current, which can then be detected using any electrochemical transduction mechanism like cyclic voltammetry and electrochemical impedance spectroscopy, for example. Gold electrodes are a preferable candidate for such biosensors owing to their biocompatibility and high conductivity. Also, because of the ability to form gold-thiol molecules, they can be used in various biorecognition settings like detecting DNA, small molecules, enzymes, and immunoglobulins.

7.3.2 Experimental Details

7.3.2.1 Instrument and Equipment Required

Substrate (paper, glass, PET sheet, etc.), tissue paper, electron beam evaporator system, and thermal coater (hind high vacuum CO. [P] LTD, Bangalore, India)

7.3.2.2 Equipment Setup

[Figure 7.6](#) shows the schematic of the basic setup generally used for the PVD. The machine used for the PVD mainly consists of the vacuum chamber, the rotary pump, the turbo molecular pump, a unit to handle and manipulate high-voltage supply, and a display panel. Inside the chamber, there will be a holder for attaching various substrates and units for evaporation through e-beam and thermal heating. The quartz crystal monitor is used to measure the thickness of the film during the deposition process. Just above the metal sources, there is a shutter arrangement to control the flow of the vapor for deposition. Graphite crucibles are used to hold the metals during the melting process.

7.3.2.3 Substrate Preparation

Cleaned substrates are attached to the substrate holder for the thin film deposition. Depending on the type of substrate, a specific cleaning protocol is followed. Usually, substrates are cleaned with acetone, isopropanol, and deionized water, along with ultrasonic cleaning to remove various impurities present on the surface. During the process, the substrate holder keeps rotating for uniform deposition.

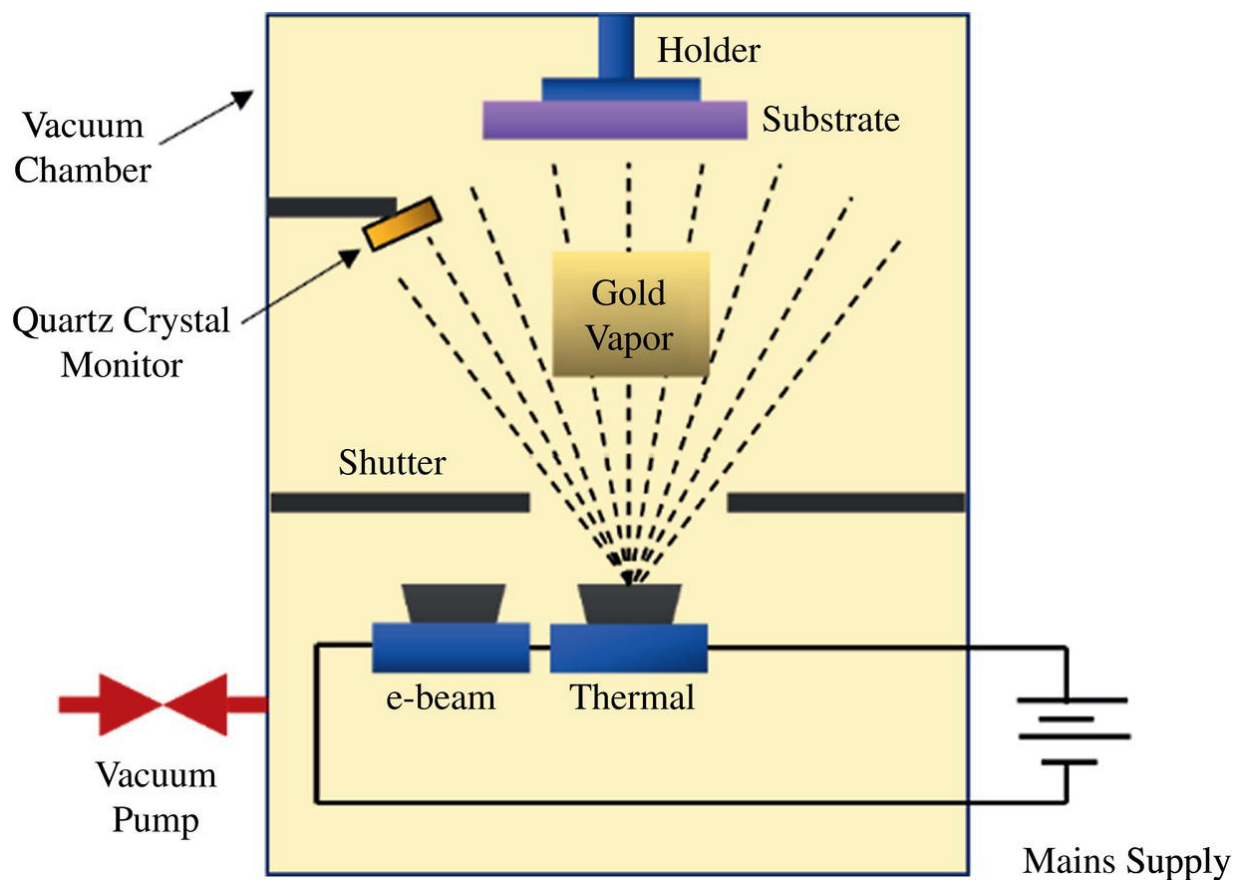


Figure 7.6 The schematic of the basic setup used in the PVD.

7.3.2.4 Deposition Process

After the substrate loading, the chamber is evacuated to a vacuum pressure of $\sim 2.0 \times 10^{-5}$ mbar. In some cases, the higher vacuum pressure may also be deployed. For the gold electrode deposition, 15 nm of the chrome layer is initially deposited for the gold adhesion using e-beam evaporation. After the 15 nm chrome deposition, gold is deposited using thermal evaporation without breaking the vacuum. The ideal deposition rate for the chrome and gold are 0.5 and 1 Å/s, respectively. As per the application, the required thickness is deposited. For electrode fabrication, 70 nm of the gold would be sufficient.

7.3.2.5 Electrode Fabrication

The desired geometry of the electrode can be made either by using lithography or a hard mask. Here, we will briefly discuss using the

hard mask for electrode fabrication. The hard mask can be made using the 200 μm stainless steel sheet (SS). The required design can be cut using an industrial laser cutter and placed over the substrate to get the deposition only at the necessary region and as per the geometry. [Figure 7.7](#) shows the schematics of the SS mask and the substrate arrangement. This technique can be used for devices without many fine features; however, lithography is the best alternative for excellent geometry.

The described technique can be deployed for various electrode designs, circuit designing, and composite thin film fabrication on various substrates for several applications.

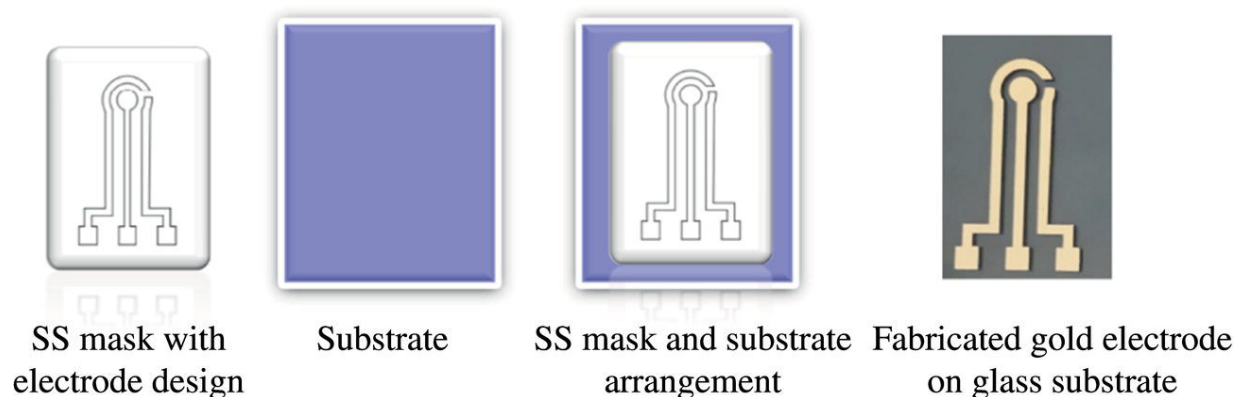


Figure 7.7 The SS masks, the substrate arrangement, and the fabricated gold electrodes.

7.3.3 Precautions

1. Handle the PVD machine with care due to high voltage and current.
2. Choose substrate and metal carefully based on requirements.
3. Control deposition rate and vacuum pressure and choose the appropriate underlayer for adhesion.

7.4 Conclusion

This chapter briefly discusses the method for the fabrication of the gold electrodes. Several lithography techniques were used to fabricate the various patterns on the thin metallic film. Using hard

mask techniques is a good alternative for a design that does not have many fine features, considering the simplicity. Moreover, using hard masks reduces the time required by manifolds, which are usually required for lithography-based techniques. The described fabricated gold electrodes can be deployed for various applications, including biosensing, due to well-established chemistry for anchoring several biomolecules on the gold surfaces.

References

- 1 Da Costa, T.H. and Choi, J.W. (2020). Low-cost and customizable inkjet printing for microelectrodes fabrication. *Micro Nano Syst. Lett.* 8 (1): 1–6.
- 2 Wu, J., Wang, R., Yu, H. et al. (2015). Inkjet-printed microelectrodes on PDMS as biosensors for functionalized microfluidic systems. *Lab Chip* 15 (3): 690–695.
- 3 Kim, Y., Kim, J.W., Kim, J., and Noh, M. (2017). A novel fabrication method of Parylene-based microelectrodes utilizing inkjet printing. *Sens. Actuators B Chem.* 238: 862–870.
- 4 Schnitker, J., Adly, N., Seyock, S. et al. (2018). Rapid prototyping of ultralow-cost, inkjet-printed carbon microelectrodes for flexible bioelectronic devices. *Adv. Biosyst.* 2 (3): 1700136.
- 5 Wu, J., Roberts, R.C., Tien, N.C., and Li, D. (2014). Inkjet printed silver patterning on PDMS to fabricate microelectrodes for microfluidic sensing. In: *Proceedings of IEEE Sensors*. IEEE (December).
- 6 Pei, Z., Hu, H., Liang, G., and Ye, C. (2017). Carbon-based flexible and all-solid-state micro-supercapacitors fabricated by inkjet printing with enhanced performance. *Nanomicro. Lett.* 9 (2): 1–11.
- 7 Kudr, J., Zhao, L., Nguyen, E.P. et al. (2020). Inkjet-printed electrochemically reduced graphene oxide microelectrode as a platform for HT-2 mycotoxin immunoenzymatic biosensing. *Biosens. Bioelectron.* 156: 112109.

- 8** Riemer, D.E. (1989). The theoretical fundamentals of the screen printing process. *Microelectron. Int.* 6 (1): 8–17.
- 9** Lin, H.W., Chang, C.P., Hwu, W.H., and Der Ger, M. (2008). The rheological behaviors of screen-printing pastes. *J. Mater. Process. Technol.* 197 (1–3): 284–291.
- 10** Srikanth, S., Jayapiriya, U.S., Dubey, S.K. et al. (2022). A lab-on-chip platform for simultaneous culture and electrochemical detection of bacteria. *iScience* 25 (11): 105388.
- 11** Ruiz-Gonzalez, A., Kempson, H., and Haseloff, J. (2023). A simple reversed iontophoresis-based sensor to enable in vivo multiplexed measurement of plant biomarkers using screen-printed electrodes. *Sensors* 23 (2): 780.
- 12** de Araújo, G.M., Cardoso, M.A., Codognoto, L. et al. (2023). Screen-printed electrodes based on conductive inks of polyaniline/graphene hybrids and their application to progesterone detection. *ECS Adv.* 2 (1): 016504.
- 13** Rafique, M.S., Rafique, M., Tahir, M.B. et al. (2020). Synthesis methods of nanostructures. In: *Nanotechnology and Photocatalysis for Environmental Applications* (ed. M.B. Tahir, M. Rafique, and M.S. Rafique), 45–56. Elsevier.
- 14** Alam, M.M., Imran, M., Abutaleb, A. et al. (2023). Fabrication approaches of nanocomposites. In: *Nanocomposites-Advanced Materials for Energy and Environmental Aspects* (ed. M.E. Khan, J. Aslam, and C. Verma), 67–85. Woodhead Publishing.

Note

* Equally Contributing Author.

8

Morphological Characterization

Dhoni Nagaraj^{1,2}, Yuvaraj Maphrio Mao^{1*}, Parvathy Nair^{1*},
Sanjeet Kumar^{1,2*}, Imran Khan¹, Amreen Khairunnisa¹, R.N.
Ponnalagu¹, Satish Kumar Dubey^{1,2}, and Sanket Goel¹*

*¹ MEMS, Microfluidics and Nanoelectronics (MMNE) Lab,
Department of Electrical and Electronics Engineering, Birla
Institute of Technology and Science (BITS) Pilani, Hyderabad
Campus, Hyderabad, Telangana, India*

*² Department of Mechanical Engineering, Birla Institute of
Technology and Science (BITS) Pilani, Hyderabad Campus,
Hyderabad, Telangana, India*

8.1 Morphological Studies with Different Techniques

8.1.1 Introduction

A crucial part of comprehending and deciphering the complex complexities of various biological, geological, and material formations is morphological characterization. Form, structure, and the general physical appearance of entities are the foundation of this field of study, which explores the intriguing world of sizes, combinations, and shapes. When used on geological formations, synthetic materials, or biological organisms, morphological characterization offers insightful information that goes well beyond aesthetic considerations. The following chapter discusses a few important and relevant nanomaterial characterization techniques.

8.2 Scanning Electron Microscopy

The development of new nanotechnologies has been made possible by the advanced capabilities of electron microscopes, which can now examine objects smaller than a micron down to individual atomic

locations. Nanoscale engineering of macro-sized components has also made astonishing advancements possible. One of the most adaptable tools for examining and analyzing the microstructure morphology and chemical composition characterizations is the scanning electron microscope (SEM).

In SEM, secondary electrons are emitted from the surface of the sample when it is hit by the primary beam of electrons. These secondary electrons have low energy and can provide information about the topography of the sample surface.

On the other hand, backscattered electrons are high-energy electrons scattered back toward the detector after being ejected from the sample due to collisions with its atoms. These electrons provide information about the composition and atomic number of the sample, as the amount of backscattered electrons depends on the atomic number of the elements present in the sample [[1](#), [2](#)].

Scanning electron microscopy can be used for different types of materials such as metals, minerals, polymers, etc. These materials can be conductive or nonconductive. Nonconductive materials required additional preparation to avoid charging effects.

In this chapter, a step-by-step process is given for performing SEM analysis.

8.3 Steps Involved in the Scanning Electron Microscope Characterization

8.3.1 Brief Overview

Scanning electron microscopy (SEM) is a surface morphological technique used to analyze the surface structure and composition of samples at high magnifications. It provides detailed, high-resolution images by scanning a focused beam of electrons across the sample surface. The following section discusses the major steps.

8.3.2 Sample Preparation

Step 1: For thin film samples, cut the sample to an approximate dimension of 5 mm × 5 mm. In the case of powder samples, use approximately 1–2 mg of the sample.

Step 2: The sample should be mounted onto the stub or holder that will fit inside the SEM chamber. Generally, adhesive carbon tape is used to do this.

Step 3: Place the prepared sample holder in the sputter coater. A sputter coater deposits a thin film (5–10 nm) of gold to prevent excess charge in the sample.

Step 4: Vent the chamber (1–2 psi) and then load the sample.

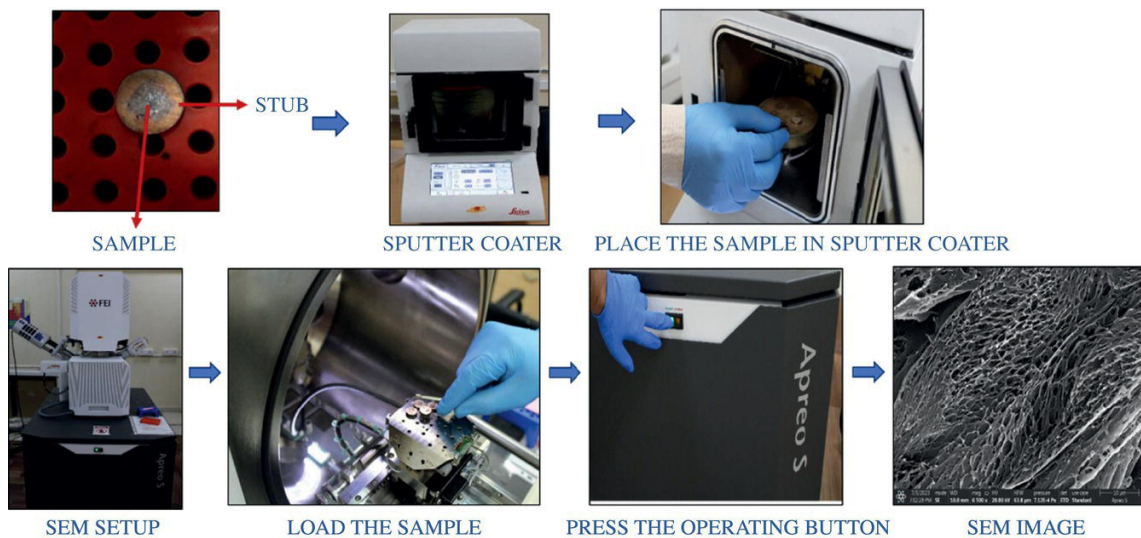


Figure 8.1 Steps involved in SEM characterization.

Step 5: Close the chamber and press the operating button.

Step 6: Create a high vacuum (10^{-4} – 10^{-6} Torr) in the chamber.

Step 7: Focus the electron beam using a magnetic lens onto the sample ([Figure 8.1](#)).

8.3.3 Instrumentation

1. Electron gun: It generates a beam of electrons.
2. Electromagnetic lenses: They control the path of the electron beam.

3. Sample stage: It is the movable stage where the sample has been placed.
4. Detectors: The scattered and backscattered electron detectors have detected the signals generated by the sample.
5. Imaging system: The observed signals are converted into visuals on a display.
6. Computer interface: Acquire images with the help of a computer interface.

8.3.4 Results and Conclusion

SEM provides data that includes the size, shape, composition, and structure of the sample. These measurements help calculate parameters such as aspect ratio and orientation angle. Additionally, they generate maps, spectra, or profiles of elemental or phase composition, as well as maps, patterns, or pole figures of crystallographic orientation, grain boundary, or defect structure. [Figure 8.2](#) shows scanning electron microscopy images taken at resolutions of 10 and 500 μm . These images demonstrate the presence of micron-sized fibers with a cylindrical shape at a scale of 500 μm , suggesting the possible formation of rGO on the Whatman paper. Additionally, the images reveal the existence of grainy connections and an increase in porosity when viewed at a higher magnification of 10 μm .

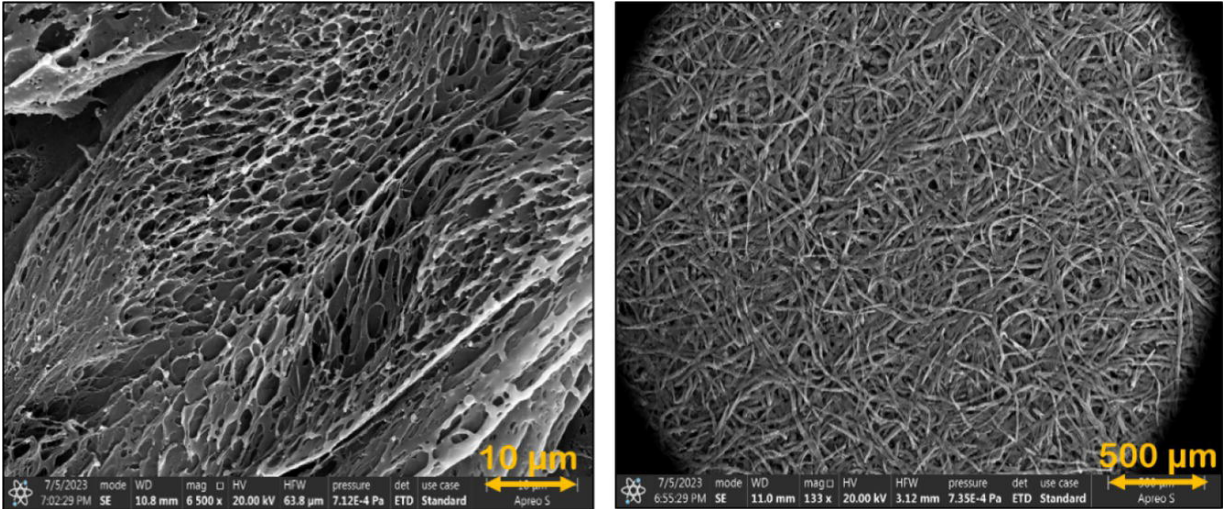


Figure 8.2 SEM image of the sample with a resolution of 10 and 500 μm .

8.4 X-Ray Diffraction (XRD)

8.4.1 Introduction

X-ray diffraction is a powerful technique used to analyze the crystal structure of materials. It can provide detailed information about the arrangement of atoms in a crystal lattice. The X-ray diffractometer (Rigaku, Japan) verifies the phase formation and purity using $\text{Cu-K}\alpha$ as a source. Stoichiometric changes and chemical substitution can also be identified with this technique. It is an important method used in material science and solid-state chemistry, like non-destructive (NDT), to collimate X-rays by specified crystallographic lattice. XRD provides brief information about the lattices of crystalline substances and the unit cell.

X-rays are electromagnetic radiations; the high voltage across the electrodes in the X-ray tube draws electrons toward the anode (metal target). In all directions, it radiates and marks a vital impact point [3]. Copper (Cu) targets are usually used because they emit their characteristics radiation $\text{K}\alpha$ with a wavelength approximately equal to the atomic plane distance, i.e., 1.54 \AA .

Crystal is the regular arrangement of the atom, and all the identical Miller indices are equally spaced and parallel to each other. As the

scattering object works, each plane is set in (hkl), which is a perpendicular direction to the plane and periodic in nature, inter planer distance d_{hkl} [4] (shown in [Figure 8.3](#)). The scattering of the X-ray from each plane radiates with spherical wavefronts and due to destructive interference, cancels out most of them only for each set of planes, making angles θ_{hkl} goes in constructive interference. Where θ_{hkl} can be obtained from Bragg's law, d_{hkl} is the interplaner distance, n is the order of reflection, and λ is the wavelength taken to be one in [Eq. 8.1](#). [Figure 8.3](#) shows the schematic diagram of Bragg's law.

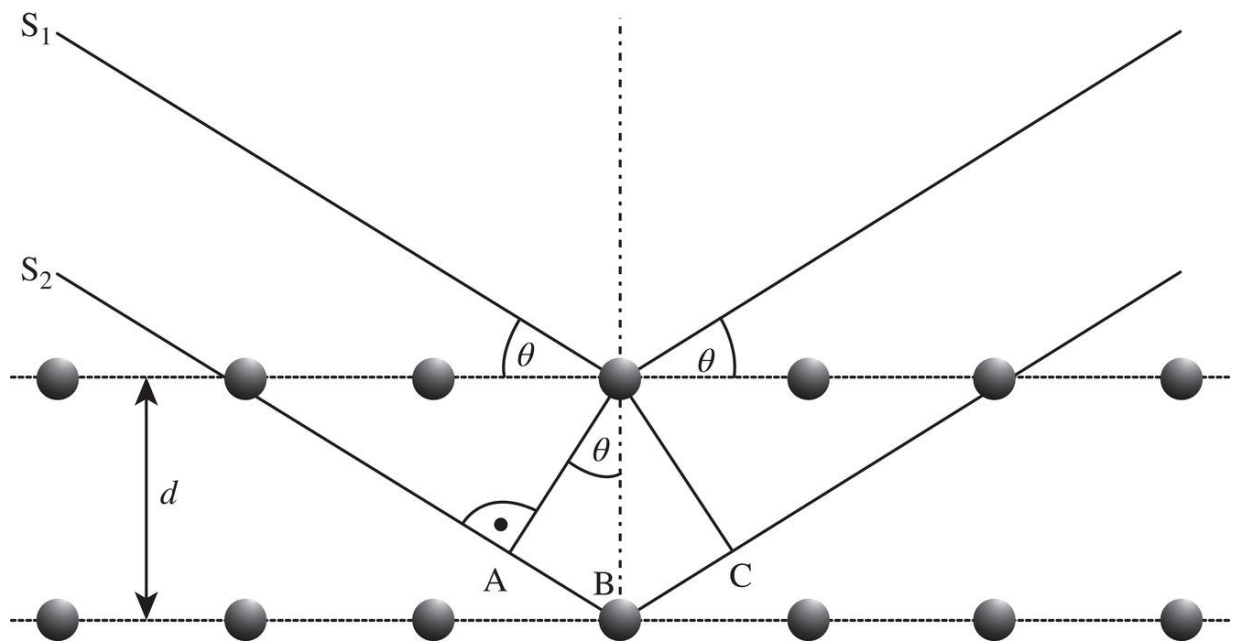


[Figure 8.3](#) The schematic diagram of brag's law.

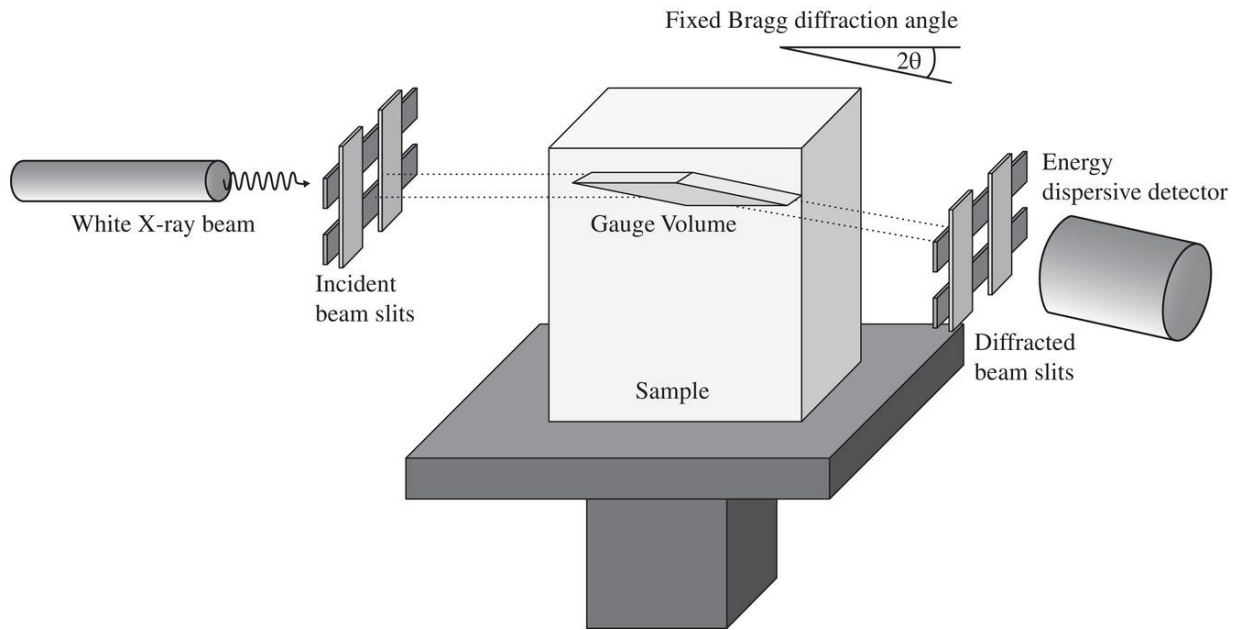


Figure 8.4 The schematic operational diagram of XRD.

$$2d_{hkl} \sin(\theta_{hkl}) = n\lambda \quad (8.1)$$

The primary operational diagram of an X-ray diffractometer shown in [Figure 8.4](#) involves a monochromatic radiation source and X-ray detector staged at the circumference of the graduated circle with the center of the powder specimen [5]. The divergence slit is laid down between the specimen and X-ray source and the specimen and the detector. These slits work for reducing background noise, limiting scattering radiation, and collimating radiation.

The goniometer has mechanically coupled with the detector and sample holder so that the detector rotated by $2\theta_{hkl}$ degrees in conjunction with specimen rotation θ_{hkl} degrees. The crystalline material has its own unique characteristic atomic structure that uniquely diffracts X-ray. The XRD pattern can compared with the database (ICDD, ICSD COD, etc.) to identify the material and to understand its nature.

8.4.2 XRD Setup

An X-ray diffraction setup consists of the following (shown in [Figure 8.5](#)):

- a. X-ray tube specifications are listed below:
 - 1. Power maximum continuous output power of 3 kW or higher.
 - 2. Input voltage 240 V.
 - 3. Rated voltage 20–50 kV or better (in steps of 1 kV).
 - 4. Rated current 5–60 mA or better (in steps of 1 mA).
- b. Sample holder: Glass sample holder.
- c. X-ray detector: Cu-type detectors are used to detect.
- d. Optics: Slit type: Automatic Computer Controlled and Programmable Variable slit.

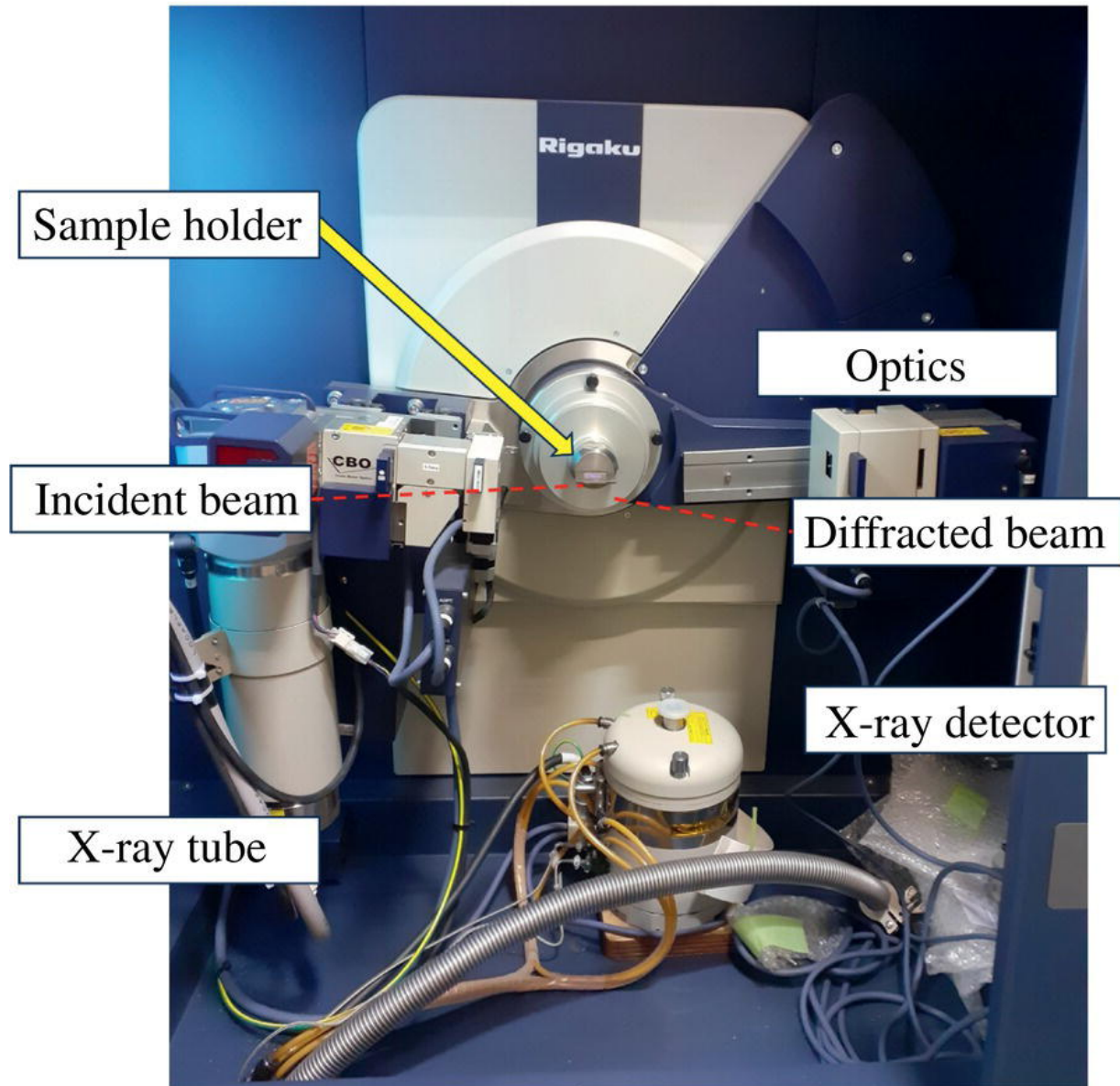


Figure 8.5 Setup for the X-ray diffraction.

8.4.3 Sample Preparations and Methodology

8.4.3.1 Brief Overview

The fundamentals of X-ray diffraction measurement are important in the material science, chemistry, and geology field, where to determine the crystal structure of material. Herein general procedure/steps for the X-ray diffraction analysis:

8.4.4 Steps Involved in Sample Preparation

Step 1: Obtain a small crystal fine powder (μm to mm) of the material you want to study.

Step 2: The sample should be clean, dry, and free from contaminants ([Figure 8.6](#)).

8.4.5 Instrument Setup

Step 1: Ensure the X-ray diffraction instrument is calibrated correctly and aligned.

Step 2: Adjust the X-ray source to the desired wavelength (typically using copper $K\alpha$ radiation, $\lambda = 1.5418 \text{ \AA}$).

Step 3: Set up the sample on a goniometer stage, ensuring that it can rotate in multiple directions.

8.4.6 Data Collection

Step 1: Place the sample in the path of the X-ray beam.

Step 2: The sample on the goniometer stage to collect data at different angles (θ) while keeping the X-ray source and detector stationary.

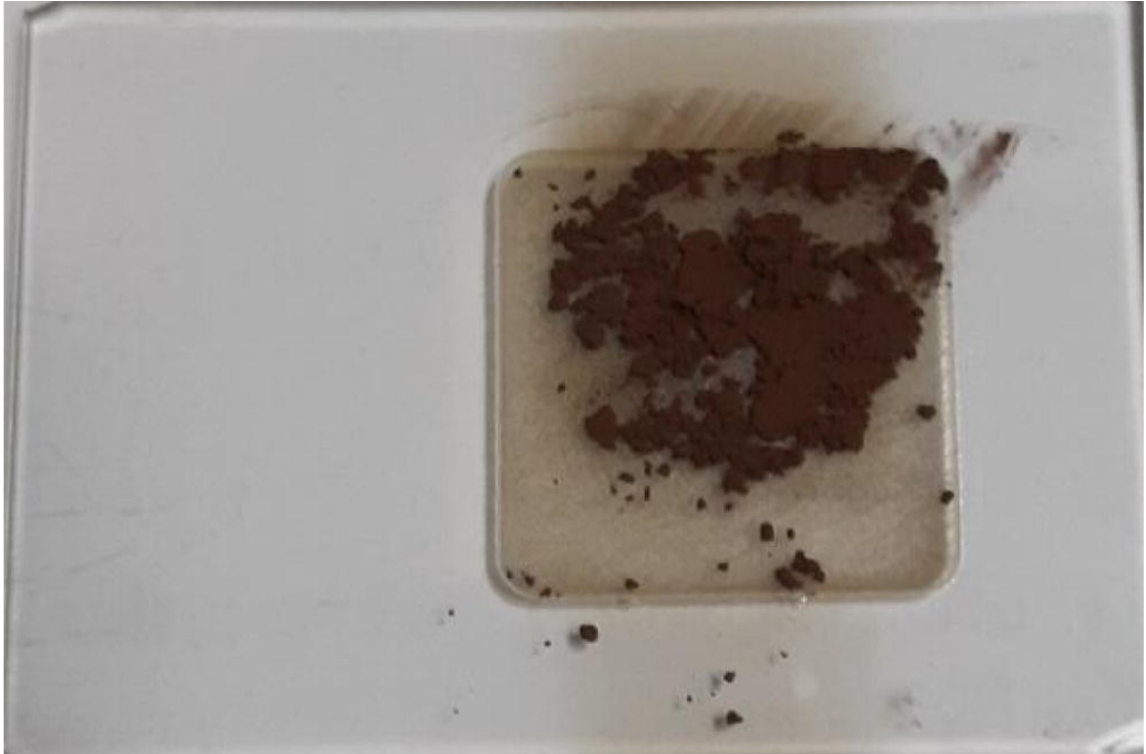


Figure 8.6 The sample preparation on the sample holder.

Step 3: Record the diffracted X-ray intensities at each angle.

Step 4: Collect data over a wide range of angles (typically from 0 to 90°) to capture as much information as possible.

8.4.7 Data Analysis

Step 1: Plot the recorded diffraction data as a function of the diffraction angle (θ).

Step 2: Use Bragg's law ($n\lambda = 2d \sin(\theta)$) to determine the interplanar spacing (d) of the crystal lattice planes that diffract X-rays at each angle.

Step 3: Calculate the 2θ values for the observed diffraction peaks.

Step 4: Compare the observed 2θ values with known values for the material or search in crystallographic databases to identify the crystal structure.

8.4.8 Crystal Structure Determination (if Necessary)

Step 1: To check the crystal structure of your material, you may need to refine it using software like Rietveld Refinement or other direct methods.

Step 2: This step can be complex and may require additional experiments, such as collecting data at various temperatures or under different conditions.

8.4.9 Data Interpretation

Step 1: Analyze the diffraction pattern to determine the crystal structure's unit cell parameters, space group, and atomic positions. The following things can be calculated:

1. Peak identification: Identify peaks: Analyze the diffraction pattern to identify the peaks corresponding to the diffracted X-rays. Each peak represents a set of planes within the crystal lattice that diffract X-rays at specific angles (2θ).
2. Indexing: Index peaks: Assign Miller indices (hkl) to each peak. Miller indices are used to describe the orientation and spacing of crystal planes that produce each diffraction peak.
3. Unit cell determination: Calculate d -spacing using Bragg's formulae.

Step 2: Use the collected data to obtain the crystal structure's unit cell parameters, identify the space group, and pinpoint atomic positions of the material's properties and behavior.

8.4.10 Conclusion

When analyzing crystalline materials, X-ray diffraction (XRD) has been shown to be an excellent method for gaining unit cell parameters, identifying the space group, and pinpointing atomic positions in their structural properties. Using a systematic approach and careful sample preparation, we have used XRD to decipher the fine features of the crystal structures in the materials we are analyzing.

8.5 Optical LED Microscope

8.5.1 Introduction

An optical light emitting diode (LED) microscope relies on LED lights for illumination. This LED light illumination significantly improves the quality and efficiency of light for examining specimens. LEDs offer a more stable, consistent, and programmable light source, which improves the imaging capabilities. In fluorescence microscopy, LED can be selected to emit light at different wavelengths, resulting in better brightness and more precise fluorescence imaging.

Optical microscopy has been used in scientific analysis and medical devices. These microscopes combine traditional optical microscopy techniques with modern LED illumination, providing various advantages such as enhanced image quality and real-time imaging over conventional light sources such as halogen or tungsten lamps. Standard imaging methods for monitoring channels and biological samples in microfluidics have been accomplished by using an optical microscope to include microfluidic channels. This chapter shows a comprehensive analysis of sample preparation and image capture techniques.

8.5.2 Sample Preparation

8.5.2.1 Prerequisites

- Substrate: Glass slides
- Material: PDMS
- Direct laser writing (DLW)
- Microscope

8.5.3 Brief Overview

The sample preparation and the analysis of the microchannel image are shown in the following step.

As shown in [Figure 8.7a](#) of the sample preparation, the Serpentine microchannel is fabricated using the UV-DLW process and designed using CatiaV5 software. The total microchannel dimensions are 30 (L) mm \times 0.32 mm (W) \times 35 μ m (H), and spacing with each cycle was around 250 μ m. [Figure 8.7b](#) shows the developed sample on the glass slide. [Figure 8.7c](#) shows the PDMS-glass fabricated continuous-flow microfluidic PCR devices. [Figure 8.7d](#) shows the dimension of the micropattern.

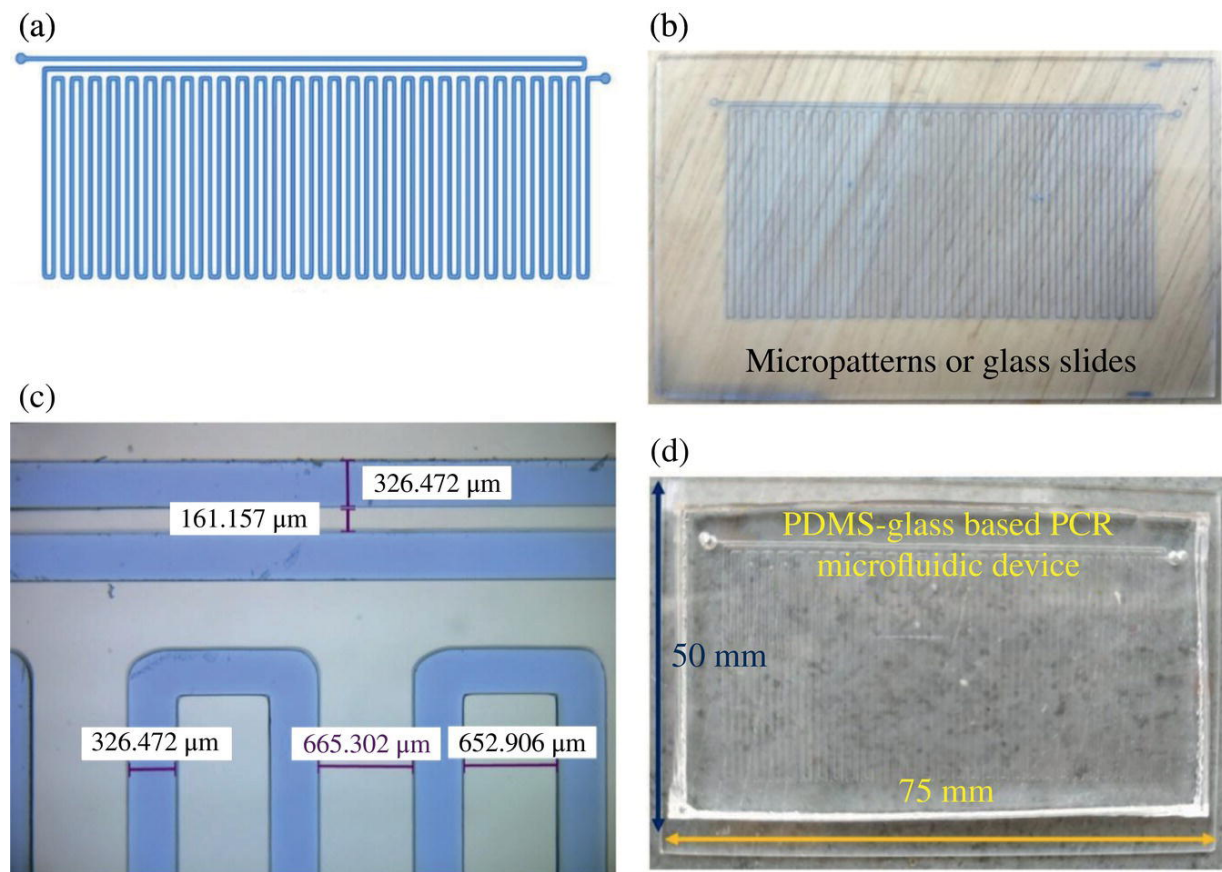


Figure 8.7 (a) Design of microchannel; (b) Developed master on glass slides using Direct Laser Writing (DLW); (c) Microchannel width dimensions of the master analyzed using an optical microscope; (d) PDMS–glass-based microfluidic device [6]/with permission of Springer Nature.

8.5.4 Principle of Optical Microscope

The principle of an upright microscope is based on the reflection and refraction of light through a series of lenses. It works as follows:

1. Light from a light source, usually a bulb or LED, enters the microscope and is directed toward the specimen placed on the stage.
2. The first lens in the optical pathway, the objective lens, is located close to the specimen and magnifies the light passing through it. The objective lens is typically mounted on a rotating nosepiece that allows for magnifications like 4×, 10×, 40×, and 100×.
3. The light then passes through a series of additional lenses, called the eyepiece, which further magnifies the image. The eyepiece is located at the top of the microscope and is viewed by the naked eye.
4. The combined magnifying power of the objective and eyepiece lenses produces an enlarged and highly magnified image of the specimen.
5. The light passes through the specimen and is bent (refracted) as it passes through its different layers. This bending of light causes the specimen to appear differently than it would without magnification.

In an upright microscope, the light source is positioned above the specimen, and the user views the specimen from above. This design is often used for routine observations of opaque specimens that require bright field illumination. The Leica DM 2000 LED (fluorescence microscope) system is used to observe biological specimens treated with fluorescent dyes or proteins ([Figure 8.8](#)). This allows researchers to visualize and study specific structures or molecules within a specimen in detail. The fluorescence microscope is helpful for various applications in the fields of cell biology, neuroscience, and medical research, among others. The Leica DM 2000 LED is a microscope used for high-resolution life and materials science imaging.

8.5.5 Sample Preparation and Instrumentation Setup

Preparation: Turn on the microscope by pressing the power button and ensure the LED light source is connected to the microscope.

Place your sample on the stage and focus the microscope using the coarse and fine focus knobs.



Figure 8.8 Optical Leica DM 2000 LED microscope.

Calculation of the magnification on the monitor: The magnification MTV on the monitor can be calculated with the following formula or measured with a stage micrometer and a cm scale:

MTV = Objective magnification x-factor of magnification changer* x TV adapter magnification x monitor diameter chip diameter of the camera

Optionally, a magnification changer, which is manually operated, can be used. On the knurled ring, the following magnification factors can be set: 4×, 10×, 40×, 100× HI plan objectives, and 10× eyepieces.

1. Bright-field imaging: Choose the bright field illumination by rotating the illumination selector dial to the BF position. Adjust the brightness of the LED light using the brightness control knob. Focus the microscope using the coarse and fine focus knobs to get a clear image of your sample.
2. Fluorescence imaging: To use fluorescence imaging, you must change the illumination to the fluorescence position by rotating the selector dial. Choose the fluorescence filter that matches the wavelength of the fluorophore you are using. Make sure that the excitation and emission filters are appropriately aligned. Adjust the LED light source and focus the microscope as needed to get a clear image of your sample.
3. Capture an image: To capture a picture, you can use the microscope's camera or connect an external camera to the microscope. Adjust the camera settings as needed to capture the image. You can also use software compatible with the Leica DM 2000 LED to control the microscope and capture photos.
4. Analysis: Once you have captured your images, you can use IMAGE J software to analyze them. You can adjust brightness, contrast, and color to get the best image possible. You can also use software tools to measure and analyze the images, such as counting cells or measuring the length of structures in your sample.

Note: Before using the microscope, ensure that the lens and stage are adequately cleaned and all safety protocols are

followed. Also, it is recommended that the user manual be consulted for specific instructions and details.

8.5.6 Conclusion

This microscope combines advanced LED illumination with high-quality optical performance, offering superior image quality and energy efficiency. It is a great option for many applications because of its cost-effectiveness and user-friendly design, which guarantees dependable and high-performance microscopy for academics, medical professionals, and researchers.

8.6 Contact Angle

8.6.1 Introduction

In contact angle measurements, the phenomena governing the behavior of the liquid over the solid membrane, including surface tension and adhesive force, are critical for understanding the surface interactions between the liquid and the solid membrane. Also referred to as the study of surface wetting properties, the following characterization techniques have gained cosmic attention in basic surface science, industrial areas, oil recovery, and other applications [7–9]. In this study/measurements let us learn the degree of wetting when the solid and liquid surfaces interact. Wetting can be defined as the ability of the liquid to maintain contact with the solid surface. In other words, it can be understood as the interactive relation between the liquid and solid surfaces. This simple approach can help one understand/decode the physical properties of the surface of the membrane/substrates e.g., interfacial tensions [10].

As seen in [Figure 8.9](#), the contact angle is used to determine the wettability of the particular substrate. If the contact angle Θ is less than 90° as seen in [Figure 8.9](#), then the substrate/membrane replicates the properties of hydrophilic nature/good wetting properties. If it is otherwise where Θ is greater than 90° , then the substrate/membrane replicates the properties of hydrophobic nature and a sign of non-wettability. In some cases, the Θ can be observed as having an angle greater than 150° , which replicates that the

substrate/membrane shows the property of superhydrophobic nature. As observed by the following, one can conclude that the wettability is inversely proportional to the contact angle [11].

$$\frac{1}{\text{Wettability}} \propto \text{Contact Angle}(\theta)$$

There are various approaches for measuring the contact angle based on the principles. Drop shape analysis is one of the approaches where one can determine the contact angle based on the sessile drop formed at the three boundary phases (solid, liquid, and gas). The second approach is known as the Wilhelmina plate method, where the surface tension and interfacial tension between the solid and liquid phase is recorded. The third approach for measuring contact angle is the Washburn method, where the angle is measured with respect to the surface free energies [11].

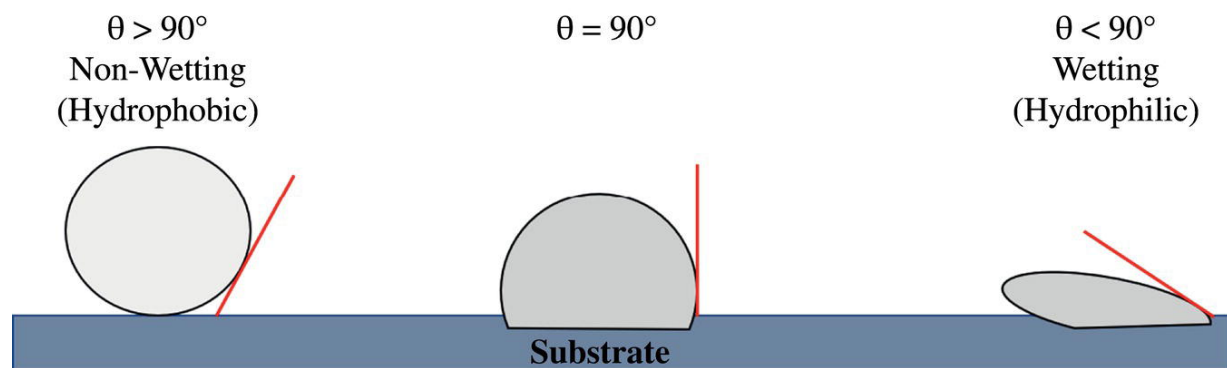


Figure 8.9. Contact angle measurement with its surface wetting.

In general, there are two types of contact angles based on the intersection of three boundary phases (i.e., solid, liquid, and gas). It can be classified as follows:

1. Static contact angle: Measured when all three phases are static. It is often used to determine the surface free energy of the substrate/membrane.
2. Dynamic contact angle: Measured when three/any of the three boundary phases are in motion. It is measured when the droplet is advancing/receding and the difference between the corresponding is known as contact angle hysteresis [12].

8.6.2 Setup Specifications

[Figure 8.10](#) shows the setup of the optical tensiometer used to measure contact angle. The instrument is specified below.

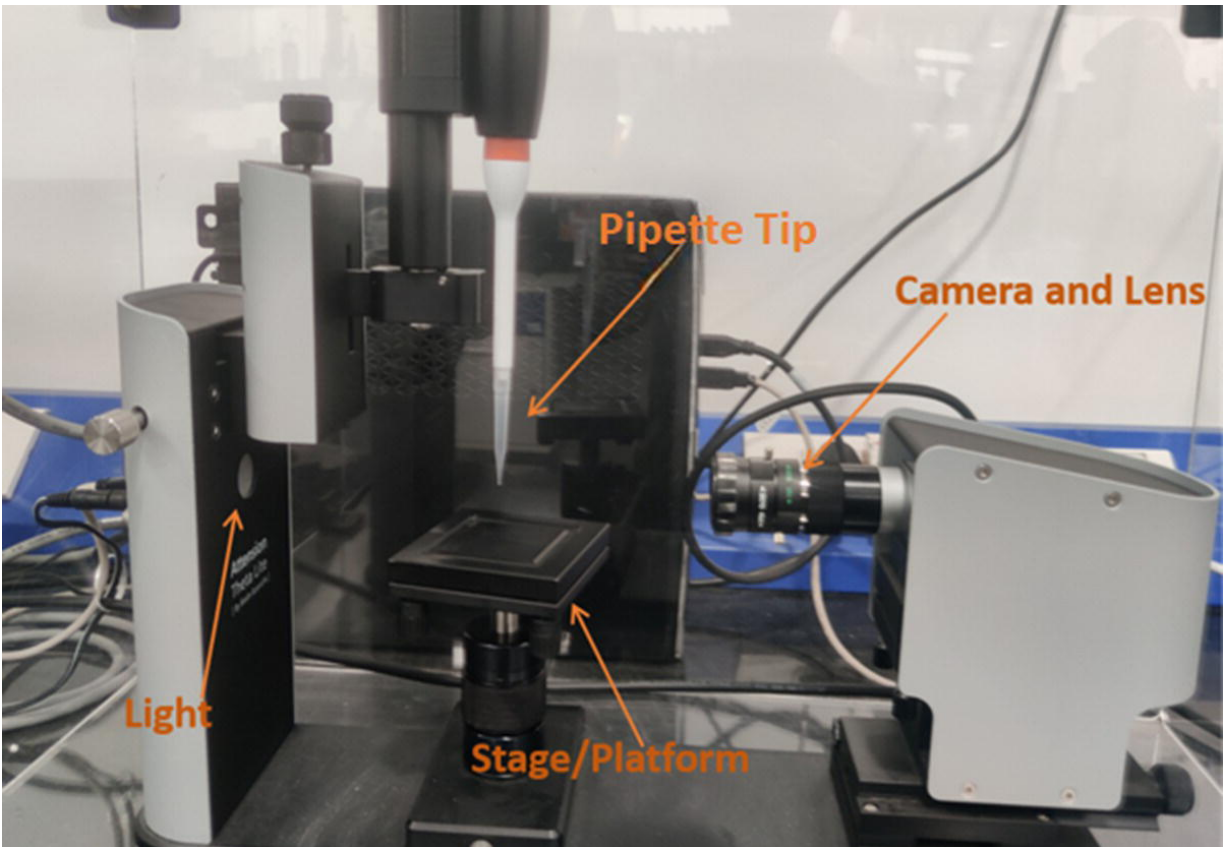


[Figure 8.10](#) Setup of contact angle measurement.

8.6.3 Biolin Scientific Theta Lite – Optical Tensiometer

These are the static and dynamic contact angle measurements:

- Number of dispensers: 2
- 1280 × 1024 px camera
- Max FPS: 2068
- Manual droplet placement
- Manual YZ sample stage
- Frame interval range: 0.33 ms–1000 s

8.6.4 Sample Preparations and Methodology

8.6.4.1 Brief Overview

The fundamentals of the contact angle measurements are of significant importance in studying the wetting properties of the materials. These measurements help to determine the hydrophobicity and hydrophilicity of the solid surfaces, providing meaningful insights into surface energy and interfacial tensions. Here is a general guidelines/procedure for conducting contact angle measurements:

Step 1: Select the substrate/membrane for the respective study. Clean the substrate thoroughly with a suitable cleaning agent. The most commonly used/appropriate cleaning agent is isopropyl alcohol/deionized water. The cleaning may not be mandatory. Log in to the software (One Attention) to continue with the contact angle measurement of the liquid.

Step 2: If calibration is required, it should be performed using a standard sample with a known contact angle.

Step 3: Place the substrate/membrane on the stage. Open the camera shutter and adjust the camera and lighting for optical image capture.

Step 4: Capture the images of the samples and use the installed software (One Attention Software) to determine further and analyze the contact angle.

Step 5: Use a pipette tip to dispense a droplet of liquid onto the substrates of the solid membrane, as controlled by the software. [Figure 8.11](#) shows the various options for controlling dispensing/filling the incorporated pipette tip.

Step 6: Perform multiple times at multiple locations to ensure the reliability and reproducibility of the selected substrate/membrane.

Step 7: Collect the recorded data from the saved file/location for further incorporation.

As an example, recorded data can be observed in [Figure 8.12](#). The measurement was done for laser-induced graphene (LIG) substrate, using deionized water as the liquid. From the above data, one can conclude that the surface of LIG has a hydrophilic nature as the contact angle Θ is around 53.79° – 56.66° , which is less than 90° .

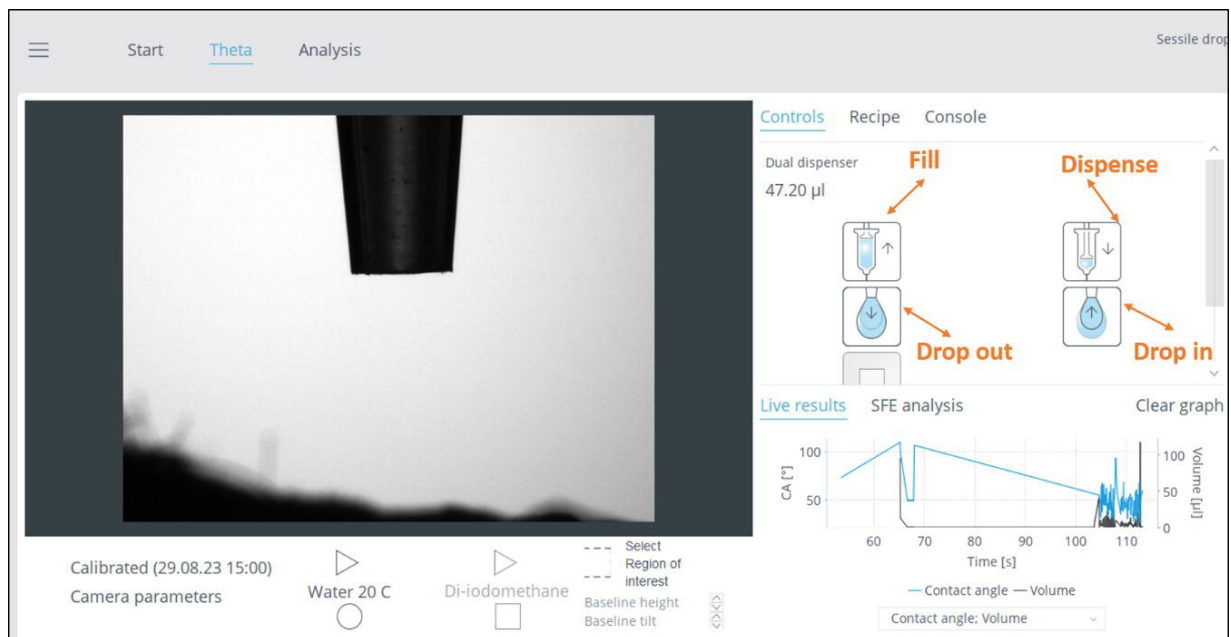


Figure 8.11 Computer software for dispensing/filling the droplet-based syringe.

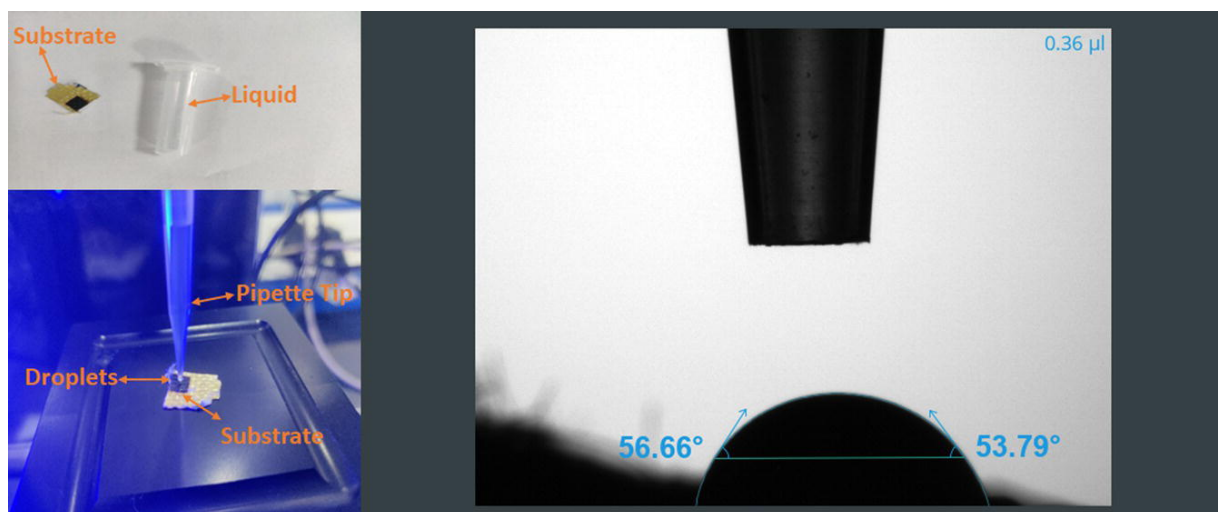


Figure 8.12 Obtained data of the contact angle measured for the substrate of laser-induced graphene (LIG).

8.6.5 Protocols to Be Followed While Operating the Instrument

The instruction specified by the instrument manufacturer in the equipment/instrument manual should be adhered to. Adjustment may be significant depending on the nature of the substrate/membrane or the wetting agent used. It is crucial to track these settings to ensure optimal accuracy and reliability in the measurement. In times of adversity/any fault, the user should immediately contact or inform the instrument in charge about the malfunctioning or any error reported during the process of experimentation.

8.6.6 Conclusions

Contact angle measurements is an essential tool for comprehending surface understanding between the liquid and solid membrane and its characteristics in a variety of disciplines, including biological and material science. The surface of the solid membrane should be cleaned using a suitable agent prior to measurement if required. Additionally, calibration must be performed with a standard sample with a known contact angle to attain an accurate output without any error. The solid membrane or the substrates can then be placed in the stage for the measurement of hydrophilicity and hydrophobicity of the solid membrane by dispensing a droplet of liquid using a pipette tip and measuring it with the help of software. Following these steps ensures reliability and accurate measurements. Its adaptability in describing wetting behavior provides insightful information for improving a range of applications, including the domain of biomedical and self-cleaning surfaces.

References

- 1 Zhou, W., Apkarian, R., Wang, Z.L., and Joy, D. (2007). Fundamentals of scanning electron microscopy (SEM). In: *Scanning Microscopy for Nanotechnology: Techniques and Applications* (ed. W. Zhou and Z.L. Wang), 1–40. New York, NY: Springer. https://doi.org/10.1007/978-0-387-39620-0_1.

- 2 Inkson, B.J. (2016). 2 – scanning electron microscopy (SEM) and transmission electron microscopy (TEM) for materials characterization. In: *Materials Characterization Using Nondestructive Evaluation (NDE) Methods* (ed. G. Hübschen, I. Altpeter, R. Tschuncky, and H.-G. Herrmann), 17–43. Woodhead Publishing. <https://doi.org/10.1016/B978-0-08-100040-3.00002-X>.
- 3 Glazer, A.M., Roleder, K., and Dec, J. (1993). Structure and disorder in single-crystal lead zirconate, PbZrO_3 . *Acta Crystallogr. B* 49 (5): 846–852. <https://doi.org/10.1107/S0108768193005129>.
- 4 Prasad Bag, S., Hou, X., Zhang, J. et al. (2020). Negative/positive electrocaloric effect in single-layer $\text{Pb}(\text{Zr}_x\text{Ti}_{1-x})\text{O}_3$ thin films for solid-state cooling device. *IEEE Transactions on Electron Devices* 67 (4): 1769–1775. <https://ieeexplore.ieee.org/abstract/document/9027847>.
- 5 Banlue, W. and Vittayakorn, N. (2009). Effect of $\text{Pb}(\text{Zn}_{1/3}\text{Nb}_{2/3})\text{O}_3$ additions on phase structure, ferroelectric and dielectric properties of PbZrO_3 ceramics. *Ferroelectrics* 382 (1): 122–126. <https://doi.org/10.1080/00150190902870028>.
- 6 Kulkarni, M.B. and Goel, S. (2024). Miniaturized DNA amplification platform with soft-lithographically fabricated continuous-flow PCR microfluidic device on a portable temperature controller. *Microfluidics and Nanofluidics* 25 (69): <https://link.springer.com/article/10.1007/s10404-021-02473-4>.
- 7 Hebbar, R.S., Isloor, A.M., Zulhairun, A.K. et al. (2017). Efficient treatment of hazardous reactive dye effluents through antifouling polyetherimide hollow fiber membrane embedded with functionalized halloysite nanotubes. *J. Taiwan Inst. Chem. Eng.* 72: 244–252. <https://doi.org/10.1016/j.jtice.2017.01.022>.
- 8 Bracco, G. and Holst, B. (2023). *Surface Science Techniques*. Springer-Verlag. <https://books.google.co.in/books?hl=en&lr=&id=nUJEAAAAQBAJ&oi=fnd&pg=PR4&dq=Bracco,+G.,+and+Holst,+B.>

<https://doi.org/10.1109/TED.2019.2913851>
<https://ieeexplore.ieee.org/abstract/document/8732592>

- 9 Puneeth, S.B. and Goel, S. (2019). Novel 3D printed microfluidic paper-based analytical device with integrated screen-printed electrodes for automated viscosity measurements. *IEEE Transactions on Electron Devices* 66 (7): 3196–3201.
<https://doi.org/10.1109/TED.2019.2913851>.
<https://ieeexplore.ieee.org/abstract/document/8732592>.
- 10 Song, J.-W. and Fan, L.-W. (2021). Temperature dependence of the contact angle of water: a review of research progress, theoretical understanding, and implications for boiling heat transfer. *Adv. Colloid Interface Sci.* 288: 102339.
<https://doi.org/10.1016/j.cis.2020.102339>.
- 11 Katyal, D., Subramanian, A.K., Venugopal, A., and Marya, A. (2021). Assessment of wettability and contact angle of bonding agent with enamel surface etched by five commercially available etchants: an in vitro study. *Int. J. Dent.* 2021: e9457553.
<https://doi.org/10.1155/2021/9457553>.
- 12 Ajaev, V.S., Gambaryan-Roisman, T., and Stephan, P. (2010). Static and dynamic contact angles of evaporating liquids on heated surfaces. *J. Colloid Interface Sci.* 342 (2): 550–558.
<https://doi.org/10.1016/j.jcis.2009.10.040>.

Note

* Equally Contributing Author.

9

Spectroscopic Characterization

Himanshi Awasthi^{1}, N.K. Nishchitha^{1*}, Sonal Fande^{1,2*}, and Sanket Goel¹*

¹ MEMS, Microfluidics and Nanoelectronics (MMNE) Lab, Department of Electrical and Electronics Engineering, Birla Institute of Technology and Science (BITS) Pilani, Hyderabad Campus, Hyderabad, Telangana, India

² Department of Pharmacy, Birla Institute of Technology and Science (BITS) Pilani, Hyderabad Campus, Hyderabad, Telangana, India

9.1 Introduction

Understanding the optical, chemical, and structural properties of materials is essential for various scientific and industrial applications. Compositional characterization employs several analytical techniques, including ultraviolet-visible (UV-Vis) characterization, X-ray photoelectron spectroscopy (XPS), Raman spectroscopy, and Fourier transform infrared spectroscopy (FTIR). UV-Vis characterization is widely used to investigate how materials interact with light in the UV and visible regions of the electromagnetic spectrum, providing insights into absorption spectra, band gap, refractive index, and extinction coefficient [1]. XPS analysis utilizes monoenergetic soft X-rays to examine the energy of emitted electrons from a sample, facilitating the verification of elements and detection of chemical shifts arising from differences in chemical potential and polarizability [2]. Raman spectroscopy is a straightforward approach for identifying substances through the inelastic scattering of monochromatic light, offering valuable information on molecular vibrations, rotations, and low-frequency transitions [2]. FTIR is mainly deployed to identify the functional group present in the organic molecules by observing their interaction with infrared electromagnetic energy, enabling the identification of unknown compounds and quantification of

impurities [3–6]. This chapter explores the principles, applications, and benefits of each compositional characterization technique, underscoring their significance in materials science and analytical chemistry.

9.2 Ultraviolet-Visible (UV-Vis) Spectrophotometers

9.2.1 Steps Involved

UV-Vis spectroscopy technique is used to measure compound concentrations and detect the formation of inhibiting molecules in solution. It is one of the most widely used analytical techniques. It's an experimental method that uses the absorption of solute of light to determine the concentration of each solute in a given solution. UV-Vis spectroscopy measures the amount of light that a sample can transmit by passing UV-Vis light through it. The extent of absorption at a particular wavelength is determined by the chemical structure of the molecule. The liquids are analyzed using a spectrophotometer. UV-Vis spectrophotometers detect the absorption or transmission of light through a material as a function of wavelength. UV-Vis spectroscopy is generally deployed for qualitative, quantitative, structural analysis, kinetic study, and checking the optical properties of the samples.

Step 1: Calibration: Prior to utilizing the spectrophotometer, it is imperative to perform a calibration procedure to ensure accurate and precise measurements can be acquired. The calibration process can be effectively conducted by utilizing a well-established standard solution, such as a potassium dichromate solution, cobalt sulfate, and sodium nitrite.

Step 2: Measurement of a blank: Conducting a measurement of a blank is crucial in order to account for any potential background absorbance accurately. In the majority of instances, the blank typically comprises the solvent employed to dissolve the sample or deionized water.

Step 3: Experiment observation: For measurement of the sample, the sample is first put in a quartz cuvette, and then the spectrophotometer is loaded with both the quartz cuvette and the process is shown in [Figure 9.1](#). Measurements of the absorbance of the sample are taken either at the wavelength of interest or throughout a spectrum of wavelengths. As shown in [Figure 9.2](#), Graphene oxide (GO) exhibits a UV-Vis absorption peak at around 225 nm, which corresponds to the $\pi \rightarrow \pi^*$ transition of C–C bonds. Furthermore, at approximately 300 nm, a shoulder peak is discovered, signifying the C=O bond transition from n to π^* [1].

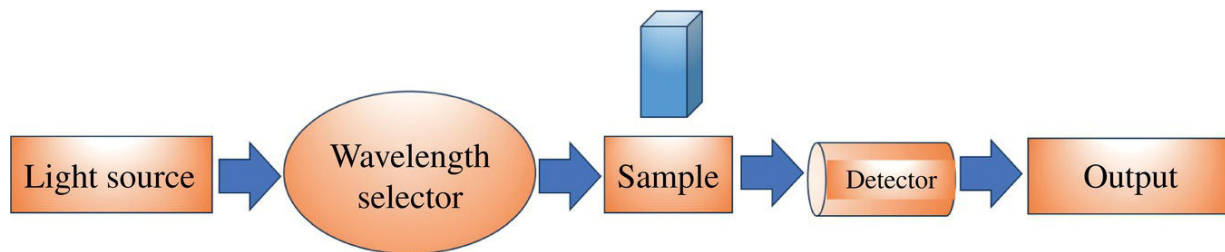


[Figure 9.1](#) Device operation flowchart.

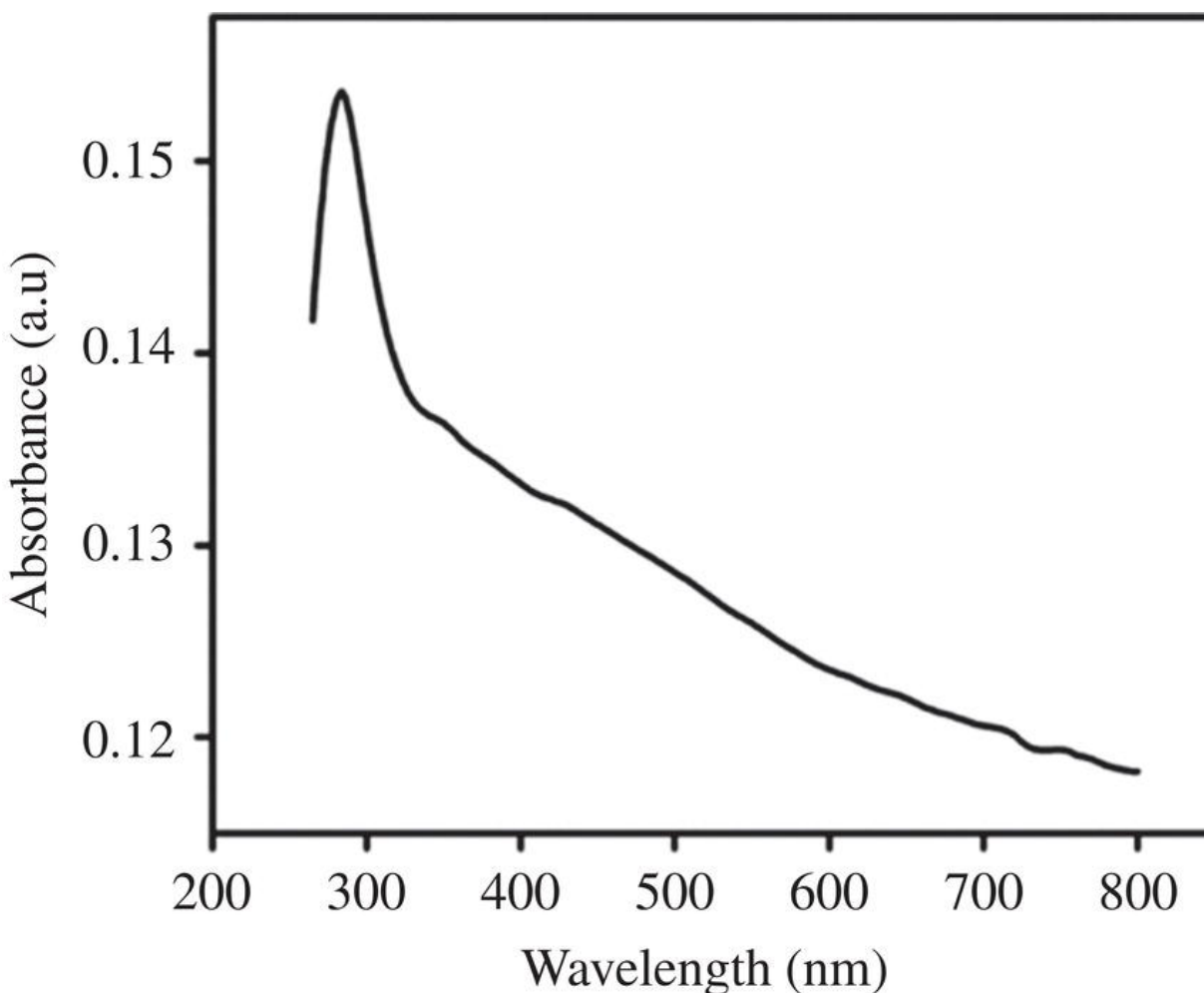


Figure 9.2 UV-Vis spectroscopy of the laser-induced reduced graphene oxide (LrGO) [1]/with permission of ELSEVIER.

Absorbance data is essential to estimating the concentration of a substance in a sample since it is directly proportional to the amount of light absorbed by it. Peak wavelength (λ_{max}) plays an important role in identifying substances. Different compounds exhibit distinct absorbance peaks at certain wavelengths, providing information about electronic transitions inside the molecule. The absorbance data that was received from the measurement of the sample is analyzed in order to ascertain the concentration of the analyte that is present in the sample. This may be accomplished with the use of a calibration curve, in which the absorbance of samples containing known concentrations of the analyte is plotted against those concentrations, and the concentration of an unknown sample is calculated based on the absorbance value graph shown in [Figure 9.2](#).

9.2.2 Conclusion

In summary, the analysis of the optical characteristics and electronic transitions of materials such as reduced graphene oxide (rGO) and GO requires the use of the UV-Vis experimental setup. Certain transitions, such as the $\pi \rightarrow \pi^*$ transition of C–C bonds and the $n \rightarrow \pi^*$ transition of C=O bonds, are identified by measuring the absorption peaks. By precisely identifying functional groups and verifying material properties, this approach offers insightful information about the structural and electrical properties.

9.3 X-Ray Photoelectron Spectroscopy (XPS)

XPS is a characterization technique for surface morphological study, with applications in almost every scientific and material analysis. It is commonly used to identify the surface composition, analyze component abundance, and determine chemical states based on the binding energies of elements. Herein, the surface composition and the chemistry of the materials are measured in the order of a few atomic layers (~ 10 – 20 nm). The chapter provides steps to follow for XPS-based surface characterization, including sample preparation and analysis.

9.3.1 Fundamentals of XPS

XPS is a photoelectric effect involving the emission of electrons from atoms when they are exposed to electromagnetic radiation. The interplay between kinetic and binding energies plays a fundamental role in the generation of XPS spectra. Atoms possess multiple orbitals at varying energy levels, leading to a diverse range of binding energies for electrons. When electrons are emitted in response to electromagnetic radiation, the resulting XPS spectrum reflects this variation in binding energies. The range of emitted electrons with different binding energies provides valuable information about the composition and chemical environment of the material being analyzed. By analyzing the kinetic energies of these emitted electrons, the binding energies of electrons in different orbitals can be determined.

The relations are represented by the following equation.

$$E_{kinetic} = E_{photon} - E_{binding} - \phi$$

where $E_{kinetic}$ is the kinetic energy of the photoelectron measured by the instrument, $E_{photons}$ are the energy of the incident photons. $E_{binding}$ is the binding energy of a given electron, and ϕ is the work function, signifying the energy difference between the vacuum energy level and the Fermi level of the solid material under study.

9.3.1.1 XPS Instruments Have the Following Components

An ultrahigh vacuum system below 10^{-9} Torr, to prevent photoelectrons with low energy from being absorbed by the air.

X-rays from Al K α and Mg α are used to excite the sample, with a monochromator and concentric hemispherical analyzer to analyze produced photoelectrons energies.

An Ar ion gun is used to clean material surfaces and analyze surface layers, while an electron flood gun minimizes surface charging during X-ray analysis.

9.3.2 Sample Preparation Steps

1. Sample types: XPS can analyze various solid samples like films, powders, and frozen liquids, including inorganic compounds, polymers, metals, and more.
2. Sample size: In most systems, samples generally can be analyzed as received or may need to be cut to fit the sample holder, with the allowed sample size dependent on the instrument configuration; usually, samples on the order of approximately $1 \times 1 \text{ cm}^2$ and less than 1 cm high can be analyzed.
3. Cleaning of samples: Use the appropriate cleaning techniques to thoroughly clean the sample surface, such as solvent cleaning, ultrasonic cleaning, or ion sputtering.
4. Sample contamination: XPS is sensitive to the top surface ($\sim 10 \text{ nm}$) of a material. Thus, it is suggested to use fresh samples. If

samples must be washed to remove surface contaminants, a light hydrocarbon solvent (e.g., hexane) is recommended. Ion beam sputtering, particularly with ions like Ar, has also been used to remove contaminants like adventitious carbon.

9.3.2.1 Sample Mounting

XPS analysis sample mounting depends on the instrument and sample type:

1. Mounting techniques: Attach the thin film samples to the sample holder with clips or clamps to secure the sample. Powders can be analyzed by mounting them on double-stick carbon tape, pressing them onto indium foil, or suspending them in a liquid on a conducting substrate, ensuring they are securely attached to prevent contamination and detector degradation. In some cases, sample cups are also being used to hold and analyze powders and granules.
2. Charge neutralization: To avoid charging effects during analysis, employ a charge-neutralization approach like a flood gun or low-energy electron flood gun if your material is insulating.
3. Alignment marks: For devices that enable it, mark the sample to help locate regions of interest during analysis.

9.3.3 Experimental Procedure

1. Vent the load lock.
2. Use clips to secure your sample to the platform. The assemble height (Z-height) adjustment should be accomplished using the respective software of the instrument.
3. Set the platform in the load lock with the letters facing the chamber. Ensure that the platform is mechanically stable against the pins.
4. Close and pump load-lock. Wait for the load-lock pressure to drop below $5\text{e-}7$ mbar.
5. Transfer the sample to the analysis chamber.

6. Create an experiment tree and set each analysis point's sample position.
7. Begin the experiment after the chamber pressure drops below 8×10^{-8} mbar.
8. Once the experiment is complete, ensure the guns have scaled down (i.e., Reducing the power, current, or intensity of the guns) and transfer the sample to the load-lock.
9. Vent the load lock and retrieve the sample. Keep the load lock closed and hoover it.

9.3.3.1 Detailed Instructions

1. Instrument startup: Start the XPS instrument and let it warm up and stabilize for a while. Generally, this period can range from 30 minutes to 1 hour. System examinations and calibrations should follow manufacturer instructions.
2. Sample load: Follow the XPS instrument loading instructions carefully to transfer the sample into the sample stage or holder.
3. Vacuum pumping: Maintain a high vacuum in the XPS chamber. This usually involves turbomolecular and ion pumps pumping down the chamber.
4. X-ray source setup: Set X-ray source parameters, including type (Al K α or Mg K α), power, and spot size.
5. Energy calibration: Use reference peaks like Au 4f $_{7/2}$ at 84.0 eV to calibrate the XPS instrument's energy scale.
6. Spectrometer setup: Set the pass energy, lens mode, and analyzer transmission for the XPS spectrometer.
7. Data acquisition: Place the samples X-ray source and analyzer over the target area. Irradiate the sample with X-rays and measure photoelectrons to get XPS spectra. Record spectra from a few eV to several hundred eV. Survey and high-resolution spectra will be required to determine the samples elemental composition and chemical states. Adjust rest time and scans to optimize signal-to-noise ratio quality.

8. Sample removal: Retrieve the sample from the XPS equipment carefully to avoid contamination.
9. Shutdown: Follow the manufacturer's instructions to shut down the XPS instrument.
10. Data analysis and interpretation: Use specialized XPS analysis software to analyze the collected spectra. The analysis software provides the tools for peak fitting, background subtraction, and deconvolution.

Peak fitting and deconvolution identify and quantify the elemental composition and chemical states after resolving the overlapping peaks.

Usually, the charging effect shifts the binding energy. Thus, it is important to address the charging effects using a common method, referencing the binding energy to the known standards, such as C 1s peak at 284.8 eV.

Apply the curve fitting algorithm and adjust the peak position, width, and intensity. Ensure the fitting model accounts for all significant contributions to the spectrum.

11. Separate the overlapping peaks by deconvolution to resolve closely spaced peaks. Quantify the elemental composition by integrating the area under each deconvoluted peak and analyze the chemical bonding states by examining shifts in binding energy.
12. Compare experimental results to reference data and known materials. Cross-check the results with known standards or literature values to validate the analysis.

The analysis of XPS data suggests the presence of carbon (C), oxygen (O), sodium (Na), and cobalt (Co). The peaks of C and O provided evidence that rGO was formed, as depicted in [Figure 9.3](#). The C 1s peak at 284 eV is made up of C atoms, while the O 1s represent the composite's oxygen atom. The non-oxygen bond between C=C and C-O is verified by the XPS spectrum of C 1s at 284.2 and 286.3 eV, respectively. Deconvoluting the Co 2p peak, as seen in [Figure 9.4](#), results in a peak at 778.1 eV that makes the presence of metallic Co clear. The Co 2p_{1/2} peak and two more satellite peaks are located at

780.1 and 796.9 eV, respectively. The Co 2p_{3/2} and Co 2p_{1/2} are denoted by 785.5 and 802 eV, respectively. The production of metallic Co and the Co (2+, 3+) oxide (Co₃O₄) phase is represented by all these peaks.

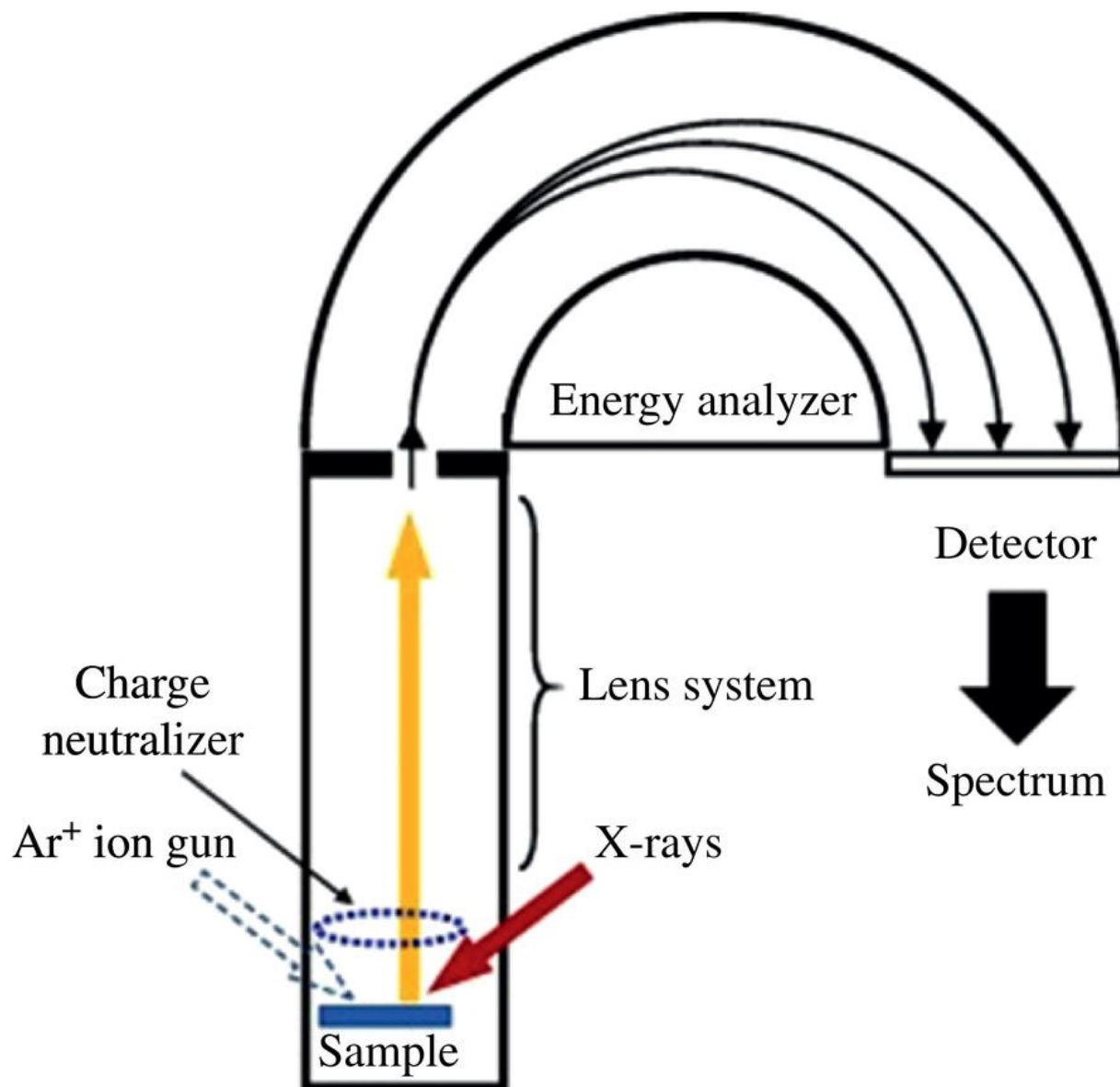


Figure 9.3 The schematic view of the photoelectron spectrometer.

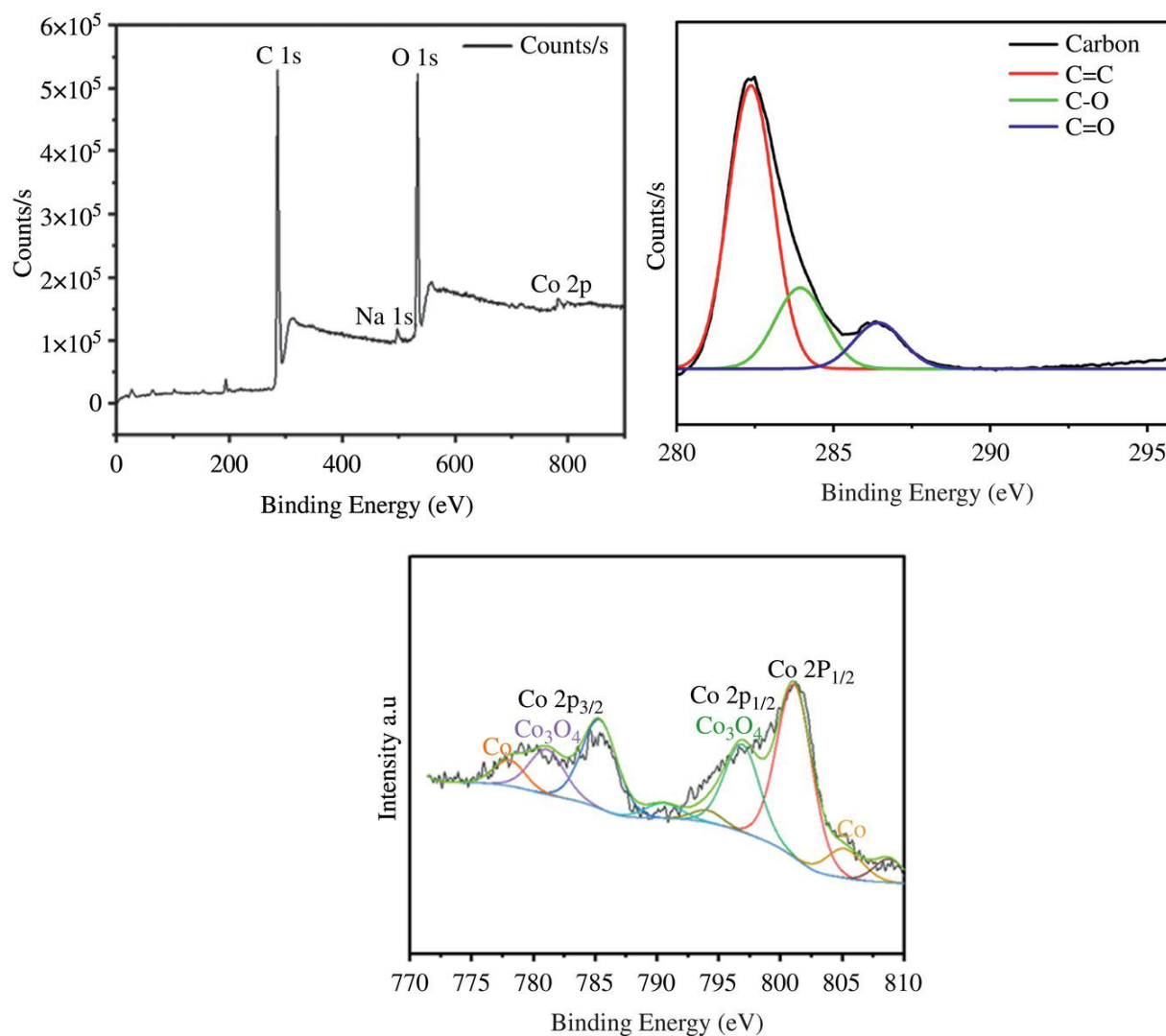


Figure 9.4 XPS analysis graphs for the Co-Co₃O₄-rGO, including survey spectra, Carbon spectra, and the elemental analysis to authorize the structure of Co and Co₃O₄ [2]/with permission of IOP Publishing Ltd.

9.3.4 Conclusion

XPS is a powerful surface characterization technique used to analyze the elemental composition, chemical states, and surface morphology of materials at a depth of 10–20 nm. Through detailed sample preparation, precise instrument calibration, and specialized data analysis software, XPS provides crucial insights into the binding energies of elements and their chemical environments.

9.4 Raman Spectroscopy

Raman spectroscopy is a powerful analytical technique widely used for identifying molecular composition, structure, and interactions due to its unique advantages. It provides a molecular fingerprint for precise identification of substances and is nondestructive, allowing for the analysis of valuable or sensitive samples. Its compatibility with water allows for the study of aqueous solutions and biological samples, while its effectiveness in analyzing crystalline structures is invaluable in materials science.

The Raman effect works on the principle of inelastic light scattering between incoming light and an irradiated substance or sample. This uses scattered light to analyze a sample's vibrational energy modes, providing chemical and structural information through Raman scattering detection. Raman scattering occurs when light interacts with molecules, causing a temporary complex formation between the photon and molecule, leading to the re-emission of scattered light. This chapter provides sample preparation and experimental steps.

9.4.1 Sample Preparation

9.4.1.1 Prerequisites

- Sample: Powders, thin films, and or liquids.
- Scoop or spatula: For moving the solid sample.
- Pipettes: For accurate liquid medium measurement.
- Vortex mixer or ultrasonicate: For mixing and homogenizing the solid-liquid suspension.
- Microscope slides or quartz plates: The usual substrates for Raman spectroscopy.
- Solvent: Clean the substrate using a solvent (DI water or 70% IPA).

9.4.2 Experimental Procedure

Step 1: Clean the substrate: To get rid of any impurities, thoroughly clean the quartz plates or microscope slides with any organic solvent such as acetone, ethanol, or isopropanol.

Step 2: Place the sample on the substrate (glass slide): Place a tiny amount of the material on the surface of a clean substrate (such as a quartz plate or microscope slide), as shown in [Figure 9.4](#). To create a thin film, drop the liquid sample and let the sample dry on the substrate. Depending on the sample and liquid utilized, this could take a few minutes to many hours. Before continuing, make sure the solvent has entirely evaporated.

Step 3: Carefully handle the substrate: To avoid contamination, handle the sample with clean gloves or tweezers after it has dried.

9.4.2.1 Instrumentation Configuration

Step 1: Ensure that the Raman spectrometer is calibrated and powered in accordance with the manufacturer's instructions. The Raman spectrometer calibration involves three different parameters: (i) spectral calibration, (ii) laser alignment and (iii) Microsoft calibration. Spectral calibration ensures accurate positioning and adjustment of spectrometer parameters using reference bands. Laser alignment is optimized through auto-alignment capabilities, ensuring consistent performance.

Step 2: Select the appropriate laser wavelength for your sample based on its characteristics. With the highest energy to bombard the sample structure, the 532 nm laser is ideal for inorganic materials. For most chemicals, the 785 nm laser offers the best economic performance with less excitation efficiency and lower fluorescence. The 1064 nm laser performs with the least amount of fluorescence but requires a relatively longer acquisition time to obtain sufficient signal levels for analysis. If special precautions are not taken, there is a higher chance that the sample will be heated.

Step 3: Adjust the laser intensity to a level that balances signal strength and sample protection.

9.4.2.2 Specific Intensity Ranges

- Biological samples: 0.1–1 mW/cm² to avoid denaturation or burning.
- Polymeric materials: 1–5 mW/cm² to prevent melting or structural changes.
- Inorganic materials: 5–50 mW/cm² depending on the hardness and thermal properties.
- Metals: 10–100 mW/cm² as they generally tolerate higher intensities without significant damage.

9.4.2.3 Sample Preparation

- Prepare your sample as described previously, ensuring that it is spotless and fixed to the substrate.
- Attach standard sample to the same stud to check Raman peaks for wavenumber calibration.

9.4.2.4 Laser Targeting

- Focus the laser beam on the samples surface using the microscope objective.

9.4.2.5 Measurement of the Baseline

- Measure without the laser (a dark measurement) to correct for any environmental signals or electronic noise.

9.4.2.6 Subtraction of Dark Signals

- Remove electronic noise from acquired Raman spectra by subtracting the dark measurement.

9.4.2.7 Spectrum Calibration

- Use known spectral lines or reference materials (such as silicon or molecular standards) to calibrate the Raman spectrum to wavenumber.

9.4.2.8 Raman Scanning

- Initiate the laser and scan the laser beam across the surface of the sample to capture Raman scattering signals.
- Acquire multiple (5–10) measurements to increase the signal-to-noise ratio. The number of measurements should be based on signal quality and system sensitivity.

9.4.2.9 Data Analysis

- Analyze the Raman spectra to determine the characteristic peaks and molecular vibrations.
- Compare the acquired spectrum to reference spectra or databases to determine sample constituents.

9.4.2.10 Data Interpretation

Interpret the Raman peaks as molecular bonds, vibrational modes, and structural information.

9.4.2.11 Data Representation

Document the main findings, including peak positions, intensities, and any molecular designations.

9.4.2.12 Cleansing

- Turn off the laser and turn off the Raman spectrometer.
- Store or dispose of all used samples

9.4.3 Results

As shown in [Figure 9.5](#), the Raman spectra, which include a D peak at 1344 cm^{-1} , explain the defect formation in the sample. Defects in graphene are characterized as anything that disrupts the symmetry of the carbon honeycomb lattice. It represents a ring breathing mode from sp^2 carbon rings, requiring adjacency to a graphene edge or a defect. The D-band arises from a single phonon lattice vibrational process. It is typically weak in graphite and high-quality graphene.

The G peak is identified at 1588 cm^{-1} and $I_D/I_G = 0.74$, indicating the removal of the oxygen groups. Generally, the I_D/I_G ratio value is ~ 0.8 to <1 for the GO, thus indicating the formation of rGO ([Figure 9.6](#)).



Figure 9.5 Schematic to show the arrangement of the sample on a glass slide for the Raman characterization.

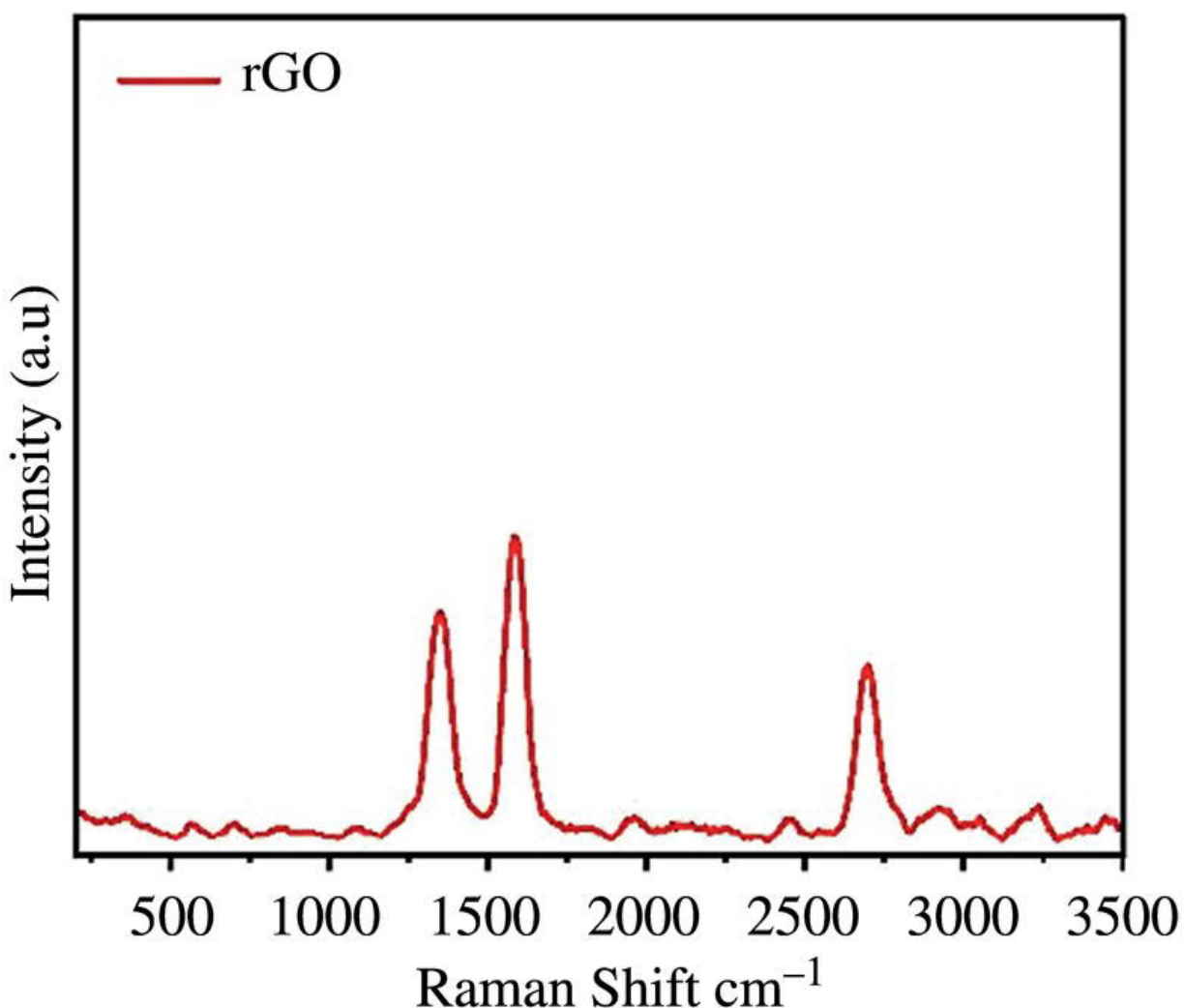


Figure 9.6 Raman spectra for the formation of rGO [2]/with permission of IOP Publishing Ltd.

9.5 Fourier Transform Infrared (FTIR) Spectroscopy

9.5.1 Brief Overview

FTIR spectroscopy is an analytical characterization technique widely used to identify organic and inorganic material for its competence to provide detailed molecular information. It measures the absorption of infrared radiation from samples, producing a unique spectral identification that indicates their molecular composition and structure. Its high sensitivity and rapid data acquisition make FTIR spectroscopy essential for advancing biomedical research and diagnostics ([Figure 9.7](#)).

9.5.2 Sampling Techniques in FTIR

There are some sampling techniques in FTIR.

1. Attenuated total reflectance: This is a simple sampling method for FTIR analysis. In ATR, the liquid and gaseous samples don't require a sample preparation procedure. When the IR beam is focused on a crystal of refractive index, which is high at a specific angle (45°), the sample interacts with the beam after it reflects off the crystal and captures the alteration in the reflected beam. It is used to examine a wide range of solids and liquids, including paints, elastics, rubbers, or coatings.

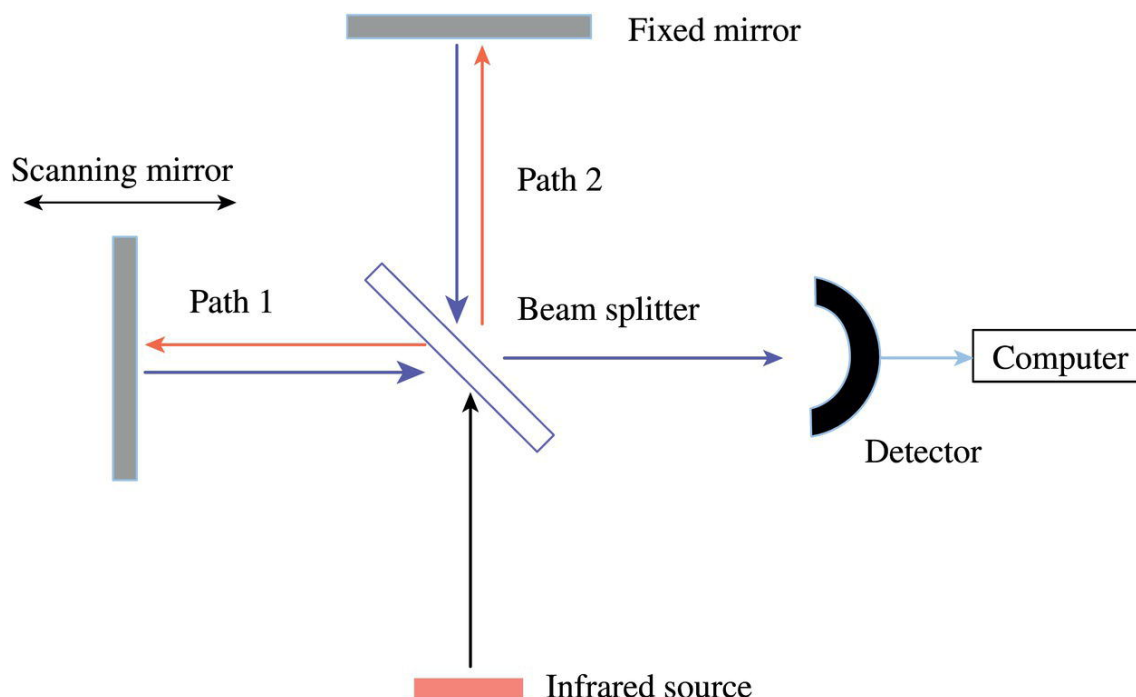


Figure 9.7 Brief overview of FTIR spectroscopy.

2. **Specular reflectance:** In specular reflectance spectroscopy, an IR beam is reflected directly off the sample surface at an angle that causes specular, or solitary and direct, reflection. It is mostly employed to assess smooth and flat surfaces such as coatings, thin films, or contaminated metal surfaces.
3. **Transmission:** The transmission FTIR is mainly used to assess solids, liquids, and gasses. The IR beam directly penetrates gas, liquid, or solid test samples, and a detector determines the sample's composition by observing the spectrum after the beam passes through the sample. It is specifically used for very thin samples [3].

9.5.3 Sample Preparation

Depending on the type of sample, like solid, liquid, or gas, and the sampling technique, multiple steps are required to prepare a sample for FTIR spectroscopy. An overview of sample preparation for FTIR analysis is provided here ([Figure 9.8](#)).

9.5.3.1 Solid Samples (Powders and Thin Films)

1. Finely grind the solid sample utilizing a mortar and pestle.
2. To make a pellet, blend a small amount (5–10 mg) of the powdered sample with KBr because of its transparency in the mid-IR region.

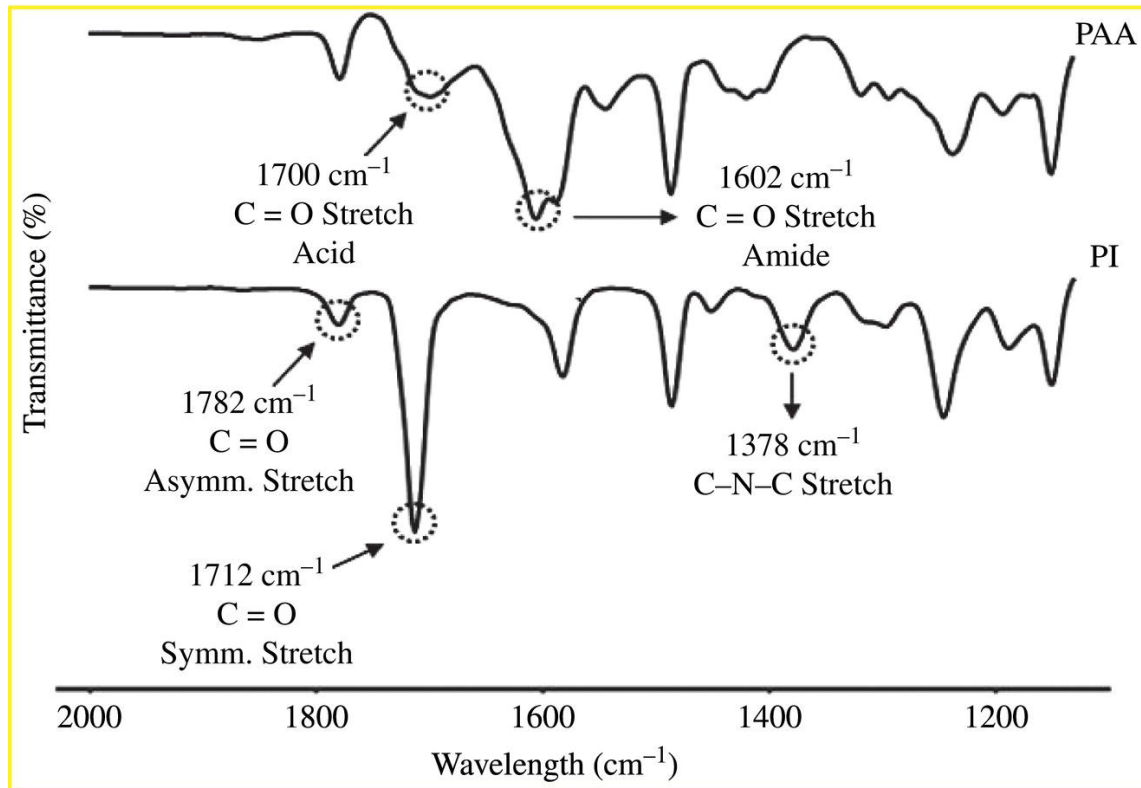


Figure 9.8 FTIR spectra of polyimide films.

3. Transfer the mixture to the die and press to form a KBr pellet.
4. The disk is subsequently put through a transmission mode analysis.

9.5.3.2 Liquid Samples

1. Put a few drops of the liquid sample between two liquid cell windows that are transparent to infrared light.
2. Slowly press the windows to produce a consistent, thin liquid film.
3. Add the liquid cell within the sample holder of the FTIR spectrometer.

9.5.3.3 Gaseous Sample

1. The sample gas is introduced into the gas cell. The cell should have windows that are transparent to infrared light.
2. Adjust the cell's path length according to the concentration of the gas and the desired sensitivity.
3. Insert the gas cell into the FTIR spectrometer sample holder.

9.5.4 Interpretation of FTIR

The chemical bond vibration energy depends on the chemical bond type (C-C, C-H, N-H, C=O) and the mode of vibration (stretching, bending). Most IR devices measure mid-IR absorbance of wavelength in the range of $4000\text{--}200\text{ cm}^{-1}$, which is shown in [Table 9.1](#). Organic and inorganic samples reveal the most important spectral regions within the fingerprint region, ranging from 1450 to 600 cm^{-1} and $1700\text{--}1500\text{ cm}^{-1}$. Stretching vibrations of C-H, N-H, and O-H bonds are typically associated with the higher wavenumber region ([Table 9.2](#)). Conversely, bending vibrations are usually observed in the lower wavenumber region [\[4\]](#).

[Table 9.1](#) IR regions and respective spectra.

Regions	Wavelength (μm)	Wave number (cm^{-1})
Near IR region	0.78–2.5	13 000–4000
Mid IR region	2.5–50	4000–200
Far IR region	50–1000	200–10

Table 9.2 Functional groups and respective frequency ranges.

S. No.	Molecules	Wavenumber (cm ⁻¹)
1	C=O	1725–1705
2	COOH	1730–1700
3	COOR	1750–1730
4	CONH ₂	1670–1640
5	O-H	3200–3600
6	N-H	3550–3060
7	C–H	3000–2850
8	C-N	1250–1000
9	C=C	1630
10	C–C	2150–2100
11	C–Cl	800–600
12	N=O	1550 and 1350

9.5.5 Conclusion

This chapter used Raman, FTIR, and UV-Vis spectroscopy to characterize the sample materials comprehensively. Raman spectroscopy revealed significant peaks at specific wavenumbers, indicating the presence of D and G peaks. FTIR is a versatile technique for the analysis of different functional groups present in solid, liquid, and gaseous samples. FTIR spectroscopy confirmed the findings with absorption bands at different wavenumbers, corresponding to functional groups present. UV-Vis spectroscopy provided further insights, showing distinct absorbance peaks at specific wavelengths.

References

- 1 Kumar, P.S. and Goel, S. (2021). First report on graphene oxide free, ultrafast fabrication of reduced graphene oxide on paper via visible light laser irradiation. *Diamond Relat. Mater.* 120: 108680. <https://doi.org/10.1016/J.DIAMOND.2021.108680>.

- 2 Nishchitha, N.K., Kumar, P.S., and Goel, S. (2023). Laser-induced in situ synthesis of nano-composite co-Co₃O₄-rGO on paper: miniaturized biosensor for alkaline phosphatase detection. *Nanotechnology* 34 (29): 295502. <https://doi.org/10.1088/1361-6528/ACCC36>.
- 3 Abidi, N. (2021). Introduction to FTIR microspectroscopy. In: *FTIR Microspectroscopy* (ed. N. Abidi), 1–12. Springer International Publishing https://doi.org/10.1007/978-3-030-84426-4_1.
- 4 Petit, T. (2018). FTIR spectroscopy of nanodiamonds: methods and interpretation. *Diamond Relat. Mater.* 89: 52–66.
- 5 Sundaraganesan, N., Ilakiamani, S., Saleem, H. et al. (2005). FT-Raman and FT-IR spectra, vibrational assignments and density functional studies of 5-bromo-2-nitropyridine. *Spectrochim Acta A Mol Biomol Spectrosc.* 61: 2995–3001. <https://doi.org/10.1016/j.saa.2004.9.016>.
- 6 Vibration Position (cm⁻¹) Intensity* Notes Alkanes, n.d.

Note

* Equally Contributing Author.

10

Microfluidic Devices

Abhishesh Pal^{1,3}, Pavar Sai Kumar^{3*}, Sreerama Amrutha Lahari^{3*}, Sonal Fande^{2,3*}, Abhishek Kumar^{3*}, Manish Bhaiyya³, Sohan Dudala³, R.N. Ponnalagu³, Satish Kumar Dubey^{1,3}, and Sanket Goel³*

¹ Department of Mechanical Engineering, Birla Institute of Technology and Science (BITS) Pilani, Hyderabad Campus, Hyderabad, Telangana, India

² Department of Pharmacy, Birla Institute of Technology and Science (BITS) Pilani, Hyderabad Campus, Hyderabad, Telangana, India

³ MEMS, Microfluidics and Nanoelectronics (MMNE) Lab, Department of Electrical and Electronics Engineering, Birla Institute of Technology and Science (BITS) Pilani, Hyderabad Campus, Hyderabad, Telangana, India

10.1 Electrochemical Detection of Bacteria, Biomarkers, Biochemical, and Environmental Pollutants

10.1.1 Introduction

An electrochemical sensor is the most robust sensor utilized in analytical chemistry, in which a particular sensing element reacts with a target analyte to give a sensing signal [1]. A specialized transducer transforms this signal into a recognized electrical signal proportional to the concentration of the target analyte, enabling qualitative or quantitative analysis, shown in Fig. 10.1. The two components that make up most of an electrochemical sensor are a transducer and a solidified sensing element [2].

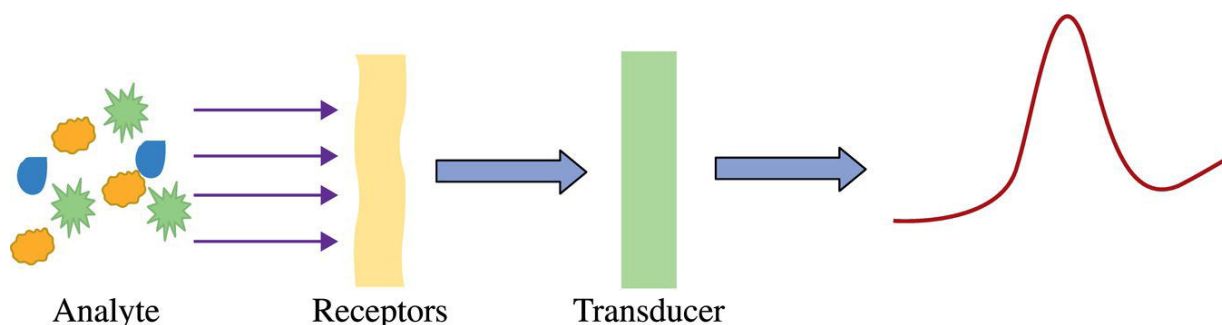


Figure 10.1 Working principle of an electrochemical sensor.

The electrochemical sensor consists of two- and three-electrode systems used for the detection of analytes of interest. Two electrodes include working and counter electrodes (CEs): for three electrodes, system reference, working, and counter. These electrodes must be in contact with one another via either an external electric circuit or an electrolyte [2]. A two-electrode sensor has many drawbacks, such as higher concentrations causing the sensor to conduct more current and experiencing a voltage drop, which alters the sensor voltage. As a result, it is better to add a third electrode to the system as a reference electrode (RE). The REs provide constant potential and help rectify the sensor voltage, which is continually measured at the working electrode (WE) [2]. This three-electrode system overcomes the limitations of two-electrode and is widely used in electrochemical sensing. Again, integrating microfluidic with sensors paves the way for sensing applications.

Microfluidic devices are gaining more attention due to their wide range of applications in food safety, healthcare management, and environmental monitoring. Integrating microfluidic with electrochemical detection increases the overall sensitivity, portability, and automation and reduces the reagent volumes, aiding in miniaturization. This device mainly consists of microfluidic channels that control the fluid flow. The sample is injected into the microfluidic channel, and the WE is functionalized with nanomaterials that interact selectively with the target molecule. The binding of the analyte with target molecules leads to changes in electric current. This chapter gives an overview of the application of microfluidic electrochemical devices for detecting bacteria.

10.1.2 Experimental Section for Detection of Bacteria (*Escherichia coli* (*E. coli*))

10.1.2.1 Brief Overview

Electrochemical detection is a versatile and powerful technique widely used in biological applications due to its sensitivity, specificity, and rapid response. In detecting bacteria, electrochemical sensors, often functionalized with antibodies or peptides, provide rapid and accurate identification of pathogens such as *E. coli* and *Salmonella*, which are crucial for clinical diagnostics and food safety. For biomarkers, which are vital in diagnosing diseases and monitoring health, electrochemical methods like immunosensors and DNA sensors, enhanced with nanomaterials, offer high sensitivity.

10.1.2.2 Prerequisites

Windows 10/11 operating system, a minimum of 4 GB RAM, storage of 250 GB, and a licensed version of a computer-aided designing (CAD) tool.

10.1.2.3 Chemicals and Equipment

Bacterial culture, Luria Bertani (LB) media, glass slide, three-electrode system, alligator clips, potentiostat, Petri dish, laminar hood, vortex machine, incubator, CO₂ laser.

10.1.2.4 Procedure

Step 1: The three-electrode approach is fabricated using the screen-printing technique. Details for the electrode fabrication using three electrode substrates are given in [Chapter 7.2](#). The fabricated electrodes are shown in [Figure 10.2a](#).

Step 2: Fabricate microfluidic reservoir using soft lithography. Fabrication details for the microfluidic device using soft lithography are given in [Chapter 6](#). The fabricated microfluidic channel is shown in [Figure 10.2b](#).

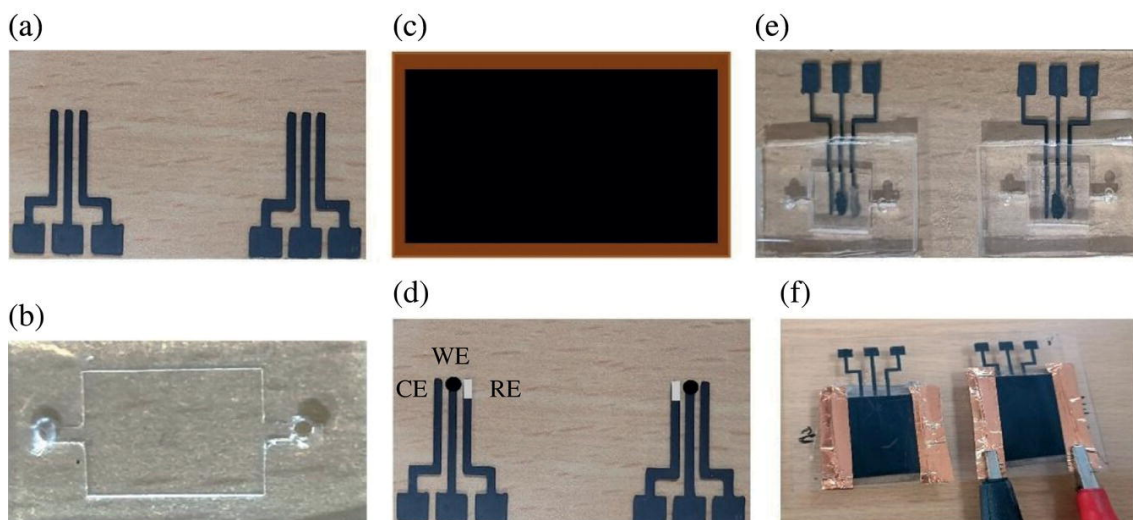


Figure 10.2 Stepwise fabrication process to develop an electro-microfluidic device for bacteria detection, (a) inkjet printed three electrode system; (b) PDMS stamp; (c) LIG heater; (d) modified RE, WE, and CE; (e) bonded microfluidic channels with three electrode system; and (f) LIG heater adhered to electrochemical sensor.

Step 3: Fabricate laser-induced graphene (LIG) heater using a CO₂ laser. The details of the fabrication of LIG are given in [Chapter 5.1](#). The fabricated LIG heater is shown in [Figure 10.2c](#).

Step 4: From the fabricated three electrodes, one was modified with Ag/AgCl to act as a RE, one with nanomaterial like gold or silver nanoparticles to act as a WE, and one kept as it acted as a CE. The modified electrodes are shown in [Figure 10.2d](#).

Step 5: Bond the microfluidic reservoir to the three-electrode system using plasma bonding. The bonded microfluidic channel with the electrode is shown in [Figure 10.2e](#).

Step 6: Paste the LIG heater on the backside of the microfluidic reservoir to incubate the bacteria culture, as shown in [Figure 10.2f](#).

Step 7: Prepare the bacterial culture by mixing 20 ml of LB broth with 200 μ l of *E. coli*.

Step 8: Inject the prepared bacterial culture into the microfluidic chamber.

Step 9: Alligator clips connect three electrodes to the electrochemical workstation.

Step 10: Perform the cyclic voltammetry to check the bacterial growth by applying a potential -1 to $+1$ with a scan rate of 0.05 V.

Step 11: The study is performed for 36 hours; check the response at intervals of 4 hours.

Step 12: The change in the current response with time signifies the bacteria's growth, as shown in [Figure 10.3](#).

10.1.3 Experimental Section for Detection of Biomarkers (Lactate)

10.1.3.1 Brief Overview

Applications of electrochemical sensors vary from lactate monitoring to detecting various biomarkers, gaining attention for their high sensitivity and rapid response. Enzyme-linked sensors in electrochemical detection measure biochemical interactions and concentrations, significantly contributing to personalized medicine by monitoring metabolic products. Integrating electrochemical sensors with microfluidic systems further enhances their functionality, allowing for more precise, real-time analysis in complex biological environments.

10.1.3.2 Prerequisites

Windows 10/11 operating system, a minimum of 4 GB RAM, storage of 250 GB, and a licensed version of CAD tool.

10.1.3.3 Chemicals and Equipment

Three-electrode system, alligator clips, potentiostat, lactate, lactate oxidase, phosphate buffer saline (PBS), ferri/ferro cyanide solution [$K_3Fe(CN)_6$], KCl, 1-Ethyl-3-(3-dimethyl aminopropyl) carbodiimide (EDC), carbon ink, polyimide sheet and N-hydroxy succinimide (NHS), inkjet printer.

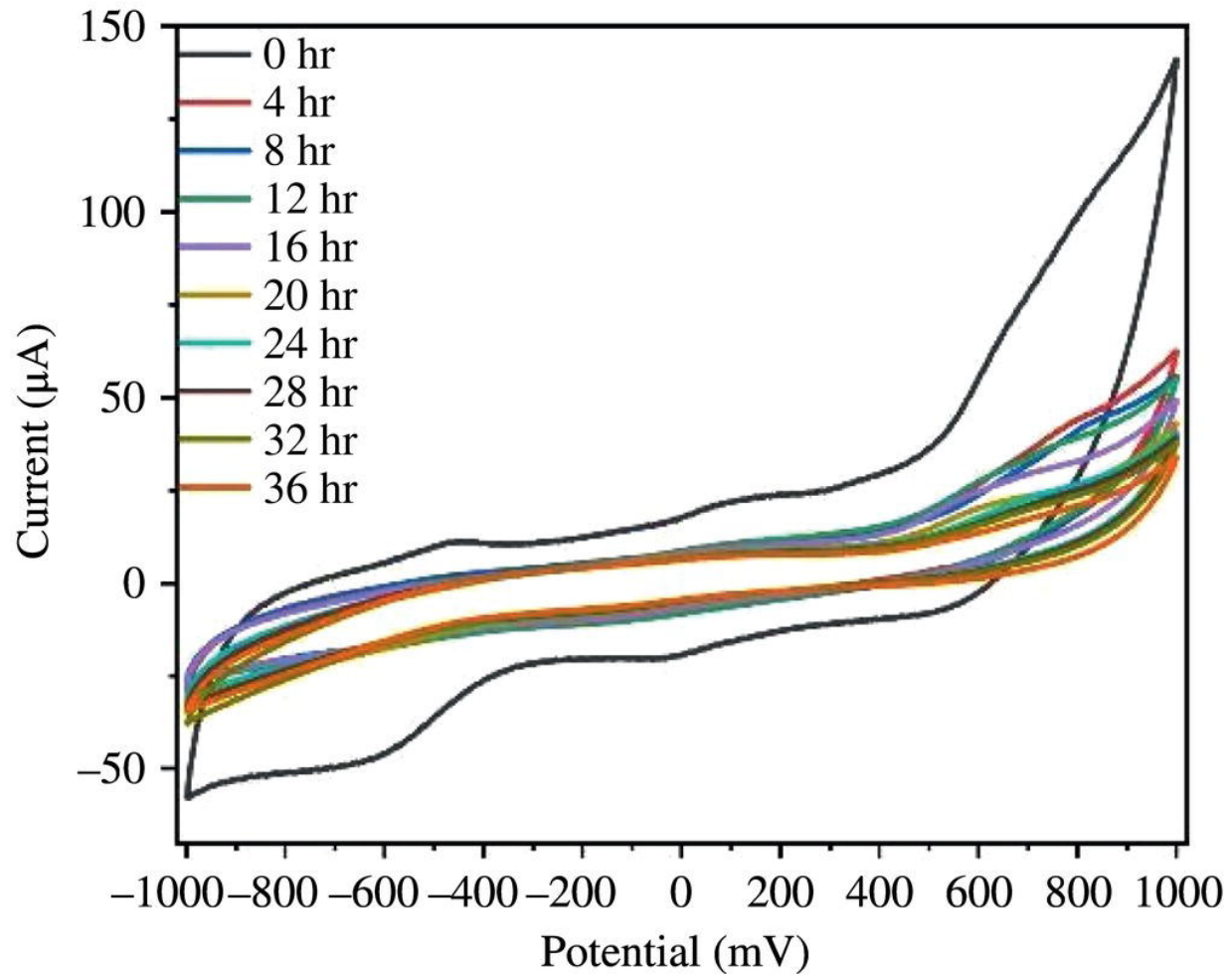


Figure 10.3 Electrochemical response from cyclic voltammetry study for bacterial growth for 36 hrs conducted over a potential range of -1 V to $+1\text{ V}$ at a scan rate of 0.05 V/s .

Source: [2]/with permission of ELSEVIER.

10.1.3.4 Procedure

Step 1: Fabricate the three-electrode system using the inkjet printing technique. Details for the electrode fabrication using three electrode substrates are given in [Chapter 7.1](#).

Step 2: Fabricate microfluidic reservoir using soft lithography. Fabrication details for the microfluidic device using soft lithography are given in [Chapter 6](#) ([Figure 10.4a](#)).

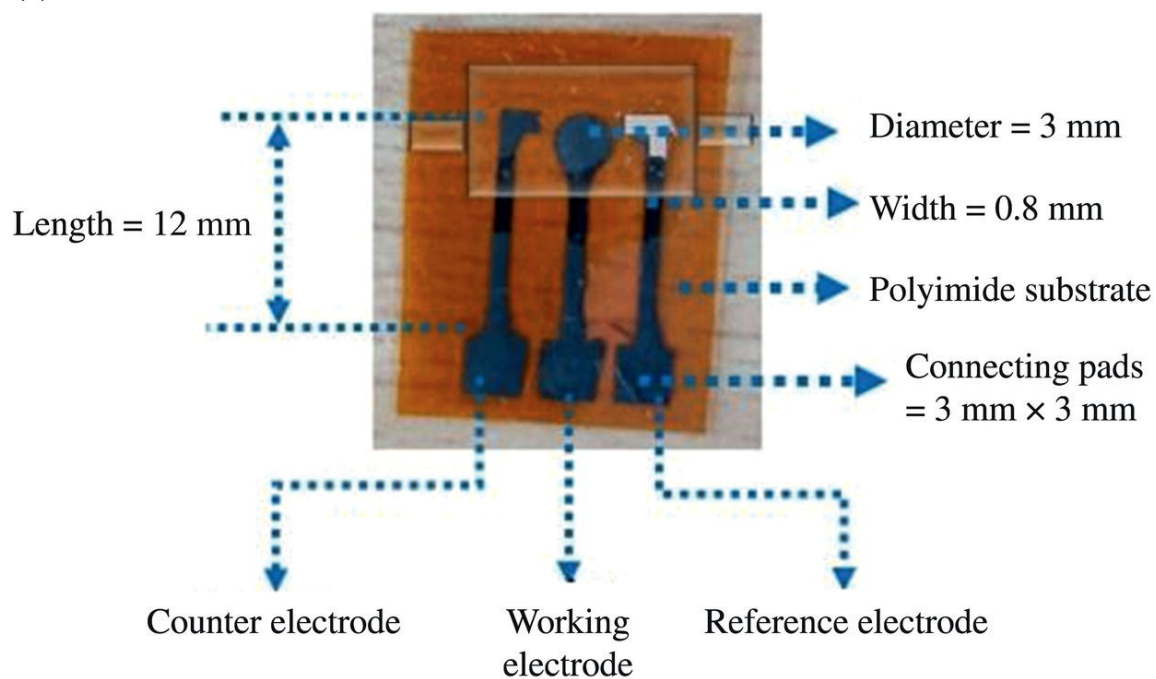
Step 3: From three electrodes, one was modified with Ag/AgCl to act as a RE, one with nanomaterial to act as a WE, and one

kept as it acted as a CE.

Step 4: EDC/NHS crosslinking immobilizes the lactate oxidase enzyme over the WE.

Step 5: Bond the microfluidic reservoir with the three-electrode system using an irreversible epoxy-thiol click reaction.

(a)



(b)

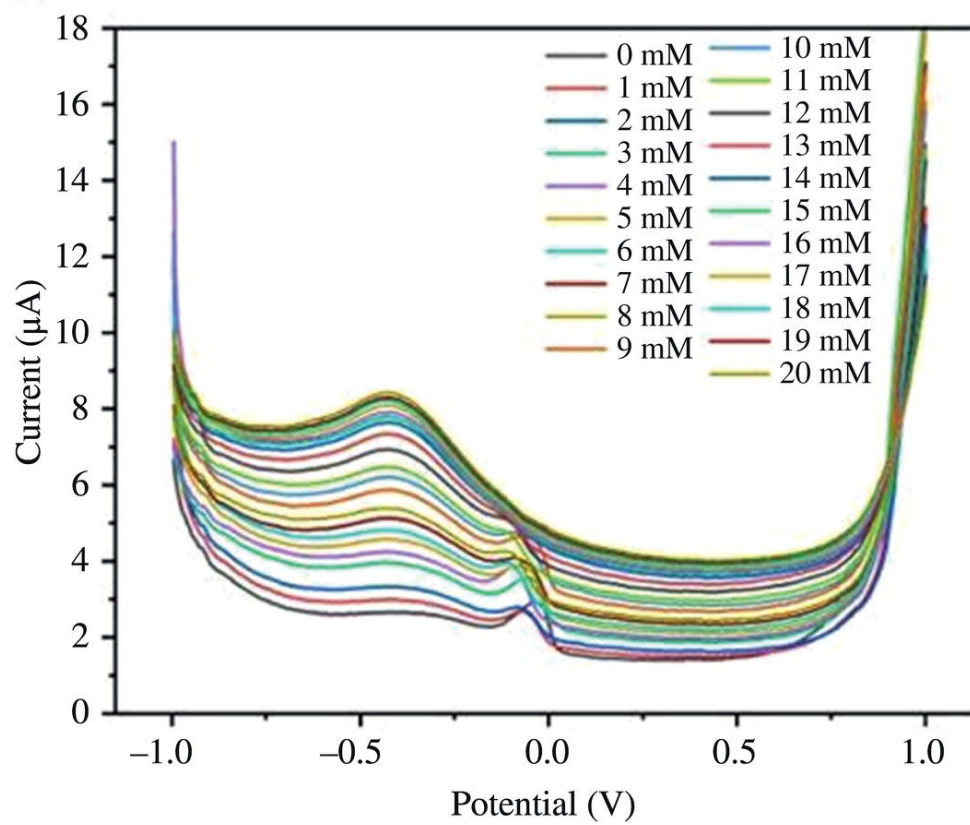


Figure 10.4 (a) A microfluidic-based device developed for lactate detection containing a working reference and counter electrode; (b) the electrochemical differential pulse voltammetry response obtained for lactate concentration effect between the potential range of -1 to $+1$ V.

Step 6: Prepare different concentrations of lactate solution in the range of 1 – 20 mM.

Step 7: Inject the lactate solution of different concentrations into the microfluidic channel.

Step 8: Alligator clips connect three electrodes to the electrochemical workstation.

Step 9: Perform the electrochemical differential pulse voltammetry to check the binding of lactate enzyme with lactate by applying a potential specified voltage with an optimized scan rate.

Step 10: Check for lactate. The increase in the current response concerning concentration signifies the detection of lactate, shown in [Figure 10.4b](#).

10.1.4 Experimental Section for Detection of Biochemical Analyte

10.1.4.1 Brief Overview

Electrochemical sensors are used to measure the interactions and concentrations of various substances, such as enzymes, hormones, and small molecules when detecting biochemicals. These sensors, often enzyme-linked, play a crucial role in monitoring metabolic processes, contributing significantly to personalized medicine. For instance, they enable the detection of neurotransmitters for neurological research and the monitoring of glucose levels in diabetes management. This synergy holds great promise for advancing diagnostic technologies and improving health outcomes.

10.1.4.2 Prerequisites

Three-electrode system, alligator clips, potentiostat, PBS, ferri/ferrocyanide solution [$\text{K}_3\text{Fe}(\text{CN})_6$], KCl, paper substrate, dopamine, uric acid, and ascorbic acid.

10.1.4.3 Procedure

[Fig. 10.5](#) show the step-by-step process to perform a general electrochemical detection of biochemicals.

Step 1: The device is developed by synthesizing reduced graphene oxide (rGO) and fabrication of three electrode designs on a paper substrate utilizing a blue laser, as stated in [Chapter 5.2](#).

Step 2: Prepare biochemical analytes like dopamine, uric acid, and ascorbic acid for the required concentration.

Step 3: Drop the prepared solution on the electrode surface and perform the cyclic voltammetry to check the change in peak current.

Step 4: Then, perform the concentration effect and scan rate effect using cyclic voltammetry, pH effect, and interference effect of another bio analyte.

Figure 10.5 Schematic of fabricated three-electrode system (a) LrGO three-electrode system; (b) CV responses of dopamine, uric acid, and ascorbic acid.

Source: [3]/with permission of IEEE.

10.1.4.4 Discussion

The rGO is synthesized on Whatman filter paper and is used for quantifying the biochemical analyte, namely dopamine, uric acid, and ascorbic acid. Each biochemical analyte reacts with the electrode at a specific potential when cyclic voltammetry is performed, and the current values change with the increase in the quantity of biochemical analyte.

10.1.5 Experimental Section for Detection of Environmental Pollutants

10.1.5.1 Brief Overview

Environmental pollutants, including heavy metals and pesticides, are detected using modified electrochemical sensors that ensure high selectivity and sensitivity. These sensors are essential for real-time monitoring of pollutants in water, soil, and air, aiding environmental protection and regulatory compliance. Although challenges like sensor stability and commercialization problems, ongoing research in advanced materials and nanotechnology aims to enhance sensor performance. Integrating electrochemical sensors with wireless communication underscores the significant impact of electrochemical detection in environmental monitoring and safety.

10.1.5.2 Prerequisites

Three-electrode system, alligator clips, potentiostat, PBS, ferri/ferro cyanide solution [$K_3Fe(CN)_6$], KCl, polyimide, fluorine, heavy metal.

10.1.5.3 Procedure

Following is the step-by-step process to perform a general electrochemical detection of environmental pollutants.

Step 1: The device is developed by synthesizing LIG and fabrication of an electrode design on a polyamide sheet utilizing a CO₂ laser, as stated in [Chapter 5.1](#).

Step 2: Prepare environmental pollutant analytes like fluorine of required concentrations from 5 to 130 μM or any different ranges of concentrations.

Step 3: Drop the prepared solution on the electrode surface and perform cyclic voltammetry to check the change in peak current.

Step 4: Then, perform the concentration effect, scan rate effect using cyclic voltammetry, pH effect, and interference effect of other environmental pollutants.

Step 5: Once the sensor is calibrated for various concentrations of fluorine using cyclic voltammetry and found free from interference, take the real sample of the environmental pollutant (naturally existing sources like wastewater) and perform the testing to know the concentration of the pollutant, shown in [Fig. 10.6](#).

10.1.6 Conclusion

This chapter focused on the application of microfluidic devices in the electrochemical detection of bacteria, biomarkers, environmental pollutants, and biochemicals. This chapter provides a stepwise procedure for fabricating microfluidic devices for different applications of electrochemical detection.

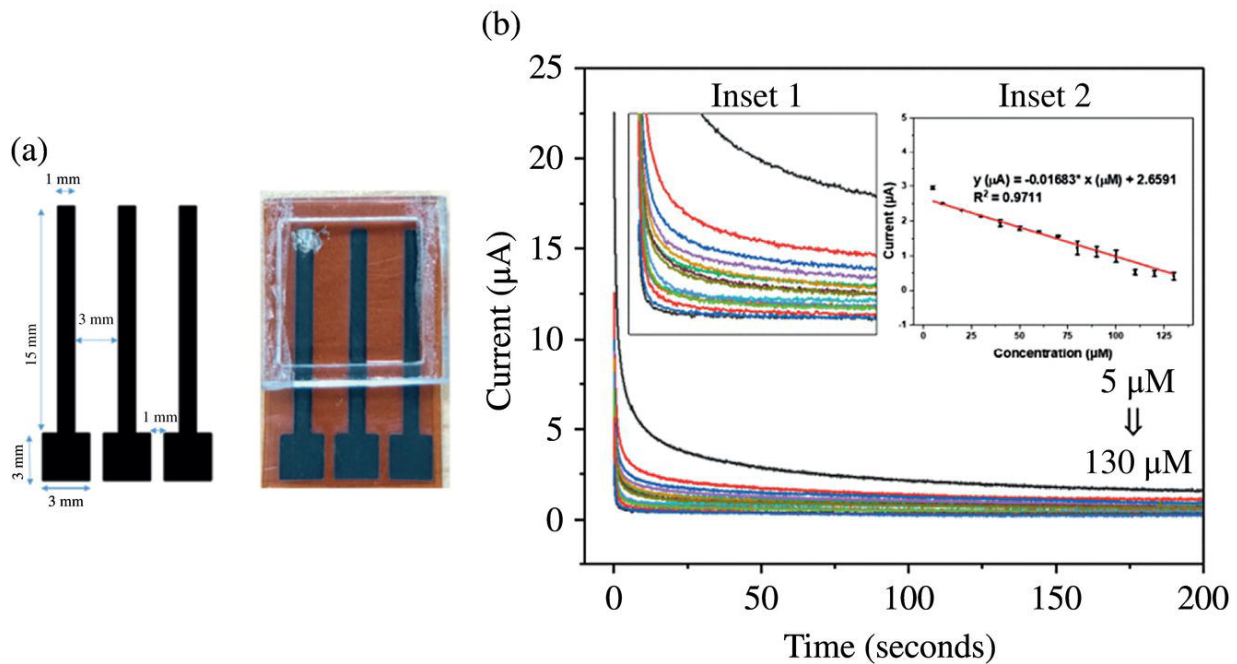


Figure 10.6 Fabrication of LIG-based electrochemical sensor for detecting (a) Fluoride ions; (b) Concentration effect of fluorine.

Source: [4]/with permission of IEEE.

10.2 Microfluidics Integrated Electrochemiluminescence System for Hydrogen Peroxide Detection

10.2.1 Introduction

Electrochemiluminescence (ECL) is a light emission phenomenon extensively employed to quantify various essential analytes. It has attracted attention from both industrial and academic-focused research. ECL is electrogenerated chemiluminescence, in which the excitation of luminophore species propagates light emission due to an electrochemical stimulus in reaction to an applied electric voltage on the electrode surface [5]. The ECL process involves the generation of redox-active luminous species initiated by the electrochemical high-energy transfer of electrons at the surface of the electrode. This technique provides promising features such as functionalities to amplify the emission signal and ultrasensitive quantification of

proteins, toxins, hormones, and enzymes in the (<pM) range. It also has unique features such as low background signal, user controllability, miniaturization, wide dynamic linear range, and ultrasensitivity. It has been found to be applicable in biological assays, environmental monitoring, genotoxicity assessment, life science research, water quality, and soil quality monitoring. It has shown its potential in rapid and multiplexing sensing of various analytes. ECL systems are of two types: (i) bipolar electrode systems and (ii) single electrode systems. The bipolar electrode system is defined as the ECL system, which consists of an electrode whose poles act separately as an anode and cathode. The bipolar electrode system is further classified into two subparts: (i) open bipolar electrode system and (ii) closed bipolar electrode system. The open bipolar electrode (OBE) electrochemiluminescence (ECL) system, also known as the OBE-ECL system, is one that consists of a bipolar electrode and two potential driving electrodes, which are covered together in an electrolyte compartment. In contrast, in a closed bipolar electrode (CBE) electrochemiluminescence system (ECL) system, also known as a CBE-ECL system, both the electrode poles of the bipolar electrode are bridged separately in a supporting and reporting channel. In single electrode ECL system configuration, two driving electrodes (cathode and anode) are immersed in the same compartment instead of using an additional bipolar electrode. [Figure 10.7](#) illustrates the types of electrode configurations in the ECL process.

ECL mechanisms leverage two major reagents: (i) luminol and (ii) ruthenium, and their co-reactant are hydrogen peroxide (H_2O_2) and tripropylamine (TPrA), respectively. When an electric potential is applied, the Luminol/ H_2O_2 and Ruthenium/TPrA ECL systems emit blue and red photons over the electrode surface, respectively. [Figure 10.8](#) highlights visual images of the emitted ECL signal over a bipolar ECL electrode system.

To fabricate ECL biosensing platforms, several approaches have been developed based on substrate materials (polyimide, copper, paper, and cloth, etc.), micro channel designs (single electrode, open bipolar electrode, and closed bipolar electrode), and electrode fabrication (printed circuit board [PCB], screen printing, LIG, 3D

printing, inkjet printing, and rGO). ECL methods provide flexibility and miniaturization capabilities that do not require sophisticated and expensive signal acquisition apparatus for other photoluminescent methods [6]. The ECL-based sensing approach has received widespread attention for clinical diagnosis, bioanalytical applications, and pharmaceutical analysis. These unique characteristics show ECL methods as the potential for rapid point-of-care (PoC) detection of various biomolecules and fabricating rapid, low-cost samples to answer platforms that can bridge the gap between patient and healthcare management.

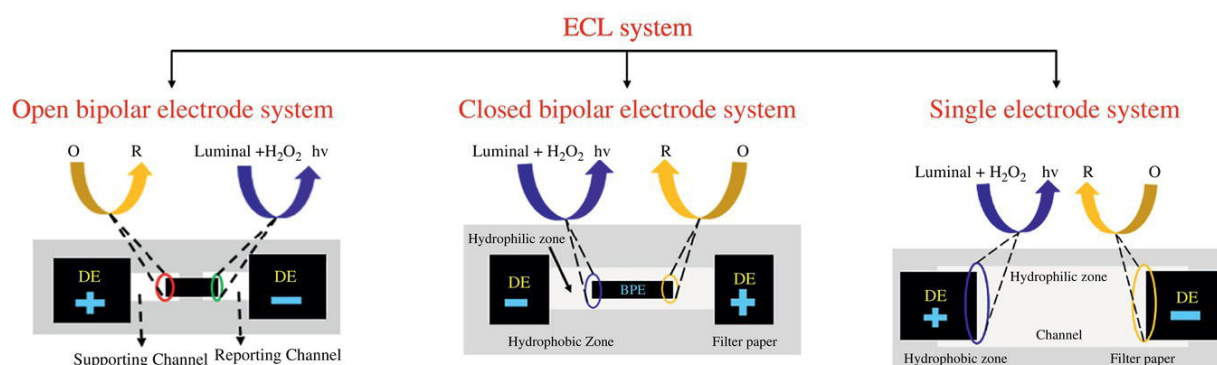


Figure 10.7 Types of electrode configurations in the ECL process.

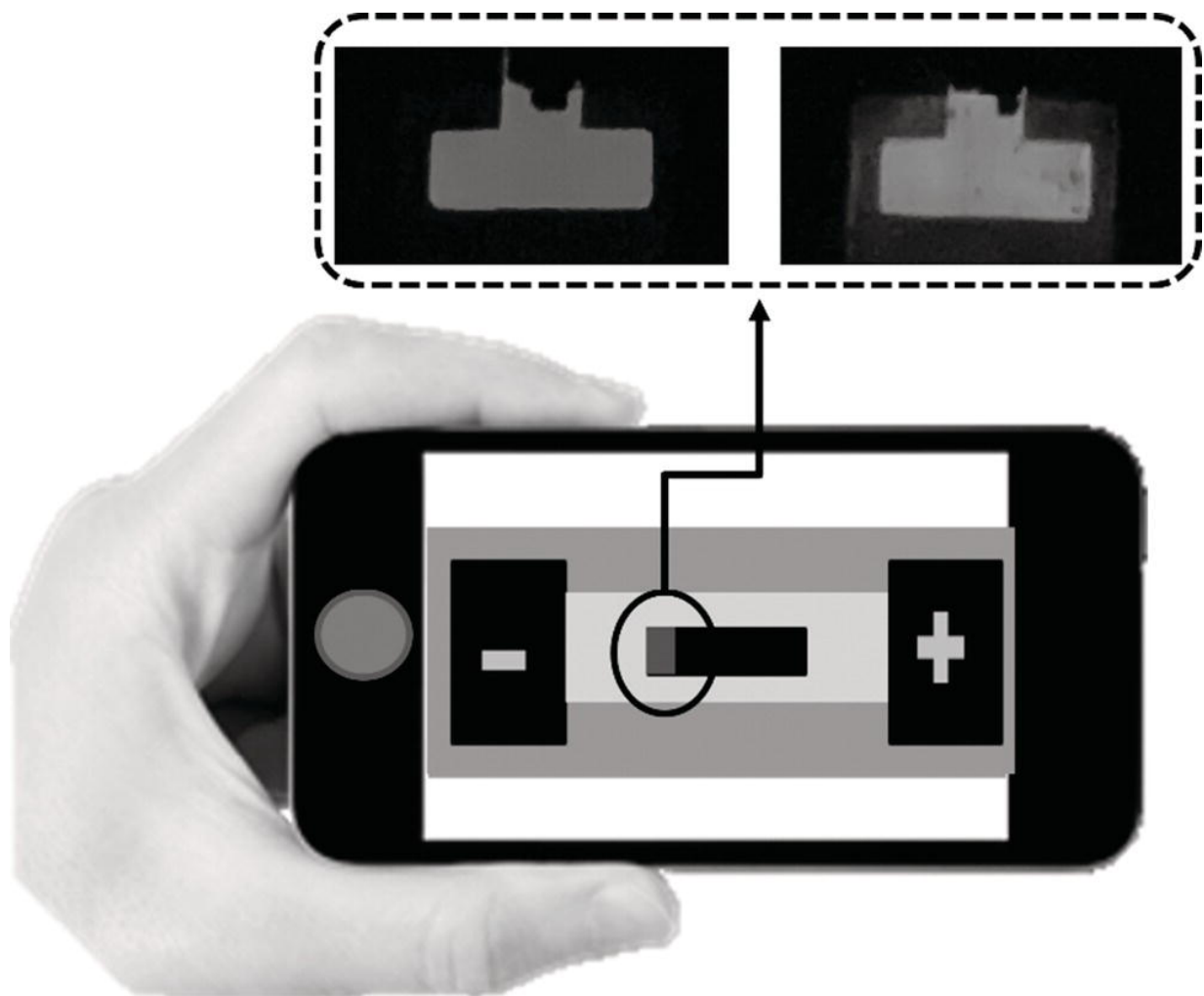


Figure 10.8 Visual image of the emitted ECL signal over a bipolar ECL electrode system.

10.2.2 Experimental Section

10.2.2.1 Brief Overview

Detecting various human metabolites near the patient site has become crucial for the rapid and early detection of disease biomarkers. The development of medical device systems based on microfluidics coupled with ECL as the analytical technique can emerge as an important tool for accurately detecting various biomarkers. ECL can overcome the challenges of existing detection techniques, such as lack of portability, bulky system, and excitation source requirement due to inherited features of electrochemistry and photoluminescence. In the experimental section, the procedure of

carrying out the simple ECL detection using luminol and hydrogen peroxide methodology for the detection of hydrogen peroxide is highlighted.

10.2.2.2 Prerequisites

Microsoft Windows 10/11 operating system, a minimum of 4 GB RAM, storage of 250 GB, and a licensed version of CAD tool.

10.2.2.3 Materials and Instrumentation

ECL devices, DC-DC buck converter, pipette set (1–100 μ l, 100–1000 μ l), alligator clips, Luminol, and hydrogen peroxide.

10.2.2.4 General Electrochemiluminescence Process Luminol and Hydrogen Peroxide

Step 1: Preparation of ECL sensor with microfluidic well, primarily consisting of electrode pads (anode and cathode) by utilizing various fabrication techniques such as photolithography, 3D printing, LIG, or screen printing.

Step 2: Prepare luminol stock solution and hydrogen peroxide stock solution of 10 mM, respectively. Briefly, the luminol stock solution of 10 mM with 50 ml volume is prepared by dissolving 80 mg of luminol powder in 47 ml of DI water in 3 ml of 1 M NaOH base solution. Similarly, the hydrogen peroxide stock solution of 10 mM concentration with 50 ml volume is prepared by dissolving 50 μ l of concentrated hydrogen peroxide (30%) in 50 ml of DI water. Further, various concentrations of luminol and hydrogen peroxide can be prepared by diluting the stock solutions.

Step 3: The prepared solution must be pipetted carefully inside the microfluidic well of the ECL sensor in dark room conditions.

Step 4: The electric voltage of 5 V is applied to the ECL sensor using alligator clips from the DC-DC buck converter.

Step 5: The generated luminescence may be recorded using various photomultiplier tubes or smartphone cameras to

perform the detection of hydrogen peroxide concentration based on the emitted light intensity.

10.2.2.5 Precautions

1. The prepared solution should be handled carefully, and gloves should be worn while experimenting.
2. The ECL sensor should be cleaned properly by immersing it in 70% IPA before and after carrying out the experiment.
3. Light exposure should be avoided when recording the emitted signal.

10.2.3 Conclusion

Herein, a general procedure for generating ECL reactions has been highlighted for luminol and hydrogen peroxide chemistry. Using the luminol/hydrogen peroxide ECL system provides us with functionalities to detect analytes whose intermediates are hydrogen peroxides such as glucose, lactate, choline uric acid, etc.

10.3 Development of Microfluidic Chip for Colorimetric Analysis

10.3.1 Introduction

In spectrophotometry, the concentration of the analyte is measured by quantifying the absorption of light that takes place as it passes through a sample solution [7]. The quantification is based on Beer-Lambert's law, which states there is a linear relationship between the absorbance of light, the sample concentration of the absorbing substance, and the path length of the sample [8] (Fig. 10.9). It is mathematically expressed as:

$$A = \varepsilon * c * l \quad (10.1)$$

where A is the total absorbance of the light by the sample, ε is the molar absorptivity of the solution at a particular wavelength of the light, c is the concentration of the substance in the solution, and l is

the path length i.e., the distance in which the light and the solution interact. A microfluidic chip is used for the generation of the chromophore i.e., a substance absorbing at a wavelength can be used to quantify the concentration of the substance [9]. In a microfluidic chip, ϵ and l remain fixed, which helps us to find a correlation between the absorbance and the concentration.

In order to develop miniaturized devices, other approaches used include chromophore generation on paper-based substrates, the use of 3D printed microfluidic chips, the use of smartphones, and optoelectronics to quantify the color formation/generation. A polydimethylsiloxane PDMS-based microfluidic chip was chosen here to achieve miniaturization and chromophore generation.

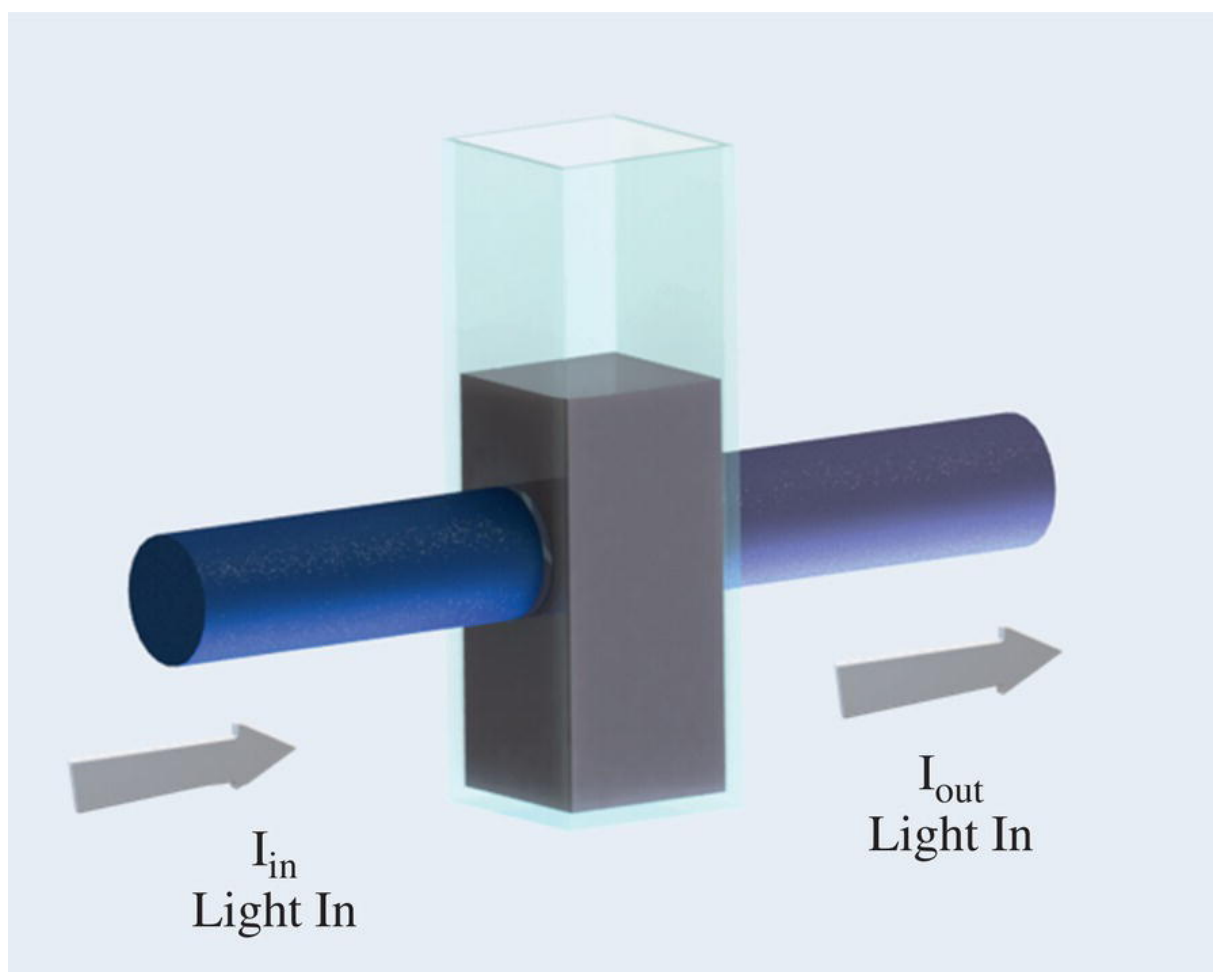


Figure 10.9 Illustrative diagram of reduction in the intensity (dark blue to light, color representation) of light exiting the fluid based on Beer-Lamberts law.

Polydimethylsiloxane (PDMS), a transparent polymer, is used to develop a microfluidic chip containing microchannels of width and height dimensions of 105 and 100 μm , respectively. A transmittance of up to 95% in the PDMS is observed, which is suitable for preparing a device for colorimetric quantification [10]. The typical configuration using a PDMS chip consists of a zone where chromophore is collected after the reaction, as shown in the [Figure 10.13](#).

10.3.2 Experimentation

10.3.2.1 Brief Overview

Microfluidics with colorimetry is crucial in various scientific and industrial applications because it can precisely manipulate small volumes of fluids and provide rapid, sensitive, and cost-effective analysis. This integration enhances the detection and quantification of chemical and biological substances by leveraging color changes in reaction to specific analytes. Applications include medical diagnostics, used for PoC testing such as glucose monitoring and pathogen detection; environmental monitoring for assessing water quality and detecting pollutants; and pharmaceuticals for drug development and quality control. The small sample volumes, reduced reagent consumption, and potential for automation make microfluidic colorimetry a powerful tool for high-throughput and real-time analysis.

10.3.2.2 Prerequisites

In order to develop a microfluidic chip, the experimentalist needs to have a polymer PDMS, silicone tubes of diameter 2 mm, photoresist SU-8, glass slide (75 mm \times 25 mm), and sodium carbonate and blunt needles. The required equipments are direct laser writing (DLW) machine (Holmarc, India) and a plasma cleaner (Femto Science). Sulfanilic Acid (Sulfanilamide), Naphthyl-ethylenediamine Dihydrochloride (NED), hydrochloric acid (HCl), orthophosphoric acid, and Milli-Q water.

10.3.2.3 Solution Preparation

Step 1: Prepared Griess reagent by taking 1.02 g of sulphanilamide (1% w/v) and 0.102 g of NED (0.1% w/v) in 102 ml of 5% orthophosphoric acid [11].

Step 2: Prepare a 1 mM solution of nitrite salt by taking 34.5 mg sodium nitrite in 500 ml Milli-Q water.

10.3.2.4 Software Required

The required software is AutoCAD to develop a pattern, and software interfaced with DLW machine such as LazyCAM, laser writing system, and Mach3Loader.

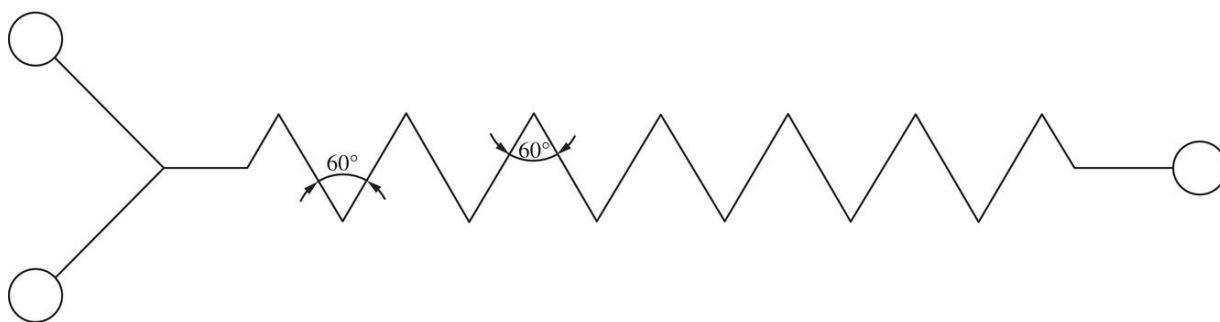


Figure 10.10 A zig-zag design to develop a photoresist using a direct laser writing tool with an angle of 60° for efficient mixing.

Designing the Microfluidic Chip

Step 1: Start AutoCAD software.

Step 2: Draw the outline of the microfluidic chip ([Fig. 10.10](#)).

Step 3: Take a glass slide of the dimensions 75 mm \times 25 mm. Use a dry film photoresist and laminate it over the glass slide using a laminator at a temperature of 110–120 $^\circ\text{C}$.

Step 4: Using the DLW machine, the photoresist will be exposed to monochromatic ultraviolet radiation. The DLW will ensure that the light passes only through the path defined by the design, as mentioned in step 2. The outcome will look similar to the [Figure 10.11a](#).

Step 5: The glass with the photoresist layer shall be taken out of the DLW machine. Take the slide and place the slide in a container having sodium carbonate solution. This solution is

prepared with 0.85% sodium carbonate (Sigma Aldrich) solution made in Milli-Q water.

Step 6: Shake the container in rotary motion to develop the photoresist, i.e., remove the photoresist that was not exposed to the UV radiation. The developed photoresist will appear like [Figures 10.11b](#) and 10.13a.

Step 7: Take the polymer, PDMS, and its curing agent in a w/w ratio of 10 : 1 and mix thoroughly.

Step 8: Eliminate all the gases and bubbles from the mixture by placing it in a desiccator and connecting a tube to a vacuum pump. This process can take 20–25 minutes.

Step 8: Pour the polymer, Polydimethylsiloxane (PDMS) on the developed mould as shown in [Figure 10.13b](#). The developed photoresist on the glass slide will act as a negative replica. Place it in an oven at 80 °C for 20 minutes. This will solidify the PDMS through polymerization so that we can obtain a clean and transparent microfluidic channel ([Fig. 10.12](#)).

Step 9: Peel off the PDMS from the glass slide by carefully cutting out the corners using a sharp blade. This will provide us with a PDMS chip, as shown in [Figure 10.13c](#).

Step 10: Punch a hole of diameter 2 mm using a blunt syringe in the PDMS chip to ensure the inlet and outlet for the fluid through the channel.

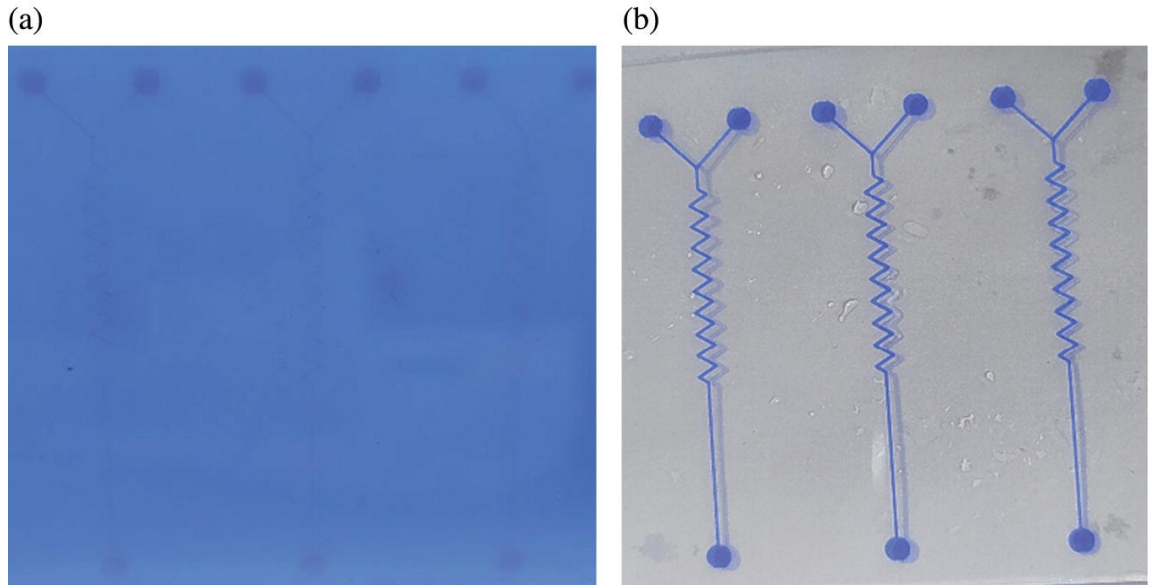


Figure 10.11 (a) UV exposed photoresist coated over a glass slide (b) post-development of the photoresist with 0.85% sodium carbonate solution in Milli-Q water.

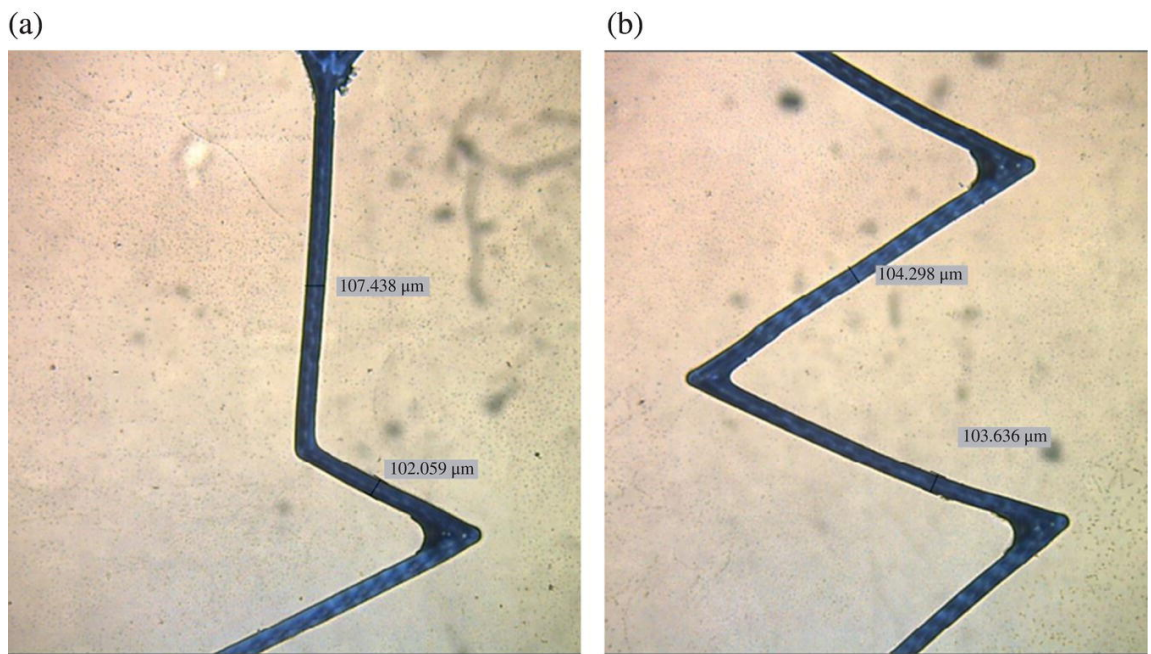


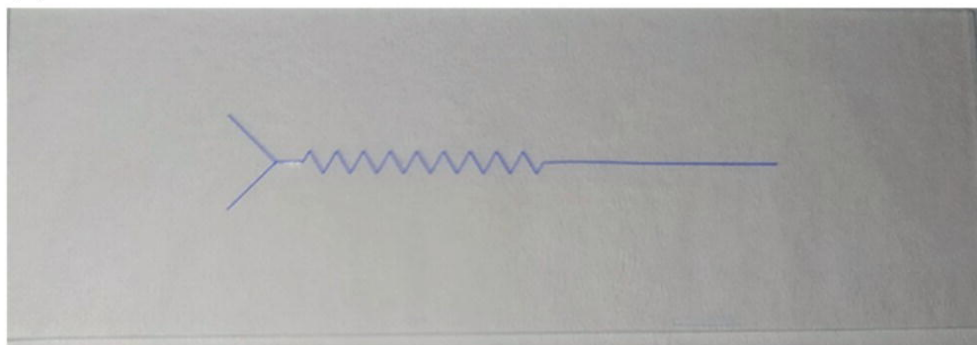
Figure 10.12 Measuring the dimensions of the developed photoresist at (a) start and (b) zig-zag sections for uniformity.

Step 11: To bond the microfluidic chip on a glass slide, expose oxygen plasma on both surfaces for 2 minutes. Place a chip on

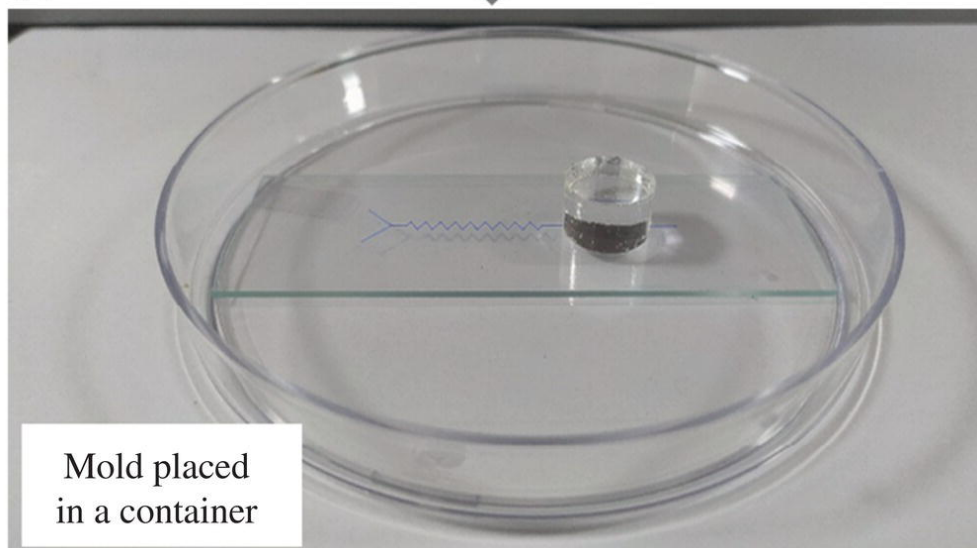
the glass to establish a strong bond. To further enhance this bond, keep it in the oven at 80 °C overnight.

Step 12: The silicone tubes of external diameter 2 mm can be attached to the punched holes to push the fluid through them to obtain mixing and, eventually chemical reaction to obtain a change in color.

(a)



(b)



(c)



Figure 10.13 Step-by-step bonding of glass and PDMS microchip to develop a microfluidic chip. (a) Developed photoresist on a glass substrate; (b) Mold formation with photoresist and cylindrical acrylic sheet of thickness 8 mm and diameter 10 mm, wherein the PDMS is to be poured to develop a microfluidic chip, and (c) bonded PDMS chip on the glass after exposing both surfaces with oxygen plasma.

10.3.3 Colorimetric Determination on Microfluidic Chip

The colorimetric reaction to determine nitrite on a microfluidic chip is given stepwise as follows:

Step 1: Prepare Griess reagent and 1 mM stock solution of sodium nitrite as given in [Section 2.2](#).

Step 2: In inlets 1 and 2 of the microfluidic chip, pass the above-mentioned solutions at a flow rate of 1 ml/min each.

Step 3: Quantify the intensity of color formation in the microfluidic chip in the container region by spectroscopic or image analysis methods.

Step 4: The characteristic peak for the detection of nitrite with the help of Griess reagent is obtained at the wavelength of 545 nm. This is the standard absorption peak for azo dye developed with the reaction of Griess reagent and nitrite.

Step 5: The intensity of the transmitted light can be correlated with the concentration of the nitrite. With higher concentration, the transmitted intensity is reduced, according to Beer and Lambert's law.

10.3.4 Conclusions

The chapter delves into the fundamentals of microfluidics and colorimetric testing methods, highlighting the principles and fabrication techniques essential for miniaturizing colorimetric sensing systems. It provides a comprehensive guide on developing PDMS microfluidic chips, detailing the fabrication steps using lithography and plasma bonding techniques. The Griess reagent-based nitrite detection method is presented as a case study, illustrating the process of colorimetric quantification.

10.4 Development of Disposable and Eco-Friendly μ PADs as Chemiluminescence Substrates

10.4.1 Introduction

Assays for targeted analyte quantifications in laboratories require bulky instrumentations and professional personnel to process the data. Assays are performed in various applications, including environmental pollutants, food pesticides, heavy metals, and biomarker detections [12]. Nevertheless, the laboratory tests hinder the right time diagnosis of the analytes, and the delay can lead to unwanted results [13, 14]. In contrast, the accelerated development of PoC devices allows the detection of analytes onsite at lowered sample resources, decreased processing times, and affordable testing costs. The advantageous properties of paper pads, paper substrates, or micro paper analytical devices (μ PADs) are known to be the best resources for PoC devices [15]. μ PADs gained interest due to their exceptional features, including lower cost, wider availabilities, eco-friendly disposability, and lower sample consumption [16].

The widely adopted lateral flow immunoassay (LFIA) tests leverage the nitrocellulose strips to perform the onsite tests [17]. The inherent capillary fluid transfer lets the reagents solubilize over the strip and allows the detection of the target analytes. Further, creating hydrophilic and hydrophobic zones on paper substrates allows fluid control. 3D printing, wax coating, and inkjet printing are commonly used methods for zone separations [18, 19]. Moreover, the recent progress in μ PAD utilization was reported in different detection methods, including chemiluminescence (CL), colorimetry, electrochemical, fluorescence, and surface-enhanced raman scatterings (SERS). However, the CL method's simplicity, sensitivity, reliability, and exceptional S/N ratio intensify as a critical detection methodology for most PoC devices [20, 21]. CL is an optical phenomenon based on the photon production initiated by chemical reactions [22].

This chapter provides insights on developing the 3D printed hydrophobic barriers on the paper pads to leverage in CL detections.

10.4.2 Real-Time Applications of This Study

Quynh et al. designed and developed a disposable paper-based biosensor for effective pathogen detection via a colorimetric approach [23]. Similarly, Noviana et al. highlight the importance of using paper analytical devices in clinical diagnostics, food analysis, and environmental testing. Moreover, it explains that using these devices promotes the progress of developing PoC diagnostic devices for onsite remote detections [24].

This chapter provides insights on developing the 3D printed hydrophobic barriers on the paper pads to leverage in CL detections.

10.4.3 Experimentation

10.4.3.1 Prerequisites

A 3D printer (Dreamer, Flashforge, China), polycaprolactone (PCL) 3D filaments, whatman grade 1 filter paper, double-sided adhesive tape to provide mechanical stiffness to the paper, Windows 10/above operating system with at least 4 GB of RAM and 250 GB of storage, and scientific oven to dry the printed paper substrates.

10.4.3.2 Software Installations

A licensed CAD software (Solidworks, in this case) and user-interfaced slicing tool of 3D printer (Flashprint in this case).

10.4.3.3 Design of Hydrophobic Barriers

Step 1: Open CAD software (Solidworks).

Step 2: Create a new sketch and draw the fluidic pattern shown in [Figure 10.14a](#) with the required dimensions.

Step 3: Exit the sketch and create an extruded length (z) of 0.3 mm, shown in [Figure 10.14b](#).

Step 4: Save the extruded file with the CAD extension for future iterations and save the file in STL format for 3D printing, as shown in [Figure 10.14b](#).

10.4.4 3D Printing of Hydrophobic Barriers

Step 1: Open the printer-specific slicing tool (Flashprint in this case).

Step 2: Import the saved STL file.

Step 3: Right-click on the file and select the respective left or right extruder.

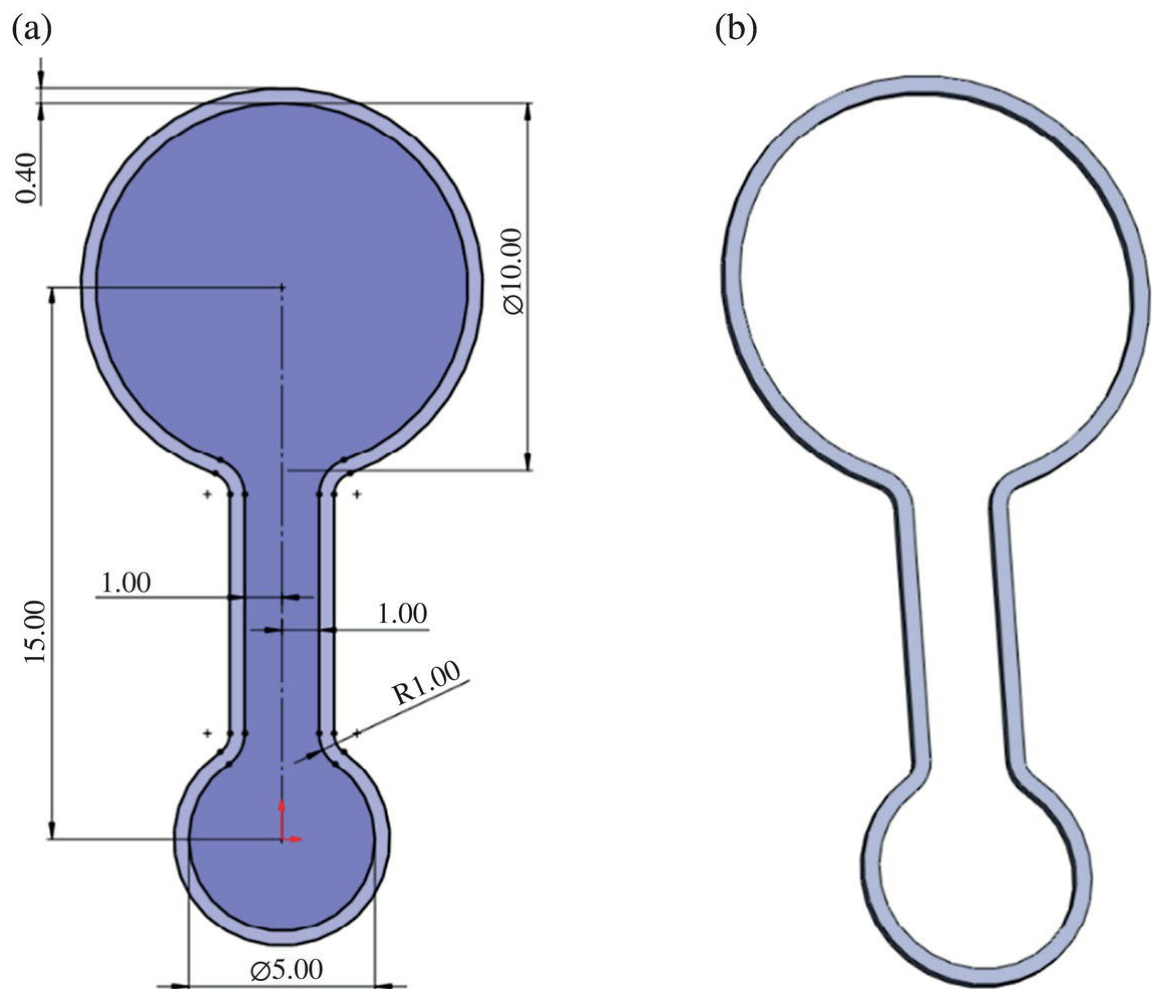


Figure 10.14 Design of hydrophobic barrier for fluidic flow (all dimensions are in mm), (a) 2D sketch with dimensions, and (b) 3D converted STL file.

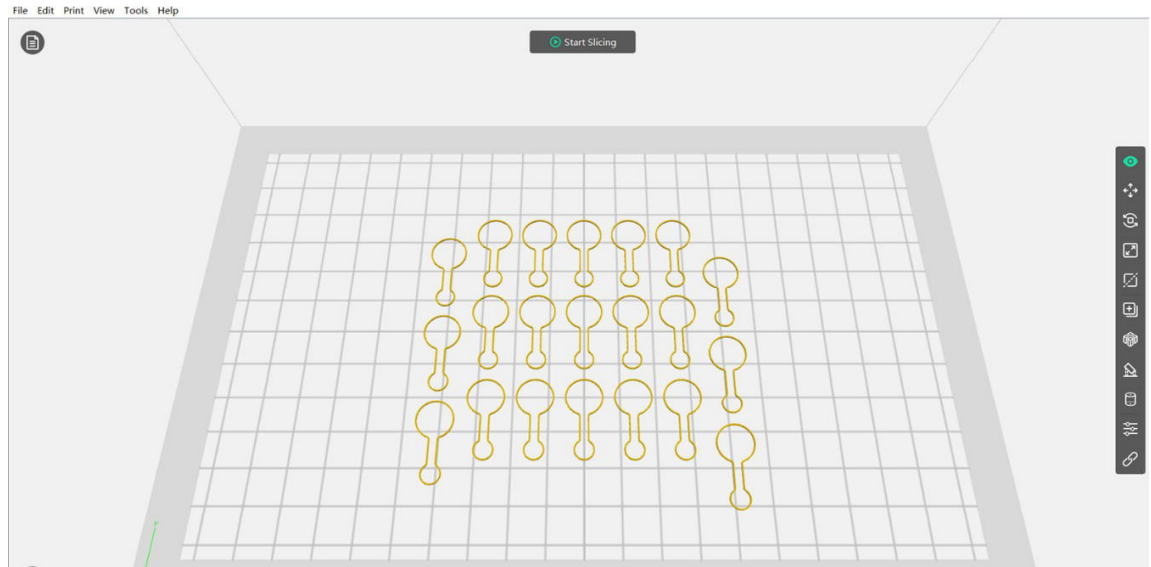


Figure 10.15 Overview of process steps to be followed in the slicing tool.

Step 4: Select the file and adjust the position using the provided toolbar at the right side window.

Step 5: Select the file and create copies by copying and pasting protocol, if needed, as shown in [Figure 10.15](#).

Step 6: Since the file does not require support, click on the start slicing option.

Step 7: In the slicing window, adjust the print extruder temperatures to 90 °C and bed temperature to 50 °C due to the usage of PCL filament. The adjustments entirely depend on the type of the filament.

Step 8: Print speed can be set to fine or can be left default.

Step 9: Select the infill density as 100%.

Step 10: Click slice to slice the file into a number of layers based on the layer resolutions set.

Step 11: Save the converted file and use it to load the same into the printer.

Step 12: Open the file in the printer and load the respective extruder with the required PCL filament into the printer.

Step 13: Place the paper substrate flat on the bed.

Step 14: Select the file and click start printing. Then, the printer reaches the set temperatures and starts printing.

Step 15: Remove the paper substrate after printing and repeat for multiple copies, as shown in [Figure 10.16](#).

Step 16: Switch off the printer after use.

Step 17: Collect the printed paper substrates and load them into the oven at 100 °C for 25 minutes so the wax content can sink into the paper, creating the hydrophobic zones.



[Figure 10.16](#) 3D printed hydrophobic barriers on paper. The traces are of PCL filament, and the region inside the traces would still be hydrophilic.

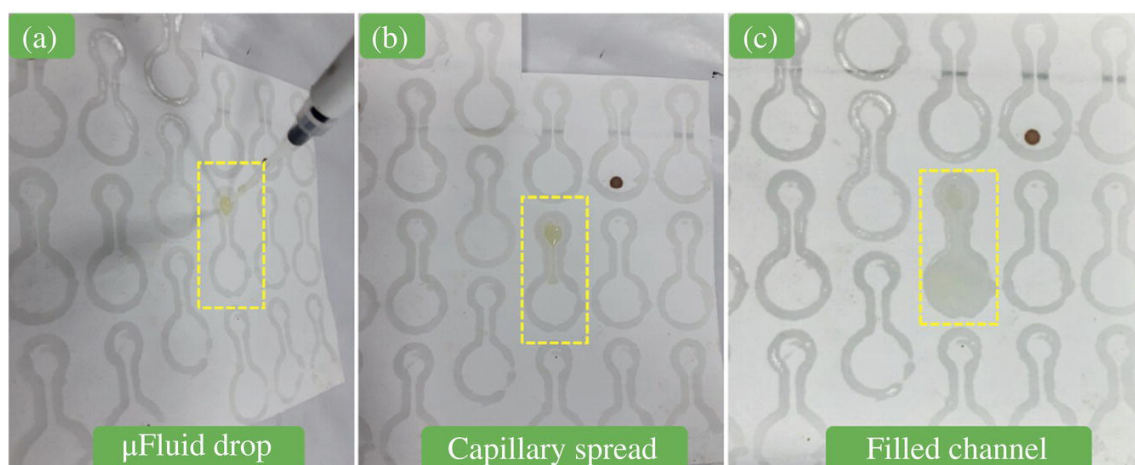


Figure 10.17 Real-time validation of fluid transport through the 3D printed PCL microfluidic channelled μ PADs, (a) initiating the fluid drop on μ PAD; (b) inherent capillary forces spread the fluid throughout the channel; and (c) the final reagent filled μ PAD.

Step 18: Repeat the steps for copies. The developed μ PADs can be leveraged in multiple applications with user-defined microfluidic channels and shapes, as shown in [Figure 10.17](#).

10.4.5 Conclusion

The hassle-free development of 3D-printed PCL hydrophobic barriers was provided to highlight the potential of μ PADs in PoC devices. The user-defined sketch can be printed on paper using the FDM-based PCL filament-loaded 3D printers. The developed patterns are loaded into the oven to sink the wax content into the paper, forming barriers for fluid flow. The provided process demonstrates a real-time fluid flow and can be leveraged for future applications.

10.5 Microfluidic Devices for Polymerase Chain Reaction (PCR)

10.5.1 Introduction

Polymerase chain reaction (PCR) is an extensively used molecular biology technique that allows for the amplification of nucleic acid sequences. Kary Mullis developed the reaction in 1983 and has since become an abundantly used tool in various biological applications, including forensics, genetic research, and medical diagnostics, amongst others. PCR is a thermally regulated process. It primarily consists of three steps – denaturation, annealing, and extension, typically at three different temperatures ranging from 55 to 95 °C, depending on the specific reactions.

The first step, denaturation, typically occurs in the range of 94–98 °C. The double-stranded DNA template, when heated to this temperature, separates or denatures, resulting in two single-stranded DNA molecules. The annealing step involves a reaction at a lowered temperature to allow short DNA primers to bind to the complementary sequences on each of the single-stranded DNA templates. Primers serve as starting points for DNA synthesis, providing a specific sequence for the DNA polymerase enzyme to initiate the synthesis of complementary strands. Typically, two primers (forward primer and reverse primer) for two separate strands are employed. The design of primers is an important task and depends on the sample to be identified and the required specificity. The temperature for the annealing step depends on the melting temperatures of primers and is often used as 5 °C lower than the melting temperature of primers. The final step in a PCR reaction is extension. For extension, the temperature is increased to around 70–78 °C in order to enable a DNA polymerase enzyme to synthesize a new strand of DNA complementary to the template strand, starting from the primers. This process extends the DNA sequence and results in the formation of a new double-stranded DNA molecule.

One cycle of PCR refers to a sequence of denaturation, annealing, and extension with varying times, which is often repeated, typically 20–40 times, exponentially amplifying the targeted DNA region of interest. Using the PCR technique, even extremely small quantities of DNA can be amplified to levels suitable for analysis and detection.

Conventionally, the PCR reaction requires a thermal cycler in addition to the reaction reagents. As the name suggests, a thermal cycler changes the temperature in a periodic and repetitive manner

(cycles). The reaction reagents are mixed in a microcentrifuge tube placed in the thermal cycler, and the heat block in the thermal cycler regulates the temperature in a cyclic fashion. The existing thermal cycler-based PCR is reliable and widely popular; however, is confined to laboratories. This is primarily challenging if the PCR reactions need to be applied to PoC diagnostics or forensic applications. This challenge can be addressed by making the entire setup portable and amenable to use with minimal skill involvement, and microfluidics offers a possible way.

In this section, a microfluidics-based device for PCR will be discussed. Unlike previous sections, where there is a set of steps that can provide the intended results, a multitude of different approaches can be utilized. Thus, this section discussing microfluidic devices for PCR will guide you toward developing the system and depends on you choosing an appropriate integration mechanism. In the conventional setup, the sample is exposed to varying cycles by changing the temperature. The important aspect is each of the processes in a cycle needs to be executed (i.e., the sample needs to be exposed to a certain temperature). Thus, the part of the reaction can occur. In a microfluidic device, the same is achieved by keeping the temperature in defined regions and moving the fluid through the microchannels.

10.5.2 Prerequisites

As described in the earlier chapters, understanding soft lithography and patterning processes is essential for successfully developing microfluidic channels for PCR applications. Experience with the use of cartridge heaters and temperature sensors (e.g., PT 100) is also essential. Peristaltic pumps/syringe pumps may be required based on the experiment's design. The required peripherals need not be particular, and suitable options for sensors, pumps, etc., may be used based on availability. This chapter section will utilize insights from previously published articles by Kulkarni et al. [[25](#), [26](#)] and Srikanth et al. [[27](#)].

10.5.3 Software Installations

A CAD software for developing patterns for DLW applications.

10.5.4 Design and Fabrication of Microfluidic Device

Step 1: Use suitable designing software to create a mold design for the channel, as shown in [Figure 10.18](#). The zones X, Y, and Z are indicative of lengths for respective processes and are dependent on the flow rate and reaction parameters. For instance, at a constant flow rate, the time for the exposure to temperatures will be directly proportional to the lengths of the regions.

Step 2: Select a suitable glass-based substrate. The overall dimensions are dependent on the choice of substrate. It is advised to use at least a 2" × 3" borosilicate glass as substrate.

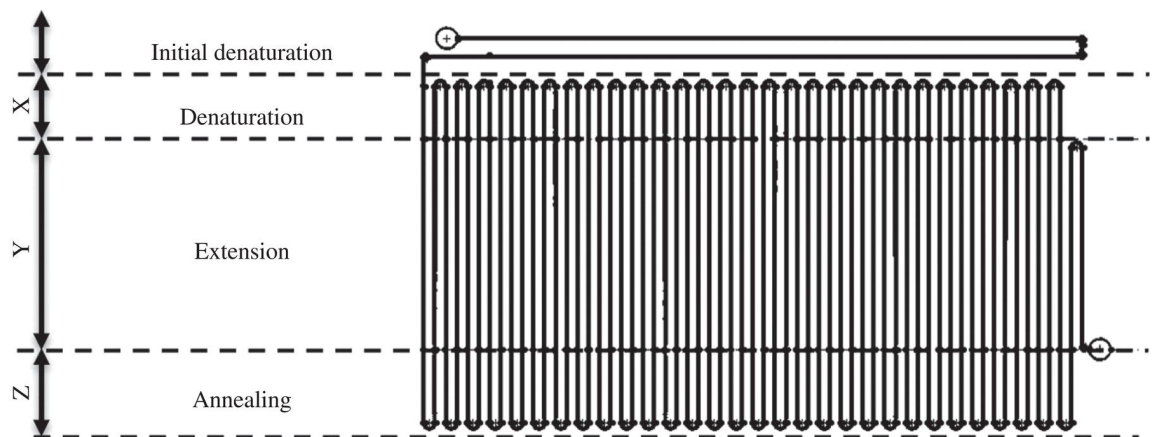


Figure 10.18 Schematic for the Microfluidic Channel. Dimensions may be selected based on available fabrication capabilities and substrate dimensions. The dimension $(X + Y + Z)$ cannot exceed the dimension of the substrate. The trace width for the mold is preferred to be in the range of 100–600 μm .

Step 3: Use DLW based photolithography [\[24\]](#) to develop patterns to create molds. Dry film photoresist may be used owing to ease of use and good geometric tolerance. In case deeper channels are needed, multiple layers of photoresist can be used.

Step 4: After the development of mold, soft lithography can be used to obtain microchannels. The PDMS channels can be bonded to the substrate using plasma bonding. Alternatively,

laser ablation on PMMA may also be used to develop microchannels.

Step 5: Post development of microfluidic device, a suitable heating mechanism may be used. There can be a multitude of steps and methods to achieve heating, the most advisable being metal block (aluminum/copper) is customized required sizes as per the initial design and dimensions (Dimensions X, Y, and Z in [Figure 10.18](#)). An integrated heating and control system may be employed [[25](#), [26](#)].

Step 6: Once the integration with heaters is complete, the microfluidic device can be used in with any set of commercial PCR reagents as per the protocol, and the system may be tweaked based on the temperature conditions needed.

Step 7: Use a suitable fluid-driving mechanism (peristaltic/syringe pump) to drive the samples and reagents through the microfluidic device.

Step 8: Post the reaction, the sample may be collected and evaluated quantitatively and qualitatively using other methods.

10.5.5 Conclusion

This section introduced microfluidic devices for PCR. The section along with the prerequisite references, will enable readers to develop their own microfluidic devices for nucleic acid amplification systems. There can be a multitude of materials for microfluidic devices as well as numerous approaches for thermal management using these microfluidic devices, which may add value to the processes and are left to the discretion of the reader to evolve the approach further.

References

- 1 Fande, S. et al. (2023). A protocol to execute a lab-on-chip platform for simultaneous culture and electrochemical detection of bacteria. *STAR Protoc.* 4 (2): 102327.
<https://doi.org/10.1016/J.XPRO.2023.102327>.

- 2** Fande, S., Amreen, K., Sriram, D., and Goel, S. (2023). Microfluidic electrochemical device for real-time culturing and interference-free detection of *Escherichia coli*. *Anal. Chim. Acta* 1237: <https://doi.org/10.1016/J.ACA.2022.340591>.
- 3** Singh, R.K., Kumar, S., Amreen, K. et al. (2023). Disposable miniaturized electrochemical sensing platform with laser-induced reduced graphene oxide electrodes for multiplexed biochemical analysis. *IEEE Trans. Nanobioscience* 22 (3): <https://doi.org/10.1109/TNB.2022.3216312>.
- 4** Lahari, S.A., Amreen, K., Dubey, S.K. et al. (2023). Polymer functionalized laser induced graphene electrochemical sensor for selective and sensitive detection of fluoride ions in real water samples. *IEEE Sens. J.* <https://doi.org/10.1109/JSEN.2023.3285664>.
- 5** Kirschbaum, S.E.K. and Baeumner, A.J. (2015). A review of electrochemiluminescence (ECL) in and for microfluidic analytical devices. *Anal. Bioanal. Chem.* 407 (14): 3911–3926. <https://doi.org/10.1007/S00216-015-8557-X>.
- 6** Bhaiyya, M., Pattnaik, P.K., and Goel, S. (2022). Multiplexed and simultaneous biosensing in a 3D-printed portable six-well smartphone operated electrochemiluminescence standalone point-of-care platform. *Microchim. Acta* 189 (2): 1–9. <https://doi.org/10.1007/S00604-022-05200-0/FIGURES/5>.
- 7** Morris, R. (2015). Spectrophotometry. *Curr. Protoc. Essent. Lab. Tech.* 11 (1): 2.1.1–2.1.30. <https://doi.org/10.1002/9780470089941.ET0201S11>.
- 8** Pal, A., Kulkarni, M.B., Gupta, H., and Ponnalagu, R.N. (2021). Portable and autonomous device for real-time colorimetric detection: validation for phosphorous and nitrite detection. *Sens. Actuators A Phys.* 330: 112896. <https://doi.org/10.1016/j.sna.2021.112896>.
- 9** Pal, A., Dubey, S.K., and Goel, S. (2022). IoT enabled microfluidic colorimetric detection platform for continuous monitoring of

nitrite and phosphate in soil. *Comput. Electron. Agric.* 195 (August 2021): 106856. doi: 10.1016/j.compag.2022.106856.

- 10** Ko, E.H., Kim, H.J., Lee, S.M. et al. (2017). Stretchable Ag electrodes with mechanically tunable optical transmittance on wavy-patterned PDMS substrates. *Sci. Rep.* 7 (1): 1–12.
<https://doi.org/10.1038/srep46739>.
- 11** Giustarini, D., Rossi, R., Milzani, A., and Dalle-Donne, I. (2008). Nitrite and nitrate measurement by Griess reagent in human plasma: evaluation of interferences and standardization. *Methods Enzymol.* 440: 361–380. [https://doi.org/10.1016/S0076-6879\(07\)00823-3](https://doi.org/10.1016/S0076-6879(07)00823-3).
- 12** Li, F. et al. (2020). Paper-based point-of-care immunoassays: recent advances and emerging trends. *Biotechnol. Adv.* 39: <https://doi.org/10.1016/J.BIOTECHADV.2019.107442>.
- 13** Bhaiyya, M., Kumar, P.S., Pattnaik, P.K. et al. (2022). Stereolithography 3D printed electrochemiluminescence platform with random grade graphite electrode: detection of H₂O₂ and cholesterol using a smartphone. *IEEE Sens. J.* <https://doi.org/10.1109/JSEN.2022.3221728>.
- 14** Calabretta, M.M. et al. (2021). Paper-based immunosensors with bio-chemiluminescence detection. *Sensors* 21 (13): 4309. doi: 10.3390/S21134309.
- 15** Liu, L., Yang, D., and Liu, G. (2019). Signal amplification strategies for paper-based analytical devices. *Biosens. Bioelectron.* 136: 60–75. <https://doi.org/10.1016/J.BIOS.2019.04.043>.
- 16** Mahato, K., Srivastava, A., and Chandra, P. (2017). Paper based diagnostics for personalized health care: emerging technologies and commercial aspects. *Biosens. Bioelectron.* 96: 246–259. <https://doi.org/10.1016/J.BIOS.2017.05.001>.
- 17** Di Nardo, F., Chiarello, M., Cavalera, S. et al. (2021). Ten years of lateral flow immunoassay technique applications: trends, challenges and future perspectives. *Sensors* 21 (15): 5185. <https://doi.org/10.3390/S21155185>.

- 18** Kumar, P.S., Bhand, S., Das, A.K., and Goel, S. (2022). Microfluidic paper device with on-site heating to produce reactive peroxide species for enhanced smartphone enabled chemiluminescence signal. *Talanta* 236: <https://doi.org/10.1016/J.TALANTA.2021.122858>.
- 19** Kumar, P.S., Madapusi, S., and Goel, S. (2023). 3D printed microfluidic chemiluminescence PoC device with self-powering and integrated incubating system: validation via ALP detection on disposable μ PADs. *Microchem. J.* 189: 108518. <https://doi.org/10.1016/J.MICROC.2023.108518>.
- 20** Lv, C. et al. (2021). Long-lasting luminol chemiluminescence emission with 1,10-phenanthroline-2,9-dicarboxylic acid copper(II) complex on paper. *ACS Appl. Mater. Interfaces* 13 (45): 53787–53797. <https://doi.org/10.1021/ACSAMI.1C14563>.
- 21** Kumar, P.S., Madapusi, S., and Goel, S. (2023). Sub-second synthesis of silver nanoparticles in 3D printed monolithic multilayered microfluidic chip: enhanced chemiluminescence sensing predictions via machine learning algorithms. *Int. J. Biol. Macromol.* 245: 125502. <https://doi.org/10.1016/J.IJBIOMAC.2023.125502>.
- 22** Kumar, P.S., Advincula, P.A., and Goel, S. (2022). First report on onsite temperature based recovery of quenched chemiluminescence signal from graphenized μ PADs: validation by catechins radical scavenging. *Nano Futur.* 6 (4): 045002. <https://doi.org/10.1088/2399-1984/AC9D78>.
- 23** Nguyen, Q.H. and Il Kim, M. (2020). Nanomaterial-mediated paper-based biosensors for colorimetric pathogen detection. *TrAC Trends Anal. Chem.* 132: 116038. <https://doi.org/10.1016/j.trac.2020.116038>.
- 24** Noviana, E., McCord, C.P., Clark, K.M. et al. (2020). Electrochemical paper-based devices: sensing approaches and progress toward practical applications. *Lab Chip* 20: 9–34. <https://doi.org/10.1039/C9LC00903E>.

- 25** Kulkarni, M.B. and Goel, S. (2021). Miniaturized DNA amplification platform with soft-lithographically fabricated continuous-flow PCR microfluidic device on a portable temperature controller. *Microfluid. Nanofluidics* 25: 69.
- 26** Kulkarni, M.B., Goyal, S., Dhar, A. et al. (2022). Miniaturized and IoT enabled continuous-flow based microfluidic PCR device for DNA amplification. *IEEE Trans. Nanobioscience* 21 (1): 97–104.
- 27** Srikanth, S., Dudala, S., Raut, S. et al. (2020). Optimization and characterization of direct UV laser writing system for microscale applications. *J. Micromech. Microeng.* 30 (9): 095003 (15pp).

Note

[*](#) Equally Contributing Author.

11

Wearable Devices

Ramya Priya Pujari^{1,2}, S. Vanmathi^{2*}, Satish Kumar Dubey^{1,2}, and Sanket Goel²*

¹ Department of Mechanical Engineering, Birla Institute of Technology and Science (BITS) Pilani, Hyderabad Campus, Hyderabad, Telangana, India

² MEMS, Microfluidics and Nanoelectronics (MMNE) Lab, Department of Electrical and Electronics Engineering, Birla Institute of Technology and Science (BITS) Pilani, Hyderabad Campus, Hyderabad, Telangana, India

11.1 Application of Laser-Induced Graphene in Breath Analysis

11.1.1 Introduction

In the era of wearable technology, wearable devices have played a promising role in point-of-care diagnosis by considering interstitial fluids such as tears, sweat, and saliva. These devices are on the verge of purporting transformative changes in management, detection, and diagnostics [1]. These wearable device-based diagnostics are utilized for the prevention and control of infectious illnesses, as well as the monitoring of health problems, in non-laboratory settings where highly trained professionals and advanced laboratory infrastructure are unavailable. Recently, with emerging technological innovations, remote monitoring techniques has been incorporated to monitor the health condition of the person [2]. Thus, incorporating bioinspired materials into wearable devices as triggers or sensors results in unique device features that can be used for detection, capture, or quick readout is explained in the following [section \[3\]](#).

Since its discovery in 2014, laser-induced graphene (LIG) has played a significant role in the field of wearable technology, thanks to its superior electrical conductivity ($5\text{--}25\text{ S.cm}^{-1}$) and thermal stability

(>900 °C) properties with the quick development of its device fabrication processes [4]. Based on the several instances in advancement in the fabrication technology of wearable sensors it is observed that the number of users for wearable health monitoring sensors have been developed. However, these wearable devices are becoming less obtrusive and more powerful, allowing patients to be monitored for longer periods of time in their natural environment. Numerous high-tech devices have been developed to be used in continuous health monitoring. Wearable sensors are a good option for medical applications because of their beneficial qualities. In this context, wearable sensors that can help with disease diagnosis are designed, created, and used in human health care systems [5].

11.1.2 Experimentation

11.1.2.1 Brief Overview

It is critical to experiment with wearable respiratory rate analysis sensors to improve their precision, dependability, and usefulness. They have the potential to completely transform workplace safety in the industry by identifying dangers associated with fatigue, improving worker well-being, and maximizing performance. These sensors make it easier to do research on respiratory health, stress reduction, sleep issues, and even psychiatric illnesses, which improves healthcare and maximizes human performance.

Prerequisites

Windows 10 or above operating system with at least 4 GB of RAM and 250 GB of storage, polyimide (PI) sheet as sensor material, licensed version of computer-aided designing (CAD) tool, licensed version KickStart software for Source meter (B2912A-Keysight technologies) data analysis.

Fabrication of Kirigami Cut Breath Sensor

Experimental Steps

Step 1: The sensor substrate, PI (converted to graphene using laser-induced approach) is chosen to make it work as the flexible

and wearable based on mechanical and electrical properties such as carbon cloth, polyamide sheet, etc. Select the required amount of commercial grade PI sheet (125 μm thickness).

Step 2: For better flexibility, design of the sensor is chosen as Kirigami (design made by cutting). The 42 mm \times 13 mm (L \times B) sensor is made with inter cuts of 0.75 mm width.

Step 3: The specified Kirigami design was drawn using CAD tools with the extension of .dxf. Then this .dxf file was transferred into the CorelDraw, which is compatible for the CO₂ laser. The outline cut and the width of the laser ablation was changed according to the preferences of the laser, which is shown in [Figure 11.1](#), by changing the speed and power, of the CO₂ laser. With this process LIG was obtained on PI. This laser-ablated PI sheet is used as a wearable breath sensor, which is helpful to analyze the breath patterns of the normal to diseased person. The pictorial representation of the fabrication is shown in the [Figure 11.1](#). For better insights in the fabrication procedure, refer to Fabrication [Chapter 5](#) (5.1).

Instrumentation

Step 1: The fabricated sensor is then attached to the source meter (B2912A-Keysight technologies) to provide voltage of 1 V supply to the sensor terminals.

Step 2: The connection of the sensor is shown in the [Figure 11.2](#).

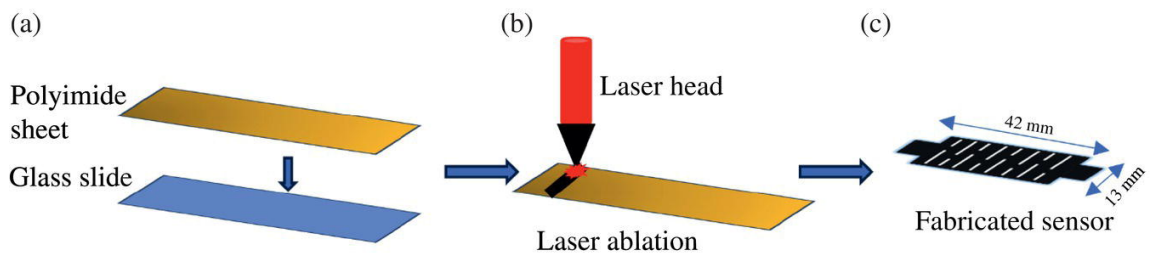


[Figure 11.1](#) Laser ablation for sensor fabrication (a) attaching the polyamide sheet to glass substrate; (b) laser engraving on the polyimide sheet; (c) fabricated sensor.

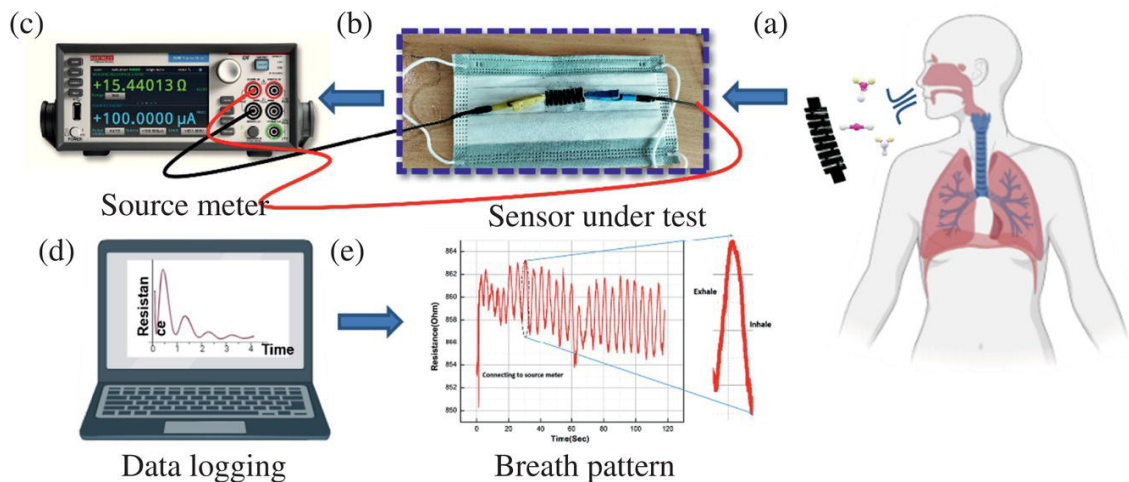


Figure 11.2 Functionality of the sensor is explained (a) when exhaled air or inhaled air interacts with sensor; (b) sensor attached to the mask; (c) source meter for calibrations of the reading; (d) GUI connected system for data Logging; (e) readout graph from the sensor when a person is exhaled and inhaled on the sensor. It has been shown that the readings are visualized as a sine wave from 858 to 863 Ω and decreased vice versa.

Source: [6]/with permission of IEEE.

Step 3: Care must be taken to activate the source meter by connecting it to the computer with an USB interface.

Step 4: Open the KickStart software, under the settings column voltage must be kept constant either 0.5 or 1 V.

Step 5: Under graph settings, choose the X axis and Y axis. Choosing Time in X axis and resistance in Y axis. For the complete analysis, the initial reading of 1 V DC with a repeat cycle of 1000 cycles are used.

Step 6: Click on the measure icon to start measuring the inhalation and exhalation pattern of the volunteer.

Note: Care must be taken that the volunteer must be sit in a relax and comfortable position wearing the sensor actuated mask.

Step 7: It is observed from the graph shown in [Figure 11.2](#) (V) that there would be a raise in resistance when there is an

exhalation happen and fall in peak when it comes with inhalation.

Step 8: Plot the graph, and the material consider is flexible, wearable, and easily can attach to mask and philtrum of a person under test [6].

11.1.3 Conclusion

The aim of the experiment is to create and access a wearable respiration rate analysis sensor by utilizing a PI sheet that has been LIG manufactured using a Kirigami – cut design. On reacting to cycles of inhale and exhalation, the manufactured sensor showed promising results for precise monitoring of breath patterns. This was proved by the variations in resistance that were recorded and displayed via a source meter and GUI-connected system. This experiment has good applications in workplace safety, healthcare, and performance optimization. Furthermore, the versatility and ease of use of sensors make them invaluable for study into respiratory health, stress reduction, sleep disorder, and psychiatric problems.

11.2 Wearable Microfluidic Device for Nucleic Acid Amplification

11.2.1 Introduction

Nucleic acid has become a crucial biomarker for biological research and healthcare diagnosis [7]. Due to their ability to amplify and analyze diseases, a lot of R&D is happening in the field of molecular biology on nucleic acid amplification. The recent global outbreak of the coronavirus serves as an example of why nucleic acid detection methods have become the standard for identifying infectious microorganisms. In the field of practical application, the first and most widely used amplification technique for identifying and amplifying low-abundance nucleic acids is polymerase chain reaction, or PCR [8]. While PCR has been widely used in many different domains, its application in resource-constrained situations and for point-of-care (POC) analysis is generally limited since it requires large and expensive heat cyclers [9].

On the contrary isothermal methods, which involve amplification, at a single temperature are said to offer potential as a more convenient and economical substitute for PCR [10]. Additionally, this isothermal technique can also be performed at simple conditions such as water bath, dry bath, or battery powered heaters. Recombinase polymerase amplification technique is one such method, which provides significant advantage of instrumentation and assay development in resource limited condition [11]. Consequently, recombinase polymerase amplification (RPA) works at a temperature of 30–40 °C, which is relatively similar to the temperature of human body. With this ability, a wearable microchannel based fabrication is done to make use of isothermal amplification [12]. As it is crucial to develop lab on chip devices that are compact user cost-effective for detecting nucleic acids. Such devices find applications in a range of areas from diagnosing conditions to monitoring environmental factors [13].

11.2.2 Experimentation

11.2.2.1 Brief Overview

Real-time, on-site diagnostics are made possible by wearable nucleic acid amplification devices, which are revolutionizing environmental monitoring, agriculture, and healthcare. Furthermore, these tools facilitate field research by offering real-time genetic analysis, speeding up scientific findings, and encouraging data-driven decision-making. All things considered, wearable nucleic acid amplification improves accuracy and responsiveness in a number of industries.

Prerequisites

Oven (Thermo Scientific™ Heratherm™ Advanced Protocol Security Oven), desiccator (sigma Aldrich – Vacuum desiccator Z119008-1EA) to degas the elastomer and curing agent of Dow Sylgard 184 mixture, licensed version of CAD tool, Recombinase polymerase amplification kit (RPA) (Twist amp basic kit), overnight cultured *Pseudomonas Aeruginosa* bacteria sample (Extract DNA from it), horizontal gel electrophoresis setup (BioBee.Tech), agarose gel.

Fabrication of Microchamber

Step 1: In this experiment, for flexibility and to have wearable compatibility the material for fabricating microchamber is chosen as polydimethylsiloxane (PDMS).

Step 2: The desired dimensions for the microchamber to perform the reaction is of 10 mm of diameter and 1 mm of height on considering 20 μ L as the reaction sample. Draw the microchamber outline using CAD tools.

Step 3: The fabrication of the wearable microchannel, which is used to analyze the nucleic acid is done on following the soft lithography techniques.

Step 4: A 1 mm thickness of acrylic sheet is cut using CO₂ laser to the required dimensions of the microchamber on choosing optimized laser power and speed (1% power and 5% speed).

Step 5: Glue the obtained piece to the glass slide and place it into the mold. Then a cleared and degassed PDMS mixture (elastomer: curing agent, 10:1) is poured on to the designed microchamber, and place it into the oven under 70 °C for 2 hours. After 2 hours the cured PDMS is cut to the edges of the channel. The open edge is bonded with the thin layer of PDMS. For easy understanding pictorial representation of the fabrication is shown in [Figure 11.3](#). The detailed description of the fabrication procedure is explained in [Chapters 3](#) and [6](#).

Instrumentation

Step 1: The main aim of this study is to check the amplification of genomic DNA using wearable micro chamber.

Step2: Considering genomic DNA as the test template extracted using Qiagen DNA extraction mini kit from the *Pseudomonas Aeruginosa* bacteria (cultured).

Step 3. Care should be taken, and the sample is prepared according to the manufacturers protocol given in the Twist Amp Basic kit bought from Twist DX [\[14\]](#).

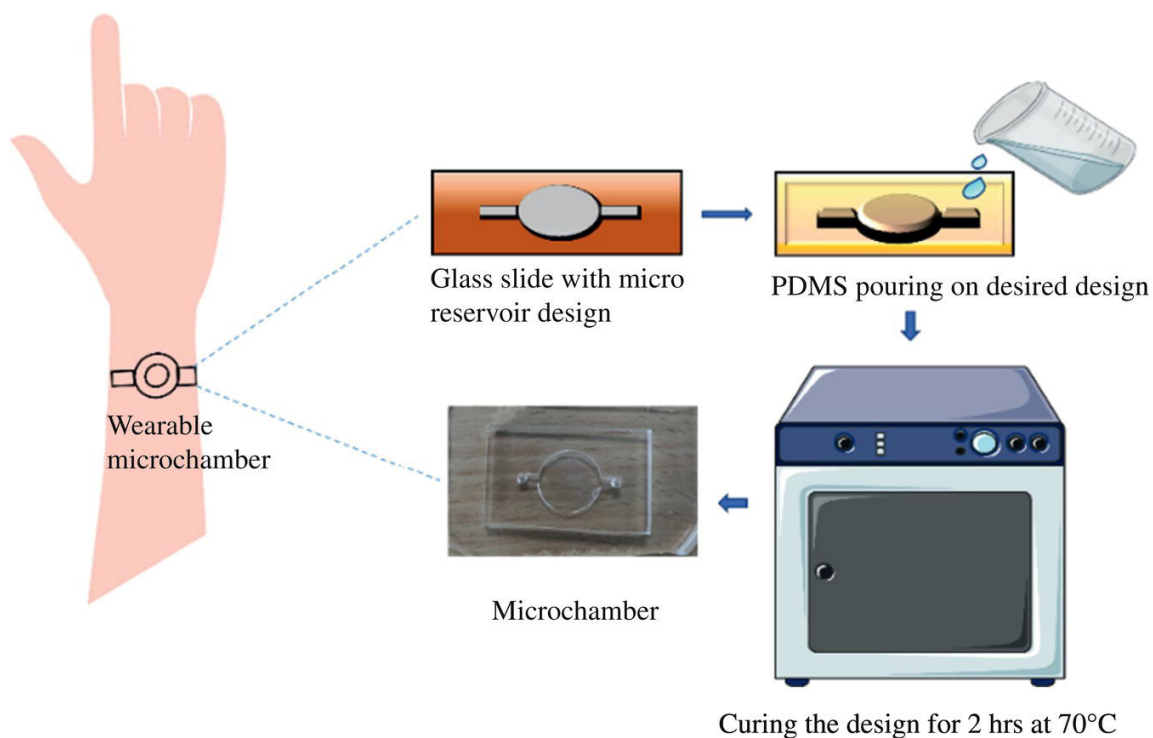


Figure 11.3 Represents the fabrication of wearable microchamber. The soft lithography method is used to easily fabricate the wearable microchamber. This chamber is adapted to the volunteer wrist to make use of body temperature for further analysis.

Step 4: Load the prepared sample into the microchamber using commercially available 10 mm diameter syringe, which is placed on the wrist of the volunteer.

Step 5: After 15–20 minutes, the sample that meets the temperature of the wrist is amplified.

Step 6: After amplification, the amplified sample should be purified using Qiagen purification kit on following the manufacturers protocol [15].

Step 7: Care should be taken to fill the desired sample (10–20 μL) of amplified product into the wells of the agarose gel.

Step 8: Run the gel using electrophoresis setup using 100 V for 30 minutes. DNA fragments get separated according to the size when electric field is applied. The results of gel electrophoresis shown in the figure (Figure 11.4).

Step 9: The detection of these *Pseudomonas aeruginosa* (Gram-negative opportunistic bacteria) can be done using gel electrophoresis. Here, it was observed at 504 bp on agarose gel.

11.2.3 Conclusion

The wearable nucleic acid amplification device developed in this work has great promise for real-time, on-site genetic analysis. The successful amplification of *Pseudomonas aeruginosa* making use of body temperature, demonstrates the ability of the device to identify bacterial infections, which can be applied to a variety of applications including environmental monitoring, agriculture, and healthcare. The use of body temperature for amplification streamlines the procedure, making it ideal for field research and quick diagnoses. Which further helps in portable real-time point-of-care needs in resource limiting areas.

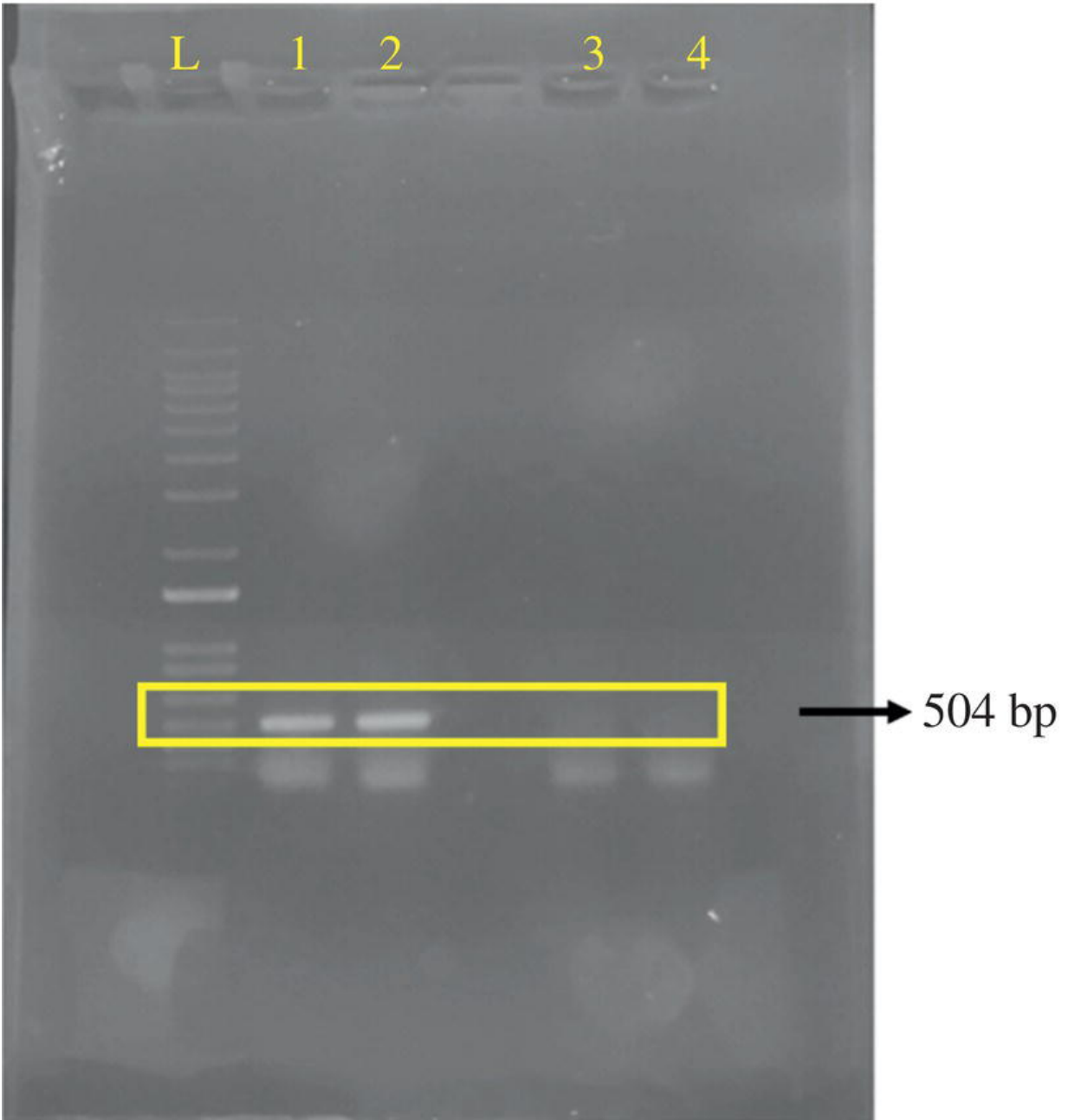


Figure 11.4. Represents the amplified product using Isothermal amplification, L represents ladder of 1 kb as a marker Lane 1 = 100 ng/ μ L and Lane 2 = 150 ng/ μ L as amplified. Lane 3 and Lane 4 are negative control. The amplified product is shown at line corresponding to 500 bp (504 bp is the size of amplified product).

11.3 Wearable Patch Biofuel Cell

11.3.1 Introduction

The wearable biofuel cell (BFC) is a miniature and made with smart patches or fabrics. BFC converts chemical energy to electrical energy using living molecules, usually enzymes or bacteria, to oxidize a fuel source (such as lactase) and decrease an electron acceptor (such as oxygen), are utilized in BFC devices that produce electrical energy [16]. These BFCs are often compact and lightweight, they can be incorporated into wearable technologies. The creation of self-powered wearable technology and the production of electricity in distant or resource-constrained areas are the potential uses for wearable patch BFCs [17].

The chemical energy held in biofuels like lactate can be converted into electrical energy by an electrochemical process. Various biosensors and microelectronics built into wearable gadgets can be powered by this energy [18]. They are a sustainable energy source for wearables since they generate power without producing any negative consequences. A wearable bandage-style self-powered lactate BFC that, when perspiration contains lactate, produces energy and wirelessly transmits the information with the help of Bluetooth.

In most cases, lactate oxidase enzymes catalyze lactate oxidation in wearable BFCs. Electrons are released as lactate is changed into pyruvate during this enzymatic process. To power the electrical components with the help of wearable device, the electrons can be employed to create an electric current. This work used lactate as a fuel and produced energy from sweat. They are also being investigated as a means of keep tracking of people health, as the makeup of bodily fluids can provide details about a person metabolic status [19].

11.3.2 Experimentation

11.3.2.1 Brief Overview

Optimizing wearable Patch Bio-Fuel Cells helps in understanding the energy output, compatibility, and durability. In the business sector, they provide eco-friendly power sources for IoT gadgets, wearable electronics, and remote monitoring systems. They support

advancements in energy harvesting and biomedical applications by enabling remote data collecting, environmental sensing, and mobile health monitoring in research.

Prerequisites

Windows 10/11 operating system, a minimum of 4 GB RAM, storage of 250 GB, and a licensed version of CAD tool and measured the data with potentiostat/Galvanostat (SP-150 from Biologic Instruments, France). The chemical used polyethyleneimine (PEI), Tetrathiafulvalene (TTF) solution (0.01%) in dimethylformamide (DMF). Lactate oxidase (LOx) and bilirubin oxidase (BOx), phosphate buffer solution (PBS).

Fabrication

Step 1: The electrode materials were chosen, such as a graphite pencil electrode and the grade 1 filter paper ($5\text{ cm}^2 \times 5\text{ cm}^2$), shown in [Figure 11.5a](#).

Step 2: Design the electrode using CAD tools, then save the file in (.dxf) format (Refer to Fabrication [Chapter 5](#) [5.1]).

Step 3: Using the Graphtec Cutter plotter GE6000-60, manage the pencil (14B) holder arrangement. The cutter plotter's operational settings, including cut pressure (2 N), velocity (2 m/s^2), and rpm (1 m/s), were maintained at constant values.

Step 4: The anode 0.19 cm^2 area of the surface was designated as the electroactive region shown in [Figure 11.5b](#), e.

Step 5: Cross-linkers are $40\text{ }\mu\text{L}$ of 0.1% PEI coated over the electrode surface, after 1 hour. Then $30\text{ }\mu\text{L}$ of TTF solution (0.01%) in DMF, and dried for 1 hour at $60\text{ }^\circ\text{C}$ at a specific time interval for proper immobilization.

Step 6: Enzymes LOx, for anode ($10\text{ }\mu\text{L}$) and BOx, for cathode ($10\text{ }\mu\text{L}$) are prepared within PBS then coated over the electrode and later up to 2 hours kept at $4\text{ }^\circ\text{C}$ storage.

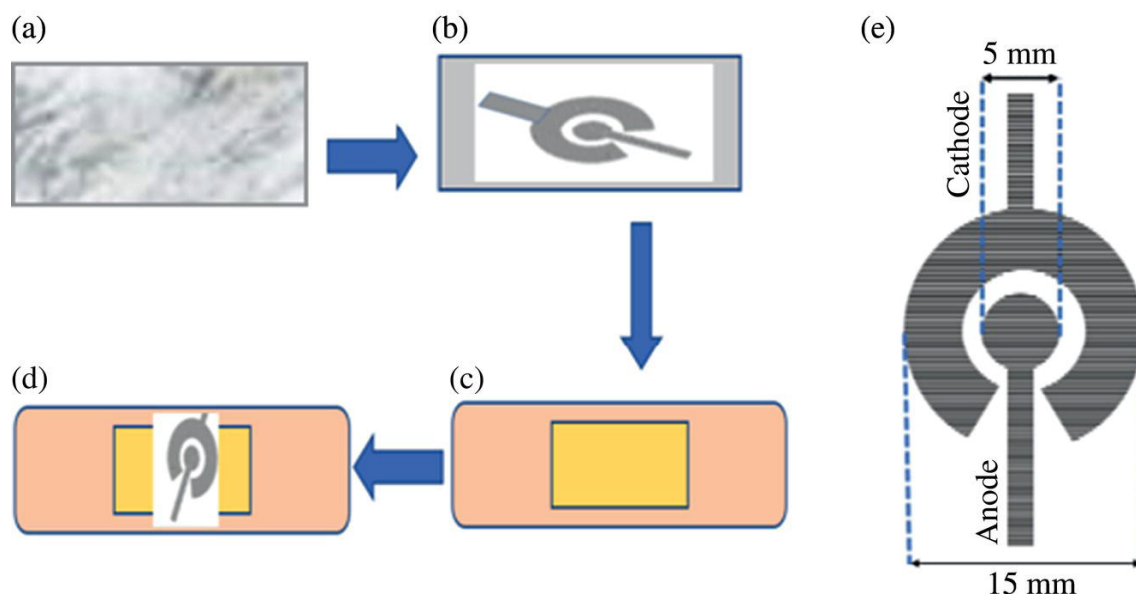


Figure 11.5 Wearable biofuel cell setup: (a) substrate grade 1 filter paper; (b) automated pencil bioelectrodes; (c) open slit for an electrode assembly; (d) complete fuel cell device of the biofuel cell; (e) complete bioelectrode design with dimensions.

Step 7: To characterization of the device morphology like SEM, EDAX, FTIR XPS, and XRD, etc. (Please refer to the Characterization Chapters 8.1 and 8.2.)

The 15 mm of anode and 5 mm of cathode electrodes had been placed on a substrate made of Grade 1 filter paper, which produced energy generation and allowed the fuel to be absorbed and transmitted to the electrodes. The bioelectrodes were then attached to a bandage that was readily accessible in the market, [Figure 11.5c](#) and used as a substrate to support the BFC while it was still intact, as shown in [Figure 11.5d](#). The process of assimilating the bioelectrodes and the actual picture of the BFC was mentioned in reference [\[20\]](#).

Instrumentation Usage to Test Device Performance

Step 1: Take the fabricated electrode kept inside the 10 mM lactate solution and later use a potentiostat wait for 15 minutes to measure the open circuit voltage (OCV).

Step 2: Connect the electrodes to a potentiostat, then use the linear sweep voltammetry (LSV), cyclic voltammetry (CV), and chronoamperometry (CA) techniques to assess the device performance.

Step 3: For electrochemical analysis, a three-electrode configuration including platinum wire, Ag/AgCl (3 M KCl), and bioelectrode as the counter electrode, reference electrode, and working electrode, respectively, was dipped in a 5 ml cell.

Step 4: Lactate should be used as the electrolyte, and LSV techniques need to be used to determine the device concentration (anode and cathode) and determine its maximum current density.

Step 5: Use a three-electrode system with 10 mM maximum concentration molarity of the device and find the oxidation current on the anodic side with lactate and without lactate with the help of CV techniques. Later, find the cathodic side reduction reaction with oxygen (O_2) without O_2 in 0.1 M PBS in pH (5.7) solution.

Step 6: Then connect the fuel cell setup (2-electrode system), use CA techniques to find the maximum OCV to 0 mV measurement for each iteration used to limit the potential window, and calculate the current density for each state.

Step 7: Calculate the skin impedance using electrochemical impedance spectroscopy (EIS) techniques to find out the real and imaginary parts of the device. The pencil graphite electrode/enzyme-modified with charge transfer resistance (R_{ct}) values were found 28 Ω .

Step 8: Find the stability of the device and measure its discharge performance from Max OCV to 0 mV.

Step 9: After connecting the device potentiostat, wait for 10–15 minutes to receive the higher potential. Then apply the max potential in CA techniques and drop the max to min voltage. Find out the current density values from each potential. To get the device power density, multiply the OCV and current density to plot the polarization performance. This device produces a

maximum current density of $75 \mu\text{A cm}^2$ power density of $11.5 \mu\text{W cm}^2$ with a max OCV of 420 mV.

11.3.3 Conclusion

This device performance was optimized with wearable state and different potential concentrations. This wearable fuel cell produces $11.5 \mu\text{W cm}^2$, and this performance in place of wearable is advantageous for microdevice fueling in wearable applications. To further enhance energy collecting and utilization for applications in real-time, fuel cells can be stacked on multiple electrodes. This effort will make the development of power sources for single-use biomedical gadgets and devices possible.

References

- 1 Ates, H.C. et al. (2022). End-to-end design of wearable sensors. *Nat. Rev. Mater.* 7 (11): 887–907.
<https://doi.org/10.1038/s41578-022-00460-x>.
- 2 Yin, R. et al. (2021). Wearable sensors-enabled human–machine interaction systems: from design to application. *Adv. Funct. Mater.* 31 (11): 2008936.
<https://doi.org/10.1002/ADFM.202008936>.
- 3 Hazra, R.S. et al. (2023). Bioinspired materials for wearable devices and point-of-care testing of cancer. *ACS Biomater Sci. Eng.* 9 (5): 2103–2128.
https://doi.org/10.1021/ACSBIOMATERIALS.1Co1208/ASSET/IMAGES/LARGE/AB1Co1208_0011.JPEG.
- 4 Nasiri, S. and Khosravani, M.R. (2020). Progress and challenges in fabrication of wearable sensors for health monitoring. *Sens. Actuators A Phys.* 312: 112105.
<https://doi.org/10.1016/J.SNA.2020.112105>.
- 5 Liu, J. et al. (2022). Laser-induced graphene (LIG)-driven medical sensors for health monitoring and diseases diagnosis. *Microchim.*

Acta 189 (2): 1–14. <https://doi.org/10.1007/S00604-021-05157-6/FIGURES/9>.

- 6 Priya, P.R., Dubey, S.K., and Goel, S. (2023). Noninvasive clean room free printed piezoresistive breath sensor for point of care application. *IEEE Sens. J.* 23 (12): 13621–13628. <https://doi.org/10.1109/JSEN.2023.3269388>.
- 7 Moccia, M. et al. (2023). Advances in nucleic acid research: exploring the potential of oligonucleotides for therapeutic applications and biological studies. *Int. J. Mol. Sci.* 25: 1, 146. <https://doi.org/10.3390/IJMS25010146>.
- 8 Kulkarni, M.B. and Goel, S. (2023). Mini-thermal platform integrated with microfluidic device with on-site detection for real-time DNA amplification. *Biotechniques* 74 (4): 158–171. <https://doi.org/10.2144/BTN-2022-0091>.
- 9 Zhu, H., Zhang, H., Xu, Y. et al. (2020). PCR past, present and future. *Biotechniques* 69 (4): 317–325. <https://doi.org/10.2144/BTN-2020-0057>.
- 10 Oliveira, B.B., Veigas, B., and Baptista, P.V. (2021). Isothermal amplification of nucleic acids: the race for the next “gold standard”. *Front. Sens.* 2: 752600. <https://doi.org/10.3389/FSENS.2021.752600>.
- 11 Munawar, M.A. (2022). Critical insight into recombinase polymerase amplification technology. *Expert Rev. Mol. Diagn.* 22 (7): 725–737. <https://doi.org/10.1080/14737159.2022.2109964>.
- 12 Patiti, C. et al. (2022). Chip-based and wearable tools for isothermal amplification and electrochemical analysis of nucleic acids. *Chemosensors* 10 (7): 278. <https://doi.org/10.3390/CHEMOSENSORS10070278>.
- 13 Trinh, K.T.L. and Lee, N.Y. (2022). Fabrication of wearable PDMS device for rapid detection of nucleic acids via recombinase polymerase amplification operated by human body heat. *Biosensors (Basel)* 12 (2): 72. <https://doi.org/10.3390/BIOS12020072/S1>.

- 14** Singpanomchai, N., Akeda, Y., Tomono, K. et al. (2019). Naked eye detection of the mycobacterium tuberculosis complex by recombinase polymerase amplification – SYBR green I assays. *J. Clin. Lab. Anal.* 33 (2): e22655.
<https://doi.org/10.1002/JCLA.22655>.
- 15** Quagen purification protocol - Google search.
<https://www.qiagen.com/cn/resources/download.aspx?id=eofab087-ea52-4c16-b79f-c224bf760c39&lang=en> (accessed 19 July2024).
- 16** Jayapiriya, U.S. and Goel, S. (2022). Patch-type wearable enzymatic lactate biofuel cell with carbon cloth bioelectrodes for energy harvesting from human sweat. *IEEE J. Flex. Electron.* 1 (1): 32–38. <https://doi.org/10.1109/jflex.2022.3157276>.
- 17** Y. Liu, Q. Sun, W. Li, K. R. Adair, J. Li, and X. Sun (2017). A Comprehensive Review on Recent Progress in Aluminum–Air Batteries. KeAi Publishing Communications Ltd.
<http://dx.doi.org/10.1016/j.gee.2017.06.006>
- 18** Rewatkar, P., Nath, D., Kumar, P.S. et al. (2022). Internet of things enabled environmental condition monitoring driven by laser ablated reduced graphene oxide based Al-air fuel cell. *J. Power Sources* 521:
<https://doi.org/10.1016/j.jpowsour.2021.230938>.
- 19** Jayapiriya, U.S. and Goel, S. (2020). Optimization of carbon cloth bioelectrodes for enzyme-based biofuel cell for wearable bioelectronics. *Proceedings of the IEEE Conference on Nanotechnology*, 150–154.
<http://dx.doi.org/10.1109/NANO47656.2020.9183700>.
- 20** Jayapiriya, U.S. and Goel, S. (2022). Body-worn enzymatic biofuel cell with automated pencil drawn bioelectrodes for energy harvesting from human sweat. *J. Micromech. Microeng.* 32 (4):
<https://doi.org/10.1088/1361-6439/ac5428>.

Note

* Equally Contributing Author.

12

Energy Devices

Himanshi Awasthi^{}, S. Vanmathi^{*}, and Sanket Goel
MEMS, Microfluidics and Nanoelectronics (MMNE) Lab,
Department of Electrical and Electronics Engineering, Birla
Institute of Technology and Science (BITS) Pilani, Hyderabad
Campus, Hyderabad, Telangana, India*

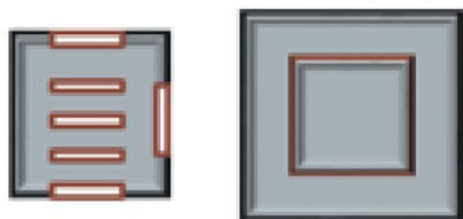
12.1 Introduction

In recent years, there has been a tremendous growth in the demand for high-performance electrochemical energy storage devices, and numerous efforts have been made to produce novel electrode materials. There are numerous applications for the energy technologies being developed to store, convert, and use energy [1]. Supercapacitors and fuel cells are mainly recently advanced technologies to store and harvest energy. The energy harvest obtained from different types of fuels to power environmental applications and increase the efficiency of fuel cells is known as energy harvesting [2]. HFCs are electrochemical devices that work through an electrochemical process to convert the chemical energy of a fuel (e.g., hydrogen) and an oxidant (generally oxygen from the air) into electrical energy, heat energy, and water [3]. These energy-harvesting devices are primarily diversified into electrochemical fuel cells, enzymatic fuel cells, and MFCs [4]. The harvested energy can be stored within supercapacitors and emerge as a crucial electronic component [5]. HFC and supercapacitor-based energy devices can be used for powering devices such as health-monitoring sensors, environmental sensors, and many microelectronics devices. The electrochemical technique is used to characterize the electrode material and device performance in all the steps for the fuel cell. The supercapacitor is covered in detail in this chapter.

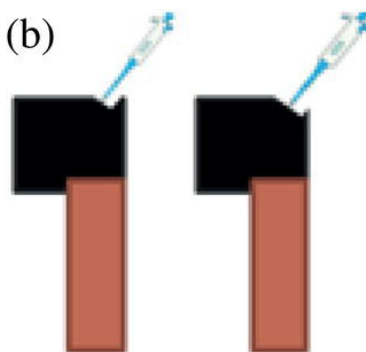
12.1.1 Hydrogen Fuel Cell

The HFC is clean energy technology and it produces hydrogen gas into electricity. They function by using a chemical process between hydrogen and oxygen to create electricity, with the only byproducts being water and heat. A viable replacement for conventional fossil-fuel-powered systems, HFCs provide electricity with no pollutants, as shown in [Figure 12.1](#). They have the potential to significantly lower the carbon footprint of many sectors and can be used to power vehicles as well as provide strong platforms for microelectronic devices [\[6\]](#).

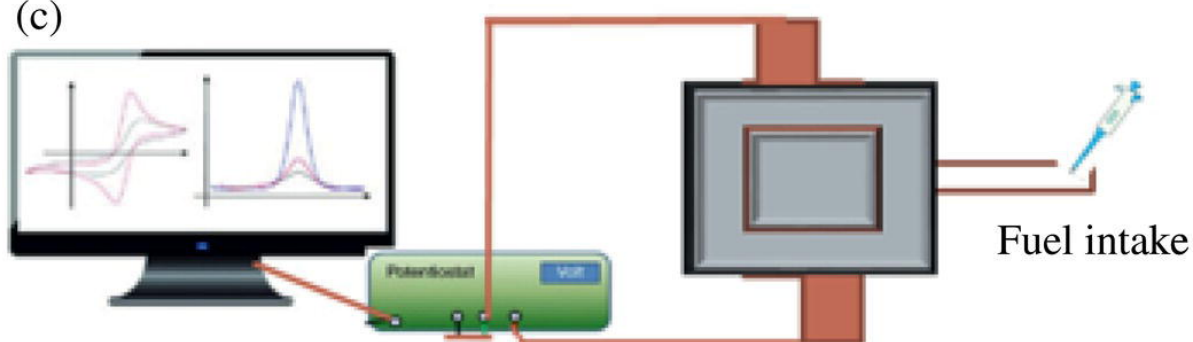
(a)



(b)



(c)



(d)

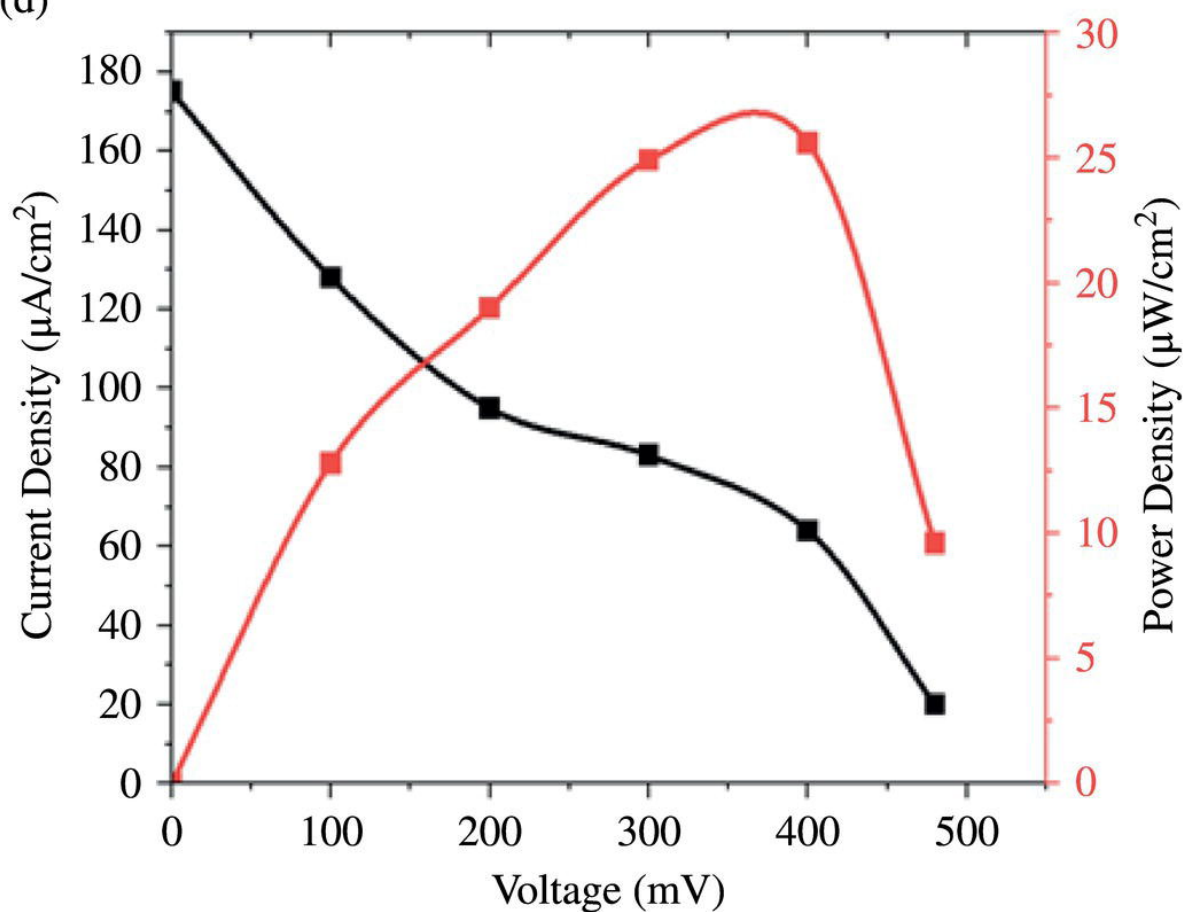


Figure 12.1 Fabrication methodology of the hydrogen fuel cell: (a) 3D printed setup; (b) carbon cloth-based electrodes; and (c) HFC testing with a potentiostat; (d) polarization performance of the hydrogen fuel cell.

12.1.2 Experimentation

12.1.2.1 Brief Overview

HFCs are environmentally safe since they release no dangerous gases, removing the need for expensive handling and storage of hazardous substances such as battery acid or diesel fuel. This experiment provides better energy harvesting devices and functions on pure hydrogen production, the only byproducts of which are heat and water. An eco-friendly, effective, and adaptable way to cut emissions and supply long-term energy is through HFCs.

12.1.2.2 Prerequisites

Carbon cloth fuel cell store, USA, Flashforge Creator Pro-FDM 3D printer, polylactic acid (PLA), blue laser system (ZMorph VX, Zmorph, Poland), $\text{CoCl}_2 \cdot 6\text{H}_2\text{O}$, platinum (Pt/C)-0.2 mg/cm²–20%, sodium hydroxide (NaOH), potentiostat/galvanostat (SP-150 from Biologic Instruments, France).

12.1.2.3 Experimentation

Step 1: Choose the device substrate based on energy production such as carbon cloth.

Step 2: Draw the 3D printed setup. CAD software and Flashforge Creator Pro-FDM 3D printer is used to print with PLA, and filaments, choosing the dimensions of the bottom base cell 1.8 cm² and top base cell 2.2 cm² as shown in [Figure 12.1a](#) (refer to Fabrication [Chapter 5, section 5.1](#)).

Step 3: The $\text{CoCl}_2 \cdot 6\text{H}_2\text{O}$ is dispersed in deionized water and agitated for 30 minutes to create a homogeneous solution. After being submerged in the solution for 3 minutes, grade 1 filter paper is dried out in a hot-air furnace for 20 minutes at 70 °C.

The CoCl_2 -coated grade 1 filter paper is lased using the blue diode laser with maximum power of 2.8 W to produce the cobalt oxide (II)-reduced graphene oxide (Co_3O_4 -rGO) composite. A prepared composite is then scratched from the substrate and ground to form a fine powder.

Step 4: The carbon cloth was taken ($1\text{ cm} \times 1\text{ cm}$) and washed with ethanol to improve the surface purification. Then the anode catalyst was prepared with ethanol mixed in cobalt (II) oxide-reduced graphene oxide (rGO) (5 mg/1 ml), and cathode catalysts were used with commercially available platinum-coated carbon cloth (Pt/C)-0.2 mg/cm²–20%), purchased from a fuel cell store, USA.

Step 5: Cobalt (II) oxide/reduced graphene oxide (rGO) was coated with 200 $\mu\text{l}/\text{ml}$ over the anode surface and then dried in a hot-air oven for 5–10 minutes, as shown in [Figure 12.1b](#).

12.1.2.4 Instrumentation for Testing Device Performance

Step 1: Connect the device to a potentiostat. Then use a three-electrode system setup (platinum wire: counter electrode; Ag/AgCl (3 M KCl): reference electrode; and fabricated electrode: working electrode) and shown in [Figure 12.1c](#).

Step 2: Utilize the prepared sodium hydroxide (NaOH): 5 ml electrolyte to determine the device concentration effect using the linear sweep voltammetry (LSV) procedures and to find out the voltage and current values.

Step 3: Then use the maximum concentration effect and maximum current and voltage using chronoamperometry (CA) procedures to assess the device performance in time vs. current.

Step 4: Determine the equivalent circuit based on the electrode material, then fit the curve using techniques from electrochemical impedance spectroscopy (EIS) and find out charge transfer characteristics (R_{Ct}) and resistance R_s(t) is 19.07.

Step 5: To narrow the potential window and determine the current density for each state, the maximum OCV to 0 mV measurement for each study.

Step 6: To get the device's power density, multiply the OCV and current density to plot the polarization performance and then measure the discharge analysis of the device.

Step 7: The developed HFC generated a 480 mV steady voltage with a maximum current density of $175 \mu\text{A}/\text{cm}^2$. A high-power density of $25.6 \mu\text{W}/\text{cm}^2$ was observed at a voltage of 400 mV, as shown in [Figure 12.1d](#).

12.1.3 Conclusion

These fuel cells offer almost zero pollution and high fuel efficiency with a power density of $25.6 \mu\text{W}/\text{cm}^2$. In addition, future generations will gain further from the enhanced application of HFC with a stacked setup. It can be applied with small energy and is useful for microelectronic circuit electrical uses. The electricity needed for applications that operate in real time is produced by the HFC. When the HFC is fully integrated with a real-time system, its performance has the best possibility of meeting the technical requirements.

12.2 Enzymatic Biofuel Cells and Microbial Fuel Cells

12.2.1 Introduction

12.2.1.1 Enzymatic Biofuel Cells

Enzymatic biofuel cells are a type of bioelectrochemical system that uses enzymes to catalyze the oxidation of organic fuels, such as glucose, to produce electricity. In the traditional fuel cells that use platinum or other expensive catalysts, enzymatic biofuel cells rely on naturally occurring enzymes as catalysts [7]. The creation of efficient and improved bioelectrodes is used in an enzymatic biofuel cell for to produce energy. The technique will become more viable when a single-step procedure is followed to create a configurable yet

appropriate bio-analyte-based electrode [8]. In recognition of its exceptional chemical, physical, electrical, mechanical, optical, and thermal properties many of porous nanomaterials have more active sites for immobilization and enhancing the catalytic activity. It has low density and flexibility. For that, to improve the surface activity of the electrode to obtained with other porous carbon nanomaterials have become increasingly popular over the past few years [9]. For improving the functionality and efficiency of enzymatic biofuel cells, porous carbon nanomaterials are an appealing option due to their high surface area, and superior conductivity.

12.2.2 Experimentation

12.2.2.1 Brief Overview

In this experimental study, a carbon cloth-based electrode was modified with an enzyme and optimized testing of the fuel cell with a microfluidic channel setup. Following its fabrication, the device was tested, which is shown in the following steps, demonstrating its power capability to miniaturize biodevices.

12.2.2.2 Prerequisites

CO₂ laser (universal laser systems), VLS 3.60, polyethylene terephthalate sheet (PET), polyethylene (PEI) glucose oxidase (GOx), (laccase), glutaraldehyde, monosodium phosphate (NaH₂PO₄), disodium phosphate (Na₂HPO₄), D-(+)-glucose (99.5%), potentiostat/galvanostat (SP-150 from Biologic Instruments, France).

12.2.2.3 Experimentation

Step 1: Select the substrate for the device preparation based on conductive carbon cloth.

Step 2: Using CAD tools, sketch up the microfluidic channel design. See the chapter on fabrication 4.1 and 5.1 and fabrication steps shown in [Figure 12.2e](#).

Step 3: A CO₂ laser was used to create a Y-shaped microchannel. The microchannel virtual Y-shaped design, which has two inlets and one outlet, was made in CAD software before production. The entire carving process was done with 3 W of power and 1 cm/s of speed, as shown in [Figure 12.2a–d](#).

Step 4: Place PET over that attached adhesive tape, and past the microfluidic channel, then keep the carbon cloth bioelectrodes over the surface.

Step 5: Preparation of bioelectrodes: Initially PEI 2 µL is drop cast on the surface and dried at room temperature for 1 hour. Then prepare enzymes glucose oxidase (GOx)(5 mg/ml), for anode (40 µL) and laccase (Lac)(5 mg/ml), for cathode (20 µL) within phosphate buffer solution (PBS). Then drop cast over the electrode surface and store them up to 2 hours at 4 °C.

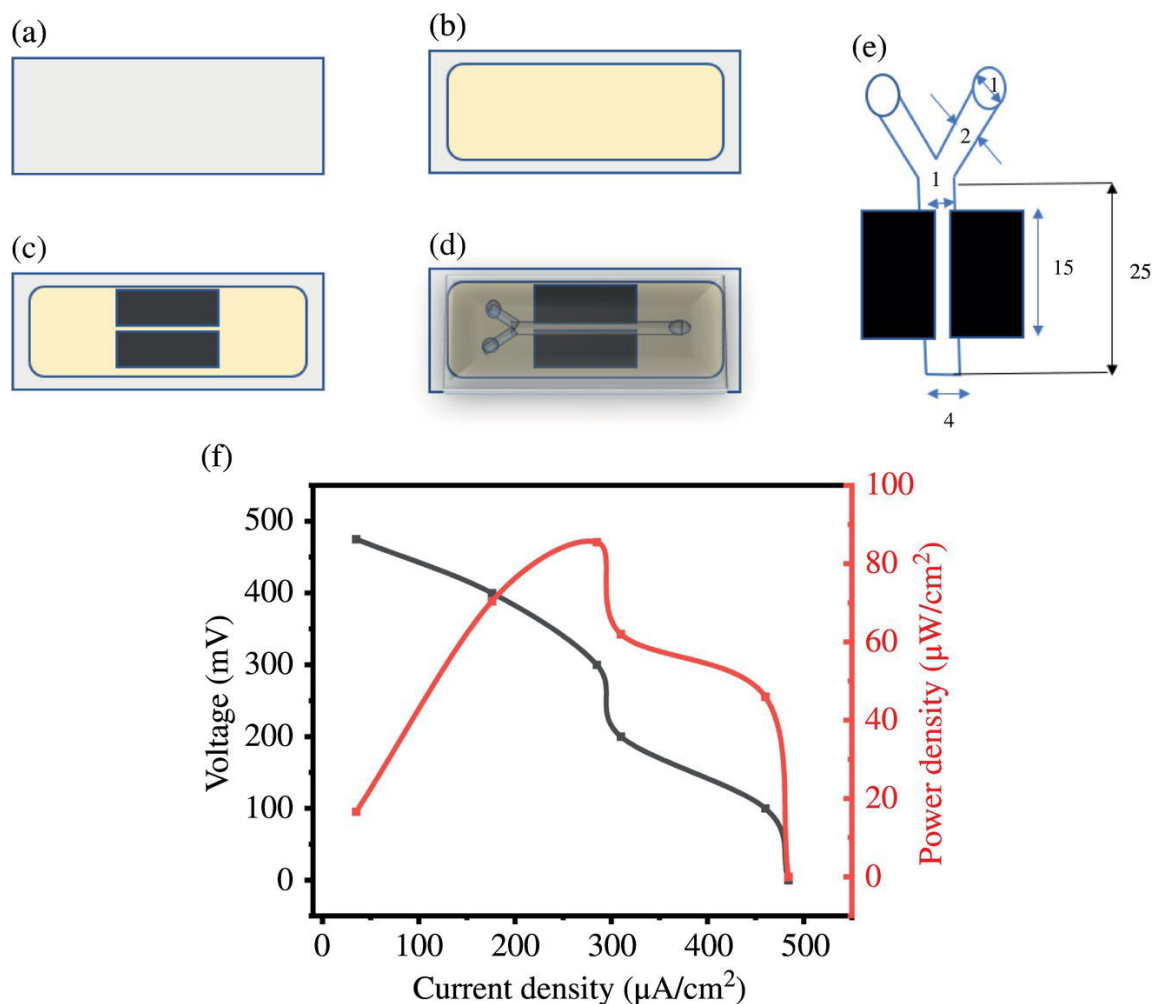


Figure 12.2 (a) PET sheet; (b) adhesive tape over PET sheet; (c) carbon cloth bioelectrodes; (d) microfluidic channel attached on surface; (e) cross-sectional image of bioelectrodes (2D); (f) polarization performance of biofuel cell.

Step 6: Cross linker glutaraldehyde 5 μL drop cast on the electrode surface at 1-hour regular intervals and washed with PBS. Keep them there until usage at 4 $^{\circ}\text{C}$.

12.2.2.4 Instrument Process to Text Device Performance

Step 1: Follow the three-electrode system; find the 40 mM glucose concentration (LSV) effect of the device, and measure the voltage and current values. Then connect the device to a potentiostat (two-electrode system) and evaluate the device

performance using CA protocols. Later drop the maximum voltage to the minimum voltage and find the highest current

Step 2: The greatest OCV to 0 mV measurement for each study is used to reduce the potential window and determine the current density for each condition.

Step 3: After determining the equivalent circuit based on the electrode material using any reference, fit the curve with the use of EIS techniques to find out R_{ct} values of the device performance; applied frequency was 100 kHz.

Step 4: To plot the polarization performance, multiply the OCV and current density to obtain the device power density. This fabricated enzymatic biofuel generated impressive open-circuit voltage (OCV) values of 475 mV and a maximum power output of $85 \mu\text{W}/\text{cm}^2$ [10] as shown in [Figure 12.2f](#).

12.2.3 Conclusion

This is the initial study that we are aware of that integrates modified carbon cloth electrodes in a paper microfluidic device produced $85 \mu\text{W}/\text{cm}^2$ and can be utilized for real-time application. Research on carbon cloth-based enzymatic biofuel cells with nano-functionalized bioelectrodes will be prompted by further advancements in nanocarbon materials, and the end product will be outstanding durability power sources that can compete in fast-paced energy markets.

12.3 Microbial Fuel Cells (MFCs)

12.3.1 Introduction

Microbial fuel cells (MFCs) form a bioelectrochemical system that uses microorganisms, such as bacteria, to generate electricity from organic matter. T-shaped biofuel cells are constructed using a simple redox mediator and inexpensive fabrication method under the co-laminar flow environment [11]. Microfluidics paper-based devices have garnered significant attention globally owing to their efficiency, accessibility, and adaptation [12]. Supercapacitors, medical field

devices, and other low-power portable devices can all benefit from using MFCs as a high-quality power source because of their natural biocompatibility, regular functioning conditions, and high specificity and sensitivity.

12.3.2 Experimentation

12.3.2.1 Prerequisites

Multiwalled carbon nanotube (MWCNT), bucky paper (BP) purchased from fuel cell, USA, glass slide, isopropyl alcohol (IPA), (Graphtec, Japan – Graphtec CE-2000), grade 1 filter paper, T-shaped microchannel, *E. coli* bacterial, sodium chloride (NaCl), Luria Bertani (LB) broth, potentiostat/galvanostat (SP-150 from Biologic Instruments, France).

12.3.2.2 Experimentation

Step 1: Highly conductive MWCNT dissolved with ethanol, and this composite BP was employed to create the bioelectrodes.

Step 2: The BP was chopped into 15 and 8 mm dimensions to create the BP-based bioelectrode and placed over a glass slide, as shown in [Figure 12.3a, c](#).

Step 3: After that, BP was cleaned with IPA to get rid of the physical, chemical, and other types of contaminations before being dried for 2 hours at 90°C in a hot-air oven.

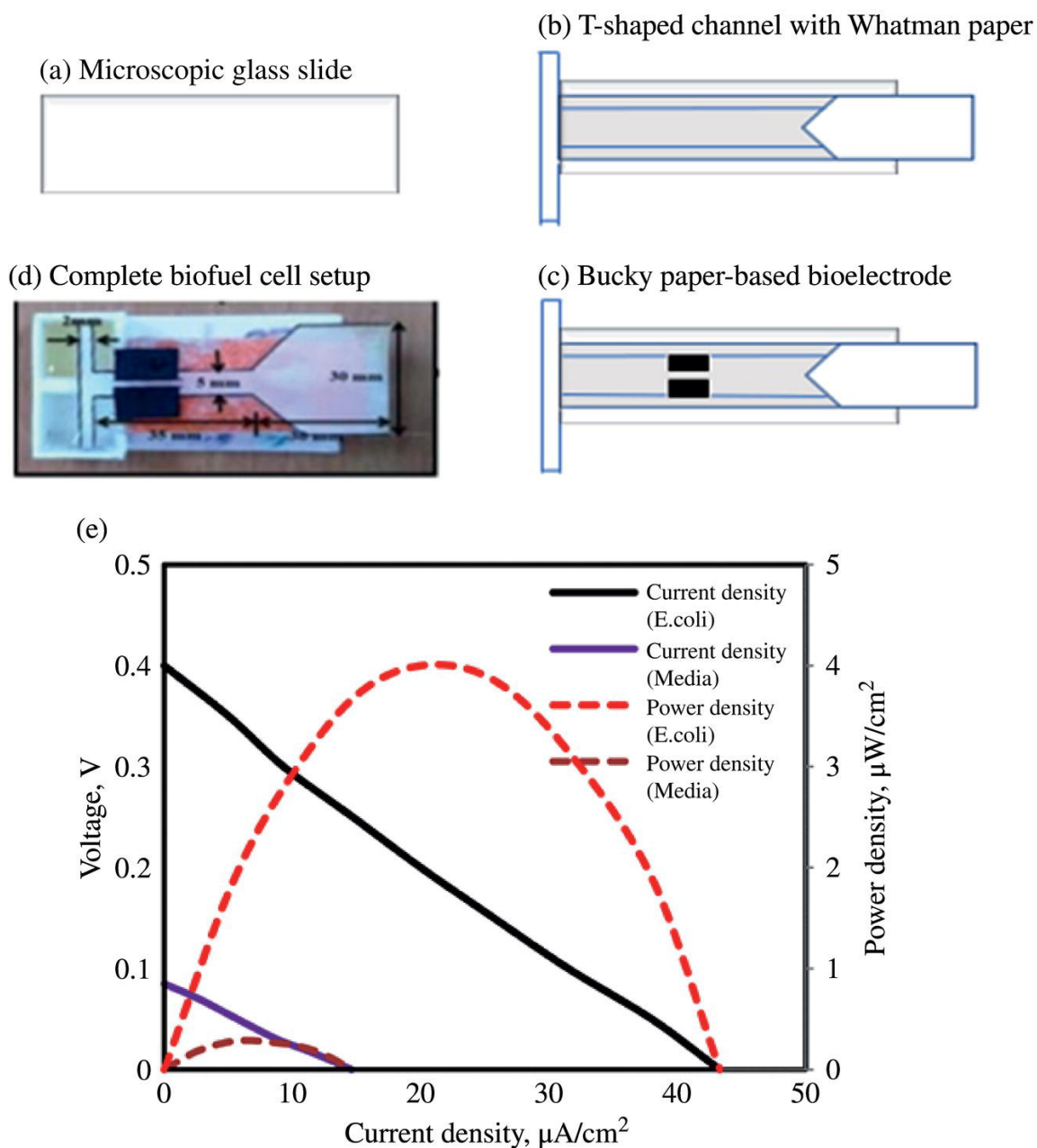


Figure 12.3 Fabrication steps of microbial fuel cell: (a) glass slide; (b) filter paper with T-channel; (c) bucky paper electrode; (d) working setup; (e) polarization performance of microbial fuel cell.

Step 4: The T-shaped pattern was etched using computer-controlled Graphtec studio software to augment a commercial cutter and plotter (Graphtec, Japan – Graphtec CE-2000) and shown in [Figure 12.3b](#).

Step 5: To make the most efficient use of the grade 1 filter paper, the entire cutting procedure was carried out at a speed of 4 cm/s and a force of 10 g.

Step 6: Two inlets and one exit were on the T-shaped microchannel. Two inlets were employed, one for oxygen (aerated water) and the other for analytes (bacteria), as shown in [Figure 12.3d](#).

Step 7: To prepare the *E. coli* bacterial culture 10 g of tryptone, 5 g of yeast, and 10 g of sodium chloride (NaCl) were added to Luria Bertani (LB) broth to create the *E. coli* bacterial culture. 200 µl of reconstituted *Escherichia coli* (*E. coli*) was allowed to incubate in a CO₂ incubator for 20 hours, then the optical density (OD) of 0.5 was determined using a calorimeter at 600 nm and calibrated with distilled water.

12.3.2.3 Process to Test Device Performance

Step 1: Take the manufactured electrode that has been placed within the electrolyte and the microfluidic paper channel will absorb the electrolyte and flow through the electrode channel then measure the open circuit voltage (OCV) with the help of potentiostat.

Step 2: Determine the device concentration (LSV) effect using the three-electrode system and measure the voltage and current of different concentrations. Using CA methods, the device performance is assessed by connecting it to a potentiostat (two-electrode setup). Then drop the voltage from max to min and find out the current density of each potential.

Step 3: Use the EIS techniques and find the impedance of the device using an equivalent circuit and apply the frequency of the device was 250 kHz.

Step 4: Use the greatest OCV to 0 mV measurement for each study to reduce the potential window and determine the current density for each condition. Then multiply the potential value and current density to get power density values.

Step 5: This device produced the maximum open-circuit potential of 398 mV, current density of $20 \mu\text{A}/\text{cm}^2$, and power density of $4 \mu\text{W}/\text{cm}^2$, as shown in [Figure 12.3e](#).

12.3.3 Conclusion

MFC is regarded as a dependable, tidy, effective technique that uses renewable sources of energy and produces no hazardous byproducts when used as an alternate form of power. This device power density of $4 \mu\text{W}/\text{cm}^2$. Current and voltage performance is demonstrated by the orientation and open circuit potential measurement in the presence of different bacterial quantities can be used for real-time purposes. By constructing, a parallel–series arrangement, this fuel cell demonstrated a great potential for low-power devices.

12.4 Electrochemical Characterization of Supercapacitor Energy Devices

12.4.1 Supercapacitor

A flexible supercapacitor is an energy storage device that combines the high-power density of capacitors with the high-energy density of batteries [\[13\]](#). It is designed to be flexible, bendable, and even stretchable, allowing electrical energy to be stored. This makes supercapacitors suitable for applications where stiff and heavy batteries cannot be used, such as in wearable technologies, flexible displays, and portable electronic gadgets [\[14\]](#). Supercapacitor works on three mechanisms: electric double layer capacitor, pseudocapacitor, and hybrid supercapacitor. EDLCs store energy by electrostatically segregating charge inside the double layer of ions formed at the electrode-electrolyte interface, enabling rapid cycles of charge and discharge [\[13\]](#). On the other hand, pseudocapacitors store energy through rapid, reversible redox processes involving electron transport at the electrode surface. The performance characterization of electrochemical supercapacitor electrode materials is typically conducted using a three-electrode system: a working electrode, a reference electrode, and a counter electrode [\[15\]](#).

In this section, the steps for the fabrication and electrochemical characterization of the boron-doped laser-induced graphene (BLIG) supercapacitor are discussed. For the electrochemical characterization, cyclic voltammetry (CV), EIS, and galvanostatic charge-discharge (GCD) methods are employed.

12.4.2 Experimentation

12.4.2.1 Brief Overview

The main objectives of testing a supercapacitor are to evaluate its storage mechanism, capacitance, energy density, and power density. This involves three key techniques: CV, electrochemical impedance spectroscopy, and galvanostatic charge-discharge.

12.4.2.2 Prerequisites

Blue laser-head diode system (ZMorph VX, Wroclaw, Poland), potentiostat (OrigaFlex-OGF500 from Origalys, France) for performance analysis and electrochemical setup. For substrate-making, polyimide (PI) resin (Abron s10) (from ABR Organics Limited) is used.

Step 1: Select the modified paper (herein BLIG paper-based electrode selected) (see [Figure 12.4](#)).

Step 2: Draw a design (20×5 as shown in [Figure 12.4](#)) in computer-aided designing software and convert it into .dxf format for engraving.

Step 3: The required area was engraved to create the conductive electrode using a visible blue light laser with a wavelength of 450 nm and a power of 2.8 W. The laser was operated at optimized settings, with speed and power set to 20% and 100%, respectively [[16](#)]. (see [Figure 12.4](#)).

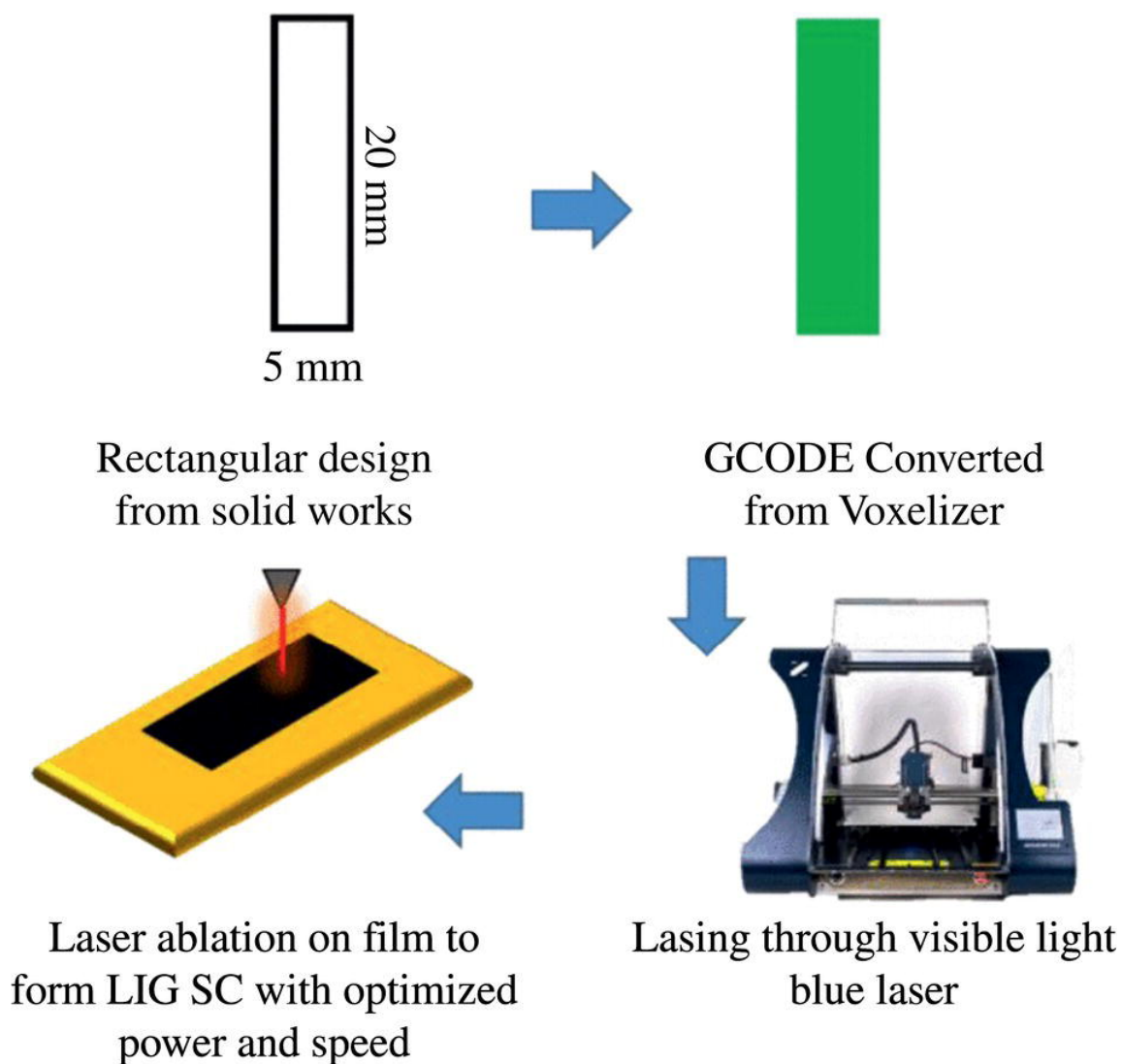


Figure 12.4 Electrode fabrication process steps to form doped laser induced graphene on the flexible substrate [16]/with permission of IEEE.

Step 4: In bulk studies, a three-electrode system is employed where a conductive electrode serves as the working electrode, a platinum rod functions as the reference electrode, and an Ag/AgCl electrode is used as the counter electrode.

Step 5: Analyze the electrochemical characterization.

12.4.3 Electrochemical Characterization Technique for the Supercapacitor Device

12.4.3.1 Cyclic Voltammetry (CV)

CV is a method used to measure the capacitance and potential of the supercapacitor. In this method, the potential of the cell is swept through a range of values while the current response is measured. The CV curve determines various electrochemical properties, such as capacitance, charge transfer resistance, and redox reaction kinetics. Regarding the parameter settings, parameters such as the voltage window and scan rate need to be set as per requirement. For instance, the voltage window should be specified, typically 0–0.8 V. The scan rate can vary from 5 to 100 mV/s, as illustrated in [Figure 12.5a, b](#). These figures show the effect of the scan rate on bare LIG and doped LIG, respectively. The comparative scan rate at 50 mV/s is depicted in [Figure 12.5a](#), with the capacitance measured at 12.3 mF/cm² for LIG and 29.7 mF/cm² for doped LIG. The areal capacitance calculation from the CV data is performed using the equation provided below:

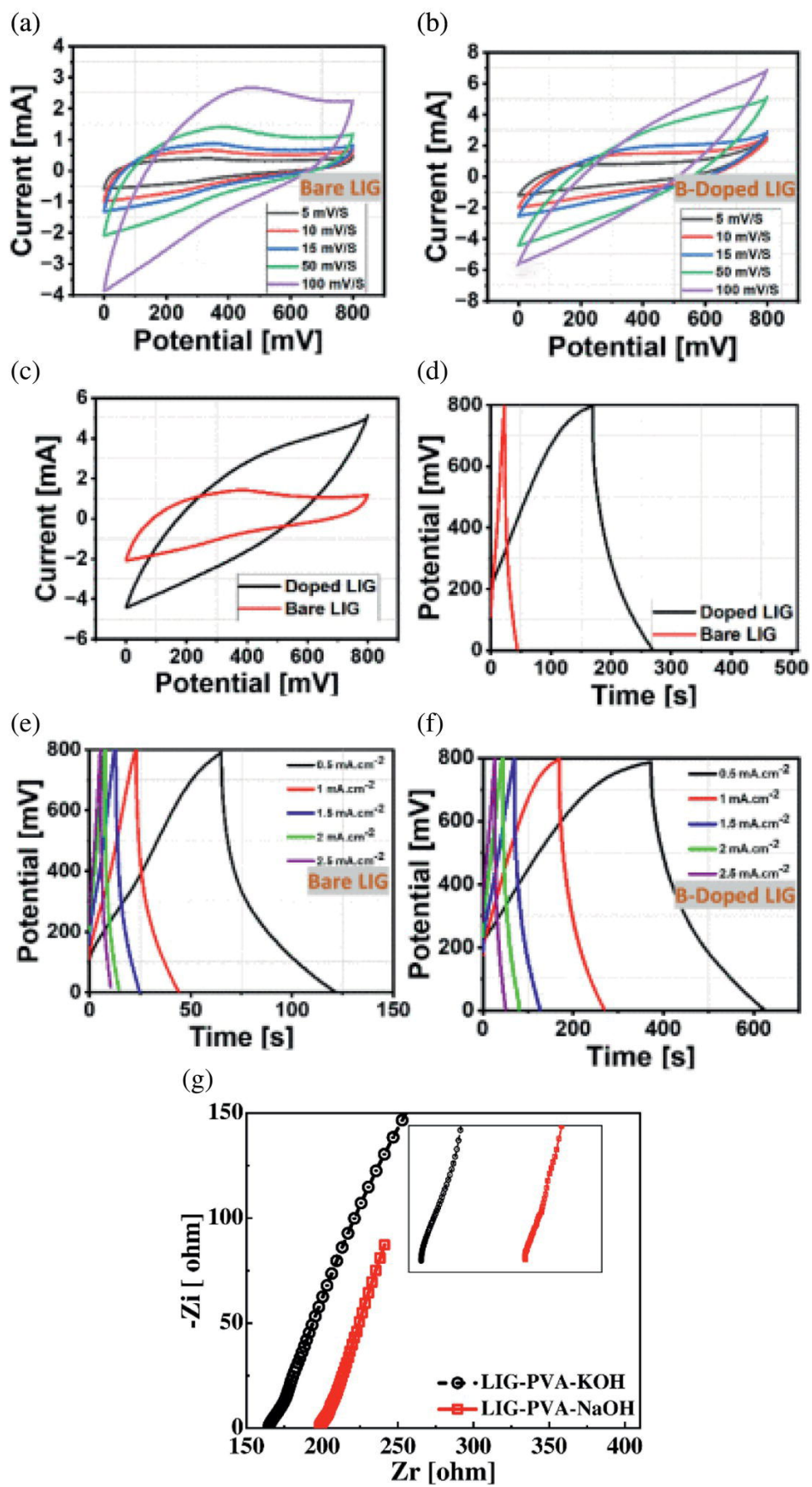


Figure 12.5 Electrochemical analysis: (a)–(c) CV, (d)–(f) GCD analysis (g) EIS [Adapted from \[13, 16\]](#).

$$C = \int_{v_1}^{v_2} IdV / S\Delta V_v \quad (12.1)$$

12.4.3.2 Galvanostatic Charge/Discharge (GCD)

This method involves charging and discharging the cell at a constant current to determine the capabilities of the supercapacitor. The capacitance of the supercapacitor, the potential difference that exists between the electrodes, and the discharge duration will all be calculated with the use of the GCD curve shown in [Figure 12.5b](#).

[Figure 12.5c](#) shows a comparative analysis of a particular single 50 mV/s scan rate and [figure 12.5f](#) shows comparative analysis of GCD in particular single current density. For GCD parameter settings, the current density should be specified as the load, and the time of the charging and discharging processes is analyzed according to the specific current density. [Figure 12.5e, f](#) show the GCD for LIG and doped LIG at different current densities ranging from 0.5 to 2.5 mA/cm². [Figure 12.5d](#) is a comparative analysis of the LIG and doped LIG that shows the areal capacitance of 15.6 and 78.1 at 2.5 mA/cm² for LIG and BLIG, respectively. The calculation has been performed using the following equation:

$$C = \frac{I \cdot \Delta t}{A \cdot \Delta V} \quad (12.2)$$

12.4.3.3 Electrochemical Impedance Spectroscopy (EIS)

EIS is a method that measures the impedance of a supercapacitor as a function of frequency. This method also provides information on the resistance and capacitance of the cell being measured on the curve shown in [Figure 12.5g](#). Regarding parameter settings, the frequency range should be provided, including minimum and maximum. In [Figure 12.5](#), the frequency range of 1 KHz–100 MHz at a constant current density of 0.5 mA/cm² is used to analyze the performance of the supercapacitor performance.

12.4.4 Conclusion

The electrochemical testing provided significant reports about the capabilities of the supercapacitor, including its areal capacitance and quick charge-discharge cycles. These findings show that the supercapacitor is efficient and reliable, making it an ideal option for energy storage applications. In CV, the areal capacitance of 29.7 mF/cm² is observed in doped laser-induced graphene at 50 mV/s. In GCD, the areal capacitance is 78.125 mF/cm² at 2.5 mA/cm² is observed. The findings direct further developments and demonstrate how supercapacitors can completely transform energy storage by providing quick charge-discharge capabilities for an efficient and sustainable energy environment.

References

- 1 Wang, Y. et al. (2019). A flexible paper-based hydrogen fuel cell for small power applications. *Int. J. Hydrogen Energy* 44 (56): 29680–29691. <https://doi.org/10.1016/J.IJHYDENE.2019.04.066>.
- 2 Reber, D., Kühnel, R.S., and Battaglia, C. (2017). High-voltage aqueous supercapacitors based on NaTFSI. *Sustain. Energy Fuels* 1 (10): 2155–2161. <https://doi.org/10.1039/c7se00423k>.
- 3 Singla, M.K., Nijhawan, P., and Oberoi, A.S. (2021). Hydrogen fuel and fuel cell technology for cleaner future: a review. *Environ. Sci. Pollut. Res.* 28 (13): 15607–15626. <https://doi.org/10.1007/s11356-020-12231-8>.
- 4 Moore, R.M., Hauer, K.H., Ramaswamy, S., and Cunningham, J.M. (2006). Energy utilization and efficiency analysis for hydrogen fuel cell vehicles. *J. Power Sources* 159 (2): 1214–1230. <https://doi.org/10.1016/j.jpowsour.2005.12.083>.
- 5 Samir De, B., Cunningham, J., Khare, N. et al. (2022). Hydrogen generation and utilization in a two-phase flow membraneless microfluidic electrolyzer-fuel cell tandem operation for

- micropower application. *Appl. Energy* 305 (September 2021): 117945. <https://doi.org/10.1016/j.apenergy.2021.117945>.
- 6** Vanmathi, S. et al. (2024). IoT enabled carbon cloth-based 3D printed hydrogen fuel cell integrated with supercapacitor for low-power microelectronic devices. *Scientific Reports* 14 (1): 16953.
 - 7** Rewatkar, P., Kothuru, A., and Goel, S. (2020). PDMS-based microfluidic glucose biofuel cell integrated with optimized laser-induced flexible graphene bioelectrodes. *IEEE Trans. Electron Dev.* 67 (4): 1832–1838.
<https://doi.org/10.1109/TED.2020.2971480>.
 - 8** Kim, M., Kwon, Y., and Ahn, Y. (2021). Paper-based mediatorless enzymatic microfluidic biofuel cells. *Biosens. Bioelectron.* 190 (April): 113391. <https://doi.org/10.1016/j.bios.2021.113391>.
 - 9** C.-H. Kuo et al. (2013). Biofuel cells composed by using glucose oxidase on chitosan coated carbon fiber cloth.
www.electrochemsci.org
 - 10** Vanmathi, S. and Goel, S. (2024). Microfluidic carbon cloth-based enzymatic glucose biofuel cell for sustainably powering a microelectronic circuit. *J. Micromech. Microeng.* 34 (8):
<https://doi.org/10.1088/1361-6439/ad5b6b>.
 - 11** Nath, D., Sai Kiran, P., Rewatkar, P. et al. (2019). Escherichia coli fed paper-based microfluidic microbial fuel cell with MWCNT composed Bucky paper bioelectrodes. *IEEE Trans. Nanobioscience* 18 (3): 510–515.
<https://doi.org/10.1109/TNB.2019.2919930>.
 - 12** Li, S., Cheng, C., and Thomas, A. (2017). Carbon-based microbial-fuel-cell electrodes: from conductive supports to active catalysts. *Adv. Mater.* 29 (8): <https://doi.org/10.1002/adma.201602547>.
 - 13** Awasthi, H., Renuka, H., Srivastava, A.K., and Goel, S. (2022). Laser-induced graphene-based flexible interdigital electrode realizing micro supercapacitor sustainable in different temperatures. *Energy Storage* e405:
<https://doi.org/10.1002/EST2.405>.

- 14** Atta, M.M. and Fahim, R.A. (2021). Flexible and wearable supercapacitors: a short review. *J. Energy Storage* Elsevier Ltd. <https://doi.org/10.1016/j.est.2021.103475>.
- 15** Libich, J., Máca, J., Vondrák, J. et al. (2018). Supercapacitors: properties and applications. *J. Energy Storage* 17 (March): 224–227. <https://doi.org/10.1016/j.est.2018.03.012>.
- 16** Awasthi, H., Rao, B.P., Thundat, T., and Goel, S. (2024). Boron doped laser-induced graphene: a suitable substrate for flexible and wearable sensor and supercapacitor. *IEEE Sens. Lett.* 8 (4): 1–4. <https://doi.org/10.1109/LSENS.2024.3375286>.

Note

* Equally Contributing Author.

Conclusion and Future Outlook

Amreen Khairunnisa

*MEMS, Microfluidics and Nanoelectronics (MMNE) Lab,
Department of Electrical and Electronics Engineering, Birla
Institute of Technology and Science (BITS) Pilani, Hyderabad
Campus, Hyderabad, Telangana, India*

The practical lab manual has been structured with the idea of providing complete hands-on experimental knowledge to undergraduate and postgraduate students. The experiments discussed are a part of the curriculum for Bachelor of Technology (B. Tech.)/Bachelor of Engineering (B.E.), Master of Technology (M. Tech.)/Master of Engineering (M.E.) programs, especially in mechanical, electrical and electronics, chemical streams. For a comprehensive learning, the manual is strategically divided into sections focusing on the basics. Hence, it is suitable for nonexperts to understand. Each section has been divided into chapters with detailed step-wise procedures. Section I covers the “Simulation” based studies.

Herein, four experimental analyses based on COMSOL simulation are discussed. Section II focuses on diverse fabrication techniques. It has four chapters covering state-of-the-art fabrication techniques and procedures. With the target group as untrained students, each of the procedures described has been performed prior, and corresponding videos are also provided. Some of the procedures, like “cleanroom assisted,” require a sophisticated setup and may not be feasible for all. Therefore, a demonstration video has also been provided. Section III primarily aims to give practical knowledge in the context of characterization techniques. Various morphological, physio-chemical, and compositional characterization methods are discussed. Each chapter in this section focuses on different characterization approaches useful for surface as well as structural analysis. Detailed step-wise procedures and corresponding videos are also given. The last section deals with experimental procedures for

various applications in areas like microfluidics, electrochemical, energy harvesting/storage, etc. Each experimental procedure described can be replicated by the reader. Versatile applications are covered to enhance the practical usage of the manual in real time as a beginners guide or curriculum.

Additionally, the manual extensively covers all the basic experimental procedures. In the future, there is a prospect for II volume with advanced experimental protocols. The study will focus on various other parameters, including the design of experiment procedures, machine-learning-based experiments, artificial intelligence, and graphic-user interface-based experiments, which can be explored. Furthermore, simulation-based experiments can also be expanded to various other fields of bioinformatics, chemical analysis, clinical assays, etc. MEMS Microfluidics and Nanoelectronics Laboratory (MMNE) lab has in-house developed protocols for the fabrication of devices for real-time analysis of environmental pollutants, soil analysis, supercapacitors, fuel cells, and wearable devices, which have been patented and are in the process of commercialization through the spin-off companies. Advanced learners can cover the fabrication of these devices. In addition to the conventional protocols of techniques like 3D-printing, soft lithography, etc., MMNE has successfully developed alternate strategies that limit the steps in fabrication, use of raw materials, single-step fabrication, embroidery-based devices, etc., which can be included as protocols as a separate manual. In addition, the curriculum of the experiments that are being carried out at industrial levels may also be explored in the future. Overall, this manual provides immense basic skill training, inculcating advanced learning in the nontechnical aspirants.

Index

a

absorbance [90](#), [91](#), [102](#), [104](#), [118](#)

absorption [89](#), [90](#), [92](#), [100](#), [103](#), [118](#), [123](#)

analyte [36](#), [43](#), [56](#), [91](#), [105](#), [106](#), [111](#)–[114](#), [117](#)–[119](#), [123](#), [124](#), [151](#), [155](#)

attenuated total reflectance [100](#)

b

Beer-lambert law [118](#), [123](#)

bending [81](#), [102](#), [103](#)

biocompatibility [30](#), [67](#), [153](#)

biomarkers [1](#), [36](#), [45](#), [64](#), [65](#), [67](#), [105](#)–[114](#), [116](#), [123](#), [138](#)

biomedical [22](#), [26](#), [35](#), [41](#), [45](#), [54](#), [60](#), [87](#), [100](#), [142](#), [145](#)

biosensing [43](#), [65](#), [69](#), [115](#)

biosensor [36](#), [37](#), [44](#), [59](#), [60](#), [62](#), [63](#), [66](#), [67](#), [124](#), [142](#)

blue laser [111](#), [149](#), [156](#)

c

capillary action [124](#), [127](#)

carbon cloth [136](#), [148](#), [149](#), [151](#), [152](#), [153](#)

carbon ink [60](#), [63](#), [109](#)

chronoamperometry (CA) studies [144](#), [150](#)

cleanroom operations [26](#)

CO₂ laser [41](#)–[44](#), [54](#), [65](#), [107](#)–[109](#), [113](#), [137](#), [140](#), [151](#)
colorimetry [119](#), [124](#).
complex designs [1](#)
composition [72](#), [73](#), [89](#), [90](#), [92](#), [94](#)–[97](#), [100](#), [101](#), [163](#)
concentration [1](#)–[10](#), [35](#), [64](#), [90](#), [91](#), [102](#), [105](#), [106](#), [108](#), [110](#), [111](#), [113](#),
[114](#), [117](#), [118](#), [123](#), [144](#), [145](#), [150](#), [152](#), [155](#)
conductive pattern [49](#), [50](#)
continuous phase [56](#)
co-reactant [115](#)
cost-effective [43](#), [82](#), [119](#), [139](#).
curing agent [55](#), [120](#), [139](#), [140](#)
cyclic voltammetry (CV) [67](#), [108](#), [109](#), [111](#)–[113](#), [144](#), [156](#)–[159](#)

d

deposition [21](#), [23](#), [24](#), [26](#), [29](#), [34](#)–[37](#), [60](#), [66](#)–[69](#)
designing [2](#), [3](#), [25](#)–[26](#), [30](#)–[32](#), [34](#), [36](#)–[37](#), [43](#), [54](#)–[57](#), [60](#)–[61](#), [68](#),
[107](#), [120](#)–[122](#), [129](#), [136](#), [156](#)
device development [22](#), [36](#), [116](#), [118](#), [123](#), [131](#), [136](#), [145](#)
digital light processing (DLP) [29](#)
direct laser writing (DLW) [55](#), [79](#), [80](#), [119](#), [120](#)
dispersed phase [149](#).
disposable [123](#)–[127](#)
DNA sensor [107](#)
droplet microfluidics [13](#), [14](#)

e

e-beam evaporation methods [67](#)

eco-friendly substrates [123](#)–127
electrical signal [105](#)
electrochemical sensing [106](#)
electrochemical sensor [41](#)–44, [62](#)–66, [105](#)–109, [111](#), [113](#), [114](#)
electrochemiluminescence [34](#)–37, [63](#), [114](#)–117
electrodes [34](#)–37, [42](#)–44, [46](#), [49](#), [59](#)–69, [74](#), [106](#)–117, [143](#)–145, [147](#), [148](#), [150](#)–157, [159](#)
electron beam [66](#), [67](#), [73](#)
electronics [22](#), [26](#), [59](#), [63](#), [91](#), [98](#), [142](#), [147](#), [156](#), [163](#)
elemental composition [94](#)–96
energy devices [147](#)–159
engraving [109](#), [137](#), [156](#)
environmental pollutants [105](#)–114, [123](#), [164](#)
enzymatic biofuel cell [150](#)–153
Escherichia coli (*E. coli*) [43](#), [106](#)–108, [153](#), [155](#)
etching [21](#), [23](#), [24](#), [26](#)
extrusion [30](#), [34](#)

f

fabrication [21](#), [23](#), [25](#), [29](#), [30](#), [34](#)–37, [41](#)–44, [53](#)–57, [59](#)–69, [107](#)–109, [111](#), [113](#)–115, [117](#), [123](#), [129](#)–131, [136](#), [137](#), [139](#), [140](#), [143](#), [148](#), [149](#), [151](#), [153](#), [154](#), [156](#), [157](#), [163](#), [164](#)
feedstock filament [34](#), [35](#)
fingerprint regions [103](#)
flexible electronics [63](#)
flowrates [6](#)
flow simulations [2](#)
flow visualization [4](#)

Fourier transform infrared (FTIR) spectroscopy [89](#), [100](#)–104
fuel cell [41](#), [63](#), [142](#)–145, [147](#)–149, [150](#)–155, [164](#)
fused deposition modeling (FDM) [29](#), [34](#)–37

g

glucose biofuel cell [160](#)
gold electrodes [67](#)–69
graphene [36](#), [41](#)–45, [65](#), [85](#), [86](#), [99](#), [100](#), [108](#), [135](#)–138, [157](#)
graphene oxide (GO) [45](#), [90](#)
graphite crucibles [67](#)
graphite pencil electrode [143](#)

h

hard mask [68](#), [69](#)
highly conductive [154](#)

i

imaging [63](#), [73](#), [79](#), [81](#), [82](#)
impact in flow
inkjet printing [29](#), [59](#)–62, [109](#), [115](#), [124](#)
intensity [94](#), [95](#), [98](#), [117](#), [118](#), [123](#)
isothermal nucleic acid amplification [131](#), [139](#), [141](#)

k

KBr pellets [102](#)
Kirigami [136](#)–138

I

laser alignment [98](#)

laser-induced graphene (LIG) [41](#), [44](#), [85](#), [86](#), [108](#), [135–138](#), [156](#), [157](#), [159](#)

laser system [43](#), [45](#), [65](#), [149](#), [151](#)

laser writing [43](#), [53](#), [55](#), [80](#), [119](#), [120](#)

layer-by-layer printing [29](#), [35](#)

layer printing

lithography [25](#), [26](#), [53–57](#), [59](#), [68](#), [69](#), [107](#), [109](#), [123](#), [129](#), [131](#), [140](#), [164](#)

low sheet resistance

luminophore [114](#)

m

masking

maskless photolithography (MPL) [54](#)

material characterization [71](#)

metal films [67](#)

microchannel inkjet printing

microchannels [13–18](#), [79](#), [80](#), [119](#), [129](#), [131](#), [139](#), [140](#), [151](#), [153](#), [155](#)

microflow

microfluidic devices [14](#), [22](#), [26](#), [31](#), [53–57](#), [80](#), [105–131](#), [138–142](#), [153](#)

microfluidics [1](#), [2](#), [13–18](#), [22](#), [26](#), [29–34](#), [53–57](#), [60](#), [63](#), [69](#), [79](#), [80](#), [105–131](#), [138–142](#), [151–153](#), [155](#), [164](#)

micromixing

micro paper analytical devices (μ PADs) [123–127](#)

miniaturized [118](#)
molecular biology [128](#), [138](#)
multiphysics [1](#)–10, [13](#)–18
multiple sensing applications

n

numerical simulation [11](#), [18](#)

o

optical LED microscope [79](#)–82

p

paper [45](#)–50, [60](#), [63](#), [67](#), [74](#), [111](#), [112](#), [115](#), [118](#), [124](#), [126](#), [127](#), [143](#),
[144](#), [149](#), [153](#)–156
paper pore distributions
papertronics [51](#)
passive microfluidics [1](#)
patch-type [146](#)
pathogen [107](#), [119](#), [124](#)
pattern [4](#), [21](#)–26, [47](#)–50, [53](#), [54](#), [55](#), [56](#), [65](#), [69](#), [73](#), [76](#), [78](#), [119](#), [125](#),
[127](#), [129](#), [131](#), [137](#), [138](#), [155](#)
pattern imprinting [55](#)
photoacoustic
photolithography [21](#)–26, [53](#), [54](#), [117](#), [131](#)
photopolymers
photoresist [21](#), [22](#), [23](#), [26](#), [53](#), [54](#), [55](#), [119](#), [120](#), [121](#), [122](#), [131](#)
photoresist development [21](#), [120](#)–122

physical vapor deposition (PVD) [66](#)–69
plasma bonding [56](#), [108](#), [123](#), [131](#)
point-of-care (PoC) [1](#), [59](#), [115](#), [135](#), [139](#), [142](#)
polydimethylsiloxane (PDMS) [53](#), [118](#)–120, [139](#)
polyimide (PI) [41](#), [43](#), [44](#), [63](#), [65](#), [66](#), [102](#), [109](#), [113](#), [115](#), [136](#), [137](#),
[156](#)
portable [64](#), [129](#), [142](#), [153](#), [156](#)
potential [36](#), [42](#), [45](#), [50](#), [53](#), [89](#), [90](#), [106](#), [108](#)–112, [114](#), [115](#), [119](#), [127](#),
[136](#), [139](#), [142](#), [144](#), [145](#), [148](#), [150](#), [152](#), [155](#), [157](#), [159](#)
potentiostat [107](#), [108](#), [111](#), [113](#), [143](#), [144](#), [148](#)–153, [155](#), [156](#)

r

Raman spectra [98](#)–100
Raman spectroscopy [89](#), [97](#)–100, [103](#)
rapid prototyping [29](#), [34](#)
reagent mixing [128](#)
reduced graphene oxide (rGO) [45](#)–50, [91](#), [111](#), [149](#)
refractive index [89](#), [100](#)
respiratory health [136](#), [138](#)

s

scanning electron microscopy (SEM) [71](#)–72
screen printing [59](#), [62](#)–66, [107](#), [115](#), [117](#)
secondary electrons [72](#)
signal [35](#), [73](#), [94](#), [98](#), [99](#), [105](#), [114](#)–117
sleep apnea
smart manufacturing

soft lithography [53](#)–[57](#), [107](#), [109](#), [129](#), [131](#), [140](#), [164](#).
spectra [73](#), [89](#), [92](#), [94](#), [96](#), [98](#)–[100](#), [102](#), [103](#)
spectral calibration [98](#)
spectrophotometer [90](#)–[92](#)
spectroscopic characterization [89](#)–[104](#)
spectroscopy [42](#), [67](#), [89](#), [90](#)–[104](#), [144](#), [150](#), [156](#), [159](#).
specular reflectance [101](#)
sputter coater [72](#), [73](#)
stereolithography (SLA) [29](#)–[34](#)
stretching [102](#), [103](#)
substrate [21](#), [22](#), [23](#), [25](#), [26](#), [36](#), [43](#), [49](#), [53](#), [54](#), [56](#), [59](#)–[63](#), [65](#)–[67](#),
[68](#), [69](#), [79](#), [83](#), [84](#), [85](#), [86](#), [87](#), [93](#), [97](#), [98](#), [107](#), [109](#), [111](#), [115](#), [118](#), [122](#)–
[127](#), [129](#), [130](#), [131](#), [136](#), [137](#), [143](#), [144](#), [149](#), [151](#), [156](#), [157](#)
supercapacitors [41](#), [45](#), [147](#), [153](#), [156](#)–[159](#), [164](#).

t

thermal management [131](#)
3D barriers [124](#), [125](#)–[127](#)
3D CAD [125](#), [149](#).
3D modelling [15](#)
3D printing [29](#)–[37](#), [46](#), [54](#), [59](#), [115](#), [117](#), [118](#), [124](#), [125](#)–[127](#), [148](#), [149](#),
[164](#).
three-electrode system [44](#), [46](#), [66](#), [106](#)–[109](#), [111](#)–[113](#), [144](#), [150](#), [152](#),
[155](#)–[157](#)
transducer [105](#), [106](#)
transduction [67](#)
transmission [90](#), [94](#), [101](#), [102](#)

u

ultrafast [51](#), [104](#).

Ultraviolet-visible (UV-Vis) spectroscopy [89](#)–[92](#), [103](#), [104](#).

UV light

v

vacuum chamber [67](#)

vacuum thermal evaporation [67](#)

vibration energy [102](#)

visible light laser [51](#), [104](#), [157](#)

voltage [67](#), [69](#), [74](#), [76](#), [106](#), [111](#), [114](#), [117](#), [137](#), [138](#), [144](#), [148](#), [150](#), [152](#)–[155](#), [157](#)

w

wavelength [45](#), [74](#), [75](#), [77](#), [79](#), [82](#), [90](#), [91](#), [98](#), [102](#), [104](#), [118](#), [123](#), [156](#)

wavenumber [98](#), [99](#), [103](#)

wearable [135](#)–[145](#), [156](#), [164](#)

wearable sensor [136](#)

working electrode (WE) [36](#), [106](#), [144](#), [150](#), [156](#), [157](#)

x

X-ray photoelectron spectroscopy (XPS) [89](#), [92](#)–[96](#)

y

Y-channel design [10](#), [31](#), [54](#)

IEEE Press Series on Sensors

Series Editor: Vladimir Lumelsky, Professor Emeritus,
Mechanical Engineering, University of Wisconsin-Madison

Sensing phenomena and sensing technology is perhaps the most common thread that connects just about all areas of technology, as well as technology with medical and biological sciences. Until the year 2000, IEEE had no journal or transactions or a society or council devoted to the topic of sensors. It is thus no surprise that the IEEE Sensors Journal launched by the newly-minted IEEE Sensors Council in 2000 (with this Series Editor as founding Editor-in-Chief) turned out to be so successful, both in quantity (from 460 to 10,000 pages a year in the span 2001–2016) and quality (today one of the very top in the field). The very existence of the Journal, its owner, IEEE Sensors Council, and its flagship IEEE SENSORS Conference, have stimulated research efforts in the sensing field around the world. The same philosophy that made this happen is brought to bear with the book series.

- *Magnetic Sensors for Biomedical Applications*
Hadi Heidari and Vahid Nabaei
- *Smart Sensors for Environmental and Medical Applications*
Hamida Hallil and Hadi Heidari
- *Whole-Angle MEMS Gyroscopes: Challenges, and Opportunities*
Doruk Senkal and Andrei M. Shkel
- *Optical Fibre Sensors: Fundamentals for Development of Optimized Devices*
Ignacio Del Villar and Ignacio R. Matias
- *Pedestrian Inertial Navigation with Self-Contained Aiding*
Yusheng Wang and Andrei M. Shkel
- *Sensing Technologies for Real Time Monitoring of Water Quality*
Libu Manjakkal, Leandro Lorenzelli, and Magnus Willander

- *Solid-State Sensors*
Ambarish Paul, Mitradip Bhattacharjee, and Ravinder Dahiya
- *Biosensors: Nanomaterials, Approaches, and Performance-Enhancement Strategies*
Baljinder Kaur, Santosh Kumar, and Brajesh Kumar Kaushik
- *Micro Electromechanical Systems (MEMS): Practical Lab Manual*
Sanket Goel

WILEY END USER LICENSE AGREEMENT

Go to www.wiley.com/go/eula to access Wiley's ebook EULA.